


# High-Pressure Studies of Macrocycle Coordination Complexes

**Jeremiah Philip Tidey MSci**

**Thesis submitted to the University of Nottingham for the degree of Doctor of Philosophy**

**November 2016**

**Declaration**

Except where specific reference is made to other sources, the work presented in this thesis is the original work of the author. The work herein has not been submitted in whole or in part for any other degree.

Signed: Jeremiah P. Tidey

Date: 06/11/2016

# Acknowledgements

I must start by extending my deepest gratitude to Prof. Sandy Blake. Throughout my PhD he has provided invaluable teaching, support and encouragement, without which there were times where I no doubt would have adopted failure and left. It is on account of his guidance that I am still on this career path. Similar thanks are owed to Prof. Martin Schröder for his own support at critical junctures that further guided my progression through this PhD and towards academia. I, of course, owe the most fundamental thanks to these gentlemen for giving me the opportunity to study here.

In Chapter 2, density functional theory calculations are included that used CASTEP. These were performed by Alice O'Connor, Dr. E. Bichoutskaia and Dr. A. Markevich, Gratitude is also owed to Graham Coxhill, for performing mass spectrometry on a minute sample of the epitaxially retrieved β phase, and to Geoffrey Lawrance of the University of Newcastle, Australia, who synthesised the original sample of [$PdCl_2$([9]ane$S_2O$)] where all this began.

In Chapters 3 through 6, DFT calculations are run employing the Amsterdam Density Functional suite. These were greatly aided by instruction and fruitful discussion with Dr. Jon McMaster, Dr. Carlo Perotto and George Marshall who was an invaluable assistance to this end. Thanks also to Dr. Tim Easun and John Whalley for their help designing and building the UV/vis rig used in Chapter 5.

Chapters 2, 5 and 6 were assisted by MSci students J. Cavan, D. Flint and A. Lisle, respectively, as they undertook research projects in the group. In each case, they assisted with synthesis and recrystallisations, helping to set up data collections, fill DACs etc. Additional thanks go to D. Brooks who assisted in the systematic repeat of data reduction for Chapter 6 during his summer project.

I would also like to specifically mention Alice O'Connor at this point. We endured many weekends at Diamond Light Source together and, even under such extreme pressure(…), she at no point ceased being completely willing to help out and cooperate in streamlining our schedules. It's been a pleasure.

Many others have supported me across my studies. Dr. Will Lewis has provided an excellent source of education and training. The post-doc's of C41 - Joe Dawson, Emma Stephen, Carlo Perotto, Tom Mitra and (briefly) Stephen Argent - are all owed their own personal thanks for supporting me, both in the lab and as I occasionally verged on the brink of madness. This is not to forget Dr. Ben Slater whose unconventional pep-talk has remained with me, even three years on. Not quite a post-doc, or indeed a C41ite, but thanks also go to Maggie Chong for her help with UV/vis, job applications, last-minute proofing and general advice.

Continuing with the people of 'my laboratoire', I would like to thank and commend everyone who was subject to sharing office space and/or the lab' with me. To George, Gemma and Joe, thank you for putting up with me, for fruitful discussions, synthetic support, coffee-breaks, cake and so on. To Nelly Franikins, you're brilliant and I wouldn't change any of it. The final 'science' mention must go to our [many] project students; "well done!"...

To the Beestonian Explorers' Guild, the Reasonable, the Shuffler &the Housecat, G& the Beautiful, H&M, Captain Ahab's Wailers and the many left unmentioned, my deep love and gratitude must be extended for walking me through some very dark woods and staying by me in spite of *everything*. Special thanks also to the few who have long refused to let my mental preoccupation have us lose touch.

My final thanks must go to those who made me. Not only to my incredibly loving and supportive parents, but also to my dearest Grandmother. I've come a long way since Grandad caught us that sea water and there's no telling where I would be without your influence: I dedicate this work to House Strong.

# Contents


| | | |
|---|---|---|
| Contents | | I |
| Publications obtained during PhD | | X |
| External dissemination of results | | XI |
| Schools attended during PhD | | XII |
| Abbreviations | | XIII |
| **Abstract** | | **XVII** |
| **Chapter 1** | **Introduction to High-Pressure Crystallography of Coordination Complexes** | **1** |
| 1. | Introduction | 2 |
| 1.1. | Experimental | 3 |
| 1.1.1. | Procedure and equipment | 3 |
| 1.1.2. | Limitations | 7 |
| 1.2. | Key principles of diffraction and their experimental impacts | 8 |
| 1.2.1. | Data collection | 9 |
| 1.2.2. | Structure solution and refinement | 11 |
| 1.2.2.1. | Structure solution | 12 |
| 1.2.2.2. | Structure refinement | 13 |
| 1.3. | Useful software | 14 |
| 1.3.1. | Crystallographic software | 14 |
| 1.3.2. | Density functional theory | 19 |
| 2. | Chemical background | 20 |
| 3. | Coordination complexes under pressure | 22 |

3.1. Geometric studies with pressure 24

3.1.1. Complexes of Cu(II) 24

3.1.2. Complexes of gold and group 10 metals 29

3.1.3. Miscellaneous species 32

3.2. Negative linear compressibility 35

3.3. Spin-crossover complexes 36

3.4. Molecular magnetic materials 38

3.5. Concluding remarks 40

4. Aims 41

- References 42

**Chapter 2 Epitaxial Retrieval of a Disappearing Polymorph 51**

1. Introduction 52

2. Experimental 55

2.1. Synthetic 55

2.1.1. 1-Oxa-4,7-dithiacyclononane ([9]ane$S_2O$) 55

2.1.2. [$PdCl_2$([9]ane$S_2O$)] (1) 56

2.1.3. [$PtCl_2$([9]ane$S_2O$)] (1) 57

2.1.4. Recrystallisations 57

2.2. Crystallography 58

2.3. Computational methods 59

3. Results and discussion 59

3.1. Crystallisation of complexes 59

3.2. Crystal structures 60

3.2.1. Structure of α-[$PdCl_2$([9]ane$S_2O$)] 61

3.2.2. Structure of α-[$PtCl_2$([9]ane$S_2O$)] 63

3.2.3. Structure of β-[$PdCl_2$([9]ane$S_2O$)] 65

3.2.4. Structure of β-[$PtCl_2$([9]ane$S_2O$)] 67

3.2.5. Structure of γ-[$PdCl_2$([9]ane$S_2O$)] 70

3.3. Computational results 71

3.4. Phase loss and retrieval 73

3.5. Phase stabilities 76

4. Conclusions 80

- References 82

**Chapter 3 High-Pressure Studies of Three Polymorphs of a Palladium(II) Macrocycle Complex 85**

1. Introduction 86

2. Experimental 88

2.1. Synthesis 88

2.2. Crystallography 88

2.2.1. High-pressure crystallography 88

2.2.2. Variable temperature crystallography 90

2.3. Density functional theory calculations 92

3. Results and discussion 93

3.1. Structures at ambient pressure and temperature 93

3.1.1. α-[$PdCl_2$([9]ane$S_2O$)] 93

3.1.2. β-[$PdCl_2$([9]ane$S_2O$)] 94

3.1.3. γ-[$PdCl_2$([9]ane$S_2O$)] 95

3.2. Pressure limits of studies 96

| | | |
|---|---|---|
| 3.3. | Pressure dependence of cell parameters | 97 |
| 3.3.1. | α-[$PdCl_2$([9]ane$S_2O$)] | 97 |
| 3.3.2. | β-[$PdCl_2$([9]ane$S_2O$)] | 97 |
| .3.3. | γ-[$PdCl_2$([9]ane$S_2O$)] | 98 |
| 3.3.4. | Relative compressibility and void space analysis | 98 |
| 3.4. | Phase transition in β-[$PdCl_2$([9]ane$S_2O$)] | 102 |
| 3.4.1. | Overview | 102 |
| 3.4.2. | Description of the high-pressure phase, β'-[$PdCl_2$([9]ane$S_2O$)] | 106 |
| 3.4.3. | Rationalisation of the β → β' transition | 107 |
| 3.5. | Pressure dependence of the coordination sphere | 110 |
| 3.5.1. | α-[$PdCl_2$([9]ane$S_2O$)] | 110 |
| 3.5.2. | β-[$PdCl_2$([9]ane$S_2O$)] | 113 |
| 3.5.3. | β'-[$PdCl_2$([9]ane$S_2O$)] | 117 |
| 3.5.4. | γ-[$PdCl_2$([9]ane$S_2O$)] | 120 |
| 3.6. | Pressure dependence of the macrocyclic conformation | 125 |
| 3.7. | Temperature-dependent studies | 126 |
| 3.7.1. | α-[$PdCl_2$([9]ane$S_2O$)] | 127 |
| 3.7.2. | β-[$PdCl_2$([9]ane$S_2O$)] | 128 |
| 3.7.3. | γ-[$PdCl_2$([9]ane$S_2O$)] | 131 |
| 3.8. | Calculated energies and bond orders | 133 |
| 3.8.1. | α-[$PdCl_2$([9]ane$S_2O$)] | 134 |
| 3.8.2. | β-[$PdCl_2$([9]ane$S_2O$)] and β'-[$PdCl_2$([9]ane$S_2O$)] | 137 |
| 3.8.3. | γ-[$PdCl_2$([9]ane$S_2O$)] | 142 |
| 4. | Conclusions | 144 |
| - | References | 149 |

**Chapter 4 High-Pressure Studies of Two Polymorphs of a Platinum(II) Macrocycle Complex 153**

1. Introduction 154

2. Experimental 155

2.1. Synthesis 155

2.2. Crystallography 155

2.2.1. High-pressure crystallography 155

2.2.2. Variable temperature crystallography 158

2.3. Density functional theory calculations 159

3. Results and discussion 160

3.1. Structures at ambient pressure and temperature 160

3.1.1. α-[$PtCl_2$([9]ane$S_2O$)] 160

3.1.2. β-[$PtCl_2$([9]ane$S_2O$)] 161

3.2. Pressure limits of studies 162

3.3. Pressure dependence of cell parameters 163

3.3.1. α-[$PtCl_2$([9]ane$S_2O$)] 163

3.3.2. β-[$PtCl_2$([9]ane$S_2O$)] 164

3.3.4. Relative compressibility and void space analysis 164

3.4. Conformational rearrangement in β-[$PtCl_2$([9]ane$S_2O$)] 167

3.4.1. Overview 167

3.4.2. Description of the structure at high-pressure 168

3.4.3. Rationalisation of the transformation 169

3.5. Pressure dependence of the coordination sphere 172

3.5.1. α-[$PtCl_2$([9]ane$S_2O$)] 172

3.5.2. β-[$PtCl_2$([9]ane$S_2O$)] 176

3.5.3. β”-[$PtCl_2$([9]ane$S_2O$)] 180

3.6. Pressure dependence of the macrocyclic conformation 183

3.7. Temperature-dependent studies 184

3.7.1. α-[$PtCl_2$([9]ane$S_2O$)] 185

3.7.2. β-[$PtCl_2$([9]ane$S_2O$)] 187

3.8. Calculated energies and bond orders 189

3.8.1. α-[$PtCl_2$([9]ane$S_2O$)] 191

3.8.2. β-[$PtCl_2$([9]ane$S_2O$)] and β”-[$PtCl_2$([9]ane$S_2O$)] 193

4. Conclusions 196

- References 201

**Chapter 5 Reversible Piezochromism in Palladium(II) Macrocycle Complex 205**

1. Introduction 206

2. Experimental 208

2.1. Synthesis of [Pd([9]ane$S_3$)$_2$]($PF_6$)$_2$ 208

2.2. Crystallography 209

2.3. UV/vis experiments 212

2.4. Density functional theory calculations 212

3. Results and discussion 213

3.1. Structures at ambient pressure 213

3.1.1. [Pd([9]ane$S_3$)$_2$]($PF_6$)$_2$·2$CH_3NO_2$ - 3a 213

3.1.2. [Pd([9]ane$S_3$)$_2$]($PF_6$)$_2$·2($CH_3$)$_2$CO - 3b 215

3.1.3. [Pd([9]ane$S_3$)$_2$]($PF_6$)$_2$·2$CH_3CN$ - 3c-II 217

3.2. Pressure transmitting medium 219

3.3. Summary of high-pressure studies on 3a and 3c 220

3.3.1. High-pressure phase of $[Pd([9]aneS_3)_2](PF_6)_2 \cdot 2CH_3NO_2$ - 3a' 223

3.3.2. High-pressure phase of $[Pd([9]aneS_3)_2](PF_6)_2 \cdot 2CH_3CN$ - 3c-II' 224

3.4. High-pressure X-ray studies of 3a/3a' 226

3.4.1. Compression of the coordination sphere 226

3.4.2. Compression of intermolecular interactions 234

3.4.3. Pressure dependence of the macrocyclic conformation 238

3.4.4. Calculated bond orders 238

3.4.5. Rationalisation of 3a → 3a' phase transition 239

3.4.6. Decompression and hysteresis 241

3.5. UV/vis absorption studies 242

3.5.1. Experimental high-pressure solid-state UV/vis spectra 242

3.5.2. Computational gas-phase UV/vis spectra 244

3.5.3. Rationalisation of piezochromic response 246

3.6. Further comments - ambient phases 247

4. Conclusions 250

- References 252

**Chapter 6 Compression Studies of a Templated Polyiodide Network 255**

1. Introduction 256

2. Experimental 260

2.1. Synthesis 261

2.1.1. Synthesis of $[18]aneS_6$ 261

2.1.2. Synthesis of $[Ag([18]aneS_6)]I_7$ 262

| | | |
|---|---|---|
| 2.2. | Crystallography | 262 |
| 2.3. | Density functional theory calculations | 264 |
| 3. | Results and discussion | 266 |
| 3.1. | Complex 4 at ambient pressure and 120 K: phase 1 | 266 |
| 3.2. | High-pressure summary | 267 |
| 3.2.1. | First high-pressure phase: phase 2 | 270 |
| 3.2.2. | Second high-pressure phase for crystal A: phase 3A | 272 |
| 3.2.3. | Second high-pressure phase for crystal B: phase 3B | 272 |
| 3.3. | Experimental considerations | 273 |
| 3.3.1. | Pressure ramping: RS3000 as a PTM | 273 |
| 3.3.2. | Specific refinement details: twinning | 275 |
| 3.4. | Macrocycle conformation and disorder | 276 |
| 3.4.1. | Conformation upon compression | 277 |
| 3.4.2. | Conformation upon decompression - crystal B | 280 |
| 3.5. | Compression of the coordination sphere | 281 |
| 3.6. | Compression of the polyiodide network | 286 |
| 3.6.1. | Interaction *D-1*: $I^-\cdots(I_2)$ | 288 |
| 3.6.2. | Bond order analysis for*D-1* | 292 |
| 3.6.3. | Interaction *D-2*: 1,3 $(I_2)\cdots(I_2)$ @ $I^-$ | 295 |
| 3.6.4. | Interaction *D-3*: 1,2 $(I_2)\cdots(I_2)$ @ $I^-$ | 298 |
| 3.6.5. | Bond order analysis for *D-2*$_{inter}$ and *D-3* | 300 |
| 3.6.6. | Angles about the iodide node | 301 |
| 3.7. | Dominating interactions and differences between crystals | 307 |
| 4. | Conclusions | 310 |
| - | References | 314 |

**Chapter 7 Summary, Conclusions and Future Work 317**

1. Introduction 318

2. Summary of scientific outcomes and proposals for future work 318

2.1. Chapters 2-4: studies of [$MX_2$([9]ane$S_2$O)] ($M$ = Pd, Pt; $X$ = Cl) 318

2.2. Chapter 5: piezochromism in [Pd([9]ane$S_3$)$_2$]($PF_6$)$_2$·2$CH_3NO_2$ 322

2.3. Chapter 6: compression of a templated polyiodide network 324

3. Wider conclusions 326

4. Closing remarks 329

- References 330

**Electronic Supplementary Information Index 331**

# Publications obtained during PhD

**Tidey**, **J**. **P**.; Wong, H. L. S.; McMaster, J.; Schröder, M.; Blake, A. J. (2016). *Acta Crystallogr., Sect. B,* **72**, 3, 357-371.

Blake, A. J.; **Tidey**, **J**. **P**.; Lisle, A. E.; Schröder, M. (2015). *Acta Crystallogr., Sect. A*, **71**, s367.

Kathirgamanathan, P.; Surendrakumar, S.; Ravichandran, S.; Kumaraverl, M.; Lara, J. A.; Ganeshamurugan, S.; Paramaswara, G.; Arkley, V.; Selvaranjan, S.; Partheepan, A.; Bushby, L. M.; **Tidey**, **J**. **P**.; Blake, A. J. (2015). "Energy Level tuning of blue emitting and electron transporting vinylene bis(vinyl quinolinyl)benzene derivatives: synthesis, crystal structure, thin film characterisation and performance in OLEDs", *J. Mater. Chem. C*, **3**, 6652-6667.

**Tidey**, **J**. **P**.; O'Connor, A. E.; Markevich, A.; Bichoutskaia, E.; Cavan, J. J. P.; Lawrance, G. A.; Wong, H. L. S.; McMaster, J.; Schröder M.; Blake, A. J. (2015). "Epitaxial Retrieval of a Disappearing Polymorph", *Cryst. Growth Des*. **15**, 115−123.

**Tidey**, **J**. **P**.; Wong, H. L. S.; Schröder, M.; Blake, A. J. (2014). "Structural Chemistry of Metal Coordination Complexes at High Pressure", *Coord. Chem. Rev.* **277–278**, 187–207.

Allan, D. R.; Bailey, D.; Bird, N.; Blake, A. J.; Champness, N. R.; Huang, D.; Keane, C. P.; McMaster, J.; Prior, T. J.; **Tidey**, **J**. **P**.; Schröder M. (2014). "High-pressure studies of palladium and platinum thioether macrocyclic dihalide complexes", *Acta Crystallogr., Sect. B,* **70**, 469−486.

Hsuan, R. E.; Hughes, J. E.; Miller, T. H.; Shaikh, N.; Cunningham, P. H. M.; O'Connor, A. E.; **Tidey**, **J**. **P**.; Blake, A. J. (2014). "{2,2'-[Ethylenebis(nitrilomethylidyne)]diphenolato-$\kappa^4$-*O*,*N*,*N*',*O*'}oxidovanadium(IV) methanol solvate (1:1)", *Acta Crystallogr., Sect. E,* **70**, m380−m381.

Blake, A. J.; **Tidey**, **J**. **P**.; Wong, H. L. S.; Schröder, M. (2012). "High Pressure Studies of a Trio of Polymorphs with Conformational Variability", *Acta Crystallogr., Sect. A,* **68**, s210.

# External dissemination of results

(presenter)

**Event:** The 29th Meeting of the European Crystallographic Association (ECM29), Rovinj, Croatia, 2015.
**Title:** "$I_7^-$: From Stoichiometry to Structural Unit" – *poster presentation*
**Authors: J. P. Tidey**, A. E. Lisle, D. T. K. Brooks, M. Schröder, A. J. Blake.

**Event:** British Crystallographic Association (BCA) Spring Meeting, University of York, and associated Young Crystallographers Group (YCG) Satellite Meeting, 2015.
**Title:** "Pressure Induced Phase Transition and Rearrangement of Coordination Geometry in $[Pd([9]aneS_3)_2](PF_6)_2 \cdot 2MeNO_2$" – *poster presentation* – ***awarded the YCG Poster Prize***
**Authors: J. P. Tidey**, D. J. Flint, A. E. O'Connor, M. Schröder, A. J. Blake.

**Event:** YCG Satellite Meeting to the BCA Spring Meeting, Loughborough University, 2014.
**Title:** "Highlights from HPXRD Studies of $[MCl_2([9]aneS_2O)]$" – *oral presentation*
**Authors: J. P. Tidey**, A. E. Lisle, D. T. K. Brooks, M. Schröder, A. J. Blake

**Event:** BCA Spring Meeting and associated YCG Satellite Meeting, Loughborough University, 2014.
**Title:** "High Pressure Studies of Various Polymorphs of $[MCl_2([9]aneS_2O)]$, $M$ = Pd, Pt: Conformational Variability and a Phase Transition" – *poster presentation*
**Authors: J. P. Tidey**, A. J. Blake, H. L. S. Wong, M. Schröder.

**Event:** The 28th Meeting of the European Crystallographic Association (ECM28), University of Warwick, and associated European Young Crystallographers Satellite Meeting, 2013.
**Title:** "Pressure studies of a trio of phases exhibiting conformational variability" – *poster presentation*
**Authors:** A. J. Blake, **J. P. Tidey**, H. L. S. Wong, M. Schröder.

**Event:** The 27th Meeting of the European Crystallographic Association (ECM27), Bergen, Norway, 2012.
**Title:**"High Pressure Studies of a Trio of Polymorphs with Conformational Variability" – *poster presentation.*
**Authors:** A. J. Blake, **J. P. Tidey**, H. L. S. Wong, M. Schröder.

# Schools attended during PhD

14th BCA/CCG Intensive Teaching School in X-ray Structure Analysis, Durham, 2013.

2013 Workshop of the IUCr Commission on High Pressure Advances in Static and Dynamic High-Pressure Crystallography, Hamburg, 2013.

Olex2 day-workshop satellite event to ECM28, Warwick, 2014.

# Abbreviations

| | |
|---|---|
| [18]ane$S_6$ | 1,4,7,10,13,16-hexathiacyclooctadecane |
| [9]ane$S_2O$ | 1-oxa-4,7-dithiacyclononane |
| [9]ane$S_3$ | 1,4,7-trithiacyclononane |
| *A* | Hydrogen-bond acceptor |
| *ADF* | Amsterdam Density Functional |
| ATR | Attenuated total reflectance |
| BASF | Batch scale factor |
| BM | Birch-Murnaghan |
| $^t$Bu | *tertiary*-butyl |
| CCD | Charge-coupled device |
| CCDC | Cambridge Crystallographic Database Centre |
| CE | Cohesive energy |
| CFSE | Crystal field stabilisation energy |
| CIF | Crystallographic information file |
| cit | Citrate |
| CSD | Cambridge Structural Database |
| *D* | Hydrogen-bond donor |
| DAC | Diamond anvil cell |
| DCTB | T-2-[3-(4-t-Butyl-phenyl)-2-methyl-2-propenylidene]malononitrile |
| DFT | Density functional theory |

| | |
|---|---|
| DMF | *N*,*N*-dimethylformamide |
| dmg | Dimethylglyoximate |
| dmit | 1,3-dithiole-2-thione-4,5-dithiolate |
| DMSO | Dimethyl sulfoxide |
| EoS | Equation of state |
| ESI | Electrospray ionisation |
| ESU | Estimated standard uncertainty |
| $Et_2O$ | Diethyl ether |
| EtOH | Ethanol |
| FTIR | Fourier transform infrared |
| gu | Guanidine |
| GUI | Graphical user interface |
| HL | Hydrostatic limit |
| HPXRD | High-pressure X-ray diffraction |
| HOMO | Highest occupied molecular orbital |
| IR | Infrared |
| *L* | Ligand |
| LUMO | Lowest unoccupied molecular orbital |
| *M* | Metal |
| MALDI | Matrix assisted laser desorption/ionisation |
| MB | Merrill-Bassett |
| Me | Methyl |

| | |
|---|---|
| MeOH | Methanol |
| MOF | Metal-organic framework |
| MS | Mass spectrometry |
| NLC | Negative linear compressibility |
| NMR | Nuclear magnetic resonance |
| OAc | Acetate |
| PBE | Perdew-Burke-Erzerhof |
| Ph | Phenyl |
| PTM | Pressure transmitting medium/media |
| *PV* | Thermodynamic component, pressure × volume |
| RMS | Root-mean-square |
| $S_{ax}$ | Axial sulfur donor |
| SCO | Spin cross-over |
| $S_{eq}$ | Equatorial sulfur donor |
| SMM | Single-molecule magnet |
| SSCI | Solid state chemical information |
| tmen | Tetramethylethylenediamine |
| TOF | Time-of-flight |
| TS | Tkatchenko-Scheffler |
| UV/vis | Ultraviolet / visible |
| vdW | van der Waals |
| *X* | Halide |

# Abstract

**Chapter 1:**

An introduction is given to high-pressure crystallography with the experimental design and equipment required outlined. The basic theory that underpins X-ray diffraction and structure solution is covered with emphasis given to points that raise considerations for high-pressure crystallographic studies; key software and their uses are briefly introduced. A literature survey of molecular coordination complexes under pressure is given that provides a detailed view of the typical phenomena observed and interrogated in such work.

**Chapter 2:**

Recrystallisation of $[PdCl_2([9]aneS_2O)]$ ($[9]aneS_2O$ = 1-oxa-4,7-dithiacyclononane), **1**, and $[PtCl_2([9]aneS_2O)]$, **2**, by diffusion of $Et_2O$ vapour into solutions of these complexes in $CH_3NO_2$ has yielded three phases of **1** and two phases of **2**. The phase of **1**, herein designated α-**1**, was obtained under ambient conditions. A second phase, designated β-**1**, was initially also obtained by this method; following the advent of a third phase, γ-**1**, all subsequent efforts over a period of a year to crystallise β-**1** yielded either γ-**1**, which was typically obtained by carrying out the recrystallisation at elevated temperature, or α-**1**, commonly found throughout the study. This persistent absence of a phase which could initially be crystallised with ease led to the conclusion that β-**1** was an example of a 'disappearing polymorph'. The first phase obtained of **2**, designated α-**2**, was obtained by recrystallisation under ambient conditions and is isomorphous and

isostructural with α-**1**. The second phase, β-**2**, was obtained by slight elevation of the recrystallisation temperature and was found to be isomorphous and isostructural with β-**1**. Subsequently, β-**2** was used to seed the growth of the disappearing polymorph β-**1**. No third phase of **2** ("γ-**2**") has been isolated. Density functional theory calculations were employed to aid in rationalising this behaviour.

**Chapter 3:**

The three reported phases of the mononuclear macrocyclic Pd(II) complex $[PdCl_2([9]aneS_2O)]$ (**1**) were each studied up to pressures exceeding 90 kbar using high pressure single crystal X-ray diffraction. The α and γ phases both exhibited smooth compression of the unit cell parameters with third-order Birch-Murnaghan bulk moduli of 14.4(8) and 7.6(6) GPa, respectively. Between 68.1 and 68.7 kbar β-**1** was found to undergo a reversible transformation to a phase denoted β' and characterised by a tripling of the unit cell volume. Across the phase transition, rearrangement of the conformation of the bound macrocycle at two of the resulting three unique sites gave rise to an extensively disordered structure. This phenomenon was largely owed to a close and approximately linear C−H···H−C approach between macrocycles. Density functional theory calculations were employed to further understand the high-pressure behaviour of the phases. Cooling from 290 to 90 K in complementary variable temperature crystallographic studies revealed similar effects as *ca.* 5 kbar pressure.

**Chapter 4:**

The two reported phases of the mononuclear macrocyclic Pt(II) complex [$PtCl_2$([9]ane$S_2O$)] (**2**) were each studied up to pressures exceeding 90 kbar using high pressure single crystal X-ray diffraction. The α phase exhibited smooth compression of the unit cell parameters with third-order Birch-Murnaghan bulk modulus of 11.8(5) GPa. Between 65.2 and 69.9 kbar β-**2** was found to undergo an incomplete rearrangement of the macrocycle that was not characterised by a phase transition as seen for the corresponding Pd(II) phase. The β phase was also indicated to be more resistant to compression than the α phase with a third-order Birch-Murnaghan bulk modulus of 13.5(5) GPa. The conformational rearrangement was again rationalised by a close and approximately linear C−H···H−C approach between macrocycles. Density functional theory calculations were employed to further understand the high-pressure behaviour of these two phases and why β-**1** and β-**2** might differ. Cooling from 290 to 90 K in complementary variable temperature crystallographic studies again revealed similar effects as *ca.* 5 kbar pressure.

**Chapter 5:**

The previously unreported solvate [Pd([9]ane$S_3$)$_2$]($PF_6$)$_2$·2$CH_3NO_2$ is studied using high-pressure crystallography, high-pressure solid-state UV/vis spectroscopy and density function theory calculations to interrogate the piezochromism previously observed by this group. Up to 49.3 kbar, gradual sky blue to dull green piezochromism was observed with considerable compression of the elongated axial Pd···S interactions. A reversible $P2_1/c \rightarrow P\bar{1}$ phase transition with doubling of the

unit cell volume was observed between 49.3 and 51.0 kbar. This was accompanied by a dull green to orange stepwise piezochromism and characterised by an organised reorientation of the coordination axes in 50 % of the cations. The phase transition had a range of effects on the axial interactions which remained compressible in the high-pressure phase. No further piezochromism was clearly observed. Density functional theory calculations showed a fair match with experimentally obtained spectra and strongly indicated that the piezochromism is primarily owed to compression of the axial interaction. These calculations also indicated that outer-sphere effects further modulate the piezochromism, but gave no evidence for a cause of the phase transition. The phase transition was thus rationalised as a response to the large value of the *PV* term of the Gibb's free energy associated with the transition. The ambient pressure structures of two other previously unreported solvates are also reported.

**Chapter 6:**

The templated polyiodide framework $[Ag([18]aneS_6)]I_7$ were studied to *ca.* 45 kbar. Each of the two crystals employed in this study underwent two phase transitions: at *ca.* 11 kbar an $R\bar{3}m \rightarrow R3m$ transition was observed in both crystals. This appeared to be ferroelectric in nature and was associated with a change in bonding of the polyiodide network from $^{3}_{\infty}[I^{-}\cdot(I_2)_{6/2}]$ to $^{3}_{\infty}[I_7^{-}]$. Analysis of the calculated Mayer bond orders for the catenating $I^{-}\cdots I_2$ interactions supported this description of the bonding. Compression of the first phase appears essentially the same for both crystals; compression through the second phase differed between crystals and the second phase transition, at *ca.* 40 kbar in both cases, resulted in

differing monoclinic phases. The second transition was associated with the ordering of the conformation of the macrocycle: one phase appeared ordered from the perspective of the refinement and the macrocycle adopted the previously unseen [84114] conformation by Dale analysis. The other phase appears disordered from the perspective of the refinement but would appear to comprise alternating enantiomers of the [333333] conformer. The differing conformation of the macrocycle in the third phase was taken as indicative of differing major components in the disordered lower phases. This point of difference in turn rationalised the different response to pressure in the second phase: compression of the second phase is limited by interactions between cations while the first phase is dependent on the catenating $I^{-}\cdots I_2$ interactions which are identical between crystals.

**Chapter 7:**

A summary of the key findings of this body of work is given along with suggested avenues for future studies. This thesis closes with the wider reaching considerations that are highlighted by this body of work.

# Chapter 1

## Introduction to High-Pressure Crystallography of Coordination Complexes: Theory and Background Literature

## 1. Introduction to high-pressure crystallography

Since von Laue's publication of the diffraction of copper sulfate (Friedrich *et al*., 1912) and William Bragg's description of the diffraction of X-rays by crystalline materials (Bragg, 1913), crystallography has been a rapidly advancing field with its centenary bringing a wealth of reviews covering this and the benefits the technique now serves (*e.g.*, Lider, 2014; Miller, 2014; Pomés *et al*., 2015). Its progress has been vastly assisted by advances in technology and computing allowing for ever more complicated experiments to be carried out on lower and lower quality crystals. Where once the reserve of highly-specialised experts with perfectly grown crystals and freedom to dedicate months to the determination of a single structure, it is routine for chemists with only very little training to obtain accurate crystal structures of molecular materials in only a couple of days from the setting up of a recrystallisation to the archiving of a crystallographic information file (CIF). This has freed those with more training and the time to dedicate to crystallographic study to turn their attention to more extensive crystallographic experiments which explore and exploit the range of insight the technique has to offer. This thesis provides an example of such experiments and, herein, the high-pressure crystallographic study of several coordination complexes is reported. This is performed along with complementary data afforded by variable temperature crystallography and/or density functional theory calculations, with a view to continuing our investigation into the behaviour of macrocyclic compounds under pressure.

## 1.1. Experimental Considerations

### 1.1.1. Procedure and equipment

Chemical processes or compounds do not commonly experience pressures greater than a few hundred times atmospheric pressure. For example, the maximum pressure employed during the Haber-Bosch process does not usually exceed *ca*. 250 atmospheres (0.25 kbar), and at such pressures solids appear to be essentially incompressible. However, above 1 kbar compression begins to exert observable and significant effects upon them, and it is at this pressure that high-pressure crystallography begins.

The first hurdle for a high-pressure crystallographer is applying pressure to the sample in such a manner as to still be able to survey it with X-rays. Diamond anvil cells (DACs) are the typical choice for this purpose, as diamonds are essentially transparent to X-rays and are of course exceptionally hard. While several DAC designs exist (Jayaraman, 1983), the Merrill-Bassett design (MB; Merrill & Bassett, 1974) appears by far the most popular for modern X-ray studies. In the modern MB DAC, two opposing diamonds are mounted in tungsten-carbide backing seats which are in turn mounted into steel plates (Fig. 1). These plates are drawn together by Allen screws to apply pressure to the sample. The experimental limitations associated with this design and the attempts made to overcome these have been widely discussed, for example by Katrusiak (2008) and Moggach *et al*. (2008); key considerations are further discussed herein.

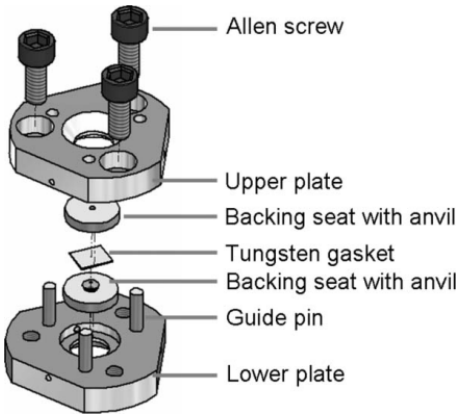



**Figure 1** Schematic drawing of the Merrill-Bassett diamond anvil cell design. Image taken from Moggach *et al*., 2008.

In a typical high-pressure crystallographic experiment, the sample is housed between three components. A small hole of around 250 μm diameter is made in a thin sheet of pre-indented metal using a spark eroder. The correct degree of indentation is vital: too much and the depth of the chamber is insufficient to house the sample; too little and the material will warp and the maximum pressure to which it may be taken is reduced. In the work reported herein, it was found that an indentation of *ca*. 80-100 μm allowed sufficient space for the sample while providing a stable gasket up to >100 kbar. The modified metal filament, the gasket, is placed between the two culet faces of the diamond anvils with which the sample chamber is formed. It is essential that the gasket is placed in the same cell with which it was indented and that it is aligned in the same manner as for indentation. If the gasket is misaligned or employed in a different cell then the hole will very likely deform or even fail.

A pressure transmitting medium (PTM) is included to allow isotropic application of pressure up to the hydrostatic limit (HL) of the PTM, since non-hydrostatic conditions may falsely promote (Kenichi, 1999) or suppress (Decker *et al*., 1979)

phenomena. Many potential PTM have been identified and they can be broadly separated into three groups: oils, including olefin mixtures (Murata *et al*., 2008; Yokogawa *et al*., 2007), silicone oils (Shen *et al*., 2004) and perfluoroethers (Varga *et al*., 2003; Sidorov & Sadykov, 2005), are usually unreactive towards samples but typically have a low HL in the order of 10-20 kbar. Small molecule solvents, including *iso*-propanol and mixtures such as 1:1 *n*-pentane/*iso*-pentane and 4:1 methanol/ethanol (*v/v*), must be selected with sample stability in mind but usually have a higher HL [43, 74 and *ca*. 100 kbar, respectively] (Piermarini *et al*., 1973; Jamieson, 1981; Angel *et al*., 2007). Inert gases which, although experimentally troublesome, are favoured for cryogenic work (Tateiwa & Haga, 2009) and have HLs comparable to 4:1 methanol/ethanol solution (Klotz *et al*., 2009), if not significantly greater (Dewaele & Loubeyre, 2007).

Fluorescence spectroscopy (Barnett*et al.*, 1973) can be used to measure the pressure inside a DAC *via* a small ruby sphere placed in the chamber alongside the compound to be studied. The ruby is excited by a laser and the resulting fluorescence is recorded. Since the position of the *R*1 fluorescence line is linearly dependent on pressure over a wide pressure range, the pressure applied within the DAC can easily be determined. While other methods of measuring the pressure are available, such as samarium fluorescence (Zhao *et al*,. 1998), ruby fluorescence is the most widely used in high-pressure crystallographic studies. It is also possible to include a second crystal of a compound with a well determined equation of state, such as NaCl (Brown, 1999) or quartz (Angel *et al*., 1997), and calculate the pressure from the compression of its unit cell parameters. This offers the advantage of tracking the pressure throughout the experiment, but requires indexing of two

separate diffraction patterns and increases the risk of sample reflections being contaminated.

Data are collected at numerous pressures to obtain a representative trend of the behaviour of the sample with pressure, up to either the pressure that the sample loses crystallinity or the hydrostatic limit of the PTM is reached. The only remaining requirement for a high-pressure X-ray crystallographic laboratory is for a slightly modified diffractometer: compared to the average laboratory instrument, a dedicated high-pressure diffractometer requires a shorter collimator and a more distant beam-stop to accommodate the DAC. In addition, long wavelength sources (*i.e.*, copper) must not be used (*vide infra*).

While it is entirely possible to undertake high-pressure crystallographic studies solely in-house, samples often do not diffract sufficiently to obtain good diffraction patterns on laboratory equipment. Equally, a dedicated high-pressure laboratory is not always within the funding reach of projects which may benefit from the insight it can bring. To this end, synchrotron facilities are indispensable, where the facility is already set up to receive and undertake the experiment. The use of a synchrotron source also offers a number of distinct advantages to the high-pressure experiment. For example, the wavelength of radiation is tuneable, and so can be lower, increasing maximum attainable resolution. The sources are also brighter, typically by a few orders of magnitude. As well as allowing study of weakly diffracting samples, this drastically decreases collection times, having a knock-on effect on reducing pressure drift and the equilibration time required after each pressure ramp before a collection may be made.

### 1.1.2. Limitations

The equipment is not without its drawbacks, the most problematic being the steel body of the DAC itself which limits the region of reciprocal space that is accessible (Katrusiak, 2008). This in turn places a limit on the completeness and redundancy that would otherwise not be present in a standard data collection. The primary effect is to increase uncertainties in structural parameters, but it can also significantly add to the challenge of structure solution, sometimes making refinements highly unstable and requiring a great number of restraints or even preventing a solution from being obtained at all. The problem of solution against incomplete data can often be overcome by employing isomorphous replacement (*cf.* Section 1.2.2.1). This quickly gives an accurate solution to the phase problem (*cf.* Section 1.2.2) *via* the generation of calculated structure factors. However, this is impossible in the event that a new pressure-induced phase is generated. It is also commonplace to survey all available regions of reciprocal space so as to obtain not only the maximum completeness available but also a high redundancy. Higher symmetry space groups serve to increase completeness and further reduce this problem (*cf.* Section 1.2.1). Data quality is also impeded by strong diamond reflections and gasket powder rings arising from certain components of the cell, though advances in data reduction and refinalisation software serve to greatly reduce their impact through rejection of reflections with outlying intensities or peak-profiles. High redundancy in the data also limits the impact of this consideration.

### 1.2. Key principles of diffraction and their experimental impacts

The extensive theory that underpins crystallographic research has been the subject of many textbooks which aim to convey this in a reduced and comprehensible form for the diligent scientist to digest (*e.g.*, Blake *et al.*, 2009; Clegg, 2015). Despite this, with the availability of powerful desktop computing and software such as that used to undertake data collection and reduction (*e.g.*, *CrysAlis*$^{PRO}$ employed for the work herein; Agilent, 2014), it is no longer strictly necessary to have a comprehensive understanding of this theory to obtain a valid crystal structure. Nevertheless, to troubleshoot even some of the most minor problems encountered during a structural analysis often requires the input of someone with crystallographic training. For example, understanding how a unit cell may fulfil certain requirements for a higher symmetry space group and yet be of lower symmetry can in some cases mark the bar for obtaining any solution at all. However, even this has become less crucial in recent years given the advent of reliable charge-flipping algorithms, such as *Superflip* (Palatinus & Chapuis, 2007). These solve the structure in the triclinic space group *P*1 and then apply symmetry considerations to determine the correct space group, providing a prime example of where recent advances in crystallography are making it ever more accessible. This section will seek to cover key aspects of the underpinning theory that hold important considerations for high-pressure crystallographic experiments, and describe the specialist software employed in structure determination and analysis.

### 1.2.1. Data collection

It is common knowledge that the periodic nature of a crystal provides a three-dimensional diffraction grating which diffracts X-rays according to Bragg's Law (*cf.* Fig. 2):

**Equation 1** $sin\theta = \left(\frac{n\lambda}{2d}\right)$

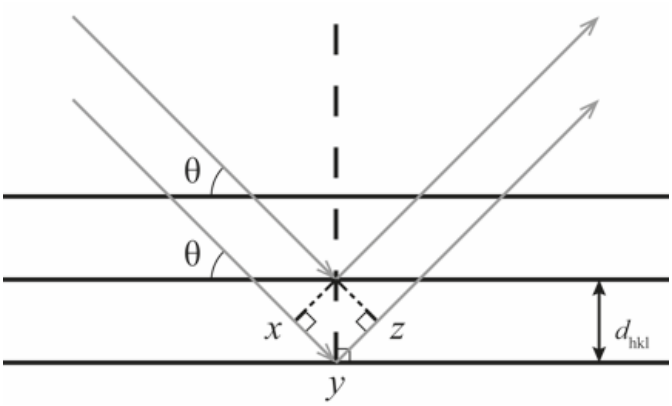



**Figure 2** Schematic of the diffraction detailed in Bragg's Law.

Where $\theta$ is the angle of incidence to the plane [*hkl*], $\lambda$ is the wavelength of radiation, and $d_{hkl}$ is the spacing between [*hkl*] planes. It is at this most fundamental point that an important consideration towards high-pressure crystallography is raised. Bragg's law dictates that the angle of the diffracted beam is, in part, dependent on the wavelength used, and a shorter wavelength will give a lower angle of scatter for a set value of *d*. Since the body of the cell used to apply pressure to the sample is opaque to X-rays, only a small cone exists through which diffraction may be observed. For this reason, X-rays with shorter wavelengths are favoured as these increase the maximum obtainable resolution and completeness for a given cone size, or opening angle. While they are less efficiently scattered, the use of a shorter wavelength also serves to minimise the effects of absorption

and extinction which are difficult to accurately address for samples housed inside a DAC.

The diffracted X-rays comprise distinct beams with very specific vectors and intensities dependent on a host of factors specific to the experiment. In modern diffractometers, these beams are recorded as reflections, “spots”, at area detectors. The intensity of each spot is recorded and assigned polar coordinates that allow them to be plotted. Since Bragg’s Law dictates that the geometry of the diffraction pattern is related to the inverse of *d*, this invokes the mathematical concept of reciprocal space and the resulting construct is named the Ewald sphere. From here, analysis of the vectors from spot to spot allows assignment of *hkl* indices and determination of the unit cell dimensions and metric symmetry. This, in combination with the symmetry of the intensities and the systematic absences observed, usually allows the Laue symmetry and space group to be determined. Herein forms another consideration of note for the high-pressure crystallographer: lower symmetry space groups give a lower symmetry diffraction patterns and so require access to greater proportion of the Ewald sphere to observe every unique reflection and thereby obtain a complete dataset. For this reason, higher symmetry systems are favoured for high-pressure study as these ultimately allow for more reliable data. Another advantage of using a high-symmetry crystal is that, where pressure-induced phase transitions typically occur with a decrease in symmetry (*vide infra*), the possible symmetry of any subsequent pressure-induced phases is increased. Thus, the chance of obtaining a good solution for any such phase is increased as the likely data completeness for said phase is increased.

In a standard structure determination experiment, an optimal collection strategy would be calculated following determination of the unit cell and orientation matrix, giving the orientation of the lattice with respect to the beam. As already mentioned, the body of the DAC obstructs a wide range of positions and, while modern software is capable of calculating strategies that account for this, the maximum possible completeness for a centrosymmetric monoclinic sample is frequently as low as 30 %. Coupled with the likelihood of obfuscating factors inherent to the use of DACs, such as gasket powder rings, diamond reflections and imprecise centring or absorption correction, it is also the case that sample reflections may be inaccurate. Consequently, a typical high-pressure data collection will record the diffraction across the maximum range of positions available and, as well as obtaining maximum possible completeness, attempt to collect to a high redundancy in doing so. This serves to reduce the loss of accuracy owed to incomplete and imprecise data as reflections or their symmetry equivalents are measured multiple times. In doing so, outliers are more readily identified and rejected while the accuracy of multi-scan absorption corrections is also increased.

### 1.2.2. Structure solution and refinement

The electron density ($\rho$) at a given position in the unit cell, denoted by fractional coordinates *xyz*, can be described by the equation:

**Equation 2** $$\rho(xyz) = \frac{1}{V}\sum_{hkl}|F(hkl)|e^{i\varphi(hkl)}e^{-2\pi i(hx+ky+lz)}$$

Where *V* is the unit cell volume, φ is the phase, and *h*, *k* and *l* correspond to Miller indices of the indexed reflection; |*F*(*hkl*)| correspond to the structure amplitudes and are related to the square root of the spot intensities. Structure factors, *F*(*hkl*),

are the product of the structure amplitude and exponent containing their phase information. The crystal structure is, therefore, obtained by the Fourier transform of the complete diffraction pattern, and most of the data required for this is directly obtained from the experiment. However, while amplitude is measured, phase information is lost; the loss of phase information is commonly referred to as the phase problem. Consequently, the primary step of structure determination (structure solution) entails assigning phases to the observed structure amplitudes and in any case there will be a threshold of correct phases required before the structure can be solved and the refinement of the structural model begun.

#### 1.2.2.1. Structure solution

Phase assignment can be performed by a number of methods: charge flipping algorithms have already been mentioned (*cf.* Section 1.2) as a powerful method for structure solution and have rapidly gained favour in recent years. However, they require high completeness and good resolution and so are rarely suitable for high-pressure experiments. The other two main methods used in structure determination are direct methods and Patterson (heavy-atom) methods. The latter is particularly effective in high-pressure studies of coordination complexes, such as those reported within, where the unit cell contains a small number of heavy atoms and a larger proportion of lighter atoms. It is also the least affected by incomplete data, although both methods can be effective for structure solution in this context. Nevertheless, isomorphous replacement represents the most attractive method for solution. This is the use of an isomorphous structure as a starting model from which to produce calculated structure factors. The phases generated as part of this are assigned to the observed structure factors and the refinement continued. The

method assumes that only small deviations to the atomic positions have occurred and is a powerful way of obtaining a starting model for a known phase but does not allow solution of most novel pressure-induced phases. With the exception of isomorphous replacement which is a more manual process, all methods for structure solution are available through *SHELXS* (Sheldrick, 2008), one of the most widely used solution packages.

### 1.2.2.2. Structure refinement

Once a viable initial solution has been obtained, the structure may be refined. This is an iterative process and can comprise two components. Peaks in the calculated electron density map are assigned as atoms of a given element and a new set of calculated structure factors, $F_{calc}$, are generated. The resulting phases are assigned to the observed structure factors, $F_{obs}$, and a new electron density map produced. This technically comprises the continued solution of the phase problem. Concurrently, $F_{obs}$ and $F_{calc}$ are compared and the differences between them used to alter $F_{calc}$, and hence the model, *via* a least-squares iterative approach. Thus, a new model is generated in which the positions, occupancies and/or thermal parameters of atoms from the previous model may be changed while new or altered peaks in the electron density map are revealed. The process is repeated until $F_{obs}$ and $F_{calc}$ have converged as much as is possible. While several measures exist, the extent of agreement between the diffraction data and the structural model is typically reported as discrepancy indices such as the conventional R factor, $R_1$ (Eq. 3) or the weighted R factor, $wR_2$ (Eq. 4):

**Equation 3** $$R_1 = \frac{\sum|F_o - F_c|}{\sum|F_o|}$$ **Equation 4** $$wR_2 = \sqrt{\frac{\sum w\left(F_o^2 - F_c^2\right)^2}{\sum w\left(F_o^2\right)^2}}$$

Where *w* corresponds to the weighting factor employed. If the calculated structure is poorly behaved, for example if the displacement parameters or atomic positions are unstable or bonding parameters do not make chemical sense, restraints or even constraints may be applied to the structure. While constraints set a defined value for a given parameter, restraints serve to provide guidance on the value of a parameter and a rigidity with which the refinement should make it so. These can in turn be divided into two categories: soft restraints are those where a parameter is sensibly linked to one or more elsewhere in the refinement; hard restraints typically add a larger degree of information to the system by providing a range in which the parameter is expected to lie. Judicious application of restraints can often greatly improve the stability and chemical sensibility of a model. Indeed, in the case of high-pressure crystallography they are often indispensable. Nevertheless, the application of too many or poorly chosen restraints and constraints can result in inaccurately reported data. Additionally, since both restraints and constraints add external information to the experiment, any parameter that has been heavily restrained and certainly those that are constrained may no longer be legitimately viable for discussion. Refinement packages typically offer a wide range of restraints and constraints: for *SHELXL* (Sheldrick, 2015) see http://shelx.uni-ac.gwdg.de/SHELX/wikis.php.

## 1.3. Useful software

### 1.3.1. Crystallographic software

There are multiple computational software suites available to the crystallographer but a few remain particularly favoured and are relied upon far more heavily. It is therefore pertinent to outline some of these. The first that should be covered is that

of refinement software. Although several programs exist, by far and away the most commonly used are those belonging to the *SHELX* suite (Sheldrick, 2008; Sheldrick, 2015). It is this and similar software packages in conjunction with graphical user interfaces (GUIs) such as *Olex2* (Dolomanov *et al.*, 2009) which have so increased the accessibility of crystallography. The work presented herein was solely solved and refined implementing *SHELX* programs through *Olex2*, finding them to prove a powerful combination.

While *Olex2* is a powerful refinement GUI with ever improving features for the analysis of data and generation of images, there are two further crystallographic software packages that are essential to the high-pressure crystallographer. The Cambridge Crystallographic Data Centre (CCDC) provides a powerful library of published crystal structures, *i.e.*, the Cambridge Structural Database (CSD; Groom *et al.*, 2016), and a range of software for the analysis and comparison of structures. One such program is *ConQuest* (Bruno *et al.*, 2002), which provides a search tool for the CSD that allows the user to search for a wide range of criteria from general motifs to specific molecules, a specific journal article or experimental condition. The software can also search geometric parameters and so pose a particularly useful tool for analysing trends in bonding. Once a search has been performed, a list of appropriate structures is returned and these, along with any specified information, may then be exported, visualised and analysed in *Mercury* (Macrae *et al.*, 2008). *Mercury* is a visualisation and analysis suite, allowing statistical analysis of data mined using *ConQuest*, and comparison and analysis of both individual molecules and extended packing motifs. While most structure images in this report were generated using *Olex2*, the program does not facilitate the

overlaying of structures and *Mercury* is far more powerful for matters concerning crystallographic packing.

The third piece of software that is almost essential to the high-pressure crystallographer, and indeed for any structural chemist who compares and considers the packing of different structures, is *CrystalExplorer* (Wolff *et al.*, 2012). This software combines basic spherical models of atomic electron density to calculate surfaces relating to the electron density distribution in a crystal. The most commonly used and widely applicable surfaces (Fig. 3) are those of Hirshfeld surfaces (Spackman & Byrom, 1997; Spackman & Jayatilaka, 2009), from which print plots can be generated, and of void-space (Turner *et al.*, 2011).

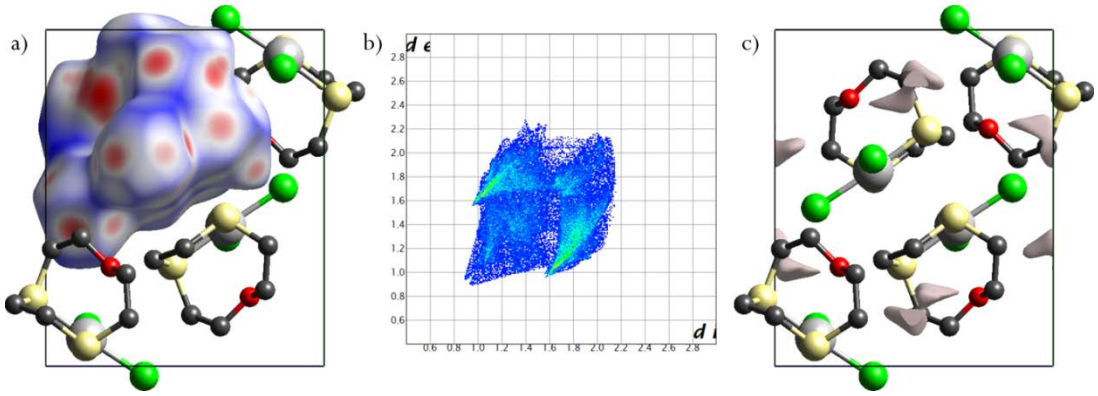



**Figure 3** Example images of the a) Hirshfeld surface, b) fingerprint plot and c) void space surface for a Pd(II) complex at 46.5 kbar; hydrogen atoms omitted for clarity.

Hirshfeld surfaces represent a spatial partition of the crystal that models the electron density. The surface defines the point at which the electron density present is 50 % owed to the atoms selected, *i.e.*, it marks the point at which the electron density becomes primarily owed to the promolecule rather than the remainder of the crystal. The surface is then coloured according to the closeness of contacts between atoms of the promolecule and those outside the surface. There are a

couple of ways in which this can be done, but the most commonly used is $d_{norm}$ (Fig. 3a) where red corresponds to contacts within the sum of the van de Waals radii, blue to those beyond it and a gradient through white. This allows a powerful visual comparison of, for example, close intermolecular contacts and bonding between polymorphs or on either side of a phase transition. This information can also be conveyed in a more quantitative form *via* conversion into a fingerprint plot (Fig. 3b). Here, the distance from the Hirshfeld surface to the closest internal ($d_i$) and external ($d_e$) atoms are plotted on Cartesian coordinates for each pixel. These plots are coloured blue, through green and yellow, to red with increasing number of pixels found to have a given set of values for $d_i$ and $d_e$.

Void space surfaces can be calculated by both *CrystalExplorer* (Fig. 3c) and *Mercury*, but the two programs do so with distinct differences. *Mercury* employs a hard-sphere atomic model: a probe of definable size is moved about the structure and a surface is mapped that defines the locations where the probe may be placed without overlapping in space with atoms of the crystal. This is not the method used in this body of work. Void space herein is calculated using *CrystalExplorer* which presents the surface where the total electron density calculated by its algorithms drops below a specified threshold. The default value of 0.002 e $A^{-3}$ was employed to calculate the surfaces presented herein, but this should not be taken as comprising the solvent accessible void space, for which 0.0003 e $A^{-3}$ has been shown as a more representative isovalue (Turner *et al*., 2011). Instead, void space discussed in this work represents compressible regions of low electron density.

For the high-pressure structural scientist, it is normal to calculate an equation of state (EoS) to quantify the compressibility of the material studied, given by the

bulk modulus, $B_0$, and its pressure derivative, $B'_0$. Molecular crystals are found to have bulk moduli <30 GPa (McKellar & Moggach, 2015), typically in the order of 7-20 GPa for coordination complexes (Tidey *et al.*, 2014 and references therein). Similarly, MOFs are also reported as spanning a range of 3-30 GPa (Serra-Crespo *et al.*, 2012) with less compressible systems since reported (*e.g.*, Spencer *et al.*, 2012), while zeolitic frameworks and inorganic / mineral phases can be much less compressible. Calculation of these requires the fitting of a polynomial to the data. While it is possible to do this without the aid of any software, Angel *et al*. provide a simple and effective program with which to do this. *EosFit7c* (Angel *et al.*, 2014), ran through *EosFit7GUI* (Gonzalez-Platas *et al.*, 2016), allows a quick testing and refinement of multiple types of EoS, each of which are covered in the lead article. It does so with graphical and numerical output, requiring only a simple text file containing certain basic parameters from the high-pressure study.

Of the equations of state made readily available through *EosFit7c*, the most commonly used is that of the 3rd-order Birch-Murnaghan (BM) EoS. This came about for the reason that it provides a refineable term for the second pressure derivative of the bulk modulus, required for accurate modelling of compressions greater than *ca.* 10 % (Angel *et al.*, 2014). While the Tait EoS also gives such a parameter, Angel *et al*. note that results from the two functions are usually indistinguishable, with the 3rd-order BM EoS typically giving slightly better measures of statistical fit. For these reasons and to maintain comparability with the literature, this is also the EoS employed in this body of work; where it could be calculated, the third-order BM EoS provided good approximation of the high-pressure behaviour.

### 1.3.2. Density functional theory

Each of the studies presented herein are accompanied by data extracted from density functional theory (DFT) calculations. Just as with the use of routine crystallography to support a synthetic chemist's work, the level of theoretical understanding required for the use of supporting calculations has been greatly reduced by the advent of powerful programs and GUIs. In essence, DFT calculations establish a wave equation for the defined system by combining approximate wave equations for the constituent atoms. These approximations are called basis sets. In doing so, it is possible to calculate molecular orbitals, energies and spectroscopic properties.

In general, properties are calculated after a stage known as geometry optimisation, which is an iterative refinement to obtain the least energetic conformation of a molecule or group of molecules. Using the programs available, *i.e.*, the Amsterdam Density Functional suite (*ADF*; Fonseca-Guerra *et al.*, 1998; Te Velde *et al.*, 2001) and *CASTEP* (Clark *et al*., 2005), this was not possible for high-pressure studies as there lacks the ability to model pressure. Thus, in performing a geometry optimisation on a high-pressure model the effects of pressure are relieved. In addition, periodic boundary programs such as *CASTEP* were not readily available. Consequently, with the exception of the ambient pressure work in Chapter 2, only gas-phase single-point calculations are employed, for which the fragments defined are the precise fragments considered by the program.

Calculations were run to predict a number of properties, including energies of the fragments, selected bond orders, partial charges and UV/vis spectra. Where energies are discussed, the specific nature of these will be briefly described in the

according chapters. The bond orders calculated using *ADF* correspond to Mayer bond orders (Bridgeman *et al.*, 2001).

## 2. Chemical background

The work in this thesis builds directly on that previously carried out in the group on thioether macrocycle complexes. A thioether macrocycle is typically defined as an aliphatic ring of size greater than 8 with three or more sulfur donors, and the class of compounds has been known since the 1930s (Tucker & Beverley, 1933). One that has received particular interest is 1,4,7-trithiacyclononane ([9]ane$S_3$). This may in part be owed to it being comparatively simple to synthesise, but there are additional benefits to its use. Being a tridentate nine-membered macrocycle, it is relatively constrained in its conformation and coordination. While the macrocycle can accommodate *exodentate* binding motifs, commonly of the bidentate coordination mode observed in [Mo([9]ane$S_3$)($C_5H_5$)$(CO)_2$]($BF_4$) (Gamelas *et al.*, 2011), it typically gives rise to facial coordination, as seen in [Cu([9]ane$S_3$)$_2$]($BF_4$)$_2$ (Glass *et al.*, 1993). In the context of metals preferring square planar coordination, for example $d^8$ metals such as Pt(II), this gives the propensity to form distorted [4+1] square-based pyramidal or [4+2] octahedral geometries. In these cases, the macrocycle binds in the normal fashion at the equatorial plane and offer its third donor in a more distant axial position: examples of [4+1] and [4+2] geometries include [Pt([9]ane$S_3$)$_2$]($PF_6$)$_2$ crystallised from water (Blake *et al.*, 1987) and [Pt([9]ane$S_3$)$_2$]($PF_6$)$_2$·$2CH_3NO_2$ (Grant *et al.*, 2005), respectively.

This conformational variability and the predisposition of thioether donors to locate at the axial positions made [9]ane$S_3$ and related macrocycles appealing targets for

electrochemical studies. Studies of *bis*-[9]ane$S_3$ found that it could stabilise a number of rare oxidation states, including Pd(III) (Stephen *et al*., 2012), Pt(III) (Blake *et al.*, 1987), Au(II) and Au(III) (Blake *et al*., 1989; Shaw *et al*., 2006), and Ni(III) (Stephen *et al*., 2011). In the latter study, tridentate azathioethers were also studied, which also showed a similar ability to stabilise Ni(III). In this and the study of Shaw *et al*. (2006), the ability of the thioether macrocycle to stabilise these oxidation states was shown to be supported by the ligand being redox non-innocent, delocalising the charge across both the metal and ligand. This coordinative flexibility and ability to stabilise high-energy electronic states made complexes of the ligand attractive targets for high-pressure study (Allan *et al*., 2006): our high pressure studies of associated complexes are covered in Section 3.1.2 as part of the review of high-pressure studies of coordination complexes.

Continuing our investigations in this area, attention was given to complexes of 1-oxa-4,7-dithiacyclononane ([9]ane$S_2$O), a tridentate macrocycle similar to [9]ane$S_3$ but with one sulfur donor replaced by an oxygen donor. This results in a slightly smaller macrocycle containing one hard and two soft donor atoms. Complexes of [9]ane$S_2$O have received comparatively little structural study, with a search of the CSD revealing only 23 hits containing the moiety, six of which are reported as part of the work on polymorphism reported in Chapter 2, while harbouring 470 [9]ane$S_3$ containing structures (Nov. 2015 release plus two updates; Groom *et al.*, 2016). The literature shows that [9]ane$S_2$O preferentially binds *via* the sulfur donors at equatorial positions in the context of palladium or platinum containing species (Lucas *et al.*, 1997; Grant *et al*., 1998; Tidey *et al*., 2015), and that even in harder metals such as Cu(II) the oxygen maintains an axial position (Grant *et al.*, 2000). Despite affecting such changes, just as with the azathioethers studied by

Shaw *et al*. (2006), [9]ane$S_2O$ was able to stabilise Au(II) and Au(III), again being shown as redox non-innocent (Huang *et al*., 2008). This combination of similar stabilising properties and conformational variability to [9]ane$S_3$ while offering a notably differing axial ligation made complexes of [9]ane$S_2O$ a logical target in our continued studies into the high-pressure structural chemistry of macrocycle compounds.

Targets for high-pressure study in the group have typically focussed on macrocycle complexes of Pd(II) and Pt(II) and this work is no exception. As mentioned above, $d^8$ Pd(II) and Pt(II) metal centres have a preference toward square planar bonding. This removes the degeneracy of the $e_g$ orbitals of an octahedral field and lowers the energy of orbitals with a *z* component. This allows the high-energy $d(x^2–y^2)$ orbitals, which point directly towards the σ donor orbitals of the ligands, to remain empty, thus minimising the ligand field stabilisation energy (LFSE). Ligation with tridentate macrocycles is thus in direct competition with this preference and, while the binding preference of the macrocycle commonly overcomes this, the geometric binding and preference of the metal centre distorts such complexes. It serves the most benefit to the LFSE that the complex remains distorted along the *z* axis, and hence results in elongated axial interactions. These long axial interactions are expected to prove particularly sensitive to the effects of pressure and allow for interesting phenomena, as exampled in the following literature review.

## 3. Coordination complexes under pressure

Although the first high pressure study of a coordination complex, describing the compressibility and high-pressure phase transition of the metalloporphyrin complex [Co(5,10,15,20-tetraphenyl-12*H*,23*H*-porphinate)], appeared in 1987

(Hazen *et al.*), it is comparatively recently that other such studies have emerged in significant numbers. There are now currently descriptions of around 60 relevant systems in the literature, three-quarters of which have appeared since 2009, when the broader area was reviewed (Moggach & Parsons, 2009). This section focuses on the review of complexes which are predominantly mononuclear at ambient pressure and includes a small number of binuclear and trinuclear species. It specifically excludes extended structures such as metal-organic frameworks (MOFs), the high-pressure behaviour of which differs notably to that of molecular crystals; a number of reviews have recently covered the study of MOFs (Gándara & Bennet, 2015; Guiseppe *et al.*, 2015; McKellar & Moggach, 2015). In addition, studies of one-dimensional polymers and certain particularly simple or borderline inorganic materials that were otherwise included for completeness in our review of the field (Tidey *et al*., 2015) along with a number of the miscellaneous structural studies therein have been omitted for brevity; what follows is not on its own an exhaustive review.

High pressure studies of organic molecules might typically generate new phases by the rearrangement and modulation of intermolecular interactions, with bonding distances and valence angles largely unaffected (Boldyreva, 2004, and references therein). In contrast, coordination compounds − where the metal geometry can be considerably more flexible − can exhibit changes in bond distances which are an order of magnitude greater than those in organic compounds. Many high pressure single crystal diffraction studies on metal complexes have been undertaken to explore variations in specific physical phenomena such as polymorphism, magnetic behaviour, conductivity, colour and spin-crossover effects (*vide infra*). While certain of these phenomena will be discussed in distinct sections, the

majority of studies have focussed on changes in geometry on increasing pressure, and this forms the primary focus of this section. It begins by describing the broad range of structural changes which are observed on increasing pressure. These changes are largely geometric, but there are also examples of associated changes in, for example, optical properties. What follows are then highlighted studies on specific avenues of structure-property relationship investigations, such as those on single-molecule magnets (SMMs).

### 3.1. Geometric studies with pressure

This section surveys the relevant literature where the main emphasis has been on structural and related changes in coordination at the metal centre rather than on specific properties or function. The chemical systems studied are highly variable and, with the exception of work on a family of Cu(II) complexes, tend to comprise individually interesting but isolated examples rather than any systematic studies. Given the high level of experimental and analytical effort required to complete a successful high pressure study, this is unsurprising. The range of structural changes observed thus far is nevertheless extensive and impressive, with characteristic reductions in the lengths of unit cell parameters and intermolecular contacts accompanied by intramolecular changes to geometry, coordination number, conformation, solvent ordering, hydrogen bonding, degree of association, colour, phase or electronic structure.

#### 3.1.1. Complexes of Cu(II)

As indicated, Cu(II) complexes comprise one of the largest single family of complexes studied by high-pressure crystallography. This is presumably owed to

the electronic structure favouring Jahn-Teller distorted complexes that provide bonding configurations which may be exceptionally sensitive to pressure. The attention was clearly warranted as the vast majority of common pressure-induced phenomena are observed in their structural studies. One exemplary study is in the polymerisation of the binuclear Cu(II) complex [guH][$Cu_2$(OH)(cit)$(gu)_2$] ($cit^{4-}$ = citrate; gu = guanidine; Fig. 4; Moggach *et al.*, 2009). Under ambient conditions, the compound packs as discrete molecules with a series of long-range interactions between an unbound carboxylate oxygen and the Cu(II) centre of a neighbouring molecule [Cu···O = 3.217(4) Å] (Fig. 4).

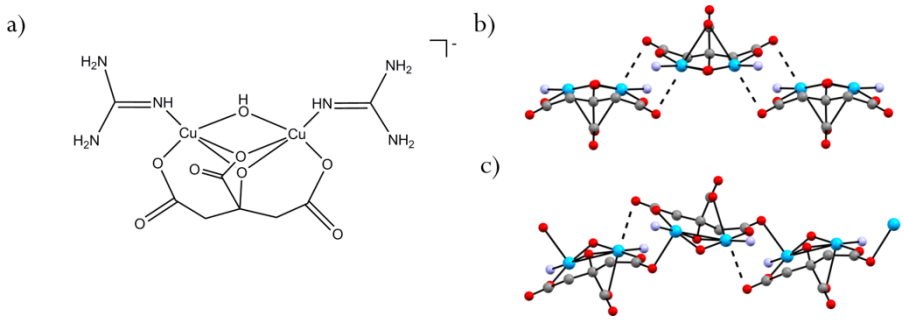



**Figure 4** a) Schematic and b-c) view of the packing of $[Cu_2(OH)(cit)(gu)_2]^-$ ($cit^{4-}$ = citrate; gu = guanidine) anions at b) ambient pressure and c) in the first high-pressure phase. For b) and c): non-bonded interactions are highlighted with dashed lines; Cu atoms are in cyan, N in pale blue, O in red and C in grey, with H atoms and the $C(NH_2)_2$ groups of the gu ligands omitted for clarity.

Application of 18 kbar brings about a contraction of 0.264(4) Å in the length of this interaction, with the apical Cu···O interaction contracting by only 0.039(4) Å. At 29 kbar, there is a phase transition from *Pnma* to $P2_12_12_1$ as two crystallographically independent Cu···O interactions of 2.879(7) and 2.610(6) Å are formed (Fig. 4). As pressure is further increased to 42 kbar there is another phase transition to space group $P2_1/c$ in which neighbouring chains of the

previously-formed polymer are no longer identical; one becomes slightly more symmetric, while breaking of one of the previously-formed intermolecular Cu···O interactions takes place in the other. The authors draw attention to the reason for phase transitions in organic systems being one of minimising repulsion between atoms. They conclude that in this study the transitions seem to involve the avoidance of Cu···O interactions with lengths of around 3.0 Å, which appears to represent an intermediate between intermolecular and intramolecular interactions. A similar result was obtained in the study of the one-dimensional coordination polymer [Cu(II)(*L*-aspartate)($H_2O$)$_2$] in which discontinuous compression of the elongated axial interactions was observed between 68 and 79 kbar that accounted for *ca*. 30 % of their total compression (Gould *et al*., 2012).

It is worth drawing attention to the observation here of a continued loss of symmetry with each phase transition. This was commented on by Hazen *et al*. (1987) in their early high-pressure X-ray diffraction (HPXRD) study. The authors mention that the decrease in symmetry is directly linked to an increase in compressibility; in losing the symmetry constraints of a higher symmetry cell, molecules gain "compressional degrees of freedom". This is exemplified in the case of $ReO_3$ (Schirber & Morosin, 1979; Schirber *et al*., 1984) and further displayed in the crystallographic studies of Casati *et al*. (2005; 2009).

Study of a related complex was published in 2010 (Galloway *et al*.) that described the effect of pressure on [guH]$_4$[$Cu_2$(cit)$_2$]·2$H_2O$ (Fig. 5), which exhibits piezochromism. At ambient pressure each Cu(II) centre is coordinated primarily by four O-donors in a distorted tetrahedral geometry and supplemented by an intramolecular Cu···O contact to a more remote O-donor of a carboxyl group. The

application of pressure causes the length of this contact to decrease from 2.628(3) to 2.407(3) Å up to 22 kbar, resulting in a more square-based pyramidal geometry. These changes are accompanied by a gradual change in the colour of the crystal from blue to green as the relative energies and symmetries of the *d*-orbital manifold are modified by the change in coordination geometry (Fig. 5).

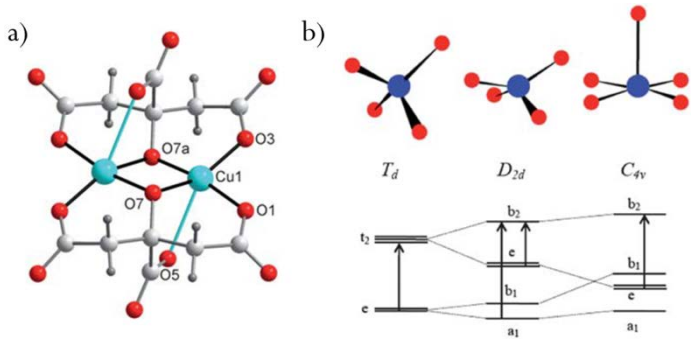



**Figure 5** a) View of the molecule $[guH]_4[Cu_2(cit)_2]\cdot 2H_2O$ (gu = guanidine; cit = citrate); Cu atoms in pale blue, O atoms in red, C atoms in grey, H atoms smaller in grey. b) Diagram depicting the effect of changing coordination geometry on the electron structure of the *d* orbitals at the Cu(II) centre in $[guH]_4[Cu_2(cit)_2]\cdot 2H_2O$. Images reproduced from Galloway *et al.*, 2010.

High-pressure crystallography has also been used to rationalise the mechanochromism observed in a copper iodide cubane cluster (Benito *et al.*, 2015), relating the phenomenon instead to compression of the Cu···Cu distances. As is typical for such complexes, the contractions in the other Cu−O bond lengths are negligible.

Other studies on Cu(II) complexes included that of Prescimone *et al.* (2010a) with the publication of a high-pressure study of three hydroxo-bridged dimers. In this report, two of the complexes gave little by way of interesting phenomena under pressure, exhibiting only small deformations to their geometry and bonding. This provides a good example of the true nature of high-pressure structural study where

oftentimes an investigation results in little by way of striking phenomena. Nevertheless, the third compound studied was notably more interesting. The application of 25 kbar to $[Cu_2(OH)_2(H_2O)_2(tmen)_2](ClO_4)_2$ (tmen = tetramethylethylenediamine) results in a $P2_1/c \rightarrow P\bar{1}$ phase transition that sees the ordered expulsion of a bound water molecule from one in every two dimers. This in turn brings a bending of the molecules in question and allows the perchlorate anions to adopt long-range binding to the copper centres (Fig. 6). The authors also correlated the structural studies with magnetic data and found links between the bridging <Cu−O−Cu angles and antiferromagnetic / ferromagnetic exchange in the molecules.

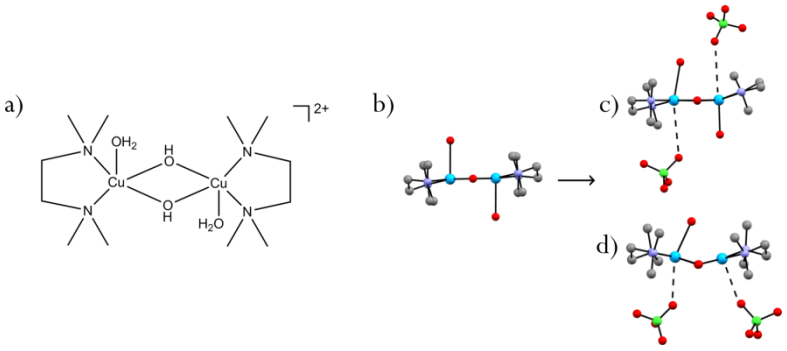



**Figure 6** a) Schematic and b-d) view of the coordination of binuclear $[Cu_2(OH)_2(H_2O)_2(tmen)_2]^{2+}$ (tmen = tetramethylethylenediamine) viewed down the O···O vector of the bridging hydroxo groups at b) ambient pressure and c-d) the pressure induced changes in the unique cations at 25 kbar. Note the significant bending and closer proximity of $ClO_4^-$ anions to the complex which undergoes the expulsion of coordinated water (d) compared to that which does not (c). Cu atoms are in cyan, Cl in green, N in pale blue, O in red and C in grey, with H atoms omitted for clarity; perchlorate ions are distant and thus omitted in the ambient pressure phase (b).

To complete the range of common results found in the high-pressure study of coordination complexes being exhibited by Cu(II) complexes, in the one study left to mention, the binuclear complex $[Cu_2(\mu_2$-1,1'-(1,3-phenylene)bis(4,4-

dimethylpentane-1,3-dionato))$_2$(*N*-methylmorpholine)$_2$] was studied at pressures of up to 9.1 kbar, above which pressure crystallinity was lost (Clegg *et al.*, 2010). While loss of crystallinity is quite common in the high-pressure study of molecular crystals, 9.1 kbar represents a particularly low pressure limit, even compared to MOFs which are typically far less stable under pressure (McKellar & Moggach, 2015).

### 3.1.2. Complexes of gold and group 10 metals

It is interesting to note that, of the *ca*. 10 studies which have appeared since the time of our review, three have been on complexes of gold. These include the work elsewhere within our group by O'Connor *et al*. (2016) for which the largest reported pressure-driven compression of an aurophillic contact was observed between ambient pressure and 106.2 kbar [Au···Au = 3.6686(5), 3.0554(12) Å, respectively]. Paliwoda *et al*. (2014) report the effects of 10 kbar to a gold(I) diethylthiocarbamate polymer in which 1D helices of alternating supported and unsupported Au···Au contacts run parallel to the *c* axis. The longest of these at ambient pressure is only 3.01 Å and the largest compression brought by pressure is in the order 0.1 Å. The primary result of this structural study is the observation of negative area compressibility in one of two phases obtainable at ambient pressure. This is perceivable as that observed in compression of a spring and results in the partial unwinding of the helical motif as the crystal transforms to an alternative phase, corresponding to the other phase obtainable at ambient pressure. The remaining update in this area provides an investigation into the effect of the length of Au···Au interactions on solid-sate luminescence in gold(I) pyrazolate-based trimers (Woodall *et al*, 2014). By use of both ligand variation and high-pressure

crystallography, alongside several other techniques, the authors provide an extensive and systematic study that exemplifies the power of the technique in establishing structure-property relationships.

These investigations add to two further studies covered in our review, one of which details negative linear compressibility (Woodall *et al*., 2013; *cf.* Section 3.2) and the other a molecular conductor (Okano *et al*., 2009). The latter comprises the study of the planar *bis*-trimethylenetetrathiafulvalenedithiolate gold(IV) complex up to 107 kbar, revealing significant compression of the $S_4$ square plane at the gold [$\Delta$Au−S = 0.051(10) Å] and the compression of extremely close intermolecular S···S contacts [2.73 Å at 107 kbar; $\Sigma_{vdW}$ = 3.6 Å (Bondi, 1964)]. The authors comment that this is in keeping with the classification of the material as a molecular conductor, likening the compression to that of a metal, the molecule itself adopting the role of the metal atom. Molecular conductors, such as this one, represent another area where high-pressure crystallography has been employed to better understand the effects of pressure on functional materials. The work of Okano *et al*. is typical of studies of molecular conductors, where compression of intermolecular contacts that form part of the conductance pathway are typically those most compressed (Konno *et al*., 1989; Guionneau, *et al*., 1996; Shirotani *et al*., 2005). In contrast to these studies, Okano *et al*.(2004) investigated the molecular conductor $[(C_2H_5)_2(CH_3)_2N][Pd(dmit)_2]_2$ ($dmit^{2-}$ = 1,3-dithiole-2-thione-4,5-dithiolate) which was known to undergo a transition to an insulator at 7 kbar (Kobayashi *et al*., 1993). The authors were able to dispel a previously held and otherwise plausible explanation for this phenomenon as the structural observations made were simply not compatible with it.

Complexes of group 10 metals are another family of complexes that have received repeated attention, both in the context of rationalising their pressure-dependant phenomena and also from our own structural investigations. For example, Byrne *et al.* (2012) investigated piezochromism in two salicylaldoximato complexes of Ni(II). As part of this work, they describe the planar molecules of [Ni(3-fluoro-salicylaldoximato)$_2$] stacking along the *c* axis to give one-dimensional chains *via* Ni···Ni interactions [3.1942(4) Å], but find that the pressure-induced contraction of this distance did not engender conductivity. This was in contrast to the case observed for [Ni(dmg)$_2$] (dmg$^-$ = dimethylglyoximate; Takeda *et al*., 2006), despite the Ni···Ni distances at 54 kbar for [Ni(3-fluoro-salicylaldoximato)$_2$] being directly comparable to those at 74 kbar for [Ni(dmg)$_2$] [Ni···Ni = 2.822(2) and 2.82 Å, respectively]. The latter complex, [Ni(dmg)] has since received further attention, showing a possible pressure-induced intramolecular proton transfer event between ligands (Bruce-Smith *et al*., 2014). The authors use periodic DFT calculations to improve modelling of the hydrogen positions and find a "peculiar" coupling between the torsion of terminal methyl groups and the potential well in which the labile proton resides. This phenomenon was previously observed in the analogous Pt(II) containing species by Konno *et al*. (1989).

In our own studies of Pd(II) and Pt(II) containing species, we displayed an example of a reversible, stepwise compression and pressure-induced increase in coordination associated to an orange → black piezochromic response and concurrent with a conformational rearrangement (Fig. 7; Allan *et al*., 2006). This phenomenon was found to be unique for the palladium *bis*-chloride homologue of the series [$MX_2$([9]aneS$_3$)] ($M$ = Pd, Pt; $X$ = Cl, Br, I), despite that all phases are isomorphous and isostructural under ambient conditions (Allan *et al*., 2014a). In all

such phases, the axial M···S interaction was found to be significantly more compressible than any other intramolecular interaction. We also report study of *M* = Pd and *X* = $PPh_3$, for which increasing the pressure results in progressive yet considerable bending at the *ipso*-carbon of one of the phosphine ligands which are engaged in a four-fold phenyl embrace (Fig. 7; Wong *et al*., 2013). This occurs so as to reduce the formation of highly repulsive close C−H···π and C−H···H−C contacts, and in turn engenders π···π stacking between the deviated phenyl moieties. Our most recent publication in this area of constitutes the work detailed in Chapter 3 (Tidey *et al*., 2016).

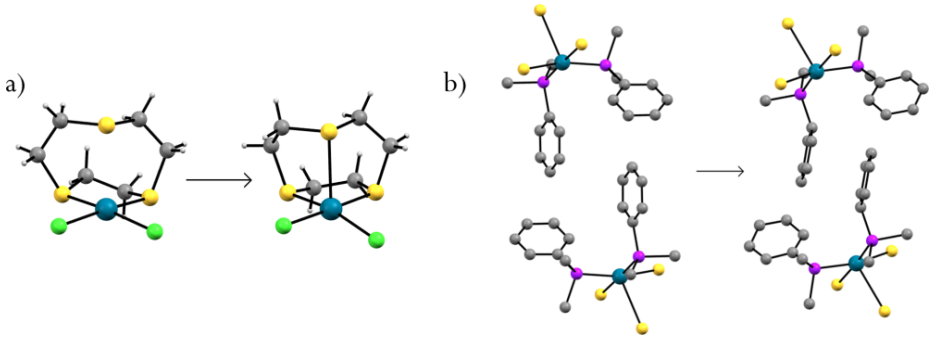



**Figure 7** a) View of [$PdCl_2$([9]ane$S_3$)] before (left, 42.5 kbar) and after (right, 46.0 kbar) the phase transition. Note the change in the conformation of the macrocycle at the top left of the molecule. b) View of the four-fold phenyl embrace in [Pd([9]ane$S_3$)($PPh_3$)$_2$]($PF_6$)$_2$ at ambient pressure (left) and 65.5 kbar (right). Note the greatly increased overlap of the π-stacked phenyl groups and the significant bending at their *ipso*-carbons. Pd atoms are in blue, Cl in green, S in yellow, P in purple and C in grey; H atoms included as small, white atoms in (a) but omitted in (b) for clarity; non-interacting phenyl moieties, macrocyclic carbons and $PF_6^-$ counter anions have been omitted from (b) for clarity.

### 3.1.3. Miscellaneous species

The nature of the field means that there remain many studies which do not fit well into a given category. Some of these are relatively straight forward, revealing only compression of cell parameters (Slebodnick *et al*., 2004; Hansson *et al*., 2006),

while others detail interesting corners of science that would otherwise have gone unseen. For example, Fabbiani *et al*. (2010) detail an ambitious study of vitamin B12 under pressure which probably corresponds to one of the largest and certainly most solvent-heavy coordination compounds investigated by these means. The study shows the application of pressure serving to increase the quality of the crystal, with the contraction of solvent channels and pressure-induced rotation of a side-chain affecting considerable solvent ordering.

Another example of solvent ordering was provided by Madsen *et al*. (2014) in the study of the three-membered linear metal chain complex $[Co_3(2,2'\text{-dipyridylamide})_4Cl_2]\cdot CH_2Cl_2$. The solvent ordering was reported along with a pressure-induced increase in a terminal Co−Cl bond length. The authors use Hirshfeld surfaces (*vide infra*) to rationalise the solvent ordering as an effect of simple close intermolecular contacts, while the lengthening of the Co−Cl bond was rationalised with the aid of computational work. This work provides a good example of how useful the two tools mentioned are towards rationalising high-pressure structural behaviour. The comparable bromide was later reported in 2015 (Madsen *et al*.), showing pressure to again affect the disorder of the solvate. Notably, the authors study the compound using 1:1 *n*-pentane/*iso*-pentane as the pressure transmitting medium, for which the hydrostatic limit is reported as 74 kbar (Klotz *et al*., 2009), yet non-hydrostatic conditions were observable even above 54 kbar. Despite this, by annealing the sample at 130 °C, reliable structures were able to be determined up to 118 kbar.

In another rare example of a systematic high-pressure crystallographic study, Allan *et al*. (2014b) investigate the series $[GeX_2\{o\text{-}C_6H_4(P(CH_3)_2)_2\}]$ (*X* = Cl, Br, I). The

study provides an excellent example of HPXRD being employed towards the understanding of secondary bonding interactions and their effect on the structure and packing. A highlight of the paper is the observation of a phase transition between 29 and 41 kbar that vastly reduces the so-called void space in the crystal *via* slippage between aromatic groups while interactions between Ge and Ge or *X* are much less affected. The study shows both the tendency of phase transitions to occur in a manner as to increase packing efficiency and also the relative strength of various intermolecular interactions. In particular, it exemplifies the power of HPXRD studies towards further developments in crystal engineering and structure prediction.

In one of the most recent high-pressure crystallographic publications, Stevens *et al.* (2016) report the slightly unexpected rigidity of a so-called Pacman complex, in which a Schiff-base calixpyrolle is folded to predispose two chromium(II) centres over each other. The authors find that the Cr···Cr distance is relatively unaffected by pressure up to 30 kbar, with no evidence in their electronic studies of the formation of a Cr···Cr bond, despite the separation being the shortest *M*···*M* separation reported for complexes of the given ligand. Instead, the main effect of pressure was on the position of an *exogenous* benzene located over the open site of the metal centre, with which it was compressed towards and became co-planar. While the authors speculate about the potential for long range interactions between the molecules, their calculations suggested this was merely to increase packing efficiency.

Further updates to the literature include that of Wu *et al*. (2015) which provides further study of photomagnetic materials comprising 3*d*-4*f* bimetallic complexes

that serves to build on their earlier publication (Wu *et al.*, 2013). The updating work provides a study of a variety of complexes related to $[Y(DMF)_4(H_2O)_3(\mu\text{-}CN)Fe(CN)_5]\cdot H_2O$ (DMF = *N*,*N*-dimethylformamide), described in the first of these publications, by variation of the metal at the iron site. These studies are rare in commenting that reliable and stable solutions could not be obtained for all pressures, but this is a common problem associated with the field and one might expect that failed collections are more commonly just not reported. The work in the recent study corrects the conclusions drawn from that of the first and interestingly links the piezochromism observed in the complex to the non-hydrostatic conditions offered by the PTM, paratone-N.

### 3.2. Negative linear compressibility

Negative linear compressibility (NLC) is the phenomenon whereby pressure causes a system to increase in length along one or more directions while undergoing an overall decrease in volume (Baughman *et al.*, 1998). Suggested applications for NLC compounds include sensors, actuators, artificial muscles and as components of advanced structural materials. One system that gives rise to NLC is the linear organoauric complex $[(C_6F_5Au)_2(\mu\text{-}1,4\text{-diisocyanobenzene})]$. The complex crystallises as alternating sheets that give rise to a ‘wine rack’ motif when viewed down the *c* axis (Fig. 8; Woodall *et al.*, 2013) but has no formal bond that forms the ‘hinge’. Upon the application of 24.2 kbar, the angle about the pivot, measured as the torsion angle NC−Au···Au−CN, closes from 74.314(9) to 63.87(18) °. It is at this pressure that a maximum in the length of the *a* axis is observed. In this pressure range a negative linear compressibility of $-12.57\ TPa^{-1}$ is thus observed. Other examples of NLC comprise largely framework materials. The largest NLC

reported [−42(5) $TPa^{-1}$ between ambient pressure and 18 kbar] was found for the metal cyanate framework $Zn[Au(CN)_2]_2$ (Cairns *et al.*, 2013). Within the structure, helices form which interact *via* aurophillic interactions. Pressure causes the helices to compress at the sides and lengthen. As these helices lie parallel to the *a* axis, it is the *a* axis that experiences the observed NLC. Two other systems that have been studied are $Ag_3[Co(CN)_6]$ (Goodwin *et al.*, 2008) and $KMn[Ag(CN)_2]_3$ (Cairns *et al.*, 2012), both of which exhibit NLC as a result of packing in a 'wine rack' framework.

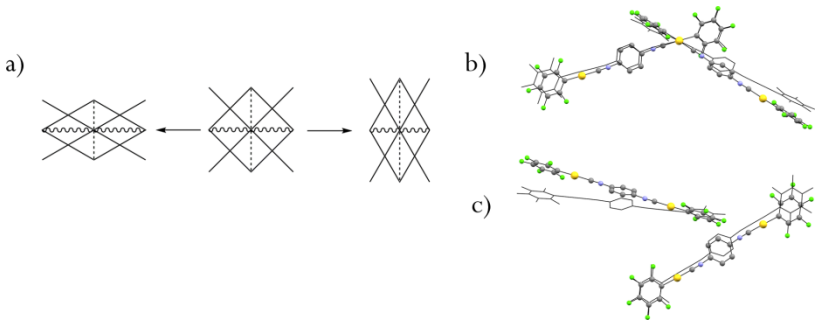



**Figure 8** a) Diagram showing the deformation associated with a 'wine rack' motif under hydrostatic pressure, with the central image representing the situation at ambient pressure. The image to the left illustrates the deformation that occurs when the interactions in the direction characterised by the wavy lines are less compressible than those characterised by the dashed lines, while the image to the right shows the opposite situation. b) & c) Overlay view of neighbouring units of $[C_6F_5Au)_2$(μ-1,4-diisocyanobenzene)] at ambient pressure (colour ball-and-stick diagram) and 43.9 kbar (monochrome stick diagram) depicting the opening of the system as viewed along the Au···Au vector (b) and from above it (c). Au atoms in yellow, F in green, N in blue and C in grey, with H atoms omitted for clarity.

### 3.3. Spin-crossover complexes

Spin-crossover (SCO) complexes are another class of material that high-pressure crystallography offers an excellent handle on and several such studies exist. SCO is a phenomenon that occurs for certain transition metal complexes whereby an

external stimulus (*e.g.*, a change in temperature or pressure, irradiation with light or the application of a magnetic field) alters the spin state between high-spin and low-spin. Because high-spin states occupy greater volumes than their low-spin counterparts, the application of pressure will tend to favour the latter and in favourable cases bring about a transition from a high-spin to a low-spin complex. The inherent bistability of the two spin states and the associated changes in physical properties such as colour or magnetism has led to proposed applications as switches, data storage devices and optical displays.

Owing to the decrease in volume of the coordination sphere that SCO from high-spin to low-spin brings, it has been possible to locate the transition point between the high and low spin states by assessment of the cell parameters (Granier *et al.*, 1993) and the volume of the coordination sphere (Shepherd *et al.*, 2011). Nevertheless, studies have shown that compression of the coordination sphere brought in these such studies is not necessarily sufficient to engender transitions in compounds that have temperature dependant SCO phenomena (Guionneau *at al.*, 2005), for example owing to the isotropic conditions inside the DAC resisting the full range of deviations necessary (Guionneau *et al.*, 2001). In the case of the complex [Fe(dipyrido[3,2-*a*:2',3'-*c*]phenazine)$_2$(NCS)$_2$]·pyridine, pressure did eventually bring about an SCO transition, but this was found to be slow and gradual. Attention was brought to the opening of the angle between the chelate ligands brought by isotropic pressure being counter to what the SCO would bring (Shepherd *et al.*, 2012a). In contrast, where the SCO transition proceeds only to 50 % completeness down to 30 K in [{Fe(2,6-bis(pyrazol-3-yl)pyridine)(NCS)$_2$}$_2$(4,4'-bipyridine)]·2MeOH, pressurisation happens to bring full conversion to the low-spin state (Shepherd *et al.*, 2012b). This was rationalised

with reference to DFT calculations (Halder *et al*., 2008) as related to an increase in the torsion angle along the bridging 4,4'-bipyridine ligand brought with cooling, not observed under pressure, which serves to disrupt communication between metal centres. Since publication of our review, one further study of a molecular SCO material with high-pressure crystallography has been released. This detailed the first example of an SCO material that exhibits an order-disorder transition (Shepherd *et al*., 2016). The authors use high-pressure and low-temperature crystallographic data which are in unusually close agreement with one another in showing how, at a critical point, the space around the anion becomes insufficient enough to accommodate dynamic disorder. Concomitant to this is a stepwise contraction in the unit cell accompanying an isostructural phase transition and a 50 % complete SCO transition, after which point further cooling / compression brings an increased contraction as the SCO slowly proceeds to completion.

### 3.4. Molecular magnetic materials

Single-molecule magnets (SMMs) are molecules that can be magnetised by a magnetic field, remaining so after the inducing field is removed. Crucially, this is a property of the actual molecule which does not depend on interactions with other structural units, in contrast to traditional magnets. Single-molecule magnetism is therefore not restricted to the solid state, and SMMs can be dispersed without losing their properties. Potential applications proposed for SMMs include high-density information storage and quantum computing. The archetype of SMMs is $[Mn_{12}O_{12}(OAc)_{16}(H_2O)_4]$ (Lis, 1980; Caneschi *et al.*, 1991) and high-pressure studies have largely focussed on such Mn-based systems, including the related complex $[Mn_{12}O_{12}(O_2CCH_2{}^tBu)_{16}(H_2O)_4]$. In the combined crystallographic and

magnetic study, it was revealed that the application of pressure served to align an otherwise disordered and ambiguous Jahn-Teller axis with the others of the molecule (Parois *et al.*, 2010). This in turn was given as explanation for the slower relaxation time at higher pressures and marked increase in the energy barrier to relaxation observed at 4.7 kbar.

High-pressure crystallography offers a particularly attractive route of study in the case of SMMs as their properties are particularly dependant on minor changes in the molecules. Without the ability to mechanically alter structure, the only way one could investigate structure-property relationships would be to vary ligation or in the fortuitous discovery of polymorphism, both of which affect numerous variables at once. This was exemplified by Prescimone *et al*. (2008; 2009a) when the relationship between the nature of the exchange between two Mn centres and the torsion angle across a two-atom bridge linking them was corroborated in the first combined high-pressure crystallographic and magnetic study, performed on two $[Mn]_6$ clusters $[Mn_6O_2(2\text{-hydroxyphenylpropanone})_6(L)_2(EtOH)_6]$ (L = $O_2CPh(Me)_2$ or naphthalene carboxylate). Two other similar studies were published around the same time, reporting the structure-property relationship for a Mn trimer (Prescimone *et al*., 2009b) and two oxo-bridged Mn dimers (Prescimone *et al*., 2010b), both of which linked the decrease in exchange energy with pressure for such systems is related to compression of the Mn···Mn separation. Since the publication of our review, only one further study of this class has been published, detailing a tetrameric $MnNa_2$ species with unusually high resistance to compression (Craig *et al*., 2015). In their study of $Na_5[Mn(L\text{-tart})_2]\cdot 12H_2O$ (L-tert = L-tartrate), the authors find the complex to have a third-order bulk modulus of $B_0$ = 23.9(6) GPa, $B_0$' = 4.2(5), close to that of common salt, with a bulk modulus of

*ca.* 25 GPa. In contrast, values in the range of 7-20 GPa for $B_0$ are more typical in such studies of molecular coordination compounds (Tidey *et al*., 2014 and references therein; *vide infra*). This incompressibility is employed to rationalise the compound's resistance to pressure of the magnetic properties.

### 3.5. Concluding remarks

Clearly, high-pressure crystallography offers great benefit to many areas of scientific research, offering distinct advantages over methods such as chemical modification, largely by allowing the separation of geometric and chemical variables, permitting far more systematic study. Correlation of high-pressure structural studies with other spectroscopic and computational techniques allows the investigator great insight into structure-property relationships and, as such, the field can be expected to continue to grow as the technique becomes more accessible with the continued advancement of both lab and synchrotron sources and equipment. The preceding survey discriminately covers only one area of high-pressure crystallographic research, which also finds great use in the study of organic (Boldyreva, 2008; 2014), protein (Kurpiewska & Lewiński, 2010), framework (Giuseppe *et al*., 2015) and inorganic phases (*e.g.*, Zhao *et al*, 2009; Hofer *et al*., 2015) and so too in areas where such materials are applied. But even absent of direct application, structural studies can provide interesting and insightful information that is otherwise unattainable to the scientist. Systematic study of classes of compounds serves to progressively increase our knowledge of weaker bonding motifs and supramolecular interactions. Through their understanding in the context of crystalline packing, high pressure crystallography in turn will aid in rational crystal design and prediction, as well as our understanding and prediction

of phenomena such as polymorphism. Furthermore, uncovering phenomena such as the appearance of stepwise compression of elongated coordination bonds as those seen in the studies of Moggach *et al.* (2009) and Allan *et al*. (2014a) may well result in smart materials that, without such high pressure structural studies, may not have been realised.

## 4. Aims

The aim of this body of work was primarily to continue our investigation into the behaviour of platinum-group metal complexes of macrocyclic ligands. Specifically, three avenues of study arose:

1) Expand our studies to include complexes of [9]ane$S_2O$.
    - Investigate and rationalise the polymorphism of [$PdCl_2$([9]ane$S_2O$)].
    - Investigate and rationalise the high-pressure behaviour of all phases of [$PdCl_2$([9]ane$S_2O$)].
    - Extend studies to include Pt(II) containing compound.
2) Investigate the optical phenomena in [Pd([9]ane$S_3$)$_2$]($PF_6$)$_2$·2$CH_3NO_2$.
3) Further investigate polyiodide catenation under pressure.

## References


Agilent (2014). *CrysAlis*$^{PRO}$. Agilent Technologies, Yarnton, England.

Allan, D. R.; Blake, A. J.; Huang, D.; Prior, T. J.; Schröder, M. (2006). *Chem. Commun.*, 4081-4083.

Allan, D. R.; Bailey, D.; Bird, N.; Blake, A. J.; Champness, N. R.; Huang, D.; Keane, C. P.; McMaster, J.; Prior, T. J.; Tidey, J. P.; Schröder, M. (2014a). *Acta Crystallogr., Sect. B*, **70**, 469-486.

Allan, D. R.; Coles, S. J.; George, K.; Jura, M.; Levason, W.; Reid, G.; Wilson, C.; Zhang, W. (2014b). *CrystEngComm.* **16**, 8169-8176.

Angel, R. J.; Allan, D. R.; Miletich, R.; Finger, L. W. (1997). *J. Appl. Cryst.* **30**, 461-466.

Angel, R. J.; Bujak, M.; Zhao, J.; Gatta, G. D.; Jacobsen, S. D. (2007). *J. Appl. Cryst.* **40**, 26-32.

Angel, R. J.; Gonzalez-Platas, J.; Alvaro, M. (2014). *Z. Kristallogr.* **229**, 405-419.

Barnett, J. D.; Block, S.; Piermarini, G. J. (1973). *Rev. Sci. Instrum.* **44**, 1, 1-9.

Baughman, R.H.; Stafström, S.; Cui, C.; Dantas, S. O. (1998). *Science*, **279**, 1522-1524.

Benito, Q.; Baptiste, B.; Polian, A.; Delbes, L.; Martinelli, L.; Gacoin, T.; Boilot, J.-P.; Perruchas, S. (2015). *Inorg. Chem.* **54**, 9821-9825.

Blake, A. J.; Clegg, W.; Cole, J. M.; Evans, J. S. O.; Main, P.; Parsons, S.; Watkin, D. J. (2009). *Crystal Structure Analysis - Principles and Practice*. 2nd ed. New York: Oxford University Press Inc.

Blake, A. J.; Gould, R. A.; Holder, A. J.; Lavey, A. J.; Odulate, M. O.; Schröder, M. (1987). *Chem. Commun.* 118-120.

Blake, A. J.; Gould, R. A.; Greig, G. J.; Holder, A. J.; Hyde, T. I.; Schröder, M. (1989). *Chem. Commun.* 876-879.

Boldyreva, E. V. (2004). *J. Mol. Struct.* **700**, 151-155.

Boldyreva, E. V. (2008). *Acta Crystallogr., Sect. A*, **64**, 218-231.

Boldyreva, E. V. (2014). *Z. Kristallogr.* **229**, 3, 236-245.

Bondi, A. J. (1964). *J. Phys. Chem.* **68**, 441-451.

Bragg, W. L. (1913). *Proc. Cambr. Phil. Soc.* **17**, 43-57.

Bridgeman, A. J.; Cavigliasso, G.; Ireland, L. R.; Rothery, J. (2001). *Dalton Trans.* 2095-2108.

Brown, J. M. (1999). *J. Appl. Cryst.* **86**, 5801-5808.

Bruce-Smith, I. F.; Zakharov, B. A.; Stare, J.; Boldyreva, E. V.; Pulham, C. R. (2014). *J. Phys. Chem. C*, **118**, 24705-24713.

Bruno, I. J.; Coles, J. C.; Edgington, P. R.; Kessler, M.; Macrae, C. F.; McCabe, P.; Pearson, J.; Taylor, R. (2002). *Acta Crystallogr., Sect B*, **58**, 389-397.

Byrne, P. J.; Richardson, P. J.; Chang, J.; Kusmartseva, A. F.; Allan, D. R.; Jones, A. C.; Kamenev, K. V.; Tasker, P. A.; Parsons, S. (2012). *Chem. Eur. J* .**18**, 7738-7748.

Cairns, A. B.; Thompson, A. L.; Tucker, M. G.; Haines, J.; Goodwin, A. L. (2012). *J. Am. Chem. Soc.* **134**, 4454-4456.

Cairns, A. B.; Catafesta, J.; Levelut, C.; Rouquette, J.; van der Lee, A.; Peters, L.; Thompson, A. L.; Dmitriev, V.; Haines, J.; Goodwin, A. L. (2013). *Nature Mater.* **12**, 212-216.

Caneschi, A.; Gatteschi, D.; Sessoli, R.; Barra, A. L.; Brunel, L. C.; Guillot, M. (1991). *J. Am. Chem. Soc.* **113**, 5873-5874.

Casati, N.; Macchi, P.; Sironi, A. (2005). *Angew. Chem. Int. Ed.* **44**, 7736-7739.

Casati, N.; Macchi, P.; Sironi, A. (2009). *Chem. Eur. J.* **15**, 4446-4457.

Clark, S. J.; Segall, M. D.; Pickard, C. J.; Hasnip, P. J.; Probert, M. I. J.; Refson, K.; Payne, M. C. (2005). *Z. Kristallogr.* **220**, 567–570.

Clegg, W.*X-ray Crystallography*. 2nd ed. Oxford: Oxford University Press Inc., 2015.

Clegg, J. K.; Hayter, M. J.; Jolliffe, K. A.; Lindoy, L. F.; McMurtrie, J. C.; Meehan, G. V.; Neville, S. M.; Parsons, S.; Tasker, P. A.; Turner, P.; White, F. J. (2010). *Dalton Trans.* **39**, 2804-2815.

Craig, G. A.; Woodall, C. H.; McKellar, S. C.; Probert, M. R.; Kamenev, K. V.; Moggach, S. A.; Brechin, E. K.; Parsons, S.; Murrie, S. (2015). *Dalton Trans.* **44**, 18324-18328.

Decker, D. L.; Petersen, S.; Debray. D.; Lambert, M. (1979). *Phys. Rev. B: Condens. Mat.* **19**, 3552-3555.

Dewaele, A.; Loubeyre, P. (2007). *High Press. Res.* **27**, 419-429

Dolomanov, O. V.; Bourhis, L. J.; Gildea, R. J.; Howard, J. A. K.; Puschmann, H. (2009). *J. Appl. Cryst.* **42**, 339-341.

Fabbiani, F. P. A.; Buth, G.; Dittrich, B.; Sowa, H. (2010). *CrystEngComm*. **12**, 2541-2550.

Fonseca-Guerra, C.; Snijders, J. G.; Te Velde, G.; Baerends, E. J. (1998). *Theor. Chem. Acc.* **99**, 391-403.

Friedrich, W.; Knipping, P.; von Laue, M. (1912). *Proc. Bavarian. Acad. Sci*. 303-322

Galloway, K. W.; Moggach, S. A.; Parois, P.; Lennie, A. R.; Warren, J. E.; Brechin, E. K.; Peacock, R. D.; Valiente, R.; González, J.; Rodríguez, F.; Parsons, S.; Murrie, M. (2010). *CrystEngComm*, **12**, 2516-2519.

Gamelas, C. A.; Bandeira, N. A. G.; Pereira, C. C. L.; Calhorda, M. J.; Herdtweck, E.; Machuqueiro, M.; Romao, C. C.; Veiros, L. F. (2011). *Dalton Trans.* **40**, 10513-10525.

Gándara, F.; Bennett, T. D. (2014). *IUCrJ*, **1**, 563-570.

Giuseppe, R.; Boldyreva, E.; Bombicz, P.; Kawano, M. (2015). *IUCrJ*, **2**, 675-690.

Glass, R. S.; Steffen, L. K.; Swanson, D. D.; Wilson, G. S. (1993). *Inorg. Chim. Acta*, **207**, 241-252.

Gonzalez-Platas, J.; Alvaro, M.; Nestola, F.; Angel, R. J. (2016). *J. Appl. Cryst.* **49**, 4, 1377-1382.

Goodwin, A. L.; Keen, D. A.; Tucker, M. G. (2008). *Proc. Nat. Acad. Sci. USA*, **105**, 18708-18713.

Gould, J. A.; Rosseinskya, M. J.; Moggach, S. A. (2012). *Dalton Trans.* **41**, 5464-5467.

Groom, C. R.; Bruno, I. J.; Lightfoot, M. P.; Ward, S.C. (2016). *Acta Crystallogr., Sect. B*, **72**, 171–179.

Guionneau, P.; Gaultier, J.; Chasseau, D.; Bravic, G.; Barrans, Y.; Ducasse, L.; Kanaawa, D.; Day, P.; Kurmoo, M. (1996). *J. Phys. I*, **6**, 1581-1595.

Granier, T.; Gallois, B.; Gaultier, J.; Real, J.-A.; Zarembowitch, J. (1993). *Inorg. Chem.* **32**, 5305-5312.

Grant, G. J.; Galas, D. F.; Jones, M. W.; Loveday, K. D.; Pennington, W. T.; Schimek, G. L.; Eagle, C. T.; VanDerveer, D. G. (1998). *Inorg. Chem.* **37**, 5299-5305.

Grant, G. J.; Jones, M. W.; Loveday, K. D.; VanDerveer, D. G.; Pennington, W. T.; Eagle, C. T.; Mehne, L. F. (2000). *Inorg. Chim. Acta*, **300**, 250-263.

Grant, G. J.; Chen, W.; Goforth, A. M.; Baucom, C. L.; Patel, K.; Repovic, P.; VanDerveer, D. G.; Pennington, W. T. (2005). *Eur. J. Inorg. Chem.* 479-485.

Guionneau, P.; Brigouleix, C.; Barrans, Y.; Goeta, A.E.; Létard, J.-F.; Howard, J.A.K.; Gaultier, J.; Chasseau, D. (2001). *Acad. Sci., Ser. IIc: Chim.* **4**, 161-171.

Guionneau, P.; Marchivie, M.; Garcia, Y.; Howard, J.; Chasseau, D. (2005). *Phys. Rev. B: Condens. Mat.* **72**, 214408.

Halder, G. J.; Chapman, K. W.; Neville, S. M.; Moubaraki, B.; Murray, K. S.; Létard, J.-F.; Kepert, C. J. (2008). *J. Am. Chem. Soc.* **130**, 17552-17562.

Hansson, C.; Carlson, S.; Giveen, D.; Johansson, M.; Yong, S.; Oskarsson, A. (2006). *Acta Crystallogr., Sect. B*, **62**, 474-479.

Hazen, R. M.; Hoering, T. C.; Hofmeister, A. M. (1987). *J. Phys. Chem.* **91** 5042-5045.

Hofer, G.; Kuzel, J.; Scheidl, K. S.; Redhammer, G.; Miletich, R. (2015). *J. Solid State Chem.* **229**, 188-196.

Huang, D.; Zhang, X.; McInnes, E. J. L.; McMaster, J.; Blake, A. J.; Davies, E. S.; Wolowska, J.; Wilson, C.; Schröder, M. (2008). *Inorg. Chem.* **47**, 9919-9929.

Jamieson, J. C. (1981). *Ann. Rev. Mater. Sci.* **11**, 233-243.

Jayaraman, A. (1983). *Rev. Mod. Phys.* **55**, 65-108.

Katrusiak, A. (2008). *Acta Crystallogr., Sect. A*, **64**, 135-148.

Kenichi, T. (1999). *Phys. Rev. B: Condens. Mat.* **60**, 6171-6174.

Klotz, S.; Chervin, J. C.; Munsch, P.; Le Marchand, G. (2009). *J. Phys. D: Appl. Phys.* **42**, 7, 075413.

Kobayashi, A.; Kato, R.; Clark, R. A.; Underhill, A. E.; Miyamato, A.; Bun, K.; Naito, T.; Kobayashi, H. (1993). *Synth. Met.* **56**, 2927-2932.

Konno, M.; Okamoto, T.; Shirotani, I. (1989). *Acta Crystallogr., Sect. B*, **45**, 142-147.

Kurpiewska, K.; Lewiński, K. (2010). *Cent. Eur. J. Biol.* **5**, 5, 531-542.

Lider, V. V. (2014). *Inorg. Mater.* **50**, 1459-1469.

Lis, T. (1980). *Acta Crystallogr., Sect. B*, **36**, 2042-2046.

Lucas, C. R.; Liang, W.; Miller, D. O.; Bridson, J. N. (1997). *Inorg. Chem.* **36**, 4508-4513.

Macrae, C. F.; Bruno, I. J.; Chisholm, J. A.; Edgington, P. R.; McCabe, P.; Rodriguez-Monge, L.; Taylor, R.; van de Streek, J.; Wood, P. A. (2008). *J. Appl. Cryst.* **41**, 466-470.

Madsen, S. R.; Thomsen, M. K.; Scheins, S.; Chen, Y.-S.; Finkelmeier, N.; Stalke, D.; Overgaard, J.; Iversen, B. B. (2014). *Dalton Trans.* **43**, 1313-1320.

Madsen, S. R.; Overgaard, J.; Dtalke, D.; Iversen, B. B. (2015). *Dalton Trans.* **44**, 9038-9043.

McKellar, S. C.; Moggach, S. A. (2015). *Acta Crystallogr., Sect. B*, **71**, 587-607.

Merrill, L.; Bassett, W. A. (1974). *Rev. Sci. Instrum.* **45**, 290-294.

Miller, R. J. D. (2014). *Science*, **343**, 1108-1116.

Moggach, S. A.; Allan, D. R.; Parsons, S.; Warren, J. E. (2008). *J. Appl. Cryst.* **41**, 249-251.

Moggach, S. A.; Parsons, S. (2009). *Spectrosc. Prop. Inorg. Organomet. Compd.* **40**, 324-354.

Moggach, S. A.; Galloway, K. W.; Lennie, A. R.; Parois, P.; Rowantree, N.; Brechin, E. K.; Warren, J. E.; Murrie, M.; Parsons, S. (2009). *CrystEngComm*, **11**, 2601-2604.

Murata, K.; Yokogawa, K.; Yoshino, H.; Klotz, S.; Munsch, P.; Irizawa, A.; Nishiyama, M.; Lizuka, K.; Nanba, T.; Okada, T.; Shiraga, Y.; Aoyama, S. (2008). *Rev. Sci. Instrum.* **79**, 085101.

O'Connor, A. E.; Nedaossadat, M.; Bhargava, S. K.; Easun, T. L.; Schröder, M.; Blake, A. J. (2016). *Chem. Commun.* **52**, 6769-6772.

Okano, Y.; Adachi, T.; Narymbetov, B.; Kobayashi, H.; Zhou, B.; Kobayashi, A. (2004). *Chem. Lett.* **33**, 938-939.

Okano, Y.; Zhou, B.; Tanaka, H.; Adachi, T.; Ohishi, Y.; Takata, M.; Aoyagi, S.; Nishibori, E.; Sakata, M.; Kobayashi, A.; Kobayashi, H. (2009). *J. Am. Chem. Soc.* **131**, 7169-7174.

Palatinus, L.; Chapuis, G. (2007). *J. Appl. Cryst.* **40**, 786-790.

Paliwoda, D.; Wawryniak, P.; Katrusiak, A. (2014). *J. Phys. Chem. Lett.* **5**, 2182-2188.

Parois, P.; Moggach, S. A.; Sanchez-Benitez, J.; Kamenev, K. V.; Lennie, A.R.; Warren, J. E.; Brechin, E. K.; Parsons, S.; Murrie, M. (2010). *Chem. Commun*. **46**, 1881-1883.

Piermarini, G. J.; Block, S.; Barnett, J. D. (1973). *J. Appl. Phys.* **44**, 5377-5382

Pomés, A.; Chruszcz, M.; Gustchina, A.; Minor, W.; Mueller, G. A.; Pedersen, L. C.; Wlodawer, A.; Chapman, M. D. (2015). *J. Allergy Clin. Immunol*. **136**, 1, 29-37.

Prescimone, A.; Milios, C. J.; Moggach, S. A.; Warren, J. E.; Lennie, A. R.; Sanchez-Benitez, J.; Kamenev, K. V.; Bircher, R.; Murrie, M.; Parsons, S.; Brechin, E. K. (2008). *Angew. Chem. Int. Ed.* **47**, 2828-2831.

Prescimone, A.; Milios, C. J.; Sanchez-Benitez, J.; Kamenev, K. V.; Loose, C.; Kortus, J.; Moggach, S. A.; Murrie, M.; Warren, J. E.; Lennie, A. R.; Parsons, S.; Brechin, E. K. (2009a). *Dalton Trans.* 4858-4867.

Prescimone, A.; Sanchez-Benitez, J.; Kamenev, K. V.; Moggach, S. A.; Lennie, A. R.; Warren, J. E.; Murrie, M.; Parsons, S.; Brechin, E. K. (2009b). *Dalton Trans.* 7390-7395.

Prescimone, A.; Sanchez-Benitez, J.; Kamenev, K. K.; Moggach, S. A.; Warren, J. E.; Lennie, A. R.; Murrie, M.; Parsons, S.; Brechin, E. K. (2010a). *Dalton Trans.* **39**, 113-123.

Prescimone, A.; Sanchez-Benitez, J.; Kamenev, K. V.; Warren, J. E.; Lennie, A. R.; Murrie, M.; Parsons, S.; Brechin, E. K. (2010B). *Z. Naturforsch., B: Chem. Sci.* **65**, 221-230.

Schirber, J. E.; Morosin, B., (1979). *Phys. Rev. Let.* **42**, 1485.

Schirber, J. E.; Morosin, B.; Alkire, R. W.; Lawson, A. C.; Vergarnini, P. J. (1984). *Phys. Rev. B: Condens. Mat.* **29**, 4150.

Serra-Crespo, P.; Stavitski, E.; Kapteijn, F.; Gascon, J. (2012). *RSC Advances*, **2**, 5051-5053.

Shaw, J. L.; Wolowska, J.; Collison, D.; Howard, J. A. K.; McInnes, E. J. L.; McMaster, J.; Blake, A. J.; Wilson, C.; Schröder, M. (2006). *J. Am. Chem. Soc.* **128**, 13827-13839.

Sheldrick, G. M. (2008). *Acta Crystallogr., Sect. A,* **64**, 112-122.

Sheldrick, G. M. (2015). *Acta Crystallogr., Sect. C,* **71**, 3-8.

Shen, Y.; Kumar, R. S.; Pravica, M.; Nicol, M. F. (2004). *Rev. Sci. Instrum.* **75**, 4450-4454

Shepherd, H. J.; Bonnet, S.; Guionneau, P.; Bedoui, S.; Garbarino, G.; Nicolazzi, W.; Bousseksou, A.; Molnár, G. (2011). *Phys. Rev. B: Condens. Mat.* **84**, 144107.

Shepherd, H.J.; Palamarciuc, T.; Rosa, P.; Guionneau, P.; Molnar, G.; Létard, J.-F.; Bousseksou, A. (2012a). *Angew. Chem. Int. Ed.* **51**, 3910-3914.

Shepherd, H.J.; Rosa, P.; Vendier, L.; Casati, N.; Létard, J.-F.; Bousseksou, A.; Guionneau, P.; Molnár, G. (2012b). *Phys. Chem. Chem. Phys.* **14**, 5265-5271.

Shepherd, H. J.; Tonge, G.; Hatcher, L. E.; Bryant, M. J.; Knichal, J. V.; Raithby, P. R.; Halcrow, M. A.; Kulmaczewski, R.; Gagnon, K. J.; Teat, S. J. (2016). *Magentochemistry*, **2**, 9.

Shirotani, I.; Hayashi, J.; Takeda, K. (2005). *Mol. Cryst. Liq. Cryst.* **442**, 157-166.

Sidorov, V. A.; Sadykov, R. A. (2005). *J. Phys.: Condens. Matter*, **7**, S3005-S3008.

Slebodnick, C.; Zhao, J.; Angel, R. J.; Hanson, B. E.; Song, Y.; Liu, Z.; Hemley, R. J. (2004). *Inorg. Chem.* **43**, 5245-5252.

Spackman, M. A.; Byrom, P. G. (1997). *Chem. Phys. Lett.* **267**, 215-220.

Spackman, M. A.; Jayatilaka, D. (2009). *CrystEngComm.* **11**, 19-32.

Spencer, E. C.; Ross, N. L.; Angel, R. J. (2012). *J. Mater. Chem.* **22**, 2074-2080.

Stephen, E.; Huang, D.; Shaw, J. L.; Blake, A. J.; Collison, D.; Davies, E. S.; Edge, R.; Howard, J. A. K.; McInnes, E. J. L.; Wilson, C.; Wolowska, J.; McMaster, J.; Schröder, M. (2011). *Chem. Eur. J.* **17**, 10246-10258.

Stephen, E.; Blake, A. J.; Carter, E.; Collison, D.; Davies, E. S.; Edge, R.; Lewis, W.; Murphy, D. M.; Wilson, C.; Gould, R. O.; Holder, A. J.; McMaster, J.; Schröder, M. (2012). *Inorg. Chem.* **51**, 1450-1461.

Stevens, C. J.; Prescimone, A.; Tuna, F.; McInnes, E. J. L.; Parsons, S.; Morrison, C. A.; Arnold, P. L.; Love, J. B. (2016). *Inorg. Chem.* **55**, 214-220.

Takeda, K.; Hayashi, J.; Shirotani, I.; Fukuda, H.; Yakushi, K. (2006). *Mol. Cryst. Liq. Cryst.* **460**, 131-144.

Tateiwa, N.; Haga, Y. (2009). *Rev. Sci. Instrum.* **80**, 123901.

Te Velde, G.; Bickelhaupt, F. M.; Baerends, E. J.; Fonseca-Guerra, C.; van Gisbergen, S. J. A.; Snijders, J. G.; Ziegler, T. (2001). *J. Comput. Chem.* **22**, 931-967.

Tidey, J. P.; Wong, H. L. S.; Schröder, M.; Blake, A. J. (2014). *Coord. Chem. Rev.* **277-278**, 187-207.

Tidey, J. P.; O'Connor, A. E.; Markevich, A.; Bitchoutskaia, E.; Cavan, J. J. P.; Lawrence, G. A.; Wong, H. L. S.; McMaster, J.; Schröder, M.; Blake, A. J. (2015). *Cryst. Growth Des.* **15**, 115-123.

Tidey, J. P.; Wong, H. L. S.; McMaster, J.; Schröder, M.; Blake, A. J. (2016). *Acta Crystallogr., Sect. B*, **72**, 3, 357-371.

Tucker, N. B.; Reid, E. E. (1933). *J. Am. Chem. Soc*.**55**, 775-781.

Turner, M. J.; McKinnon, J. J.; Jayatilaka, D.; Spackman, M. A. (2011). *CrystEngComm*. **13**, 1804-1813.

Varga, T.; Wilkinson, A. P.; Angle, R. J. (2003). *Rev. Sci. Instrum.* **74**, 4564-4566

Wolff, S. K.; Grimwood, D. J.; McKinnon, J. J.; Turner, M. J.; Jayatilaka, D.; Spackman, M. A. (2012). *CrystalExplorer* version 3.1, University of Western Australia, Australia.

Wong, H. L. S.; Allan, D. R.; Champness, N. R.; McMaster, J.; Schröder, M.; Blake, A. J. (2013). *Angew. Chem. Int. Ed.* **52**, 5093-5095.

Woodall, C. H.; Beavers, C. M.; Christensen, J.; Hatcher, L. E.; Intissar, M.; Parlett, A.; Teat, S. J.; Reber, C.; Raithby, P. R. (2013). *Angew. Chem. Int. Ed.* **52**, 9691-9694.

Woodall, C. H.; Fuertes, S.; Beavers, C. M.; Hatcher, L. E.; Parlett, A.; Shepherd, H. J.; Christensen, J., Teat, S. J.; Intissar, M.; Rodrigue-Witchel, A.; Suffren, Y.; Reber, C.; Hendon, C. H.; Tiana, D.; Walsh, A.; Raithby, P. R. (2014). *Chem. Eur. J.* **20**, 16933-16942.

Wu, L.-C.; Overgaard, J.; Madsen, S. R.; Schmoekel, M. S.; Iversen, B.B. (2013). *J. Ch. Chem. Soc.* **60**, 929-934.

Wu, L.-C.; Nielsen, M. B.; Bremholm, M.; Madsen, S. R.; Overgaard, J.; Newville, M.; Chen, Y.-S.; Iversen, B. B. (2015). *Chem. Commun.* **51**, 8868.

Yokogawa, K.; Murata, K.; Yoshino, H.; Aoyama, S. (2007). *Jap. J. Appl. Phys.* **46**, 3636-3639.

Zhao, Y.; Barvosa-Carter, W.; Theiss, S. D.; Mitha, S.; Aziz, M. J.; Schiferl, D. (1998). *J. Appl. Phys.* **84**. 4049-4059.

Zhao, J.; Ross, N. L.; Angel, R. J.; Carpenter, M. A.; Howard, C. J.; Pawlak, D. A.; Lukasiewicz, T. (2009). *J. Phys.: Condens. Matter*, **21**, 235403.

# Chapter 2

## Epitaxial Retrieval of a Disappearing Polymorph

## 1. Introduction

Polymorphism, the phenomenon of a material packing in multiple distinct crystalline forms, is commonplace for small molecules. In the case of organic compounds this is particularly well documented: for example, an analysis of 245 polymorph screens carried out at the SSCI (Solid State Chemical Information, West Lafayette) showed that *ca*. 50 % of the compounds studied exhibited polymorphism (Stahly, 2007). This polymorphism arises from the presence of multiple competing intermolecular bonding modes and, particularly for larger molecules, multiple conformations that the molecule can adopt: these factors can give rise to a variety of packing systems that may differ only slightly in energy. In contrast, far fewer polymorphic systems are reported for inorganic coordination complexes. One likely reason for this is simply that the phenomenon is not routinely investigated in these complexes: to quote McCrone, "the number of polymorphic forms for a given compound is proportional to the time and money spent in research on that compound" (McCrone, 1965). Polymorphism is of extreme importance in the pharmaceutical industry where different phases can have vastly different physical properties (Blagden *et al.*, 2007) and so the compounds produced, typically organic in nature, are thoroughly screened to understand their habits, properties and preferences. Coordination complexes are often synthesised in a research environment where the aim of the crystallographic study is to characterise the molecular structure: usually there is neither need nor incentive to screen for polymorphs.

A great number of techniques exist for polymorph control including variation of the solvent system and the use of additives (Llinas & Goodman, 2008).

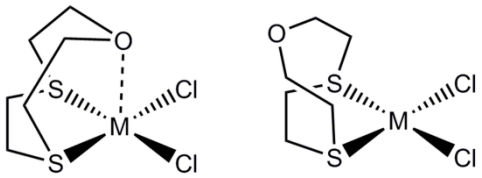
Nevertheless, it is not unknown for a phase to be obtained and later ‘disappear’ following the appearance of a more thermodynamically stable form. Seeds of this new form pervade the crystallisation environment and prevent the formation of the less stable polymorph. This phenomenon of disappearing polymorphs has been described extensively by Dunitz and Bernstein (1995), who detail the common causes and problems. Examples of such occurrences are taken almost exclusively from the field of organic rather than coordination chemistry, most likely for the reasons mentioned above. A well-documented case is that of 1,2,3,5-tetra-*O*-acetyl-β-D-ribofuranose (Bombicz *et al.*, 2003), for which metastable ‘polymorph A’ was first prepared in 1947; it ‘disappeared’ in 1954 following the discovery of the higher-melting ‘polymorph B’. Polymorph A was then irreproducible across numerous countries until 1981,when scientists in Budapest were able to recover it (Czugler *et al.*, 1981), presumably because their laboratory had remained free from contamination by the stable B form. One particularly high-profile case was that of Ritonavir which is prescribed as an anti-HIV medication: two years after it was introduced, the formation of a more stable polymorph with lower solubility and bioavailability led to its temporary withdrawal (Bauer *et al.*, 2001).

One method used for polymorph control is epitaxy, whereby the surface of another crystalline solid is used to promote the growth of a given phase or orientation of a crystal. The technique is employed to obtain the correct polarity of GaN for electronics (Wong *et al.*, 2013) and to attach metal-organic frameworks to surfaces (Liu & Fischer, 2011), typically using surfaces of a different chemical composition to that of the desired product; in these examples sapphire and gold are used, respectively. Rather counter-intuitively, it has also been observed that in some

cases the stable phase of a compound will bring about growth of the metastable phase during crystal growth, for example with sulfathiazole (Munroe *et al.*, 2011) and the steroid reported by Stoica *et al.* (2005). In a research setting, epitaxy offers an appealing solution to the challenge of obtaining metastable polymorphs. Ideally, the obvious seed for this would be an isomorphous system of a chemically similar compound where the desired phase is stable. For this approach to be viable, the seed phase also needs to be stable to the recrystallisation conditions, for example by being insoluble in the solution used.

As an extension of our investigations into the unusual properties of thioether macrocycle complexes (Stephen *et al.*, 2011; Allan *et al.*, 2014), attention was given to complexes of analogous oxathioether macrocycles, specifically, of [9]ane$S_2$O (1-oxa-4,7-dithiacyclononane). With respect to the thioether macrocycle [9]ane$S_3$ (1,4,7-trithiacyclononane), one soft sulfur donor has been replaced with a hard oxygen donor to result in a marginally smaller macrocycle. This switch of donor typically corresponds to a change in axial ligation without detracting from the redox non-innocence of the macrocycle (Shaw *et al.*, 2006). While studying [$PdCl_2$([9]ane$S_2$O)], **1**, two previously unreported phases were discovered, designated β-**1** and γ-**1**: the preparation of the first of these to be discovered (β-**1**) could not be reproduced following discovery of the γ-**1** form and it was therefore eventually designated as a disappearing polymorph. The previously unreported analogous complex [$PtCl_2$([9]ane$S_2$O)], **2**, was also investigated and a phase suitable for the epitaxial retrieval of the disappearing polymorph β-**1** was identified. These new crystallographic phases are reported herein with discussion of the potential causes of the instability of β-**1** with reference to structural

characteristics and DFT calculations. The work in this chapter has been reported (Tidey *et al.*, 2015).




**Scheme 1** Scheme showing *endodentate* (left) and *exodentate* (right) conformers of [*M*$Cl_2$([9]ane$S_2$O)] (*M* = Pd, Pt).

## 2. Experimental

### 2.1. Synthetic

Reagents were used as received from Sigma-Aldrich, Fischer Industries, Acros Organics, Alfa Aesar and Merck Schuchardt. NMR spectroscopy was carried out at 400 MHz using Bruker AV400 ($^{13}$C) and Bruker AV(III)400 ($^{1}$H) spectrometers. IR spectroscopy was carried out using a Thermoscientific Nicolet iS5 FTIR spectrometer with an iD5 ATR attachment. ESI mass spectrometry was undertaken using a Bruker Daltonics microTOF electrospray mass spectrometer and MALDI mass spectrometry using a Bruker Ultraflex III spectrometer equipped with a matrix-assisted laser desorption/ionisation source and used a DCTB matrix. Elemental analysis was undertaken using an Exeter Analytical CE-440 Elemental Analyser.

#### 2.1.1. 1-Oxa-4,7-dithiacyclononane ([9]ane$S_2$O)

Dimethylformamide (500 $cm^3$) was added to $Cs_2CO_3$(16.9 g, 87.6 mmol) and heated to 100 °C. Under vigorous stirring, solutions of mercaptoethylether (4.5 $cm^3$, 36 mmol) and dibromoethane (3.2 $cm^3$, 37 mmol) in dimethylformamide

(40 $cm^3$, 40 $cm^3$) were added drop-wise at a rate of 1.2 $cm^3$ $hr^{-1}$. After addition, the solution was allowed to cool and thereafter was stirred for 3 days. The resulting suspension was filtered and the volume reduced *in vacuo* to yield a yellow/brown oil that solidified after repressurisation. This oil was dissolved in $CH_2Cl_2$ (100 $cm^3$) and washed with water (2 × 50 $cm^3$), aqueous NaOH (0.1 M, 4 × 50 $cm^3$), and water again (4 × 50 $cm^3$). Excess $MgSO_4$ was added and the suspension stirred overnight. The product was purified by Kugelrohr distillation as the first fraction and yielded a colourless oil (yield = 1.668 g, 10.15 mmol, 28 %). Mass spectrometry (ESI, $CH_3CN$): 187 $[M+Na]^+$. $^1H$ NMR $\delta_H$/ppm (400 MHz; $CD_3CN$): 2.75 (4H, t, $^2J_{HH}$ = 4.0 Hz, C*H*$_2$), 3.00 (4H, s, C*H*$_2$), 3.68 (4H, t, $^2J_{HH}$ = 4.0 Hz, *CH*$_2$). $^{13}C$ NMR $\delta_c$/ppm (400 MHz; $CD_3CN$): 34.31 (*sp*$^3$*C*), 35.90 (*sp*$^3$*C*), 74.95 (*sp*$^3$*C*). Anal. Calcd. for $C_6H_{12}OS_2$: C = 43.86 %, H = 7.36 %, N = 0 %. Found: C = 43.65 %, H = 7.30 %, N = 0 %.

### 2.1.2 $[PdCl_2([9]aneS_2O)]$ (1)

1-Oxa-4,7-dithiacyclononane (150 mg, 0.91 mmol) in $CH_3CN$ (15 $cm^3$) was added to a suspension of $PdCl_2$ (142 mg, 80 mmol) in $CH_3CN$ (10 $cm^3$) and stirred for 30 min before filtering. The solids were washed with $CH_3CN$ (10 × 5 $cm^3$), the washings combined with the mother liquor and the volume reduced *in vacuo* (~10 $cm^3$). $Et_2O$ (40 $cm^3$) was added slowly, causing a bright orange powder to precipitate. This was obtained by filtration and dried in air (yield = 97.4 mg, 0.28 mmol, 35 %). Mass spectrometry (ESI, $CH_3CN$): 342$[M+H]^+$. Anal. Calcd. for $C_6H_{12}Cl_2OPdS_2$: C = 21.1 %, H = 3.54 %, N = 0 %. Found: C = 20.96 %, H = 3.36 %, N = 0 %. IR $\nu$/$cm^{-1}$ (ATR): 2972 (w), 2934 (w), 2873 (w), 1489 (w),

1467 (w), 1423 (w), 1414 (w), 1400 (w), 1299 (w), 1282 (w), 1227 (w), 1195 (w), 1140 (w), 1122 (s), 1056 (w), 1018 (m), 1003 (m), 921 (m), 805 (w), 787 (w).

### 2.1.3. [$PtCl_2$([9]ane$S_2$O)](2)

1-Oxa-4,7-dithiacyclononane (75 mg, 46 mmol) in $CH_3CN$ (5 $cm^3$) was added to a solution of $PtCl_2$ (106 mg, 0.400 mmol) in $CH_3CN$ (20 $cm^3$) and the suspension stirred at 60 °C for 19 hours. Upon cooling, a green precipitate formed which was collected by filtration, washed with $Et_2O$ (4 × 2 $cm^3$) and dried in air (yield =124 mg, 0.287 mmol, 72 %). Mass spectrometry (ESI, $CH_3CN$): 453 $[M+Na]^+$. Anal. Calcd. for $C_6H_{12}Cl_2OPtS_2$: C = 16.7 %, H = 2.81 %, N = 0 %. Found: C = 16.69 %, H = 2.66 %, N = 0 %. IR ν/$cm^{-1}$ (ATR): 2972 (w), 2930 (w), 2873 (w), 1485 (w), 1464 (w), 1422 (w), 1412 (w), 1399 (w), 1300 (w), 1281 (w), 1228 (w), 1194 (w), 1141 (w), 1125 (s), 1056 (w), 1018 (m), 1001 (m), 916 (m), 803 (w), 787 (w).

### 2.1.4. Recrystallisation

Saturated solutions of **1** and **2** were prepared by stirring excess compound in $CH_3NO_2$ overnight at 35 °C before allowing the solution to cool and residual solid to settle. Vapour diffusion recrystallisations were then carried out using the decanted saturated solutions with $Et_2O$ as the antisolvent. These were carried out at room temperature (15−20 °C), 25, 30 and 35 °C using either the saturated solution or diluted concentrations (75, 50 or 25 %) thereof. Crystal growth rates were controlled by varying the number of apertures in the lid of the vessel containing the solution of **1** or **2**, using either standard 0.5 dram glass vials or NMR tubes.

For the epitaxial growth experiments, a crystal of β-**2** was fixed to a glass capillary using the minimum amount of epoxy resin. The crystal was held just above the surface of a saturated solution of **1** in $CH_3NO_2$ and a vapour diffusion recrystallisation using $Et_2O$ as the antisolvent was carried out. Crystals obtained were broken off and analysed using single crystal X-ray diffraction, or dissolved in nitromethane for MALDI mass spectrometry (*vide infra*). The same procedure was also carried out using γ-**1** as the seed, either with saturated solutions of **2** or with solutions which were saturated first with **2** and then with **1**.

### 2.2. Crystallography

Data were collected for β-**Epitaxy** using a Rigaku SuperNovaII and for all other phases a Rigaku SuperNova diffractometer equipped with a microfocus sealed-tube source focussing mirror-monochromated Mo-*K*α radiation (λ = 0.71073 Å) detected at an Eos CCD area detector. Cell refinement and data reduction was performed using *CrysAlis*$^{PRO}$ (Agilent, 2014). Crystals were mounted using silicon grease on MiTeGen MicroMounts$^{TM}$ and data were collected at 293 K. Numerical absorption corrections based on Gaussian integration over a multifaceted crystal model were applied through *CrysAlis*$^{PRO}$ (Agilent, 2014). Structure solution was undertaken using *SHELXS*14 direct methods (Sheldrick, 2008). Structures were refined to convergence using *SHELXL*14 (Sheldrick, 2015). Structure solution and refinement were implemented through *Olex2* (Dolomanov *et al*., 2009). Specific refinement details are embedded in the relevant CIFs which can be found along with the experimental tables in the supplementary information.

### 2.3. Computational Methods

The relative total energies and cohesive energies (CEs) of the five phases revealed in this study, as well as those for a hypothetical third phase of **2** (designated γ-**2**) which is isomorphous and isostructural with γ-**1**, were calculated using density functional theory (DFT) with on-the-fly ultra-soft pseudopotentials and the Perdew-Burke-Ernzerhof (PBE; Perdew *et al.*, 1996) exchange-correlation functional, as implemented in the *CASTEP* code (Clark *et al.*, 2005). A plane-wave basis set with an energy cut-off of 800 eV was used for the valence electron wave functions. The Brillouin zone was sampled within the Monkhorst-Pack scheme (Monkhorst & Pack, 1976) using a (3 × 3 × 3) Γ-centred *k*-points grid. To account for the dispersion interactions between molecules in the crystal, the semi-empirical methods of Grimme (2006) and Tkatchenko-Scheffler (TS; Tkatchenko & Scheffler, 2009) were examined. The initial structures of unit cells for the investigated polymorphs were taken from the crystallographic data obtained in this study. The lattice parameters and atomic positions were subsequently optimised for each polymorph structure and are provided in Section 3.3.

## 3. Results and discussion

### 3.1.Crystallisation of complexes

Diffusion of $Et_2O$ vapour into a saturated solution of **1** in $CH_3NO_2$ at 15−20 °C yielded clear orange blocky crystals primarily of the phase α-**1**. β-**1** was initially obtained as the minor product of the aforementioned recrystallisation. Repetition of these conditions yielded only α-**1**. All further efforts to yield the β-**1** phase gave either α-**1** or a second previously unreported phase designated γ-**1** with higher

recrystallisation temperatures favouring the latter. Crystals of α-**2** were obtained by diffusion of $Et_2O$ vapour into a saturated solution of **2** in $CH_3NO_2$ at 15-20 °C, while β-**2** was obtained by performing these recrystallisations at elevated temperatures of 30 or 35 °C.

Orange block-shaped crystals of β-**1** were grown by epitaxy using a pale green crystal of β-**2** as the seed (Fig. 1). The crystals were easily separated from the seed crystal and were identified (*vide infra*) as being of the same phase as the original crystals (β-**1**) and designated β-**epitaxy** to distinguish them from the original crystals of this phase. Attempts to use the same technique to obtain an equivalent γ phase of **2** using a saturated solution of **2** and crystals of γ-**1** were unsuccessful, resulting in the dissolution of the seed crystal and the recovery of α-**2**. The use of a solution which had been sequentially saturated in **2** and **1** yielded the same result.

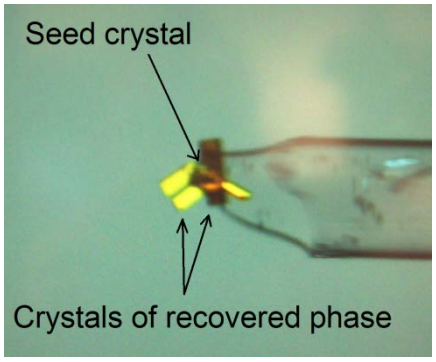



**Figure 1** Crystals of β-**1** grown epitaxially on a seed crystal of β-**2**, viewed under polarised light.

### 3.2.Crystal structures

The phases α-**1** and α-**2** are isomorphous and isostructural with one another, as are β-**1** and β-**2**. Uniquely, γ-**1** comprises the third distinct phase amongst this series. Cell parameters for the phases are given in Table 1.

**Table 1** Table of the cell parameters at ambient temperature and pressure for the five phases detailed in this chapter and further investigated in chapters 3 and 4.

| Phase | Space group | *a* / Å | *b* / Å | *c* / Å | β/ ° | *V* / Å$^3$ |
|---|---|---|---|---|---|---|
| α-**1** | $P2_1/n$ | 8.4502(4) | 12.1807(5) | 10.3745(4) | 105.125(4) | 1030.85(8) |
| α-**2** | $P2_1/n$ | 8.45248(18) | 12.2690(2) | 10.3536(2) | 105.542(2) | 1034.45(4) |
| β-**1** | $P2_1/c$ | 9.3384(3) | 12.6575(4) | 9.0498(3) | 92.260(3) | 1068.87(6) |
| β-**2** | $P2_1/c$ | 9.41666(18) | 12.6646(2) | 9.03760(16) | 91.5297(17) | 1077.43(3) |
| γ-**1** | $P2_1/n$ | 7.02123(16) | 11.4020(3) | 13.3817(3) | 96.785(2) | 1063.78(5) |

### 3.2.1. Structure of α-[$PdCl_2$([9]ane$S_2O$)]

Crystals of α-**1** were readily obtained as orange blocks by diffusion of $Et_2O$ vapour into a solution of **1** in $CH_3NO_2$ at room temperature. They were also recovered from recrystallisations carried out at 30 and 35 °C.

The structure of α-**1** has been previously described (Lucas *et al.*, 1997). The Pd(II) centre is bound in a square plane by two mutually *cis* chloride donors and two macrocyclic sulfur donors (Fig. 2, Table 2). The macrocycle binds facially in an *endodentate* configuration and adopts a [234] conformation following a less strict Dale analysis (Dale, 1973) with corners at C3, C6 and C8. This provides a distant apical oxygen donor [Pd1⋯O1 = 2.958(4) Å] within the sum of the van der Waals radii [$\Sigma_{vdW}$ = 3.15 Å (Bondi, 1964)] to form a [4+1] square based pyramidal geometry at the metal. The metal centre is located slightly [0.0128(10) Å] out of the equatorial plane in the direction opposite from the apical oxygen.

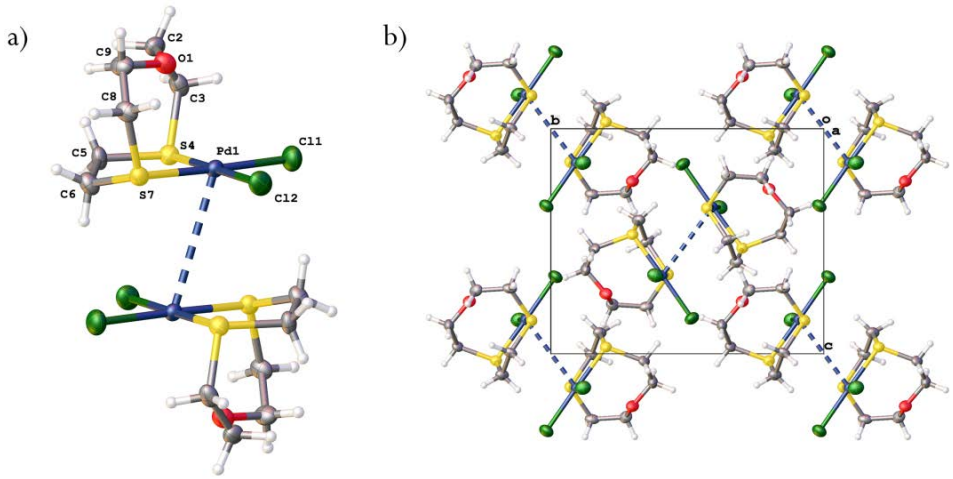



**Figure 2** a) View of the dimer formed in the structure of $[PdCl_2([9]aneS_2O)]$ in α-**1**. b) View of the herringbone packing of $[PdCl_2([9]aneS_2O)]$ dimers in α-**1** viewed along the *a* axis. Intermolecular Pd···Pd vectors are highlighted using a dashed bond; displacement ellipsoids shown at 50 % probability. α-**1** and α-**2** are isostructural and isomorphous.

**Table 2** Coordination environment and macrocycle conformation for α-**1**

| Bond Length /Å | | Bond Angle /° | | Torsion Angle /° | |
|---|---|---|---|---|---|
| Pd1−Cl1 | 2.3278(17) | Cl1−Pd1−Cl2 | 93.06(6) | O1−C2−C3−S4 | 44.9(7) |
| Pd1−Cl2 | 2.3296(18) | Cl2−Pd1−S7 | 88.53(6) | C2−C3−S4−C5 | 44.2(6) |
| Pd1−S4 | 2.2649(18) | S7−Pd1−S4 | 90.24(6) | C3−S4−C5−C6 | −125.5(5) |
| Pd1−S7 | 2.2546(16) | S4−Pd1−Cl1 | 88.17(7) | S4−C5−C6−S7 | 31.2(7) |
| Pd1···O1 | 2.958(4) | Cl1−Pd1−S7 | 177.90(7) | C5−C6−S7−C8 | 81.9(6) |
| | | Cl2−Pd1−S4 | 178.77(6) | C6−S7−C8−C9 | −51.6(6) |
| | | | | S7−C8−C9−O1 | −51.2(7) |
| | | | | C8−C9−O1−C2 | 143.4(6) |
| | | | | C9−O1−C2−C3 | −130.2(5) |

The mononuclear units pack base-to-base about an inversion centre such that the Pd(II) centre in one molecule rests over the Pd1−S7 bond of another (Table 3) with the coordination planes parallel to each other to form dimeric units. The Pd1···Pd1_#1 separation of 3.7903(10) Å (symmetry code #1 = $-x$, $2-y$, $-z$) lies significantly outside the sum of the relevant van der Waals radii [$\Sigma_{vdW}$ = 3.26 Å

(Bondi, 1964)]. The perpendicular separation of the $Cl_2S_2Pd$ least squares planes is 3.6246(15) Å and the centroid-centroid shift is 1.182(2) Å. These dimers form ABAB alternating sheets in the *bc* plane, generating a herringbone-like motif when viewed along the *a* axis (Fig. 2).

**Table 3** Intradimer geometry for α-**1**. Symmetry code #1 = −*x*, 2 − *y*, −*z*.

| Atomic Distance /Å | | Angle /° | |
|---|---|---|---|
| Pd1···Cl1_#1 | 5.0385(18) | Pd1···Pd1_#1−Cl1_#1 | 108.51(5) |
| Pd1···Cl2_#1 | 4.5035(18) | Pd1···Pd1_#1−Cl2_#1 | 91.59(5) |
| Pd1···S4_#1 | 4.3453(18) | Pd1···Pd1_#1−S4_#1 | 87.95(5) |
| Pd1···S7_#1 | 3.7942(17) | Pd1···Pd1_#1−S7_#1 | 72.80(4) |
| Pd1···Pd1_#1 | 3.7903(10) | Pd1···S7_#1−Pd1_#1 | 72.61(4) |

### 3.2.2. Structure of α-[$PtCl_2$([9]ane$S_2O$)]

Crystals of α-**2** were readily obtained as pale green blocks by diffusion of $Et_2O$ vapour into solutions of **2** in $CH_3NO_2$at room temperature. They were also often found in recrystallisations carried out at 30 or 35 °C.

α-[$PtCl_2$([9]ane$S_2O$)] is isomorphous and isostructural with α-[$PdCl_2$([9]ane$S_2O$)]. The Pt(II) centre is bound in a square plane by two mutually *cis* chloride donors and two macrocyclic sulfur donors (Fig. 3, Table 4). The macrocycle binds facially in an *endodentate* configuration and adopts a [234] conformation following a less strict Dale analysis (Dale, 1973) with corners at C3, C6 and C8. This provides a distant apical oxygen donor [Pt1···O1 = 3.077(4) Å] within the sum of the van der Waals radii [$\Sigma_{vdW}$ = 3.154 Å (Bondi, 1964)] to form a [4+1] square based pyramidal geometry at the metal. The metal centre is located slightly [0.0094(8) Å] out of the equatorial plane in the direction opposite from the apical oxygen.

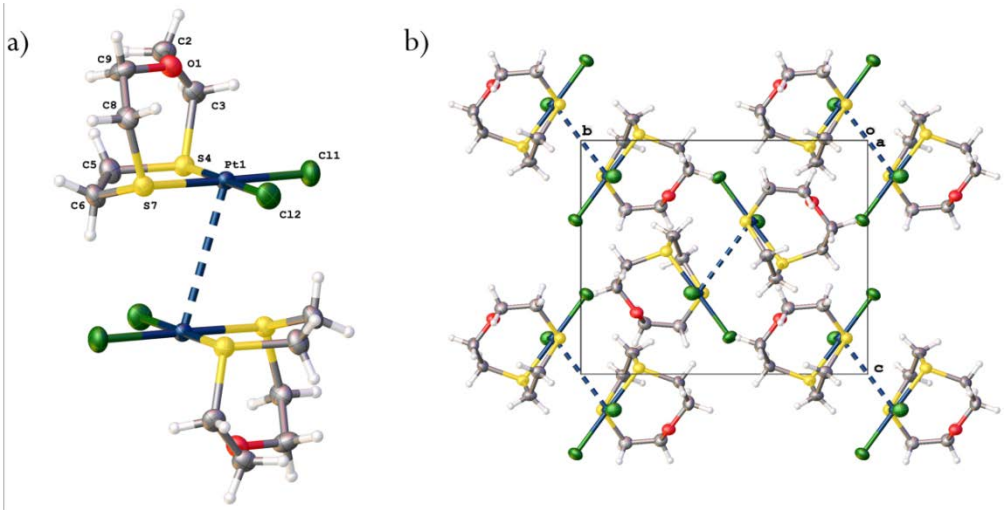



**Figure 3** a) View of the dimer formed in the structure of [$PtCl_2$([9]ane$S_2$O)] in α-**2**. b) View of the herringbone packing of [$PtCl_2$([9]ane$S_2$O)] dimers in α-**2** viewed along the *a* axis. Intermolecular Pt···Pt vectors are highlighted using a dashed bond; displacement ellipsoids shown at 50 % probability. α-**2** and α-**1** are isostructural and isomorphous.

**Table 4** Coordination environment and macrocycle conformation for α-**2**.

| Bond Length /Å | | Bond Angle /° | | Torsion Angle/° | |
|---|---|---|---|---|---|
| Pt1−Cl1 | 2.3302(17) | Cl1−Pt1−Cl2 | 91.60(6) | O1−C2−C3−S4 | 48.0(7) |
| Pt1−Cl2 | 2.3276(16) | Cl2−Pt1−S7 | 89.36(6) | C2−C3−S4−C5 | 41.7(5) |
| Pt1−S4 | 2.2455(16) | S7−Pt1−S4 | 90.57(6) | C3−S4−C5−C6 | −124.1(5) |
| Pt1−S7 | 2.2409(15) | S4−Pt1−Cl1 | 88.47(6) | S4−C5−C6−S7 | 29.7(7) |
| Pt1···O1 | 3.077(4) | Cl1−Pt1−S7 | 178.75(6) | C5−C6−S7−C8 | 82.5(5) |
| | | Cl2−Pt1−S4 | 179.84(6) | C6−S7−C8−C9 | −49.8(6) |
| | | | | S7−C8−C9−O1 | −54.9(7) |
| | | | | C8−C9−O1−C2 | 141.5(5) |
| | | | | C9−O1−C2−C3 | −128.0(6) |

The mononuclear units pack base-to-base about an inversion centre such that the Pt(II) centre in one molecule rests over the Pt1−S7 bond of another (Table 5) with the coordination planes parallel to each other to form dimeric units. The Pt1···Pt1_#1 separation of 3.8237(4) Å (symmetry code #1 = −*x*, 2 − *y*, −*z*) lies

significantly outside the sum of the relevant van der Waals radii [$\Sigma_{vdW}$ = 3.27 Å (Bondi, 1964)]. The perpendicular separation of the $Cl_2S_2Pt$ least squares planes is 3.6815(14) Å and the centroid-centroid shift is 1.120(2) Å. These dimers form ABAB alternating sheets in the *bc* plane, generating a herringbone-like motif when viewed along the *a* axis (Fig. 3).

**Table 5** Intradimer geometry for α-**2**. Symmetry code #1 = −*x*, 2−*y*,−*z*.

| Atomic Distance /Å | | Angle /° | |
|---|---|---|---|
| Pt1···Cl1_#1 | 5.0218(17) | Pt1···Pt1_#1−Cl1_#1 | 106.86(4) |
| Pt1···Cl2_#1 | 4.4972(17) | Pt1···Pt1_#1−Cl2_#1 | 90.60(5) |
| Pt1···S4_#1 | 4.4178(17) | Pt1···Pt1_#1−S4_#1 | 89.52(4) |
| Pt1···S7_#1 | 3.8600(16) | Pt1···Pt1_#1−S7_#1 | 73.93(4) |
| Pt1···Pt1_#1 | 3.8237(4) | Pt1···S7_#1−Pt1_#1 | 72.16(4) |

### 3.2.3. Structure of β-[$PdCl_2$([9]ane$S_2O$)]

Crystals of β-**1** were originally obtained as orange blocks by diffusion of $Et_2O$ vapour into a saturated solution of **1** in $CH_3NO_2$ at room temperature and were observed alongside crystals of α-**1**. All subsequent attempts to obtain β-**1** by means of standard recrystallisation methods proved unsuccessful.

The Pd(II) centre is bound in a square plane by two mutually *cis* chloride donors and two macrocyclic sulfur donors (Fig. 4, Table 6). The macrocycle binds equatorially in an *exodentate* fashion with the oxygen donor atom directed away from the metal centre [Pd1···O1 = 3.404(3) Å] with the result that no apical interaction supplements the square planar geometry at the metal. The ligand conformation is assigned as [36] following Dale analysis (Dale, 1973) with corners at C3 and C6, but if a less strict definition of gauche angles is allowed this tends towards a [234] conformation with an additional pseudo corner at C8. The

equatorial plane is distorted by out-of-plane bending of S7−Pd1−Cl1 [174.81(5)°] resulting in the metal locating slightly out the plane [0.0328(7) Å] in the direction away from the oxygen. However, when considering the ideal plane formed by S4, S7 and Cl2, the metal centre is found to locate 0.0197(10) Å out of the plane towards the oxygen.

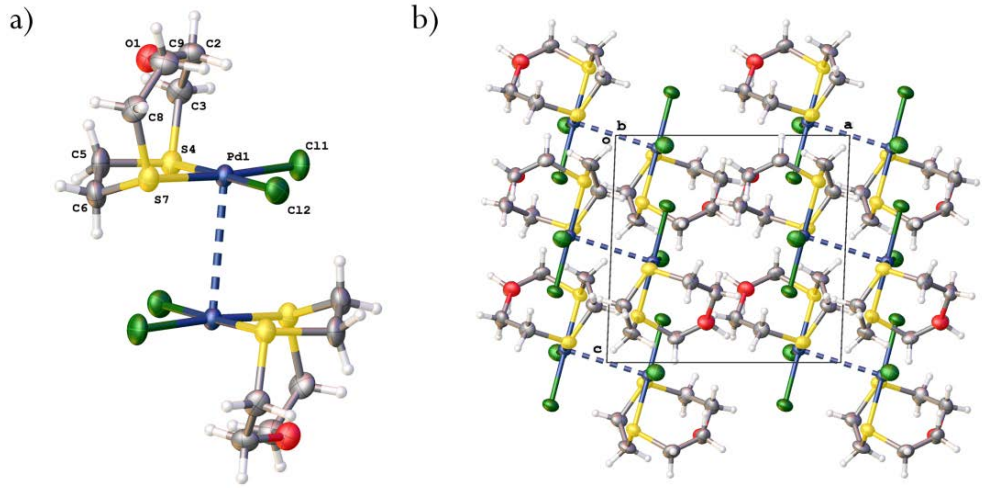



**Figure 4** a) View of the dimer formed in the structure of [$PdCl_2$([9]ane$S_2$O)] in β-**1**. b) View of the herringbone packing of [$PdCl_2$([9]ane$S_2$O)] dimers in β-**1** viewed along the *b* axis. Intermolecular Pd···Pd vectors are highlighted using a dashed bond; displacement ellipsoids shown at 50 % probability. β-**1** and β-**2** are isostructural and isomorphous.

**Table 6** Coordination environment and macrocycle conformation for β-**1**.

| Bond Length /Å | | Bond Angle /° | | Torsion Angle/° | |
|---|---|---|---|---|---|
| Pd1−Cl1 | 2.3124(12) | Cl1−Pd1−Cl2 | 94.27(4) | O1−C2−C3−S4 | −58.0(4) |
| Pd1−Cl2 | 2.3214(11) | Cl2−Pd1−S7 | 88.78(4) | C2−C3−S4−C5 | 79.5(4) |
| Pd1−S4 | 2.2699(11) | S7−Pd1−S4 | 90.08(4) | C3−S4−C5−C6 | −133.8(4) |
| Pd1−S7 | 2.2601(12) | S4−Pd1−Cl1 | 86.94(4) | S4−C5−C6−S7 | 45.4(5) |
| Pd1···O1 | 3.404(3) | Cl1−Pd1−S7 | 174.81(5) | C5−C6−S7−C8 | 70.3(4) |
| | | Cl2−Pd1−S4 | 178.50(5) | C6−S7−C8−C9 | −95.3(4) |
| | | | | S7−C8−C9−O1 | 65.2(4) |
| | | | | C8−C9−O1−C2 | −131.3(4) |
| | | | | C9−O1−C2−C3 | 135.5(4) |

Similarly to α-**1**, the mononuclear units pack base-to-base about an inversion centre, in this case with the Pd(II) centres locating much more centrally over each other (Fig. 4, Table 7; *cf.* Fig. 2, Table 3), with the coordination planes parallel to each other to form dimeric units. The Pd1···Pd1_#2 separation of 3.4946(7) Å (symmetry code #2 = −*x*, 1 − *y*, −*z*) lies significantly outside the sum of the relevant van der Waals radii [$\Sigma_{vdW}$ = 3.26 Å (Bondi, 1964)]. The perpendicular separation of the $Cl_2S_2Pd$ least squares planes is 3.5237(11) Å and the centroid-centroid shift is 0.4171(17) Å. These dimers form sheets in the *bc* plane with intradimer vectors aligned approximately parallel to the *a* axis, generating alternating hydrophobic and hydrophilic layers.

**Table 7** Intradimer geometry for β-**1**. Symmetry code #2 = −*x*, 1 − *y*, −*z*.

| Atomic Distance /Å | | Angle /° | |
|---|---|---|---|
| Pd1···Cl1_#2 | 4.4577(14) | Pd1···Pd1_#2−Cl1_#2 | 98.22(4) |
| Pd1···Cl2_#2 | 4.0822(13) | Pd1···Pd1_#2−Cl2_#2 | 86.69(3) |
| Pd1···S4_#2 | 4.2415(13) | Pd1···Pd1_#2−S4_#2 | 92.26(3) |
| Pd1···S7_#2 | 4.0319(13) | Pd1···Pd1_#2−S7_#2 | 86.14(4) |
| Pd1···Pd1_#2 | 3.4946(7) | | |

### 3.2.4. Structure of β-[$PtCl_2$([9]ane$S_2$O)]

Crystals of β-**2** were obtained as pale-green blocks by diffusion of $Et_2O$ vapour into saturated solutions of **2** in $CH_3NO_2$ at 30 and 35 °C.

β-[$PtCl_2$([9]ane$S_2$O)] is isomorphous and isostructural with β-[$PdCl_2$([9]ane$S_2$O)]. The Pt(II) centre is bound in a square plane by two mutually *cis* chloride donors and two macrocyclic sulfur donors (Fig. 5, Table 8). The macrocycle binds equatorially in an *exodentate* fashion with the oxygen donor atom directed away from the metal centre [Pt1···O1 = 3.450(2) Å] with the result that no apical

interaction supplements the square planar geometry at the metal. The ligand conformation is assigned as [36] following Dale analysis (Dale, 1973) with corners at C3 and C6, but if a less strict definition of gauche angles is allowed this tends towards a [234] conformation with an additional pseudo corner at C8. The equatorial plane is distorted by out-of-plane bending of S7−Pd1−Cl1 [175.71(3) °] resulting in the metal locating slightly out the plane [0.0235(4) Å] in the direction away from the oxygen. However, when considering the ideal plane formed by S4, S7 and Cl2, the metal centre is found to locate 0.0252(5) Å out of the plane towards the oxygen.

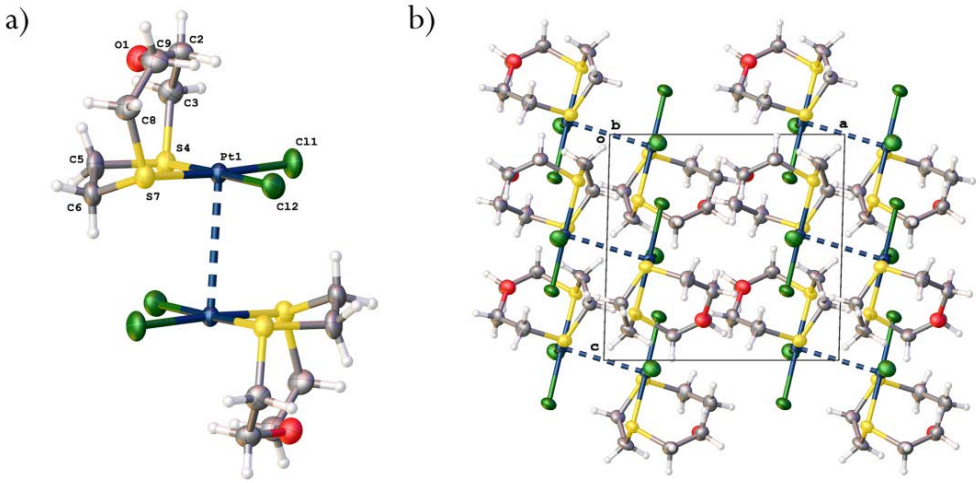



**Figure 5** a) View of the dimer formed in the structure of [$PtCl_2$([9]ane$S_2$O)] in β-**2**. b) View of the herringbone packing of [$PtCl_2$([9]ane$S_2$O)] dimers in β-**2** viewed along the *b* axis. Intermolecular Pt···Pt vectors are highlighted using a dashed bond; displacement ellipsoids shown at 50 % probability. β-**2** and β-**1** are isostructural and isomorphous.

**Table 8** Coordination environment and macrocycle conformation for β-**2**.

| Bond Length /Å | | Bond Angle /° | | Torsion Angle/° | |
|---|---|---|---|---|---|
| Pt1−Cl1 | 2.3221(8) | Cl1−Pt1−Cl2 | 92.75(3) | O1−C2−C3−S4 | −57.4(3) |
| Pt1−Cl2 | 2.3266(8) | Cl2−Pt1−S7 | 89.61(3) | C2−C3−S4−C5 | 78.9(2) |
| Pt1−S4 | 2.2542(7) | S7−Pt1−S4 | 90.29(3) | C3−S4−C5−C6 | −133.2(2) |
| Pt1−S7 | 2.2494(7) | S4−Pt1−Cl1 | 87.43(3) | S4−C5−C6−S7 | 43.3(3) |
| Pt1···O1 | 3.450(2) | Cl1−Pt1−S7 | 175.71(3) | C5−C6−S7−C8 | 72.3(2) |
| | | Cl2−Pt1−S4 | 178.74(3) | C6−S7−C8−C9 | −95.4(3) |
| | | | | S7−C8−C9−O1 | 64.7(3) |
| | | | | C8−C9−O1−C2 | −131.2(3) |
| | | | | C9−O1−C2−C3 | 135.4(3) |

The mononuclear units pack base-to-base about an inversion centre, in this case with the Pt(II) centres locating much more centrally over each other than in α-**2** (Fig. 5, Table 9; *cf*. Fig. 3, Table 3), with the coordination planes parallel to each other to form dimeric units. The Pt1···Pt1_#2 separation of 3.5294(2) Å (symmetry code #2 = −*x*, 1 − *y*, −*z*) lies significantly outside the sum of the relevant van der Waals radii [$\Sigma_{vdW}$ = 3.27 Å (Bond, 1964)]. The perpendicular separation of the $Cl_2S_2Pt$ least squares planes is 3.5565(8) Å and the centroid-centroid shift is 0.4068(12) Å. These dimers form sheets in the *bc* plane with intradimer vectors aligned approximately parallel to the *a* axis (Fig. 5), generating alternating hydrophobic and hydrophilic layers.

**Table 9** Intradimer geometry for β-**2**. Symmetry code #2 = −*x*, 1 − *y*, −*z*.

| Atomic Distance /Å | | Angle /° | |
|---|---|---|---|
| Pt1···Cl1_#2 | 4.4569(9) | Pt1···Pt1_#2−Cl1_#2 | 97.06(2) |
| Pt1···Cl2_#2 | 4.0974(9) | Pt1···Pt1_#2−Cl2_#2 | 86.23(2) |
| Pt1···S4_#2 | 4.2702(8) | Pt1···Pt1_#2−S4_#2 | 92.51(2) |
| Pt1···S7_#2 | 4.0736(8) | Pt1···Pt1_#2−S7_#2 | 86.67(2) |
| Pt1···Pt1_#2 | 3.5294(2) | | |

### 3.2.5. Structure of γ-[$PdCl_2$([9]ane$S_2O$)]

Similarly to β-**1**, the Pd(II) centre is bound in a square plane by two mutually *cis* chloride donors and two macrocyclic sulfur donors (Fig. 6, Table 10). The macrocycle binds equatorially in an *exodentate* fashion with the oxygen donor atom directed away from the metal centre [Pd1···O1 = 3.378(3) Å] with the result that no apical interaction supplements the square planar geometry at the metal. The ligand conformation is assigned as [36] following Dale analysis (Dale, 1973) with corners at C5 and C8, but if a less strict definition of gauche angles is allowed this tends towards a [234] conformation with an additional pseudo corner at C2. The metal locates slightly out the plane [0.0243(8) Å] in the direction away from the oxygen. In contrast to the other two phases, the γ phase does not form dimers: instead, the oxygen donor atom of one molecule is directed towards the base of another [Pd1···O1_#3 = 3.213(3) Å; symmetry code #3 = 0.5 − *x*, −0.5 + *y*, 1.5 − *z*] (Fig. 6). The interaction lies slightly outside the sum of the van der Waals radii [$\Sigma_{vdW}$ = 3.15 Å (Bondi, 1964)] but is considered to have the potential to form chains that run in alternating directions parallel to the *b* axis.

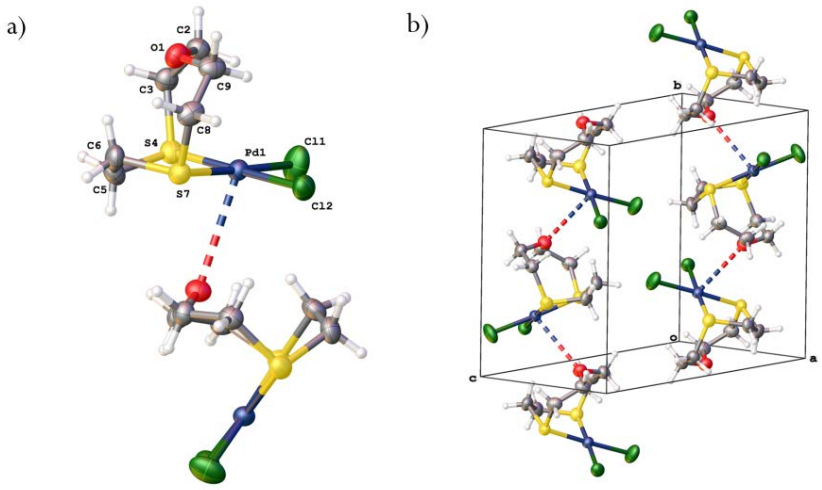



**Figure 6** View of a) the proto-chain formation and b) the unit cell of [$PdCl_2$([9]ane$S_2$O)] in γ-**1**. Intermolecular Pd···O interactions are highlighted using a dashed bond, hydrogen atoms are omitted for clarity and displacement ellipsoids shown at 50 % probability.

**Table 10** Coordination environment and macrocycle conformation for γ-**1**. Symmetry code #3 = 0.5 − *x*, −0.5 + *y*, 1.5 − *z*.

| Bond Length /Å | | Bond Angle /° | | Torsion Angle/° | |
|---|---|---|---|---|---|
| Pd1−Cl1 | 2.3079(12) | Cl1−Pd1−Cl2 | 94.08(5) | O1−C2−C3−S4 | −70.3(5) |
| Pd1−Cl2 | 2.3245(12) | Cl2−Pd1−S7 | 87.29(4) | C2−C3−S4−C5 | 97.9(4) |
| Pd1−S4 | 2.2575(13) | S7−Pd1−S4 | 89.94(4) | C3−S4−C5−C6 | −69.5(4) |
| Pd1−S7 | 2.2665(12) | S4−Pd1−Cl1 | 88.67(5) | S4−C5−C6−S7 | −45.6(5) |
| Pd1···O1_#3 | 3.212(3) | Cl1−Pd1−S7 | 177.94(5) | C5−C6−S7−C8 | 135.4(4) |
| | | Cl2−Pd1−S4 | 177.10(5) | C6−S7−C8−C9 | −81.0(4) |
| | | | | S7−C8−C9−O1 | 57.9(5) |
| | | | | C8−C9−O1−C2 | −132.5(4) |
| | | | | C9−O1−C2−C3 | 133.4(4) |

### 3.3. Computational results

DFT calculations with dispersion corrections were carried out using *CASTEP* (Clark *et al.*, 2005) to obtain total electronic energies and cohesive energies of investigated polymorph structures. Geometry optimisation of individual molecules has been performed in a cubic supercell with dimensions of 20 Å and results

matched well the experimentally observed values (Table 10 & 11). The dispersion interactions were added using semi-empirical methods of Grimme (G06; 2006) and Tkatchenko-Scheffler (TS; Tkatchenko &Scheffler, 2009). The DFT-G06 and DFT-TS energies returned for **1** were comparable to within 0.005 % and the difference between the energies of the phases was only marginally greater with DFT-G06. Consequently, the results presented correspond to calculations which employ the methods of Tkatchenko-Scheffler, *i.e.*, DFT-TS calculations.

**Table 10** Unit cell parameters after *CASTEP* (Clark *et al.*, 2005) geometry optimisation using the dispersion correction of Tkatchenko and Scheffler (2009) and their percentage deviation from experimentally obtained values.

| | Lattice parameters from geometry optimisation /Å | | | | | % deviation of calculated from experimental* | | | | |
|---|---|---|---|---|---|---|---|---|---|---|
| | α-**1** | α-**2** | β-**1** | β-**2** | γ-**1** | α-**1** | α-**2** | β-**1** | β-**2** | γ-**1** |
| *a* (Å) | 8.544 | 8.547 | 9.468 | 9.514 | 7.012 | −1.1 | −1.1 | −1.4 | −1.0 | 0.1 |
| *b* (Å) | 12.223 | 12.34 | 12.715 | 12.625 | 11.471 | −0.6 | −0.3 | −0.5 | 0.3 | −0.6 |
| *c* (Å) | 10.367 | 10.331 | 8.914 | 8.947 | 13.395 | 0.2 | 0.1 | 1.5 | 1.0 | −0.1 |
| β (°) | 105.64 | 106.29 | 91.25 | 90.73 | 96.96 | −0.7 | −0.5 | 1.1 | 0.9 | −0.2 |
| *V* (Å$^3$) | 1042.58 | 1045.95 | 1072.95 | 1074.52 | 1069.58 | −1.1 | −1.1 | −0.4 | 0.3 | −0.5 |

*Unit cell parameters calculated for hypothetical "γ-**2**" are as *a* = 6.964, *b* = 11.757, *c* = 13.273 Å, β = 97.507° and *V* =1077.34 Å$^3$.

**Table 11** Selected structural parameters after *CASTEP* (Clark *et al.*, 2005) geometry optimisation using the dispersion correction of Tkatchenko and Scheffler (2009) and their percentage deviation from experimentally obtained values.

| | Calculated structural parameters | | | | | | % deviation from experimental | | | | | |
|---|---|---|---|---|---|---|---|---|---|---|---|---|
| | α-**1** | α-**2** | β-**1** | β-**2** | γ-**1** | "γ-**2**" | α-**1** | α-**2** | β-**1** | β-**2** | γ-**1** | "γ-**2**" |
| *M*-Cl1 | 2.35 | 2.36 | 2.34 | 2.34 | 2.34 | 2.33 | −1.0 | −1.3 | −1.2 | −0.8 | −1.4 | n/a |
| *M*-Cl2 | 2.35 | 2.36 | 2.34 | 2.34 | 2.34 | 2.34 | −0.9 | −1.4 | −0.8 | −0.6 | −0.7 | n/a |
| *M*-S4 | 2.26 | 2.24 | 2.27 | 2.25 | 2.26 | 2.25 | 0.2 | 0.2 | 0.0 | 0.0 | −0.1 | n/a |
| *M*-S7 | 2.26 | 2.24 | 2.27 | 2.25 | 2.26 | 2.26 | −0.2 | 0.0 | −0.4 | 0.2 | 0.3 | n/a |

### 3.4. Phase loss and retrieval

A very small number of crystals of the previously unreported phase β-**1** were originally recrystallised in the upper region of a vial, the lower part of which contained a mass of crystals identified as α-**1**. Attempts to cut crystals of β-**1** induced an incomplete β → α phase transformation. The resulting diffraction pattern comprised multiple components, with 90 % of reflections indexing to six components all identified as α-**1**, 4 % to a single β-**1** lattice and the remaining 6 % unindexed. In view of this interesting phenomenon, more crystals of β-**1** were sought in order to investigate it further.

It had already been established that the temperature of the laboratory in which the crystals were originally obtained could fluctuate significantly during the day. The distinctive location of β-**1** crystals in the upper part of the vial suggested that they grew in the later stages of the experiment following the influx of antisolvent, and on this basis a number of tentative inferences were made. It is possible that the temperature of the sample varied with the temperature of the surrounding resulting in the dissolution and subsequent recrystallisation of a small amount of material at higher temperatures: in these circumstances, the relative concentrations of complex, solvent and antisolvent present in the system could be significantly different from those for the recrystallisation of α-**1**. The hypothesis of the temperature and solvent environment playing a key role in the crystallisation of these two conformational polymorphs was supported by work carried out by Lucas *et al.* (1997), who showed using temperature-dependent NMR that, when solvated in DMSO, an increase in temperature brings about an increase in fluxionality in the macrocycle of **1** that is not seen when the experiment is carried out in

nitrobenzene. An additional consideration in phase growth is that a seed crystal present in the recrystallisation vial may have acted as a nucleation site. Consequently, three factors were considered as potentially affecting the phase obtained: the temperature of the recrystallisation medium, the relative concentrations of the components and the presence of seed crystals.

To test for location-dependent seeding affects, a possibility discussed by Dunitz and Bernstein (1995), ambient temperature recrystallisations by vapour diffusion were undertaken in a number of different laboratories, including the one in which the original result was obtained: all yielded only the α-**1** phase. To investigate the effect of temperature on the system, similar recrystallisations were carried out at 30 and 35 °C, yielding crystals of the new phase γ-**1**, occasionally accompanied by crystals of α-**1**. Variation of the concentration of the starting solution by diluting the saturated solution was attempted for all temperatures but there were no systematic effects on the outcome of the recrystallisation. Noting the similarity between α-**1** and β-**1**, it appeared reasonable that the presence of a seed crystal of α-**1** might help to seed the growth of β-**1**. Recrystallisations were therefore set up which replicated significant temperature fluctuations occurring during the original recrystallisation after the formation of some α-**1**, but these attempts yielded crystals of α-**1**, γ-**1** or a mixture of the two phases. Recrystallisation of **2** by vapour diffusion at ambient temperature yielded crystals of α-**2**, while at 30 or 35 °C these experiments yielded either α-**2** or β-**2**. No experiment yielded crystals of the hypothetical γ-**2** phase.

The solubility of complex **2** in $CH_3NO_2$ was found to be significantly lower than that of **1** and, combined with the close phase match of β-**1** and β-**2** (Table 12),

leading to the conclusion that it should be possible to grow a crystal of β-**1** directly on a crystal of β-**2** using epitaxial techniques. By the end of this experiment, the pale green seed crystal was surrounded by protrusions of deep orange single crystals (see Fig. 1) which were readily separated from the seed crystal (and called β-**epitaxy** to distinguish them from the original β-**1** crystals). The experiment also yielded crystals identified as α-**1** which had grown conventionally on the walls of the vessel.

**Table 12** Unit cell parameters for β-**1** and β-**2** showing their close phase match. Also shown are the unit cell parameters for β-**epitaxy**.

| Phase | a/Å | b/Å | c/Å | β/° | V/Å$^3$ |
|---|---|---|---|---|---|
| β-**1** | 9.3384(3) | 12.6575(4) | 9.0498(3) | 92.260(3) | 1068.87(6) |
| β-**2** | 9.41666(18) | 12.6646(2) | 9.03760(16) | 91.5297(17) | 1077.43(3) |
| β-**epitaxy** | 9.3451(4) | 12.6701(5) | 9.0724(4) | 92.424(4) | 1073.25(8) |

The crystals of β-**epitaxy** were characterised by MALDI mass spectrometry and single crystal X-ray diffraction to ascertain whether there was any residual contamination by β-[$PtCl_2$([9]ane$S_2$O)], either by solid-state diffusion or *via* partial dissolution of the seed material in the recrystallisation solution. Mass spectrometry revealed peaks with isotope patterns corresponding to the Pd(II)-containing complex, but none from the Pt(II) complex. Competitive crystallographic refinement of the occupancy of the metal site by Pd and Pt showed that no significant amount of Pt was present. Comparison of the unit cell parameters (Table 12) of the epitaxially-grown crystals with those of β-**2** and the original β-**1** showed a considerably closer correspondence with the latter. Similarly, comparison of selected structural parameters for β-**epitaxy** show close matches

with those of β-**1** (Table 13). Although the *M*−S and *M*−Cl bond lengths do not differ greatly between β-**1** and β-**2**, and so do not provide effective discrimination, the intermolecular *M*···*M* and intramolecular *M*···O separations vary more significantly and therefore provide a clear indicator of the metal present in the crystal. *M*···*M* and *M*···O distances in β-**epitaxy** are within one sigma of those calculated for β-**1** but differ much more significantly from those of β-**2** (Table 13). It is therefore concluded that β-**epitaxy** represents a successful recovery of the previously "lost" β-**1** phase.

**Table 13** Selected interatomic distances (Å) for β-**1**, β-**2** and β-**epitaxy**. The values for β-**epitaxy** are generally much closer to those of β-**1** than of β-**2**.

| Phase | *M*···*M* | *M*···O | *M*−S4 | *M*−S7 | *M*−Cl1 | *M*−Cl2 |
|---|---|---|---|---|---|---|
| β-**1** | 3.4946(7) | 3.404(3) | 2.2699(11) | 2.2601(12) | 2.3124(11) | 2.3214(11) |
| β-**2** | 3.5294(2) | 3.450(2) | 2.2542(7) | 2.2494(7) | 2.3221(8) | 2.3266(8) |
| β-**epitaxy** | 3.4937(6) | 3.406(3) | 2.2729(10) | 2.2604(10) | 2.3168(11) | 2.3265(11) |

### 3.5. Phase stabilities

The relative stabilities of phases can be inferred from their crystal densities (Bernstein, 2002). For molecular crystals, it is generally the case that the densest phase will be the most thermodynamically stable, and the densities of the phases can be readily calculated from crystallographic data (Table 14). From these values, it can be inferred that the α phases are significantly more thermodynamically stable than the β phases, and γ-**1** marginally more stable than β-**1**. The densities calculated from the DFT-TS optimised structures (Table 14) are in a good agreement with those derived from the experimentally determined structures and corroborate the same trend.

**Table 14** Densities (g $cm^{-3}$) of the various phases taken from experimentally determined and DFT-TS optimised structures.

| Phase | Conformation | Experimental | Computational |
|---|---|---|---|
| *α*-**1** | *Endodentate* | 2.201 | 2.176 |
| *β*-**1** | *Exodentate* | 2.123 | 2.115 |
| *γ*-**1** | *Exodentate* | 2.133 | 2.121 |
| *α*-**2** | *Endodentate* | 2.763 | 2.733 |
| *β*-**2** | *Exodentate* | 2.653 | 2.660 |
| "*γ*-**2**" | *Exodentate* | n/a | 2.659 |

Comparison of the total energies calculated for each phase (Table 15) confirms that the *endodentate* α phases are significantly more stable compared to the *exodentate* phases. It was found that the energy per molecule of β-**1** is 7.43 kJ $mol^{-1}$ higher than that of α-**1**, and for γ-**1** it further increased by 0.58 kJ $mol^{-1}$ in contrast to the order inferred from the crystal densities and the observation that γ-**1** is the preferred *exodentate* modification of **1**. The calculated energy difference between β-**1** and γ-**1** is, however, too small to make any firm conclusions about the relative stability of these two phases owing to the possible errors associated with approximations adopted in the computational method. Nevertheless, the differences in both the energies and densities between *endodentate* and *exodentate* polymorphs are much larger than between β-**1** and γ-**1**.

**Table 15** Relative total energies, Δ*E*, and cohesive energies, CE, for the different phases of **1** and **2**. In each case, the total energy of the most stable α phase is assigned as zero.

| Phase | ΔE, kJ mol$^{-1}$ | CE, kJ mol$^{-1}$ |
|---|---|---|
| α-**1** | 0 | 225.29 |
| β-**1** | 7.43 | 188.92 |
| γ-**1** | 8.01 | 188.34 |
| α-**2** | 0 | 226.26 |
| β-**2** | 8.59 | 188.92 |
| "γ-**2**" | 11.19 | 186.41 |

Given the structural similarities and the energies of the phases, the appearance of a β → α phase transformation in a crystal of β-**1** is perhaps unsurprising. The existence of such a phase transition in the hindered environment of a macroscopic single crystal suggests that the barrier for this transformation is relatively low. Therefore, it seems reasonable to conclude that β-**1** is not seen because it would be favourable for it to relax to α-**1** in the early stages of crystal growth. As the energies are so similar for γ-**1** and β-**1**, the observation of γ-**1** seems less surprising. It is also noteworthy that the *exodentate* conformation of the macrocycle in γ-**1** gives rise to specific intermolecular O···Pd and C−H···Cl interactions that are not observed in β-**1** and these would stabilise the *exodentate* conformer during growth of γ-**1**. This, coupled with there being no obvious route for it to convert to the stable α phase, would provide a rationale as to why γ-**1** is observed when β-**1** is not.

In the case of β-**2**, which was the only *exodentate* modification of **2** obtained in the study, the total energy was found to be 8.59 kJ mol$^{-1}$ higher than α-**2**. A calculation on a hypothetical phase of **2**, which is isomorphous and isostructural to γ-**1** and is designated γ-**2**, yielded an energy 2.6 kJ mol$^{-1}$ higher than β-**2**. The total difference

in energy of 11.19 kJ mol$^{-1}$ between α-**2** and γ-**2** suggests that the latter is not observed as it is less favoured thermodynamically.

The cohesive energies (CEs) were also calculated for these systems (Table 15). This is defined as the difference between the total energy of the crystalline material at equilibrium (per molecule) and the energy of a free molecule in its ground state. Comparison of these again shows the α phases to be the most thermodynamically favourable, with CEs of 225.29 and 226.26 kJ mol$^{-1}$ for α-**1** and α-**2**, respectively. For **1**, the *exodentate* phases were again found to be very similar (188.92 and 188.34 kJ mol$^{-1}$ for β-**1** and γ-**1**, respectively) with the difference in CE between β-**2** and the hypothetical γ-**2** phases being slightly larger (188.92 and 186.41 kJ mol$^{-1}$, respectively). These data corroborate the conclusions drawn in the preceding paragraphs.

In γ-**1** the charge on the Pd(II) centre is calculated as being 0.72 e, whereas in γ-**2** the charge on the Pt(II) centre is predicted to be only 0.36 e (Table 16); the charge on the macrocyclic O donor is found to be the same in both phases (0.49 e). A stronger *M*···O interaction would be expected in γ-**1** than in γ-**2** since a hard O donor would experience greater electrostatic attraction to the more highly-charged Pd(II) centre. Given that the metal centres are otherwise shielded from their surroundings by the remaining atoms in the molecule, and the comparatively small differences in the charges of these other donors between the phases, the proto-chain forming *M*···O interaction constitutes the principal distinction between the intermolecular bonding in the two phases. The CEs indicate a slightly weaker set of intermolecular interactions in γ-**2** compared with γ-**1** (186.41 and 188.34 kJ mol$^{-1}$, respectively). These comparisons lend weight to the inference that

the proto-chain forming interaction between the metal centre and macrocyclic O donor of the γ phase would be weaker for **2** than it is for **1**. Given the likely role of the *M*···O interaction in the formation of the γ phase, its relative weakness in **2** provides further rationalisation for the absence of the γ-**2** phase.

**Table 16.** Calculated partial atomic charges (/e) for the metal and donor atoms of the phases discussed.

| Phase | *M* | O | Cl | S |
|---|---|---|---|---|
| α-**1** | 0.66 | −0.49 | −0.48 | 0.34 |
| β-**1** | 0.65 | −0.52 | −0.465 | 0.33 |
| γ-**1** | 0.72 | −0.49 | −0.48 | 0.325 |
| α-**2** | 0.33 | −0.49 | −0.435 | 0.385 |
| β-**2** | 0.32 | −0.52 | −0.425 | 0.375 |
| "γ-**2**" | 0.36 | −0.49 | −0.435 | 0.37 |

## 4. Conclusions

In two new phases of $[PdCl_2([9]aneS_2O)]$ (**1**), designated β-**1** and γ-**1** in order of their discovery, the $[9]aneS_2O$ macrocycle adopts *exodentate* conformations, in contrast to the *endodentate* conformation found in the previously reported α-**1** polymorph. Two phases of the previously unreported complex $[PtCl_2([9]aneS_2O)]$ (**2**) were also obtained, designated α-**2** and β-**2**, which are isomorphous and isostructural with the correspondingly-designated phases of **1**. The inability to reproduce the crystallisation of β-**1** by standard methods led to the conclusion that β-**1** is a "disappearing polymorph", with γ-**1** being the preferred *exodentate* form of **1**. In contrast, β-**2** is the only phase of **2** obtained in this investigation which exhibits an *exodentate* conformation for the macrocycle. No polymorph of **2** corresponding to γ-**1** has been isolated despite attempts to seed its growth using a crystal of the latter phase.

A crystal of β-**2** was successfully used to seed the epitaxial growth of the disappearing polymorph β-**1**, and the resulting crystals were shown by MALDI mass spectrometry and single crystal X-ray diffraction to be free from any significant content of **2**.

DFT analysis reveals the order of phase stability to be α>β ≈γ for **1** and α>β> "γ" for **2** (where the γ-**2** phase is hypothetical and based on the structure of γ-**1**), with a greater difference between the energies for**2** than for**1** suggesting that the polymorphic behaviour observed for **1** is not a result of the final energies of the phases. β-**1** exhibits a partial β → α phase transformation brought about by the mechanical pressure of cutting the crystal, whereas no such phase transition on cutting is observed for β-**2**. This suggests that the β phase lies in a potential energy well close to that of the stable *endodentate* α phase and that the energy barrier between them is particularly low in the case of **1**. The β-**1** form is, therefore, not recoverable by conventional recrystallisation as the β → α transformation is facile in the early stages of crystal growth. In γ-**1**,not only do intermolecular Pd···O and C–H···Cl interactions give rise to proto-chains of molecules, they may also stabilise the *exodentate* conformer of the macrocycle during crystal growth; there is evidence to suggest that these interactions are weaker in γ-**2** and so would not stabilise growth of this phase to the same extent.

## References


Agilent (2014). *CrysAlis$^{PRO}$*. Agilent Technologies, Yarnton, England.

Allan, D. R.; Bailey, D.; Bird, N.; Blake, A. J.; Champness, N. R.; Huang, D.; Keane, C. P.; McMaster, J.; Prior, T. J.; Tidey, J. P.; Schröder, M. (2014). *Acta Crystallogr., Sect. B*, **70**, 469-486.

Bauer, J.; Spanton, S.; Henry, R.; Quick, J.; Dziki, W.; Porter, W.; Morris, J. (2001). *Pharm. Res.* **18**, 859-866.

Bernstein, J. (2002). *Polymorphism in Molecular Crystals*; Oxford: International Union of Crystallography / Oxford University Press; 40-41.

Blagden, N.; de Matas, M.; Gavan, P. T.; York, P. (2007). *Adv. Drug Delivery. Rev.* **59**, 617-630.

Bombicz, P.; Czugler, M.; Tellgren, R.; Kálmán, A. (2003). *Angew. Chem., Int. Ed.* **42**, 1957-1960.

Clark, S. J.; Segall, M. D.; Pickard, C. J.; Hasnip, P. J.; Probert, M. I. J.; Refson, K.; Payne, M. C. (2005). *Z. Kristallogr.* **220**, 567-570.

Czugler, M.; Kálmán, A.; Kovács, J.; Pintér, I. (1981). *Acta Crystallogr. Sect. B*, **37**, 17-177.

Dale, J. (1973). *Acta Chem. Scand.* **27**, 1115-1129.

Dolomanov, O.V.; Bourhis, L. J.; Gildea, R. J.; Howard, J. A. K.; Puschmann, H. (2009). *J. Appl. Cryst.* **42**, 339-341.

Bondi, A. J. (1964). *J. Phys. Chem.* **68**, 441-451.

Dunitz, J. D.; Bernstein, J. (1995). *Acc. Chem. Res.* **28**, 193-200.

Grimme, S. (2006). *J. Comput. Chem.* **27**, 1787-1799.

Liu, B.; Fischer, R. A. (2011). *Sci. China Chem.* **54**, 1851-1866.

Llinas, A.; Goodman, J. M. (2008). *Drug Discovery Today*, **13**, 198-210.

Lucas, C. R.; Liang, W.; Miller, D. O.; Bridson, J. N. (1997). *Inorg. Chem.* **36**, 4508-4513.

McCrone, W. C. (1965). *Physics and Chemistry of the Organic Solid State*; New York: Interscience, Vol. 2, 727.

Monkhorst, H. J.; Pack, J. D. (1976). *Phys. Rev. B*, **13**, 5188-5192.

Munroe, Á.; Croker, D.; Hodnett, B. K.; Seaton, C. C. (2011). *CrystEngComm.* **13**, 5903-5907.

Perdew, J. P.; Burke, K.; Erzanhof, M. (1996). *Phys. Rev. Lett.* **77**, 3865-3868.

Shaw, J. L.; Wolowska, J.; Collison, D.; Howard, J. A. K.; McInnes, E. J. L.; McMaster, J.; Blake, A. J.; Schröder, M. (2006). *J. Am. Chem. Soc.* **128**, 13827-13839.

Sheldrick, G. M. (2008). *Acta Crystallogr., Sect. A*, **64**, 112–122.

Sheldrick, G. M. (2015). *Acta Crystallogr., Sect. C*, **71**, 3-8.

Stahly, G. P. (2007). *Cryst. Growth Des.***7**, 1007-1026.

Stephen, E.; Huang, D.; Shaw, J. L.; Blake, A. J.; Collison, D.; Davies, E. S.; Edge, R.; Howard, J. A. K.; McInnes, E. J. L.; Wilson, C.; Wolowska, J.; McMaster, J.; Schröder, M. (2011). *Chem., Eur. J.* **17**, 10246-10258.

Stoica, C.; Tinnemans, P.; Meekes, H.; Vlieg, E. (2005). *Cryst. Growth Des.* **5**, 975-981.

Tidey, J. P.; O'Connor, A. E.; Markevich, A.; Bitchoutskaia, E.; Cavan, J. J. P.; Lawrence, G. A.; Wong, H. L. S.; McMaster, J.; Schröder, M.; Blake, A. J. (2015). *Cryst. Growth Des.* **15**, 115-123.

Tkatchenko, A.; Scheffler, M. (2009). *Phys. Rev. Lett*. **102**, 073005.

Wong, M. H.; Keller, S.; Nidhi; Dasgupta, S.; Denninghoff, D. J.; Kolluri, S.; Brown, D. F.; Lu, J.; Fichtenbaum, N. A.; Ahmadi, E.; Singisetti, U.; Chini, A.; Rajan, S.; DenBaars, S. P.; Speck, J. S.; Mishra, U. K. (2013). *Semicond. Sci. Technol.* **28**, 074009.

# Chapter 3

## High-Pressure Studies of Three Polymorphs of a Palladium(II) Macrocycle Complex

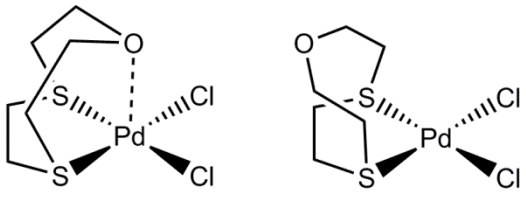
## 1. Introduction

The literature reveals that complexes of Group 10 ($d^8$) metals have received a proportionately large amount of study by high-pressure X-ray diffraction compared to those of other groups. This is primarily in the case of simple planar complexes where stacking of molecules gives rise to 1D chains of *M*···*M* interactions that are associated with pressure-dependent electronic and spectroscopic properties. These studies have shown resistivity in [*M*(dmg)$_2$] (*M* = Ni, Pt; dmg = dimethylglyoximate) to be linked to the *M*···*M* separation where pressure ultimately engenders conductivity (Takeda *et al*., 2006), while in [Ni(3-fluoro-salicylaldoximato)$_2$] no such increase in conductivity was observed despite similar *M*···*M* separations being obtained (Byrne *et al*., 2012; Konno *et al*., 1989). Instead, reversible piezochromism was observed which, instead of being attributed to the closing proximity of the metal centres, was rationalised as an effect of the slight compression on the equatorial donor set.

In our own studies of Group 10 ($d^8$) metals, we have looked at the effect of pressure on complexes of the nine-membered tridentate thioether macrocycle 1,4,7-trithiacyclononane ([9]aneS$_3$). Complexation with this ligand results in distant apical interactions reminiscent of the Jahn-Teller distorted interactions at copper(II) centres which can be expected to be similarly sensitive to the effects of pressure. In the series [*MX*$_2$([9]aneS$_3$)] (*M* = Pd, Pt; *X* = Cl, Br, I) molecules pack in such a way as to orient an equatorial S donor from one molecule towards the open face of the metal in a neighbouring molecule (Allan *et al*., 2014). In the case of [PdCl$_2$([9]aneS$_3$)], a phase transition was observed at 44 kbar, associated with the stepwise contraction of this intermolecular interaction and the distant apical Pd···S interaction (Allan *et al*., 2006). While these distant interactions were found

to be compressible in the other members of this series, no other system yielded any discontinuous phenomenon (Allan *et al.*, 2014). In switching the π-donating halide donors for π-accepting phosphines, the length of the distant apical interaction can be decreased (Blake *et al.*, 1996). Our study of $[Pd([9]aneS_3)(PPh_3)_2](PF_6)_2$ showed this distant apical interaction contracting by only 0.033(13) Å over 65.5 kbar, while the major effects of pressure were instead to induce π-π stacking between phenyl rings and bring about a 20° out-of-plane bend at the *ipso* carbon of one of the phenyl moieties (Wong *et al.*, 2013).

Continuing our investigations in this area, we turned our attention to complexes of 1-oxa-4,7-dithiacyclononane ($[9]aneS_2O$), a tridentate macrocycle similar to $[9]aneS_3$ but with one sulfur donor replaced by an oxygen donor. This results in a slightly smaller macrocycle containing one hard and two soft donor atoms. In the context of the reported Pd(II) complex this donor replacement translates to a change in the apical ligation of the complex. Herein the response of three polymorphs of $[PdCl_2([9]aneS_2O)]$ (**1**) to pressure is reported alongside complementary variable temperature and computational studies. The work in this chapter has been reported (Tidey *et al.*, 2016) and the high-pressure data for γ-$[PdCl_2([9]aneS_2O)]$ is briefly discussed by Tidey (2012) and Wong (2014).




**Scheme 1** Scheme showing *endodentate* (left) and *exodentate* (right) conformers of $[PdCl_2([9]aneS_2O)]$.

## 2. Experimental

### 2.1. Synthesis

Complex **1** was prepared as described in Chapter 2 and by Tidey *et al*. (2015). Crystals of α-**1** were obtained by diffusion of $Et_2O$ vapour into a solution of the complex in $CH_3NO_2$ at 20 °C. Crystals of β-**1** were obtained by epitaxial growth off an isomorphous phase of [$PtCl_2$([9]ane$S_2O$)]. Crystals of γ-**1** were obtained by diffusion of $Et_2O$ vapour into a solution of the complex in $CH_3NO_2$ at 35 °C.

### 2.2. Crystallography

#### 2.2.1. High-pressure crystallography

For α-**1**, high-pressure data were collected using a crystal of dimensions 0.10 × 0.10 × 0.03 $mm^3$ at 0.001, 5.0, 17.1, 32.2, 46.5, 55.2, 79.2, 89.6, 103.4, 117.8, 127.1 and 135.6 kbar. For β-**1**, high-pressure data were collected using a crystal of dimensions 0.12 × 0.07 × 0.05 $mm^3$ at 0.001, 8.3, 14.1, 30.9, 43.5, 57.5, 80.4, 97.4 and 118.7 kbar, then the pressure was ramped and cycled to obtain collections at 60.5, 65.4, 71.4,68.7, and 68.1 kbar. For γ-**1**, high-pressure data were collected using a crystal of dimensions0.11 × 0.10 × 0.02 $mm^3$ at 0.001, 11.6, 19.1, 30.1, 52.4, 74.1, 98.6, 124.5 kbar and on decompression at 50.5 kbar; no viable datasets were obtained following collection at 98.6 kbar.

The sample chamber of a Merrill-Bassett diamond anvil cell (DAC) was formed by the 600 μm culet faces of the Boehler-Almax diamonds and by laser-cut tungsten sheet (Goodfellow Metals, thickness 200 μm) indented to a thickness of *ca*. 80 μm with a gasket hole of diameter 200 μm drilled using a BETSA electric discharge machine. In each case, the sample crystal was fixed to one culet face by means of

silicone grease alongside a ruby sphere which allowed pressure measurement using the ruby fluorescence method (Barnett *et al.*, 1973). Methanol/ethanol (4:1 *v*/*v*) was used as the pressure transmitting medium (PTM), except in the case of in-cell data collections at ambient pressure for which no PTM was used. After each pressure ramp, the pressure inside the DAC was allowed to equilibrate for a minimum of 16 hours before data collection was initiated. Pressure measurements were taken immediately before and after each collection and the pressure reported is the average of these. The average uncertainty in pressure across this study is 1.2 kbar with specific error bars drawn on Figures as 0.5 times the magnitude of the drift plus 0.5 kbar attributed to the inherent uncertainty of the ruby fluorescence method (Holzapfel, 2003).

Data were collected for γ-**1** using a Rigaku SuperNova and for α-**1** and β-**1** a SuperNovaII diffractometer equipped with a microfocus sealed-tube source focussing mirror-monochromated Mo-*K*α radiation (λ = 0.71073 Å) detected at an Eos CCD area detector. Cell refinement and data reduction was performed using *CrysAlis*$^{PRO}$ (Agilent, 2014). For ambient temperature (293 K) and pressure collections collected outside the cell, crystals were mounted using silicon grease on MiTeGen MicroMounts$^{TM}$ and numerical absorption corrections based on Gaussian integration over a multifaceted crystal model were applied. For all other data, multi-scan absorption corrections were applied with an empirical absorption correction using spherical harmonics, implemented in SCALE3 ABSPACK scaling algorithm (Clark & Reid, 1995) through *CrysAlis*$^{PRO}$ (Agilent, 2014). Structure solution was undertaken using *SHELXS*14 direct methods (Sheldrick, 2008) for the ambient pressure structures and for the structure obtained at 80.4 kbar for β'-**1**. All other structures were solved by isomorphous replacement with an appropriate

model. Structures were refined to convergence using *SHELXL*14 (Sheldrick, 2015). Structure solution and refinement were implemented through *Olex2* (Dolomanov *et al*., 2009). Specific refinement details are embedded in the relevant CIFs which can be found along with the experimental tables in the supplementary information.

### 2.2.2. Variable temperature crystallography

For α-**1**, a single crystal of dimensions 0.23 ×0.17 × 0.13 $mm^3$ was mounted with epoxy resin on a glass fibre. Collections were made at 290, 340, 390, 340, 290, 240, 190, 140 and 90 K, where the first collection at 290 K, both at 340 K and collections at 140 and 190 K were limited to unit cell determinations. The ramp rate was 60 K $hr^{-1}$ with a standing time of 5 mins prior to each collection. Data were collected on a Bruker SMART APEX diffractometer equipped with a sealed-tube source using graphite monochromated Mo-*K*α radiation (λ = 0.71073 Å) detected at a Bruker SMART APEX CCD area detector. For full collections, cell refinement and data reduction was performed using SAINT+ (Bruker, 2007) and multi-scan absorption corrections were applied with an empirical absorption correction using spherical harmonics, implemented through SADABS (Bruker, 2001; Sheldrick, 1996). For matrix-only collections, cell refinement was performed using *CrysAlis*$^{PRO}$ (Agilent, 2014).

For β-**1**, a single crystal of dimensions 0.09 × 0.05 × 0.04 $mm^3$ was mounted in a Fomblin film on a MiTeGen MicroMount$^{TM}$. Collections were made at 290, 280, 270, 260 (×2), 240, 230, 220, 210, 200, 190, 180, 170, 160, 150, 140, 130, 120, 110, 100, 90, 290, 310, 330, 350, 370, 390, 410, 430, 450 and 470 (×2) K with a ramp rate of 60 K $hr^{-1}$ and a standing time of 5 mins prior to each collection. When

attempted data collections at 250 and 490 K failed owing to technical problems, alternative collections were carried out at 260 and 470 K, respectively. Data were collected using a Rigaku SuperNovaII diffractometer equipped with a microfocus sealed-tube source focussing mirror-monochromated Cu-*K*α radiation (λ = 1.5418 Å) detected at an Atlas CCD area detector. Cell refinement and data reduction was performed using *CrysAlis*$^{PRO}$ (Agilent, 2014) and numerical absorption corrections based on Gaussian integration over a multifaceted crystal model were applied.

For γ-**1**, a single crystal of dimensions 0.21 × 0.14 × 0.05 mm$^3$ was mounted in a Fomblin film on a MiTeGen MicroMount$^{TM}$. Collections were made at 290, 242, 192, 142, 99, 290, 335, 388, 438 and 488 K with a ramp rate of 60 K hr$^{-1}$ and a standing time of 5 minutes prior to each collection. Owing to technical problems, the temperature for the second 290 K dataset was not reliably recorded and the corresponding data are omitted. Diffraction data were collected using a Rigaku SuperNova diffractometer equipped with a microfocus sealed-tube source focussing mirror-monochromated Cu-*K*α radiation (λ = 1.5418 Å) detected at an Atlas CCD area detector. Cell refinement and data reduction was performed using *CrysAlis*$^{PRO}$ (Agilent, 2014) and numerical absorption corrections based on Gaussian integration over a multifaceted crystal model were applied.

In all cases, temperatures were regulated using Oxford Cryostreams open-flow cryostats (Cosier & Glazer, 1986), and structures were solved by isomorphous replacement with an appropriate model and refined to convergence using *SHELXL*14 (Sheldrick, 2015). Solution and refinement were implemented through *Olex2* (Dolomanov *et al*., 2009). Specific refinement details are embedded in the

relevant CIFs which can be found along with the experimental tables in the supplementary information.

### 2.3. Density functional theory calculations

Single-point density functional theory calculations were carried out on models derived directly from the experimentally obtained crystal structures using the Amsterdam Density Functional suite version 2014.02 (*ADF*; Fonseca-Guerra *et al.*, 1998; Te Velde *et al.*, 2001). Slater-type orbital triple-ζ-plus double polarization basis sets were used from the ZORA/TZP2 database of the *ADF* suite: for Pd, a frozen core approximation up to and including 4*p* was used; for S and Cl, up to and including 2*p*; for C and O, only including 1*s*. Scalar relativistic approaches were used within the ZORA Hamiltonian and the local density approximation with correlation potential due to Vosko *et al.* (1980) were used in all calculations. Gradient corrections were performed using the functionals of Becke (1988) and Perdew *et al.* (1986). For α-**1**, DFT calculations were carried out on a dimer fragment as described in Section 3.1.1. For β-**1**, DFT calculations were carried out on a dimer fragment as described in Section 3.1.2. For β'-**1**, DFT calculations were also carried out on fragments corresponding to each of the three unique dimer combinations as described in Section 3.4.2. For γ-**1**, DFT calculations were carried out on a two-molecule fragment of a chain as described in Section 3.1.3.

## 3. Results and discussion

### 3.1. Structures at ambient pressure and temperature

Structures for the ambient pressure phases are fully reported in Chapter 2 but it is pertinent to highlight certain features for the sake of discussion. Details of the unit cell parameters at ambient temperature and pressure for the phases discussed in this chapter are given in Table 1.

**Table 1** Unit cell parameters for the three reported phases of **1** at ambient temperature and pressure and for the high pressure β' modification at 68.7 kbar in which $Z = 12$. For all other phases $Z = 4$.

| Phase | Space group | $a$ / Å | $b$ / Å | $c$ / Å | β/ ° | $V$ / Å$^3$ |
|---|---|---|---|---|---|---|
| α-**1** | $P2_1/n$ | 8.4502(4) | 12.1807(5) | 10.3745(4) | 105.125(4) | 1030.85(8) |
| β-**1** | $P2_1/c$ | 9.3451(4) | 12.6701(5) | 9.0724(4) | 92.424(4) | 1073.25(8) |
| β'-**1** | $P2_1/n$ | 12.4719(10) | 11.7860(8) | 18.2203(14) | 108.659(7) | 2537.5(3) |
| γ-**1** | $P2_1/n$ | 7.02123(16) | 11.4020(3) | 13.3817(3) | 96.785(2) | 1063.78(5) |

#### 3.1.1. α-[$PdCl_2$([9]ane$S_2O$)]

The Pd(II) centre in α-**1** is bound in a square plane by two mutually *cis* chloride donors [Pd−Cl = 2.3278(17) and 2.3296(18) Å] and two macrocyclic sulfur donors [Pd−S = 2.2649(14) and 2.2546(16) Å] (Fig. 1). The macrocycle binds in an *endodentate* configuration providing a distant apical oxygen donor [Pd1···O1 = 2.958(4) Å] within the sum of the van der Waals radii [$\Sigma_{vdW}$ = 3.15 Å (Bondi, 1964)] to form a [4+1] square based pyramidal geometry at the metal. The mononuclear units pack base-to-base (Fig. 2) with the coordination planes parallel to each other to form dimeric units [Pd1···Pd1_#1 = 3.7903(10) Å; symmetry code #1 = $-x$, $2 - y$, $-z$]. This value lies significantly outside the sum of the relevant van der Waals radii [$\Sigma_{vdW}$ = 3.26 Å (Bondi, 1964)]. The perpendicular separation of the $Cl_2S_2Pd$ least squares planes is 3.6246(15) Å and the centroid-centroid shift is

1.182(2) Å. These dimers form ABAB alternating sheets in the *bc* plane, generating a herringbone-like motif when viewed along the *a* axis (Fig. 2).

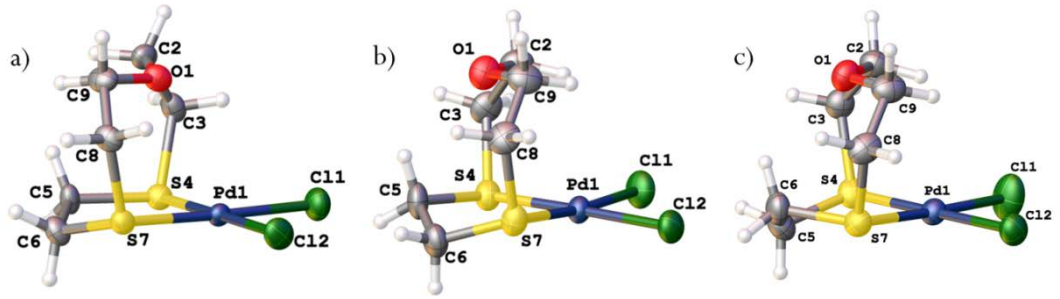



**Figure 1** View of complex **1** in the a) α, b) β and c) γ phases. Non-H atoms are labelled in accordance with text and anisotropic displacement parameters are drawn at 50 % probability.

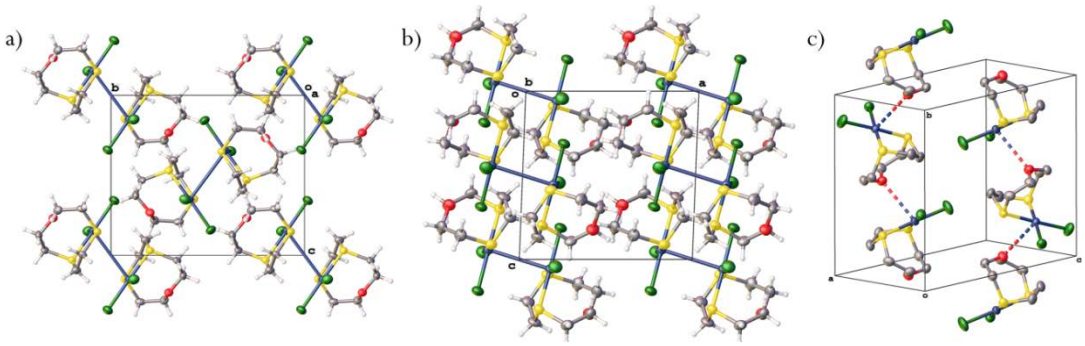



**Figure 2** a) View of herringbone packing of α-**1** viewed along the *a* axis; Pd···Pd interactions within dimeric units are highlighted by an additional blue bond. b) Layered packing of β-**1** viewed along the *b* axis; Pd···Pd interactions within dimeric units are highlighted by an additional blue bond. c) The formation of chains and their packing in γ-**1**; chain-forming Pd···O interactions are highlighted as dashed bonds.

### 3.1.2. β-[$PdCl_2$([9]ane$S_2O$)]

The Pd(II) centre is bound in a square plane by two mutually *cis* chloride donors [Pd−Cl = 2.3167(10) and 2.3265(11) Å] and two macrocyclic sulfur donors [Pd−S = 2.2729(10) and 2.2605(10) Å] (Fig.1). The macrocycle binds in an *exodentate* fashion with the oxygen donor atom directed away from the metal centre

[Pd1···O1= 3.406(3) Å] with the result that no apical interaction supplements the square planar geometry at the metal. Similarly to the *α* phase, these units pack base-to-base (Fig.2) with the coordination planes parallel to each other to form dimeric units [Pd1···Pd1_#2 = 3.4937(6) Å; symmetry code #2 = −*x*,1 − *y*,−*z*]. This value again lies significantly outside the sum of the relevant van der Waals radii [$\Sigma_{vdW}$ = 3.26 Å (Bondi, 1964)]. The perpendicular separation of the $Cl_2S_2Pd$ least squares planes is 3.5258(9) Å and the centroid-centroid shift is 0.4113(15) Å. These dimers form sheets in the *bc* plane with intradimer vectors aligned approximately parallel to the *a* axis, generating alternating hydrophobic and hydrophilic layers.

### 3.1.3. γ-[$PdCl_2$([9]ane$S_2O$)]

The Pd(II) centre is bound in a square plane by two mutually *cis* chloride donors [Pd−Cl = 2.3079(12) and 2.3245(12) Å] and two macrocyclic sulfur donors [Pd−S = 2.2575(12) and 2.2665(12) Å] (Fig.1). As with the β phase the macrocycle binds in an *exodentate* fashion with the oxygen donor atom again directed away from the metal atom [Pd1···O1 = 3.378(3) Å] such that there is no significant apical interaction. In contrast to the other two phases, the γ phase does not form dimers: the oxygen donor atom of one molecule is directed towards the base of another [Pd1···O1_#3 = 3.213(3) Å; symmetry code #3 = 0.5 − *x*, −0.5 + *y*, 1.5 − *z*] (Fig. 2). The interaction lies slightly outside the sum of the van der Waals radii [$\Sigma_{vdW}$ = 3.15 Å (Bondi, 1964)] but is considered to have the potential to form chains that run in alternating directions parallel to the *b* axis.

### 3.2. Pressure limits of studies

All phases were studied in a PTM of methanol/ethanol (4:1 *v/v*), which is reported as having a hydrostatic limit of 105 kbar (Klotz *et al.*, 2009), and the maximum pressures to which data is reported are 103.4, 97.4 and 98.6 kbar for the α, β and γ phases, respectively. The use of a PTM is necessary in high-pressure crystallographic studies to give isotropic compression of the sample, which is given up to the hydrostatic limit of the PTM. After this point pressure gradients are generated (Piermarini *et al.*, 1973). While these ultimately lead to degradation of the crystal (*e.g.*, Connor *et al.*, 2015), data collected under non-hydrostatic conditions can be subject to an axial bias in pressure that serves to convolute trends and can promote or suppress phenomena such as phase transitions (Ballaran *et al.*, 2013 and references 32−40 therein). Even under hydrostatic conditions, for the majority of high pressure crystallographic studies of coordination complexes the pressure limit appears to be dictated by the resilience of the sample, with crystals failing to diffract sufficiently well long before the hydrostatic limit of the PTM is reached (Tidey *et al.*, 2014 and references within). This was not the case in this study and two of the three phases continued to give good quality data well beyond the expected hydrostatic limit of the PTM. The quality of diffraction from α-**1** had not significantly degraded even by 135.6 kbar. Nevertheless, data collected above the hydrostatic limit of the PTM will not be discussed as they deviate significantly from the trends observed under hydrostatic conditions (Fig.S1, S2, S6-S11). For β-**1**, the crystal appears to be intact and diffracting well even at 119.8 kbar, but this data set is also discounted from discussion for similar reasons (Fig. S13-S31). In the case of γ-**1**, the highest pressure at which a viable dataset could be collected

was 98.6 kbar: data quality was obviously poorer at this pressure and no useable datasets could be obtained at higher pressures.

### 3.3. Pressure dependence of cell parameters

#### 3.3.1. α-[$PdCl_2$([9]ane$S_2O$)]

Between ambient pressure and 103.4 kbar, smooth contractions of 7, 10, 9 and 24 % were observed for *a*, *b*, *c* and *V*, respectively (Fig. 3). For the third-order Birch-Murnaghan (BM) equation of state (EoS) calculated using *EoSFit7c* (Angel, 2014), $B_0$ = 14.4(8) GPa, $B'_0$ = 7.8(6) and $V_0$ = 1026.7(18) $Å^3$. Of the three phases, α-[$PdCl_2$([9]ane$S_2O$)] was found to be the most resistant to compression.

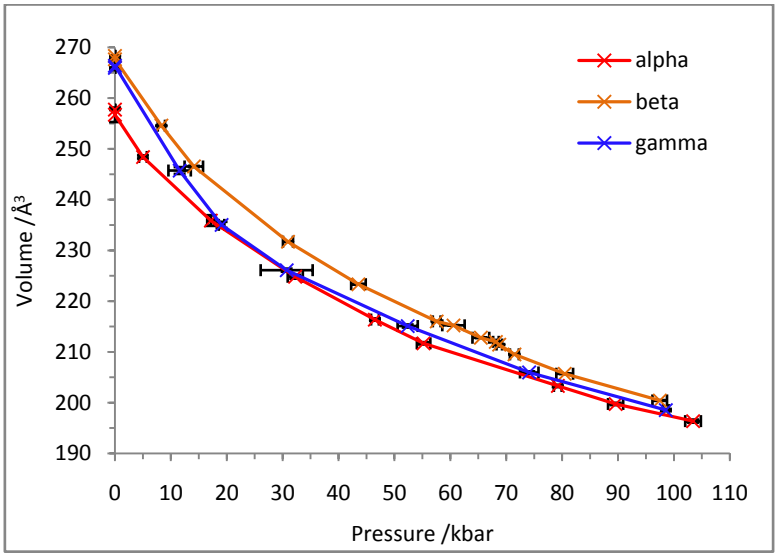



**Figure 3** The effects of pressure on the average molecular volume, *V*/*Z*, for the three phases investigated.

#### 3.3.2. β-[$PdCl_2$([9]ane$S_2O$)]

Between ambient pressure and 68.1 kbar, smooth contractions of 8, 7, 8 and 21 % were observed for *a*, *b*, *c* and *V*, respectively. For the third-order BM EoS, $B_0$ = 12.8(8) GPa, $B'_0$ = 7.4(7) and $V_0$ = 1070.6(2)$Å^3$, making it only marginally more

compressible than the α phase. This result is unsurprising given the similarities in packing between the α and β phases. Between 68.1 and 68.7 kbar a reversible phase transition was observed involving a tripling of the unit cell volume with retention of the *b* axis to give the high pressure phase, designated β'-[$PdCl_2$([9]ane$S_2O$)]. Compression continues to occur smoothly above this point but there are insufficient data points to calculate the bulk modulus for the high pressure phase. Analysis of a *V*/*Z* plot (Fig. 3) shows a small discontinuity in compression at the phase transition, indicative of a denser packing of the molecules in the unit cell in the high pressure modification. The total relative compression observed in *V*/*Z* up to 97.4 kbar is 25 %.

### 3.3.3. γ-[$PdCl_2$([9]ane$S_2O$)]

Between ambient pressure and 98.6 kbar, smooth contractions of 8, 11, 9 and 25 % were observed in *a*, *b*, *c* and *V*, respectively. The comparatively high degree of compression in the *b* axis is attributed to the more compressible intermolecular chain-forming Pd···O interactions forming along this axis. The γ phase is notably more compressible than the other two with a third-order BM EoS of $B_0$ = 7.6(6) GPa, $B'_0$ = 13.0(11) and $V_0$ = 1065.5(12)Å$^3$.

### 3.3.4. Relative compressibility and void space analysis

An overview of the pressure dependence of the three ambient phases is given in Fig. 3 in the form of a *V*/*Z* plot. From this it can clearly be seen that the β phase compresses at a similar rate to the α phase, while the γ phase is significantly more compressible and by a pressure of *ca.* 20 kbar has compressed to a similar density

as that of the α phase despite initially being 3.2 % less dense. Notably, while the α and β phases have highly typical bulk compressibilities for molecular materials, the bulk modulus for γ-**1** is right at the lower bounds of what is typically seen for coordination complexes. Where the intramolecular and notable intermolecular interactions compress at similar rates for all three phases (*vide infra*), another rationale is required to explain this behaviour. In this case, this can be done largely by analysis of crystal void space. Fig. 4 maps the void space present in each structure as a function of pressure, calculated with a 0.002 e $Å^{-3}$ isovalue using *CrystalExplorer* (Turner *et al*., 2011; Wolff *et al*., 2012) and the trends seen here closely resemble those seen for the *V*/*Z* plot.

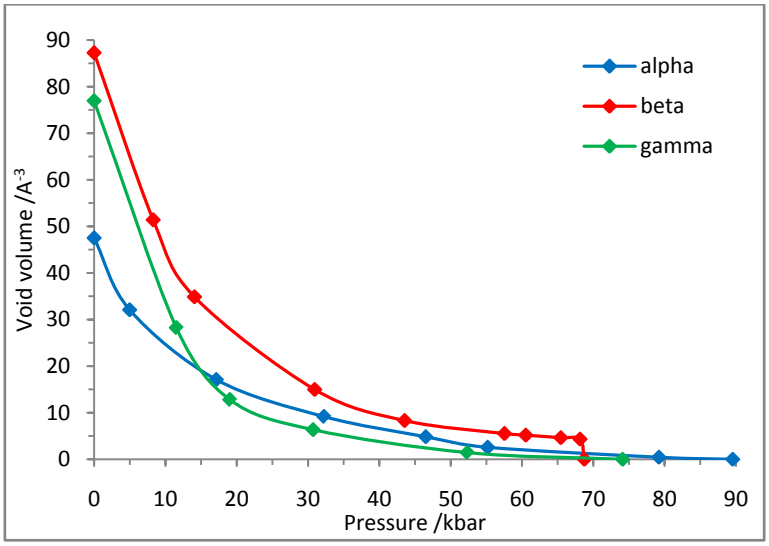



**Figure 4** The effects of pressure on the void volume in each phase, calculated using *CrystalExplorer* (Turner *et al*., 2011; Wolff *et al*., 2012) at 0.002 e $Å^{-3}$.

The differing rates of compression appear to be directly related to the location and volume of easily-compressible void space and the weak intermolecular interactions that govern them. The α phase, which is the densest and least compressible of the phases, contains only 4.6 % void space under ambient conditions which is located

in pockets around the dimers (Fig. 5). These spaces appear to be relatively inaccessible to the molecule, which is already in the most energetically favourable conformation (Park *et al.*, 2004) and does not undergo any significant changes to its shape across the study (*vide infra*). The phase is consequently relatively hard as the void space is depleted very slowly and compression relies first on the compression of other much closer intermolecular contacts and of the molecules themselves.

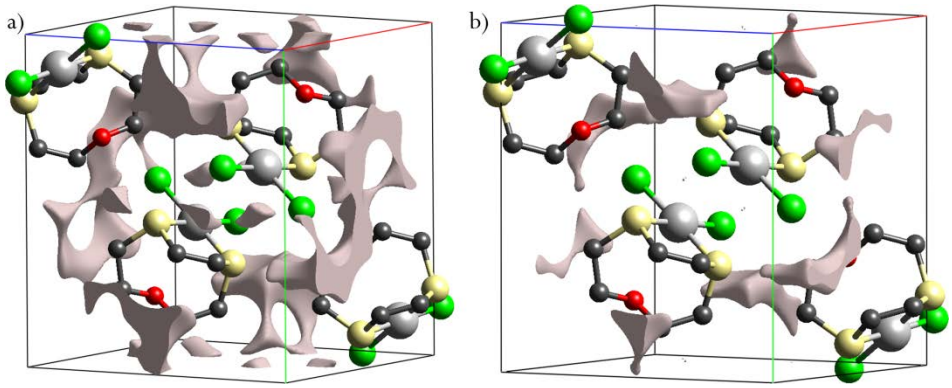



**Figure 5** The distribution of void space in α-**1** at a) ambient pressure and b) 17.1 kbar calculated using *CrystalExplorer* (Turner *et al.*, 2011; Wolff *et al.*, 2012) at 0.002 e $Å^{-3}$. Hydrogen atoms omitted for clarity; *a* axis in red, *b* axis in green, *c* axis in blue.

The β phase is calculated as having almost twice the proportion of void space under ambient conditions as the α phase (8.2 %). This void space is located partially between neighbouring dimers within layers but more prominently in the region between dimer layers (Fig. 6). As pressure is increased, the void space between neighbouring dimers is readily depleted whereas the void space between these layers appears significantly less compressible. Notably, there are highly persistent pockets of void that remain entirely unfilled across the entire pressure range in which the ambient modification is maintained (Fig. 6). This is indicative

of both the higher resistance of C−H···H−C interactions to compression compared to C−H···*X* interactions and of an inefficient packing between dimer sheets.

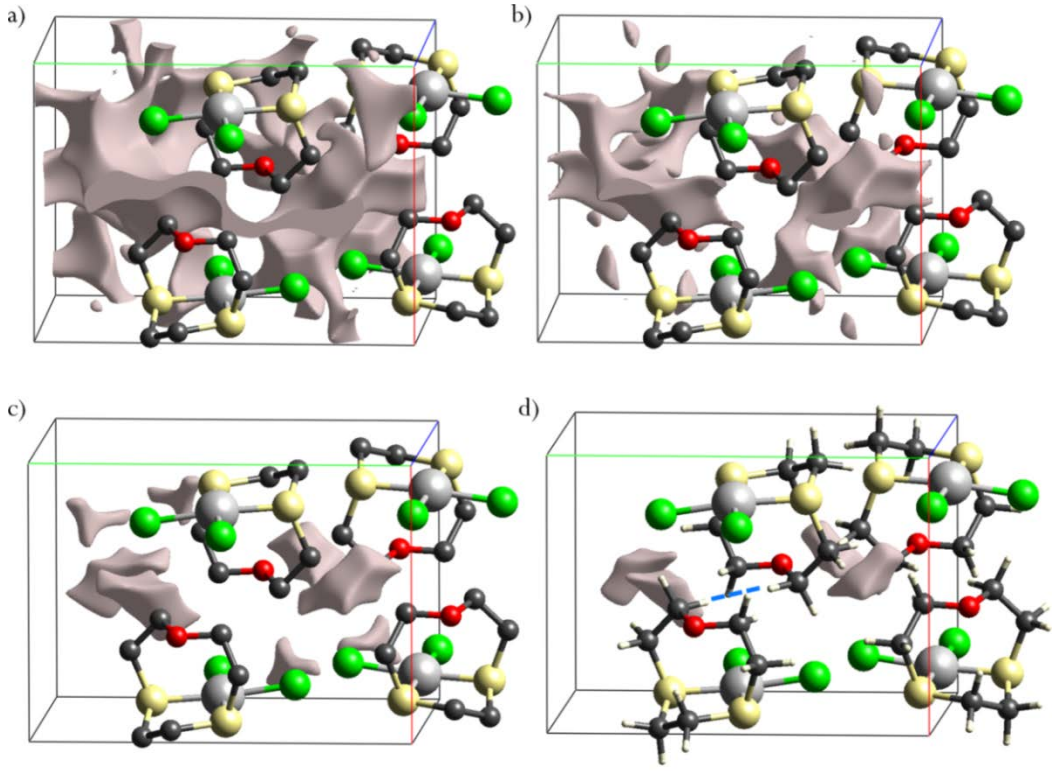



**Figure 6** The distribution of void space in β-**1** at a) ambient pressure, b) 14.1 kbar, c) 30.1 kbar and d) 57.5 kbar calculated using *CrystalExplorer* (Turner *et al*., 2011; Wolff *et al*., 2012) at 0.002 e Å$^{-3}$. Hydrogen atoms omitted for clarity except at 57.5 kbar where the close C−H···H−C approach described in Section 3.4.3 is highlighted by the addition of a dashed blue line; *a* axis in red, *b* axis in green, *c* axis in blue.

At ambient temperature and pressure, γ-**1**and β-**1**contain a similar amount of void space (7.2 %), located almost exclusively between neighbouring chains (Fig. 7). While under ambient conditions the directionality of intermolecular interactions results in a less dense packing than the α phase, similar in density to that of the β phase, these appear comparably deformable and compressible. The dominating interactions that surround the void space are C−H···*X* interactions, just as between dimers within sheets in the β phase. Consequently, by 19.1 kbar the void space has

been rapidly reduced to only 1.4 %. The alternating chain motifs thus appear to allow for relatively efficient packing under increased pressure, with zigzag rows interdigitating with each other. After most of this space between chains has been squeezed out, compression of both the void space and unit cell changes abruptly, continuing in a manner similar to that of the α phase at the corresponding pressure (Fig. 5 & 6).

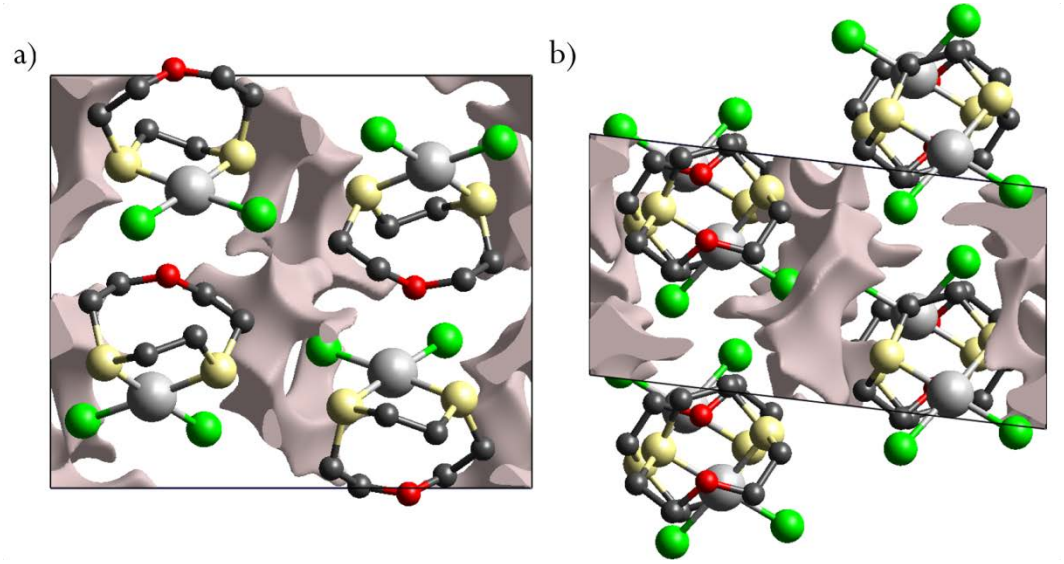



**Figure 7** The distribution of void space in γ-**1** at ambient pressure as viewed along the a) *a* axis and b) *b* axis calculated using *CrystalExplorer* (Turner *et al*., 2011; Wolff *et al*., 2012) at 0.002 e au$^{-3}$. Hydrogen atoms are omitted for clarity.

### 3.4. Phase transition in β-[$PdCl_2$([9]ane$S_2O$)]

#### 3.4.1. Overview

For the α and γ phases, the effects of pressure were smooth and continuous across the entire pressure ranges interrogated. The β phase exhibited smooth effects of pressure up to 68.1 kbar. Between 68.1 and 68.7 kbar a reversible $P2_1/c \rightarrow P2_1/n$ phase transition occurred without observable hysteresis. Across the phase transition there is retention of the *b* axis whereas *a* and *c* are redefined by the transformation matrix [1 0 1 / 0 1 0 / $\bar{1}$ 0 2] such that the unit cell volume is tripled.

Given the relationship and notable crystallographic similarity between the two phases (Fig. 8, 9, 10) the resulting phase is designated as β'-**1**.

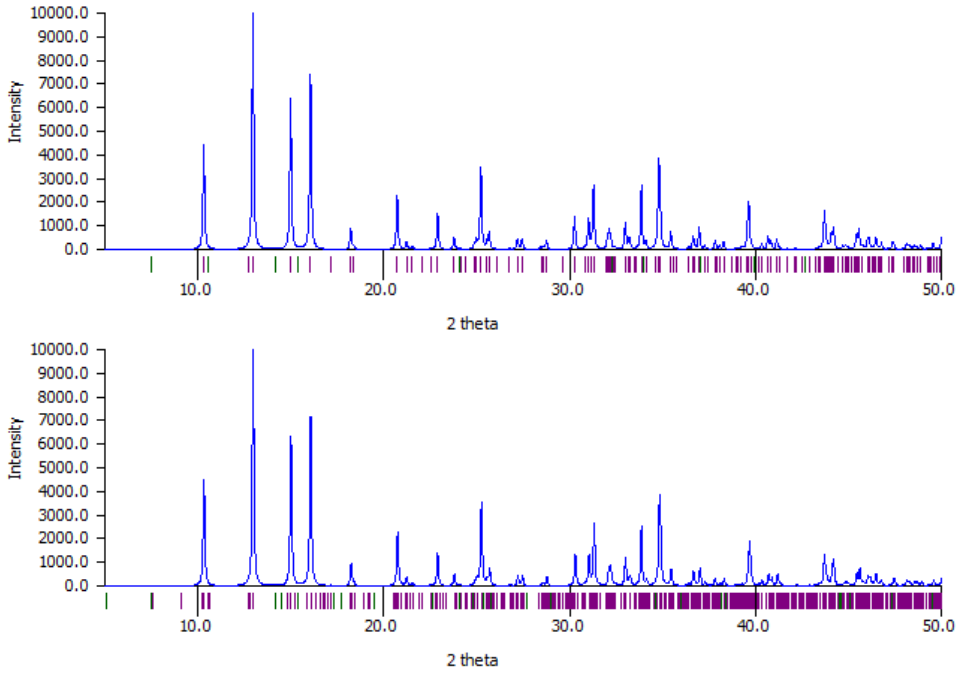



**Figure 8** Simulated powder patterns for the β and β' phases at 68.1 and 68.7 kbar demonstrating the general crystallographic similarity between them. Patterns simulated using *Mercury* (Macrae, 2006; Macrae, 2008).

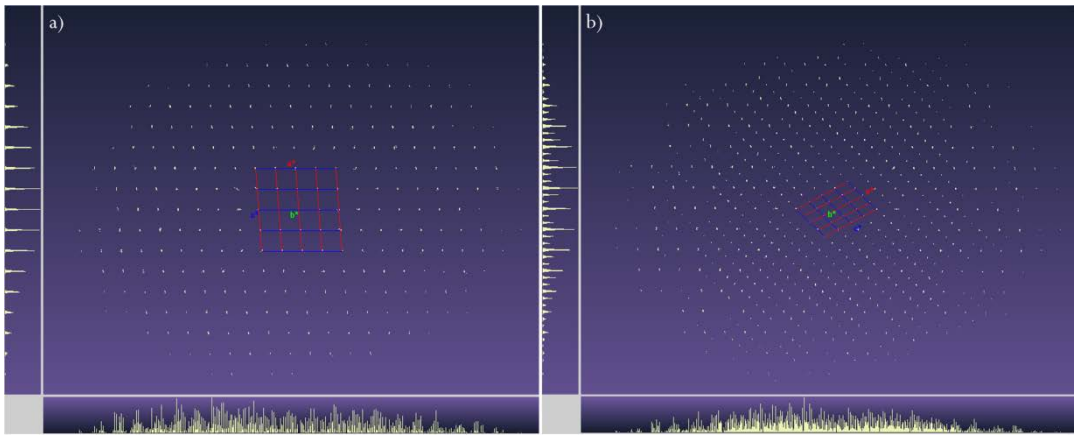



**Figure 9** Views of the reciprocal lattices for a) β-**1** at 68.1 kbar and b) β'-**1** at 71.4 kbar, as viewed down the common *b** axes, showing the distribution of super-cell peaks associated with the high-pressure phase. Views generate using *CrysAlis*$^{PRO}$ (Agilent, 2014).

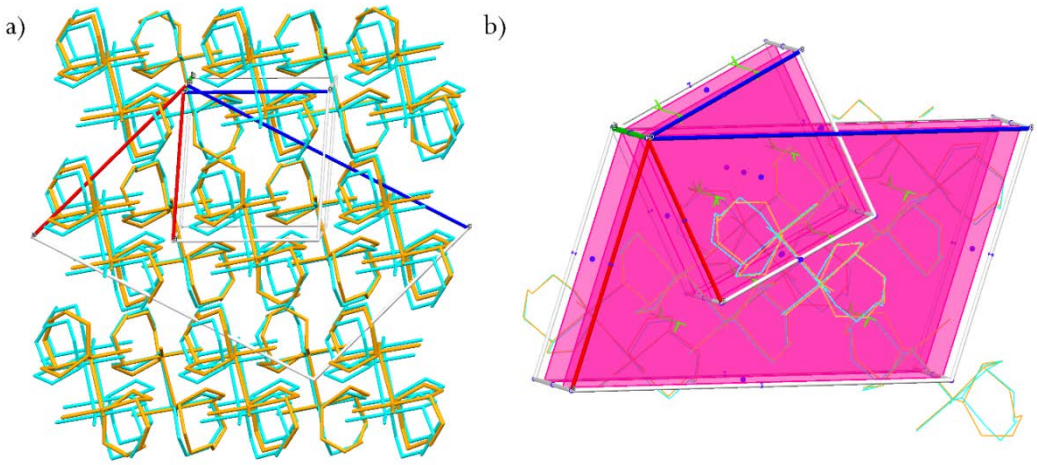



**Figure 10** Overlay images of a) the packing as viewed down the *b* axis of the β' phase and b) the symmetry elements in the β and β' phases to display the relation of one to the other. Overlap in (a) maximised for the dimer resident across the *b* axis; overlap in (b) maximised for the *b* axis; β phase in cyan and β' phase in orange; smaller cells correspond to β phase; hydrogen atoms and disorder component for dimer 'Pd3-Pd4' suppressed for clarity.

This phase transition is in marked contrast to the destructive partial β → α phase transition observed upon the application of anisotropic pressure, for example when cutting these crystals (Tidey *et al*., 2015). The absence of such a destructive transformation in this study is likely due to the isotropic application of pressure resisting the necessary expansion along certain vectors that would be required for the aligned dimeric motifs in the layered packing of β-**1** to rotate relative to one another and give rise to the herringbone packing of α-**1** (Fig. 11). Furthermore, the extensive conformational rearrangement of the macrocycle form *exodentate* to *endodentate* binding would require a large degree of freedom about the molecule that is also resisted under high isotropic pressure. Such processes would incur a far greater energy penalty at high isotropic pressures than under the pressure of cutting at otherwise ambient conditions.

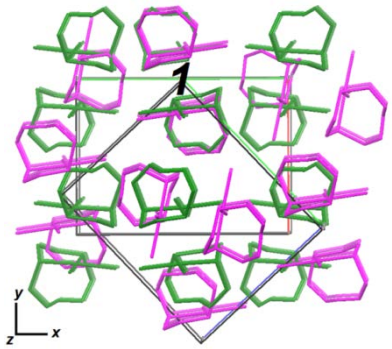



**Figure 11** Overlay of α-**1** (magenta) and β-**1** (green) at ambient pressure for maximised overlap of site 1. Note how, although resulting in a denser phase, a β → α phase transition would require significant rotation of entire dimeric motifs in a fashion as to force apart the neighbouring two dimers.

Although the symmetry of the β phase is broken and supercell peaks from the β' phase are observed at 68.7 kbar, analysis of various geometric parameters indicate that interactions within the resulting phase undergo a period of equilibration up to 71.4 kbar (*vide infra*). Above this pressure, trends in the behaviour of reliable geometric parameters became stable, for example in the intradimer Pd···Pd separation (see Section 3.5.3). We conclude that the pressure range 68.1−71.4 kbar is therefore associated with increased compressibility due to the breaking of the original packing constraints and the subsequent equilibration of interactions in the new phase.

Data quality beyond the phase transition was notably diminished with increased standard uncertainties on geometric parameters. We explored a broad range of structural models, seeking the one most compatible with both the diffraction data and the chemistry. The extensively disordered model reported, in which there is isotropic refinement of all displacement parameters, was chosen to achieve a balance between sensible intramolecular and intermolecular parameters, the

number of restraints employed and the data/parameter ratio. The discussion of the pressure dependence of the phases will therefore involve the behaviour of the form found at ambient pressure (β), which is ordered and subject to standard uncertainties of similar magnitude as the other phases, and of the high pressure form (β') for which the magnitude of the standard uncertainties place more limitations on the extent of the discussion and comparisons possible.

### 3.4.2. Description of the high-pressure phase, β'-[$PdCl_2$([9]ane$S_2O$)]

The cell parameters for this phase at 68.7 kbar are given in Table 1. Each of the three molecules found in the asymmetric unit of the β' phase is subject to whole molecule disorder as an effect of disordered partial conformational rearrangement of the macrocycle at two of the three unique sites (Fig. 12). The rearrangement does not alter the *exodentate* coordination mode - the Pd(II) centres remain bound by on $Cl_2S_2$ donor sets - but results in the macrocycle adopting an unprecedented [135] conformation in the affected molecules (Fig. 12). The supramolecular layered motif of dimers persists in the high pressure modification. Analysis of specific geometric parameters will form part of the wider discussion of the pressure-dependent behaviour below. Full details of the atom naming system employed in the CIF is given in Table 2 but discussion will be made employing the atom names used in β-**1** (Fig. 1) with reference to the specific metal centre of the molecule in question as shown in Fig. 12 (see also Table 2). In this case, dimers are formed of the molecules at Pd1 and Pd2, Pd1A and Pd2A, and Pd3 and Pd4, where molecules at Pd2A and Pd4 are subject to the conformational rearrangement.

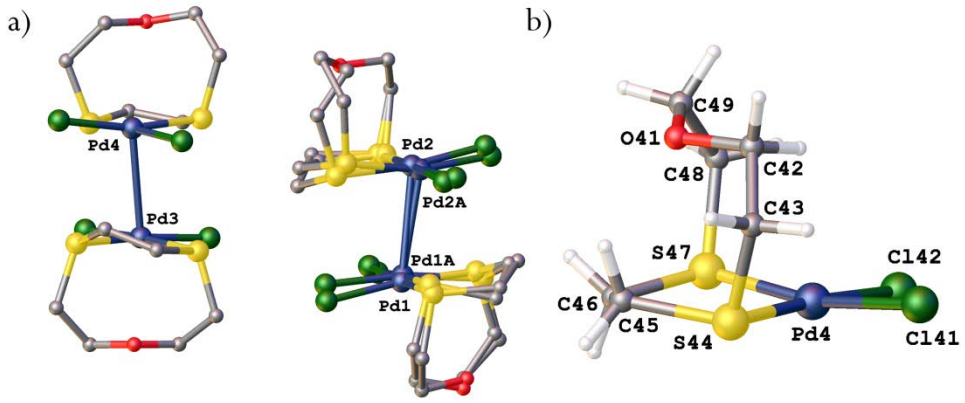



**Figure 12** a) Ball-and-stick view of the asymmetric unit of β'-**1** at 68.7 kbar. The dimer corresponding to molecules at Pd3 and Pd4 is disordered across an inversion centre approximately halfway along the Pd3···Pd4 vector and the corresponding disorder component is generated by the symmetry operation $1 - x, -y, 1 - z$ and omitted for clarity. Hydrogen atoms omitted for clarity. b) Ball-and-stick representation of the [135] conformation of the macrocycle in the Pd4 molecule in β'-**1** at 68.7 kbar.

**Table 2** Corresponding labelling system of unique sites in β'-**1** relative to that in the ambient β-**1** modification.

| *Phase* | β-**1** | β'-**1** | | | | | |
|---|---|---|---|---|---|---|---|
| *Site* | n/a | 1 | 1A | 2 | 2A | 3 | 4 |
| | Pd1 | Pd1 | Pd1A | Pd2 | Pd2A | Pd3 | Pd4 |
| | Cl1 | Cl11 | Cl13 | Cl21 | Cl23 | Cl31 | Cl41 |
| | Cl2 | Cl12 | Cl14 | Cl22 | Cl24 | Cl32 | Cl42 |
| | S4 | S14 | S14A | S24 | S24A | S34 | S44 |
| | S7 | S17 | S17A | S27 | S27A | S37 | S47 |
| | O1 | O11 | O11A | O21 | O21A | O31 | O41 |
| | C2 | C12 | C12A | C22 | C22A | C32 | C42 |
| | C3 | C13 | C13A | C23 | C23A | C33 | C43 |
| | C5 | C15 | C15A | C25 | C25A | C35 | C45 |
| | C6 | C16 | C16A | C26 | C26A | C36 | C46 |
| | C8 | C18 | C18A | C28 | C28A | C38 | C48 |
| | C9 | C19 | C19A | C29 | C29A | C39 | C49 |

### 3.4.3. Rationalisation of the β → β' transition

The application of pressure toβ-**1**results in the near-linear approach of two C−H moieties (C9−H9b···H9b_#4−C9_#4; symmetry code #4 = $1 - x, 1 - y, -z$; Fig.

13), behind each of which lies the persistent region of void space described earlier in Section 3.3.4 (Fig. 6). Raising the pressure to 68.1 kbar brings this interaction close to the sum of the relevant van der Waals radii [H9b···H9b_#4 = *ca.* 2.63 Å; $\Sigma_{vdW}$ = 2.4 Å (Bondi, 1964)], at which point the region of void behind the $CH_2$ moieties in question allows the macrocycle to rearrange so as to relieve this repulsive contact. While this separation appears clearly outside the sum of the van der Waals radii, it should be noted that the positions of the hydrogen atoms are geometrically constrained based on the geometry of the parent atom and hence their positions are not directly refined. Implicit to this is that the C−H bond length is fixed at the X-ray crystallographic standard of 0.97 Å. If the bond length was selected to be more reminiscent of those obtained from neutron studies (Schmidtmann *et al.*, 2014) then this separation would be around 0.2 Å lower and the repulsive contact more apparent.

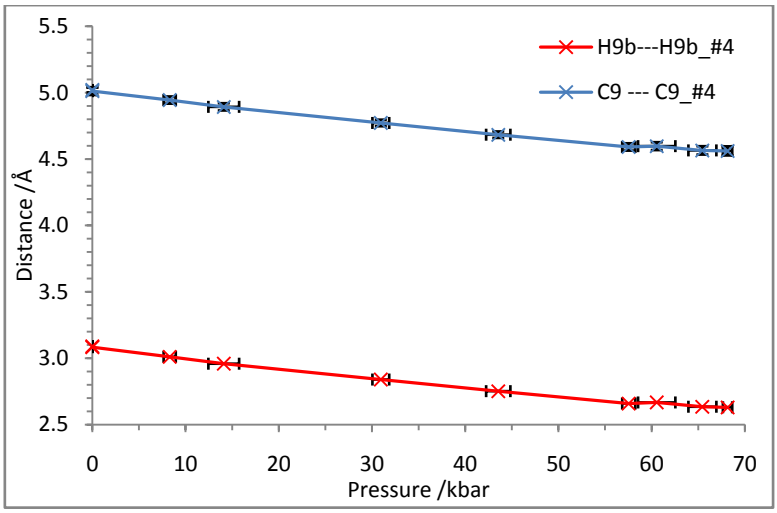



**Figure 13** The effects of pressure on the approximately linear approach of C9−H9b···H9b_#4−C9_#4 (symmetry code #4 = 1 − *x*, 1 − *y*, −*z*). C−H bond lengths are constrained at 0.97 Å.

As pressure is applied to β-**1**, two relevant sets of close contacts are formed which also have implications for this transformation. Up to the phase transition, close S···Cl contacts are formed between the bases of molecules within dimers, as too are contacts between H6a and the two chloride donors of the paired molecule (Fig. 14). The rearrangement serves to alleviate one of the S···Cl contacts by lifting the affected sulfur donor from the plane, alongside a simultaneous flattening of the S4−C6−C6−S7 torsion angle. This in turn relieves the close contact between H6a and the chloride donors of the neighbouring molecule. While these two interactions are not presented as primary drivers of the phase transition, their effects on the macrocycle would assist conformational rearrangement.

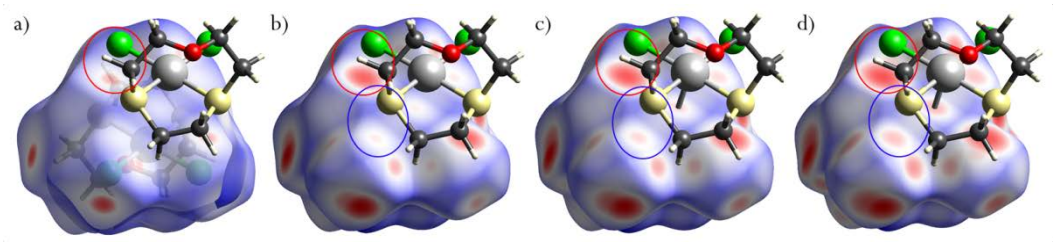



**Figure 14** Hirshfeld surfaces for β-**1** at a) ambient pressure, b) 30.9 kbar, c) 43.5 kbar and d) 65.4 kbar showing the effect of pressure on intradimer intermolecular contacts at the base of the molecule. Note the swift development of red spots at one pair of Cl and S donors (Cl2 and S4; circled in red, symmetry equivalent contacts not circled) compared to the other pair (Cl1 and S7; circled in blue, symmetry equivalent contacts not circled).

Additionally, the rearrangement results in more efficient space filling as the $CH_2$ moiety at C9 moves to fill the previously inaccessible void space. This brings a discontinuity in compression across the phase transition which serves to decrease the *PV* term in the energy of the system: a stepwise compression in *V*/Z of 0.53 $Å^3$ at 68.5 kbar corresponds to a total decrease in energy of 2.2 kJ $mol^{-1}$. This value is comparatively small with regards to the calculated increase in energy associated to

the conformational changes observed (*vide infra*) and the energies released in phase transitions attributed to energy lowering of this sort (Satthaphut *et al*., 2014; see also chapter 5). Consequently, it is likely the main driving force of the rearrangement is the relief of the repulsive H···H contact described earlier and that the decrease in the *PV* term is incidental.

### 3.5. Pressure dependence of the coordination sphere

Given the strength and rigidity of the bonding interactions present in the organic solid state, the "application of pressure is usually expected to only significantly affect torsion angles and intermolecular interactions" (Fabbiani *et al.*, 2007; Moggach *et al*., 2008 and references within). In contrast, metal-ligand interactions and coordination geometries are weaker and more susceptible to pressure (Tidey *et al.*, 2014 and references within). Within this class of softer interactions there are further subdivisions and many metal-ligand combinations have bimodal (or higher) distributions of bond lengths. These different regions also respond differently to pressure. Predictably, the shorter, stronger interactions are typically less affected and the results of this study provide no exception, with equatorial *M*−*L* bonds contracting by an order of magnitude less than the longer, softer apical interactions.

#### 3.5.1. α-[$PdCl_2$([9]ane$S_2O$)]

A pressure of 103.4 kbar leads to relatively uniform compression of the equatorial donor set of *ca.* 0.02 Å (Fig. S6; shown also in Fig. 45). The apical Pd···O interaction undergoes significantly greater compression across this pressure range

and contracts approximately linearly by 0.217(5) Å, reaching a final length of 2.741(3) Å at 103.4 kbar (Fig. 15). The compression observed in the intradimer Pd···Pd interaction is greater still, with a smooth contraction of 0.6447(19) Å resulting in a final Pd···Pd separation of 3.1456(16) Å (Fig. 15); by *ca*. 66 kbar the separation has fallen below the sum of the van der Waals radii [$\Sigma_{vdW}$ = 3.26 Å (Bondi, 1964)]. Throughout this contraction, the general arrangement of the dimer remains stable and the centroid-centroid slippage of the two least squares planes defined by the $Cl_2S_2$ donor sets is relatively unchanged at *ca.* 1.19 Å under hydrostatic conditions (Fig. S8).

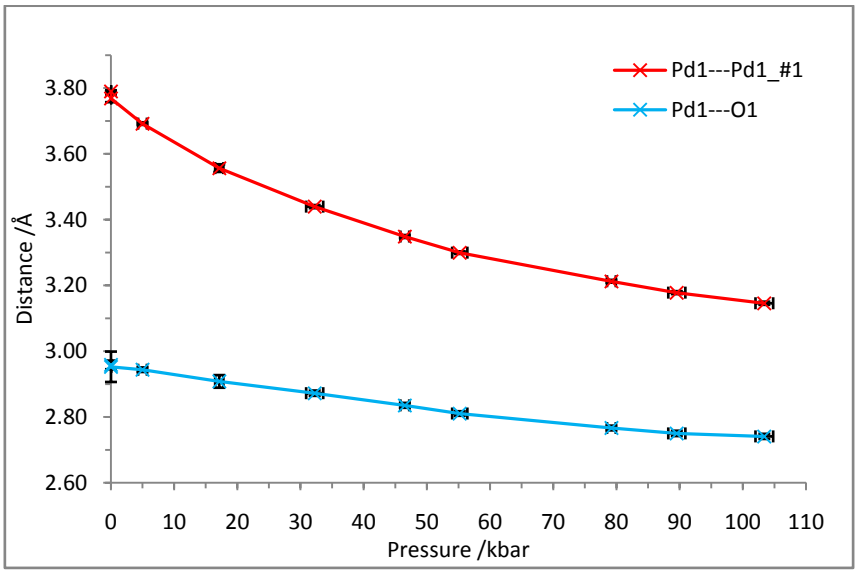



**Figure 15** Compression of axial parameters as a function of pressure. Symmetry code #1 = −*x*, 2 − *y*, −*z*.

Concomitant with these contractions is an approximately symmetrical distortion of the coordination plane whereby the *trans* coordination angles move further from 180 ° (Fig. 16); the Pd(II) centre moves steadily out of the $Cl_2S_2$ plane and away from the incoming O donor [by 0.0528(13) Å at 103.4 kbar] while the RMS

deviation of the defining atoms from the plane remains stable at *ca.* 0.125Å (Fig. 17).

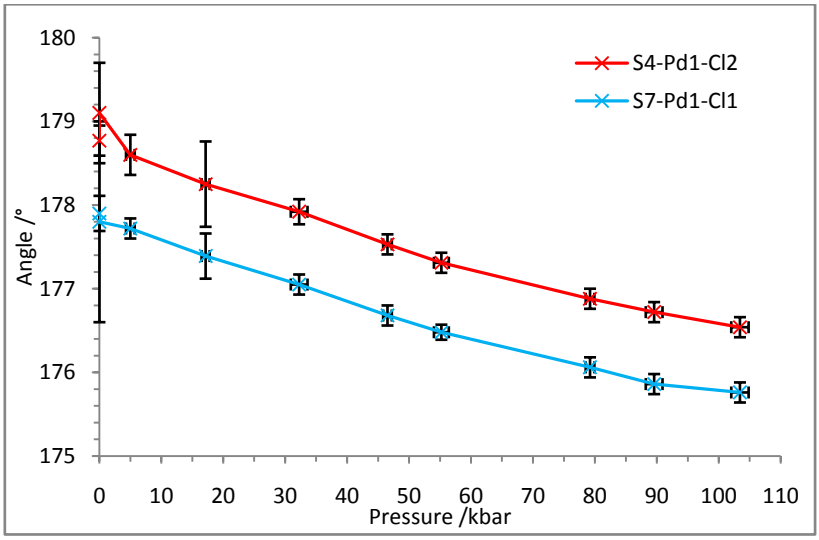



**Figure 16** The effects of pressure on the *trans*-coordination angles in α-**1**.

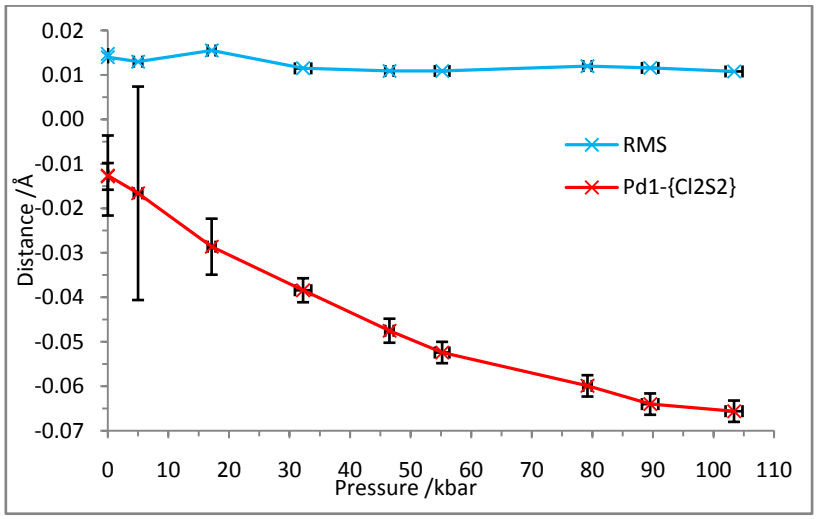



**Figure 17** The effects of pressure on the deviation of the Pd(II) centre from the least squares mean plane defined by the $Cl_2S_2$ donor set in α-**1**.

It is likely that there are two main factors that contribute to the deformation of the equatorial plane. The first is simply that sulfur and chloride donors have larger van der Waals radii than the Pd(II) centres and so enter a repulsive regime with each

other at a greater distance than the metal centres (Fig.18). Secondly, the Pd···O interaction is more resistant to compression than the corresponding Pd···Pd interaction. Consequently, as the base of the two molecules within the dimer are brought together, the $Cl_2S_2$ donor sets resist the compression while the O donors exert an additional force on the Pd···Pd interaction, resulting in its observed deviation from the mean square plane defined by the donor atoms.

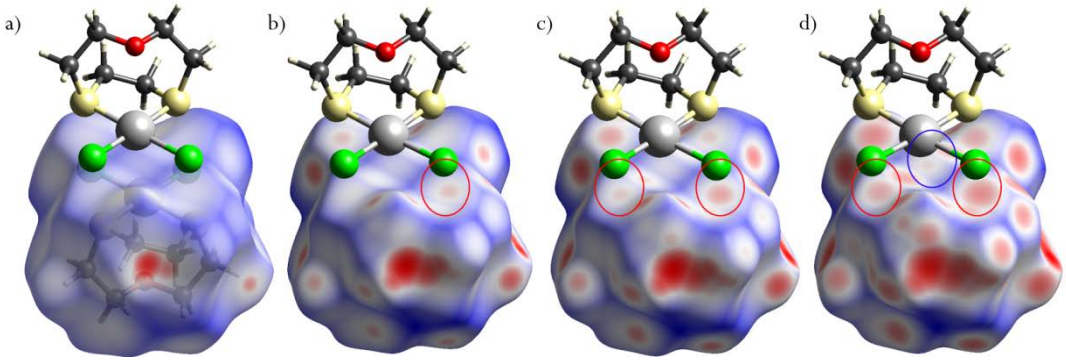



**Figure 18** Hirshfeld surfaces for α-**1** showing the base of the molecule within the dimer at a) ambient pressure, b) 32.2 kbar, c) 46.5 kbar and d) 79.2 kbar. Note the generation of red spots between the Cl and S donors (circled in red; symmetry equivalents not circled) from much lower pressures than between Pd(II) centres (circled in blue).

### 3.5.2. β-[$PdCl_2$([9]ane$S_2$O)]

The application of pressures of up to 68.1 kbar brings about slightly greater compression of the equatorial donor set in β-**1**than that seen across the entire pressure range of 103.4 kbar inα-**1**. Nevertheless, this compression is still very small and the average reductions in Pd−S and Pd−Cl distances are only 0.035(2) and 0.019(2) Å, respectively (Fig. S13).

As seen for the α phase, the length of the Pd···Pd interaction in the β-**1** form is significantly affected by pressure and by 68.1 kbar has fallen by 0.4185(11) Å to 3.0752(9) Å. In contrast to α-**1**, by *ca.* 25 kbar the Pd···Pd distance has fallen

below the sum of the van der Waals radii [$\Sigma_{vdW}$ = 3.26 Å (Bondi, 1964)] and by *ca*. 50 kbar has already reached the minimum distance observed for α-**1** at 103.4 kbar (Fig. 19, *cf*. Fig. 15).

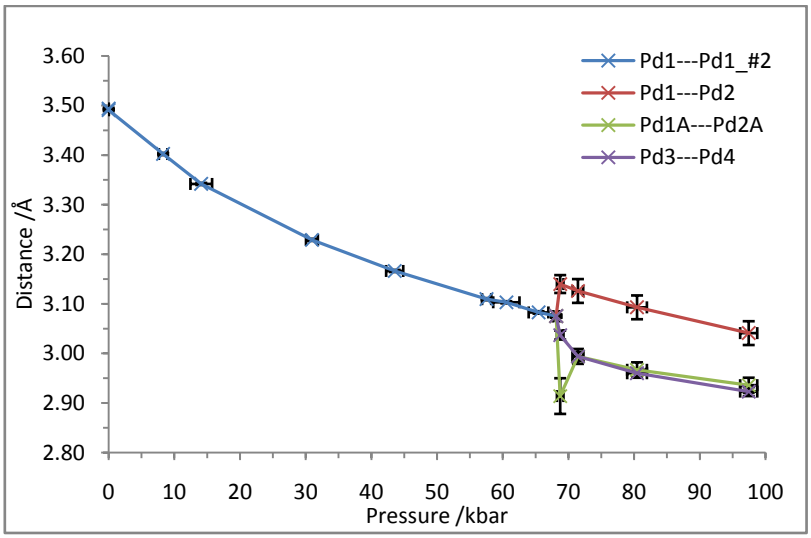



**Figure 19** The effects of pressure on the Pd···Pd interactions in the β and β' phases. Symmetry code #2 = −*x*, 1 − *y*, −*z* in β-**1**.

The most prominent effect of pressure on the coordination plane of the molecule is the deviation of the *trans* S7−Pd−Cl1 angle from 180 ° (Fig. 20), the result of Cl1 moving out of the plane away from approach of the other molecule in the dimeric motif. Of the *cis* angles, those involving Cl1 are the most deformed by pressure (Fig. 21).

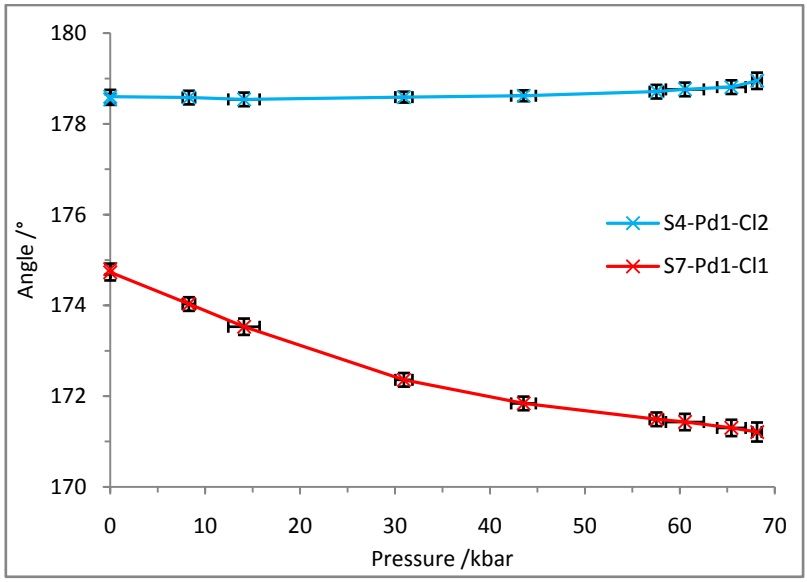



**Figure 20** The effects of pressure on the *trans* coordination angles in β-**1**.

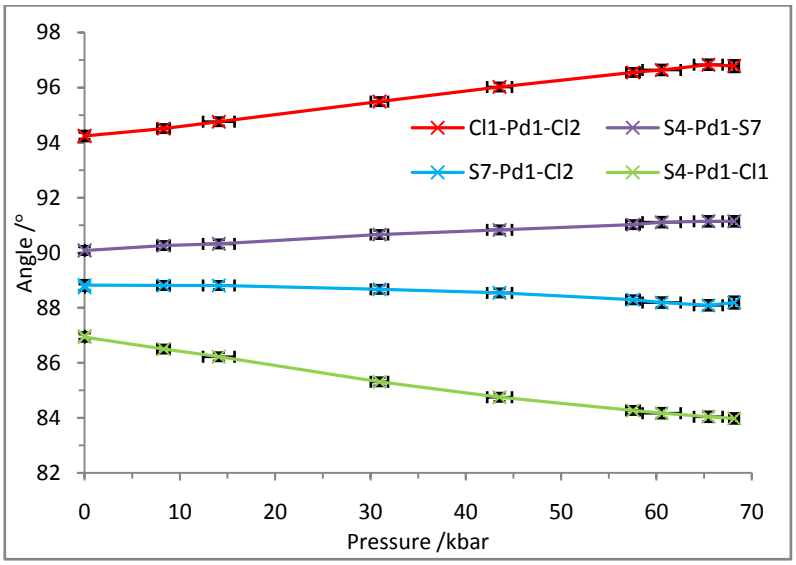



**Figure 21** The effects of pressure on the *cis* coordination angles in β-**1**.

It is likely that this behaviour is the result of two repulsive contacts that exert a force from below the Cl1 donor in the direction of a region of void space above. The greater of these forces is likely to involve the corresponding S7 donor of the molecule with which the dimer is formed. Analysis of the Hirshfeld surfaces shows a steady increase of repulsive S4···Cl2_#2 (symmetry code #2 = $-x$, $1-y$, $-z$) and

symmetry-equivalent contacts, shown as red spots (Fig. 14). These contacts are rapidly compressed with pressure yet no such contacts are observed between the deviated Cl1 and S7_#2 or the symmetry-equivalent contact below 43.5 kbar. After this point, which also coincides with a decrease in the rate of change in S7−Pd1−Cl1, red spots begin to show, signifying the onset of significant close contacts. Complimentary to this, the earlier described region of persistent void space is found to be located above the deviated Cl1 donor. It is likely that repulsion between S7_#2 and Cl1 is the driving force for the deformation of S7−Pd1−Cl1, while the void allows the movement of Cl1, which also explains the absence of features on the Hirshfeld surface corresponding to the contact of these atoms. Furthermore, the corresponding molecule of the dimer pair affords a C−H moiety directed between the two chloride donors. This readily forms close contacts with both chloride donors and contributes a complimentary force in the direction up, out of the plane. These close contacts can be seen as red spots of increasing size on the Hirshfeld surfaces (Fig. 14).

To discuss the behaviour of the Pd(II) centre with regards to the coordination plane it is important to first consider the behaviour of the donor atoms and define the plane accordingly. As discussed above, Cl1 deviates from the plane of the molecule and the mean plane is, therefore, defined by the donors Cl2, S4 and S7. It can be seen that there is almost no movement of the metal centre with respect to this plane in the low pressure modification (Fig. 22). This behaviour also supports our earlier contention that the incoming O donor gives rise to the deviation of the Pd(II) centre from the plane in α-**1**.

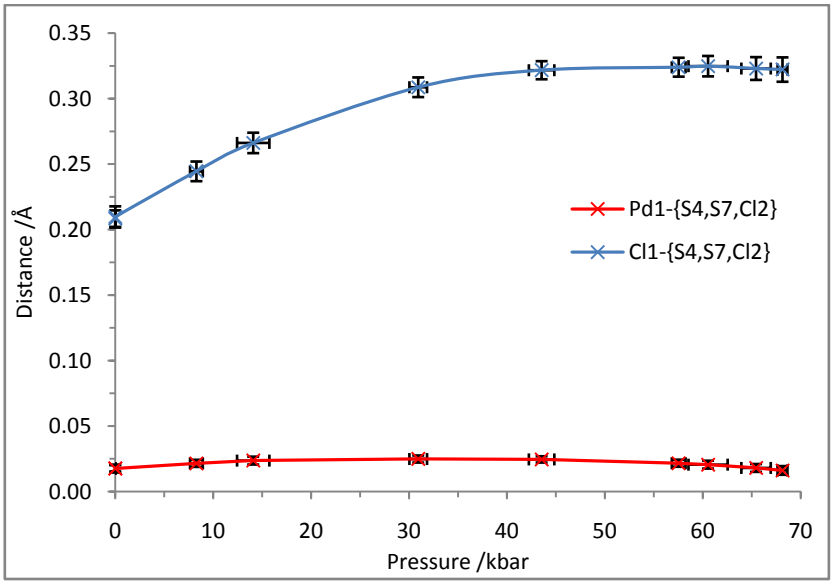



**Figure 22** The effects of pressure on the position of Pd1 and Cl1 with regards to the plane defined by S4, S7 and Cl2.

### 3.5.3. β'-[$PdCl_2$([9]ane$S_2O$)]

Beyond the phase transition, the extensive disorder and generally limited quality of the data for this phase cause trends for β'-**1** to become obscured by the magnitude of uncertainties associated with the derived geometric parameters (Figs. S13-S31). Furthermore, owing to the extensive disorder in the system, Hirshfeld surface analysis is also no longer viable. As a consequence of this, few firm conclusions can be drawn regarding the compression and deformation of the coordination plane across the study of the phase itself, though some conclusions can still be drawn in relation to β-**1**. For ease of discussion, this will be made employing the atom names used in β-**1** with reference to the specific metal centre of the molecule in question, as described in Section 3.4.2 and Fig. 12.

The most notable effect of the conformational rearrangement is to distort the coordination plane of the affected molecule (*i.e.*, those at Pd2A and Pd4), lifting S7 up and away from the paired molecule of the dimer (Figs. 23, S23, S25). This in

turn results in a flattening of the S4−C5−C6−S7 unit towards a torsion angle of zero (Figs. S40, S42), rotating H6a so that it points less directly at the chloride donors. The effect of these modifications on the paired molecules (*i.e.*, those at Pd1A and Pd3) is that the S···Cl and C−H···S repulsive forces previously implicated in the bending of Cl1−Pd1−S7 in β-**1** are now relieved (Figs. 23, S21, S24). This relief could also be an effect of the rearrangement filling the void above the deviated Cl and so introducing an opposing force to the repulsion between the two donor atoms.

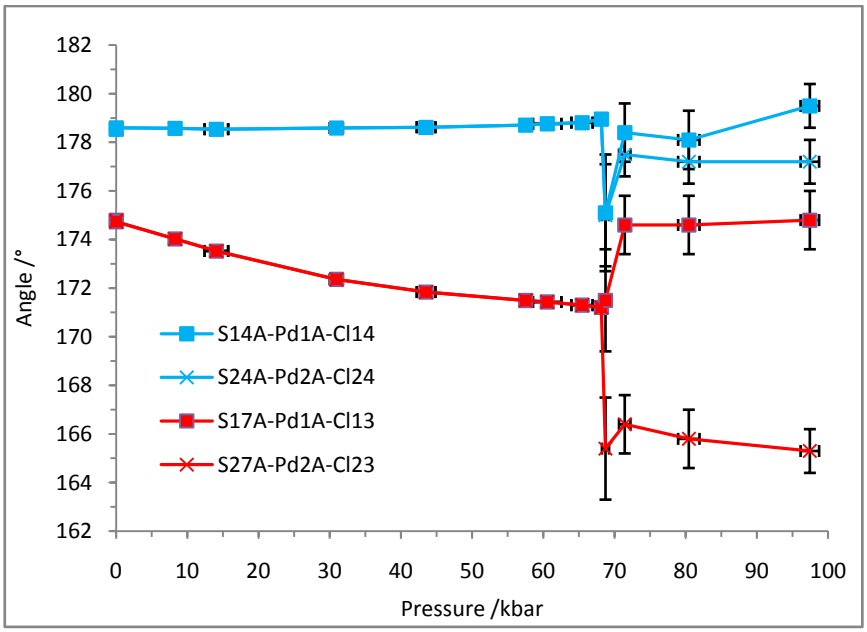



**Figure 23** The effects of pressure and the β → β' phase transition on the *trans* coordination angles for the Pd1A···Pd2A dimer wherein the macrocycle bound to Pd2A has undergone conformational rearrangement.

The phase transition produces three unique Pd···Pd combinations (Fig. 19), all of which behave slightly differently over the proceeding *ca.* 3 kbar before all three continue to compress by *ca.* 0.7 Å up to 97.4 kbar. The interaction designated Pd1···Pd2 corresponds to the only dimer in which neither molecule undergoes conformational rearrangement. In this case, a discontinuous expansion of 0.065(6)

Å is observed in the Pd···Pd separation between 68.1 and 68.7 kbar before compression continues in a manner similar to that of before the phase transition. In contrast, the remaining two dimers, each of which contains one molecule subject to the conformational change, undergo stepwise compression of this interaction. This divergence in the various Pd···Pd distances is primarily due to molecules in the dimeric motif slipping relative to one another rather than a change in the intradimer separation. The two dimers in which conformational rearrangement is observed undergo a significant decrease in the centroid-centroid slippage of their $Cl_2S_2Pd$ least squares planes, while in the remaining dimer a significant increase is seen (Fig. 24). The most probable cause for this decrease in the slippage is in the displacement of one of the sulfur donors from the equatorial plane, brought by the conformational rearrangement. This decreases the S···Cl repulsion at one corner of the dimer, allowing the molecules to tilt and so relieve the Cl···S interaction in the opposing corner. For the dimer to then maintain occupation of a similar region of space, slipping of the molecules relative to one another would be required. While there is no immediately apparent cause for the increase in slippage for the remaining dimer, it seems reasonable to suggest that this occurs as a response to the change in contacts surrounding it owed to the rearrangement of neighbouring molecules. Alternatively, DFT data discussed later in Section 3.8 of this chapter and in Section 3.8 of Chapter 4 indicates that this may instead come about as an integral part of the phase transition, not only reducing the repulsion of S···Cl contacts but also between the Pd(II) centres.

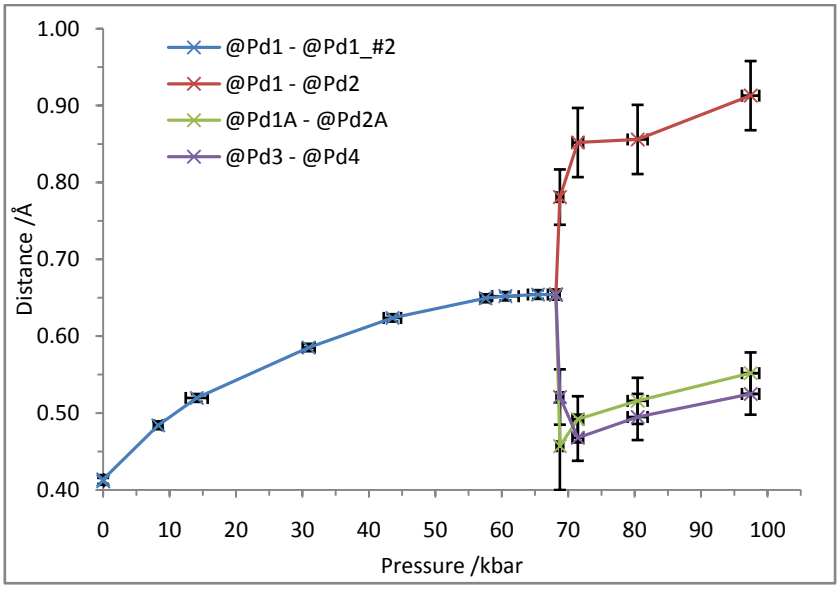



**Figure 24** The effects of pressure on the centroid-centroid slippage distances for the $Cl_2S_2Pd$ least squares planes within dimers in β-**1** (blue) and β'-**1** (red, green, purple).

Notably, with the exception of the behaviour across the phase transition, the slippage of the planes increases steadily with pressure. This slippage direction is coincident with the S7−Pd−Cl1 bond vector, and it is reasonable to suggest that it alleviates the increasing repulsion between S4 and Cl2_#2 (symmetry code #2 = $-x$, $1-y$, $-z$) and in the symmetry-equivalent contact as the pressure is raised.

### 3.5.4. γ-[$PdCl_2$([9]ane$S_2O$)]

The effect of pressure on the coordination bonds of γ-**1** closely matches that observed for the preceding ambient phases (Fig. S32, *cf.* figs. S6 & S13). The decreases in the equatorial Pd−Cl distances are linear across the pressure range, and by 98.6 kbar these have reached 0.033(2) and 0.028(2) Å for Pd1−Cl1 and Pd−Cl2, respectively. There is a slightly greater variation in the degree of compression for the Pd−S bonds [0.024(3) and 0.050(2) Å for Pd1−S4 and

Pd1−S7, respectively], linked to the formation of an intermolecular S···Cl contact involving S7 which can be seen as a red spot on the Hirshfeld surface (Fig. 25).

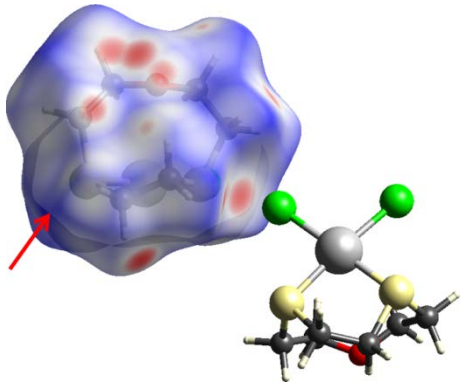


**Figure 25** Image showing the close intermolecular contact between S7 and Cl1_#5 (symmetry code #5 = 0.5 + *x*, 0.5 − *y*, −0.5 + *z*), shown at 19.1 kbar. Note also the protruding blue region at the other sulfur (arrowed), indicating the lack of similarly close contacts.

The intermolecular Pd···O interaction in γ-**1** is highly compressible across the full pressure range studied and contracts by 0.382(9) Å to a value of 2.831(8) Å at 98.6 kbar. The length of the Pd···O interaction crosses the sum of the relevant van der Waals radii [$\Sigma_{vdW}$ = 3.15 Å (Bondi, 1964)] at *ca.* 8 kbar but there is no significant indication that this behaviour is anything but gradual and continuous (Fig. 26).

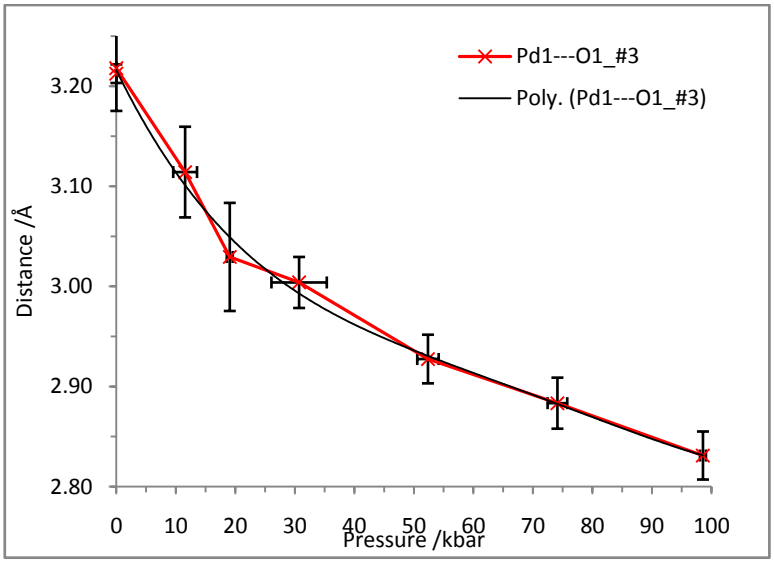



**Figure 26** The effects of pressure on the intermolecular, chain-forming Pd···O interaction between Pd1 and O1_#3 (symmetry code #3 = 0.5 − *x*, −0.5 + *y*, 1.5 − *z*).Note the good fit within the uncertainties of the polynomial fit; the inflection at *ca*. 20 kbar is attributed to the magnitude of the uncertainties in the measurements relating to it and the neighbouring two points.

The effect on the geometry of the coordination plane also mirrors that seen in the β phase, with a bending of the *trans* S4−Pd1−Cl2 angle away from linearity by 4.16(18) ° and the remaining *trans* coordination angle, S7−Pd1−Cl1, bending towards linearity, settling at *ca.* 179 ° by 20 kbar (Fig. 27). The bending of S4−Pd1−Cl2 is again traceable to the deviation of the chloride donor (Cl2) from the coordination plane and the only *cis* angles notably affected by pressure are those involving Cl2 (Fig 28).

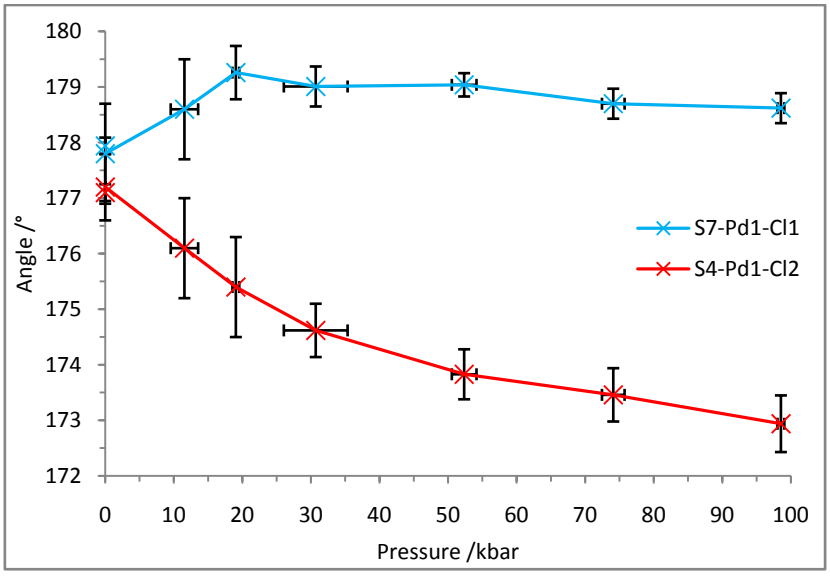



**Figure 27** The effects of pressure on the *trans* coordination angles of γ-**1**.

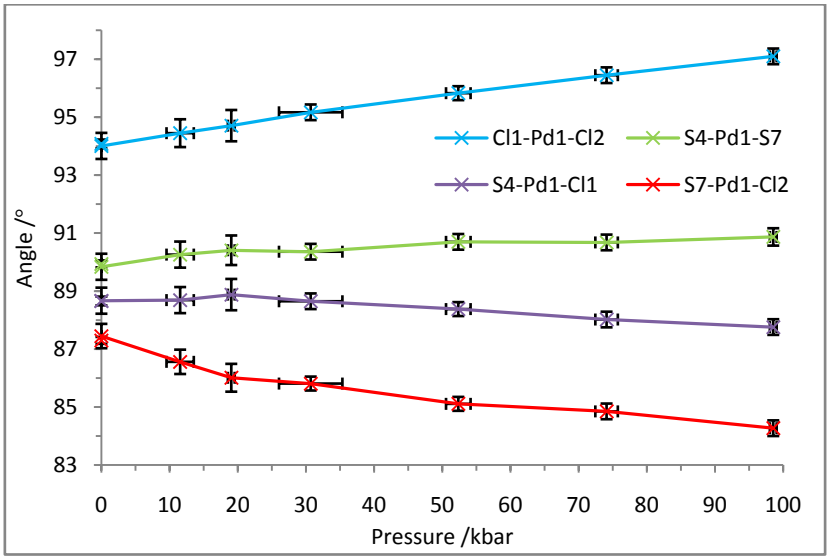



**Figure 28** The effects of pressure on the *cis* coordination angles of γ-**1**.

There appears to be no single identifiable interaction that brings about this deformation. Instead, a number of C−H···Cl contacts exert a net force all around Cl2, with the exception of a small region where even at 98.6 kbar no close contacts are observed (Fig. 29). The effect of this is that Cl2 is displaced slightly towards this region, resulting in the bending of S4−Pd1−Cl2 away from linearity and

concomitant narrowing of S7−Pd1−Cl2 and widening of Cl1−Pd1−Cl2. In contrast, Cl1 is almost entirely encircled by void space at lower pressures and therefore no anisotropic effects influence the bond angles involving this atom.

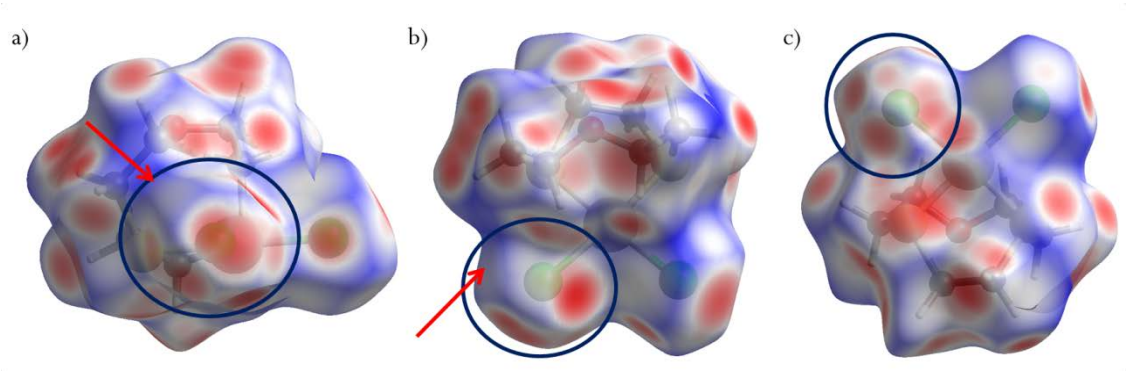



**Figure 29** Hirshfeld surface of γ-**1** at 98.6 kbar viewed along the vector of the Pd1−Cl2 bond (a), and from above (b) and below (c) the molecule. Regions associated with Cl2 are circled in blue; note the blue protrusion (arrowed in red) on the surface.

Similar to the situation in α-**1** where compression of the intramolecular Pd···O distance appears to displace the metal centre in the opposite direction and out of the coordination plane, the intermolecular approach of the oxygen to the metal centre in γ-**1** appears also to repel the Pd(II) centre. At ambient pressure the Pd(II) centre resides slightly out of the mean plane defined by S4, S7 and Cl1 in the direction of the O donor [Pd···plane = −0.0306(10) Å]; by 20 kbar it lies almost exactly in the plane where it remains for the rest of the study (Fig. 30). In contrast, Cl2 is deviated from an approximately similar displacement at ambient pressure to *ca.* 0.20 Å by 50 kbar where it resides for the remainder of the experiment. This trend appears to be interrelated with the deformation of the *trans* bond angle S7−Pd1−Cl1.

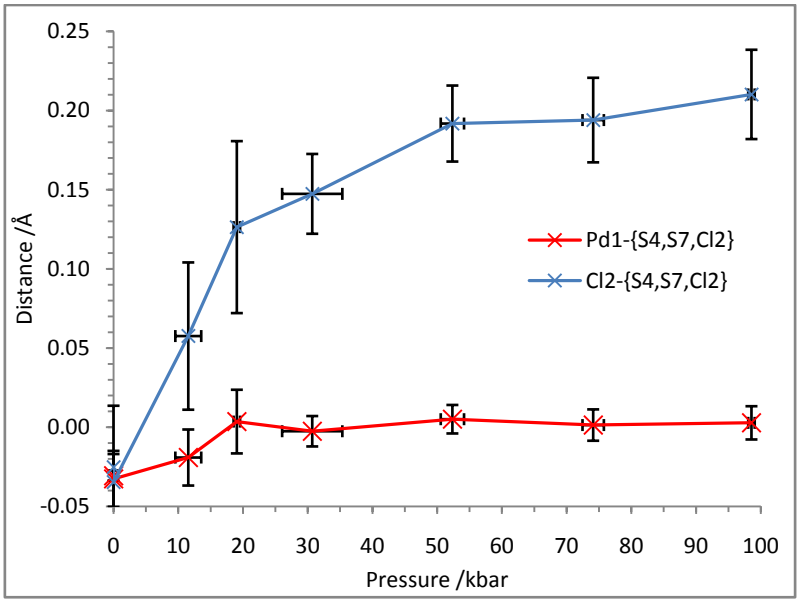



**Figure 30** The effects of pressure on the positions of Pd1 and Cl2 in γ-**1** with respect to the mean plane defined by Cl1, S4 and S7.

### 3.6. Pressure dependence of the macrocyclic conformation

Throughout this study there are no notable changes to the conformation of the macrocycles in α-**1** and γ-**1** (Fig. S36 and S43, respectively). As discussed in Section 3.4.3 above, this is not the case for β-**1** (Fig. S37-S42): after the phase transition the resulting β' phase exhibits a disordered conformational arrangement involving a previously unseen [135] conformation for two of the three macrocyclic rings (Fig. 31, S40, S42).

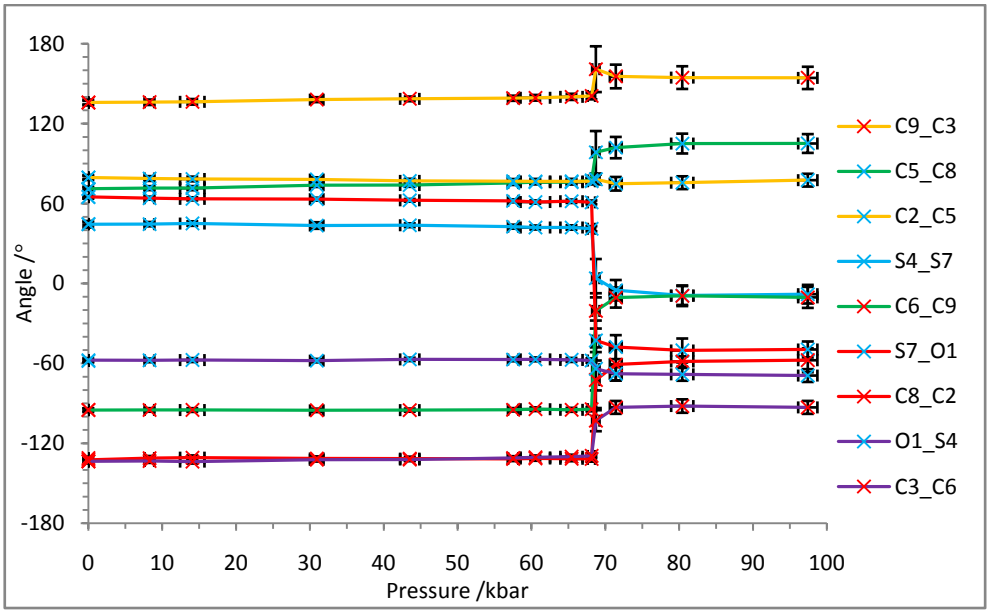



**Figure 31** The effects of pressure on the torsional angles for the macrocycle bound to Pd4 in β'-**1** (>68.4 kbar) and to Pd1 in β-**1** (<68.4 kbar).

### 3.7. Temperature-dependent studies

Variable-temperature single-crystal X-ray diffraction studies were carried out in the ranges 90−390 K, 90−470 K, and 99−488 K for the α, β and γ phases, respectively. For α-**1**, collections were made at 50 K intervals upon heating from 290 K to 390 K and then with cooling to 90 K. For β-**1** and γ-**1**, collections were made by first cooling from 290 K to the minimum at 10 and 50 K intervals, respectively. The temperature was then ramped back to 290 K and collections made at increments of 20 K for β-**1** and ca. 50 K for γ-**1**, up to the maximum temperatures. In the case of β-**1** and γ-**1**, *ca.* 1 % discrepancy is observed when comparing the cell volume at 290 K as synthesised with those later collected after the cooling cycle (Fig. 32). Similar artefacts were observed in data collected on a related set of phases, where recollection at a higher ramp-rate gave no such artefacts. This would indicate that these are associated to an insufficient ramp rate,

corroborated by the slight stepping in the unit cell volume of β-**1** upon cooling also indicating a problem with the instrument.

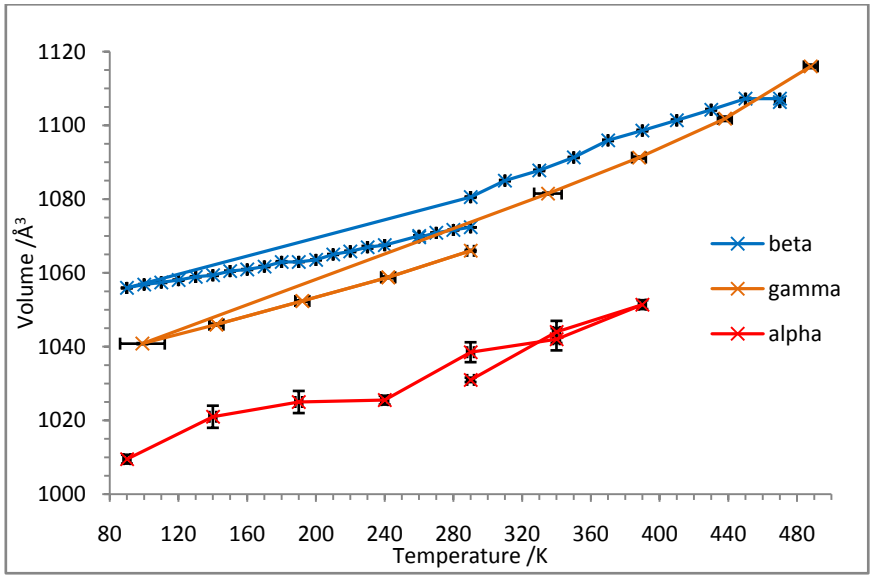



**Figure 32** The effects of temperature on the cell volume for the three phases of **1**.

The temperature dependence of the unit cell volume of the three phases is given in Figure 32. Smooth positive thermal expansion was observed in all phases, with no indication of any thermally induced phenomena. In each of the graphs in this section, the lines track the progress of the experiments, each starting at 290 K.

### 3.7.1. α-[$PdCl_2$([9]ane$S_2O$)]

The length of the apical Pd1···O1 interaction varies linearly by a total of 0.022(3) Å over the temperature range 90−390 K (Fig. 33). The total effect of temperature between 90 and 390 K on the separation of Pd1···Pd1_#1 (symmetry code #1 = $-x$, $2-y$, $-z$) is found to be 0.131(10) Å. The effect of cooling from 290 to 90 K was equivalent to c*a.* 5 kbar pressure with a contraction of 0.012(2) and 0.0768(8) Å observed in Pd1···O1 and Pd1···Pd1_#1, respectively.

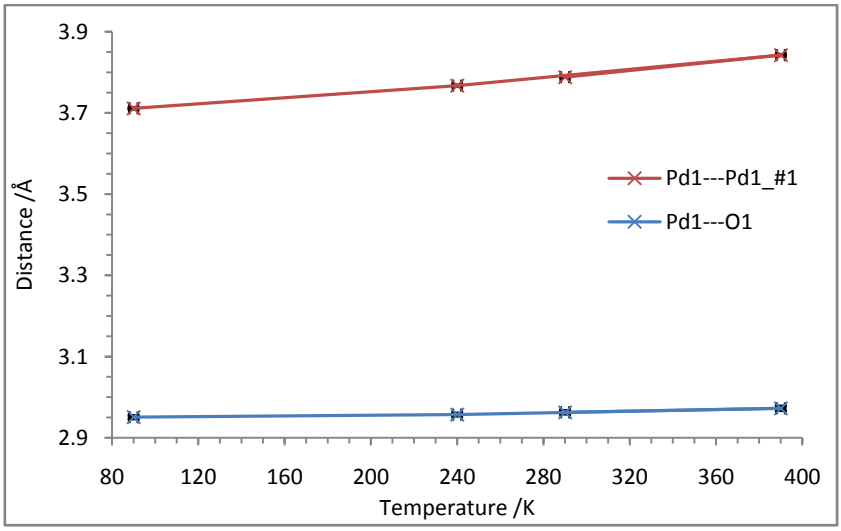



**Figure 33** The effects of temperature on the apical interactions to Pd1 in α-**1**. Symmetry code #1 = −*x*, 2 − *y*, −*z*.

Temperature variations exert negligible effects on the other intramolecular parameters (Fig. S44-S47). For example, the deviation of Pd1 from the $Cl_2S_2$ least squares mean plane is statistically insignificant over the entire temperature range (90−390 K), moving by only 0.0013(5) Å.

### 3.7.2. β-[$PdCl_2$([9]ane$S_2O$)]

Similarly to α-**1**, variation of the temperature from 90 to 470 K has little effect on the main structural parameters in β-**1**. Between 90 and 470 K the intradimer Pd1···Pd1_#2 (symmetry code #2 = −*x*, 1 − *y*, −*z*) separation varies linearly by a total of 0.1055(9) Å (Fig. 34). Cooling from 290 to 90 K gives a contraction of 0.0435(6) Å [*cf.* 0.0481(6) Å expansion upon heating back to 290 K], equivalent to the compression associated with *ca.* 4 kbar pressure.

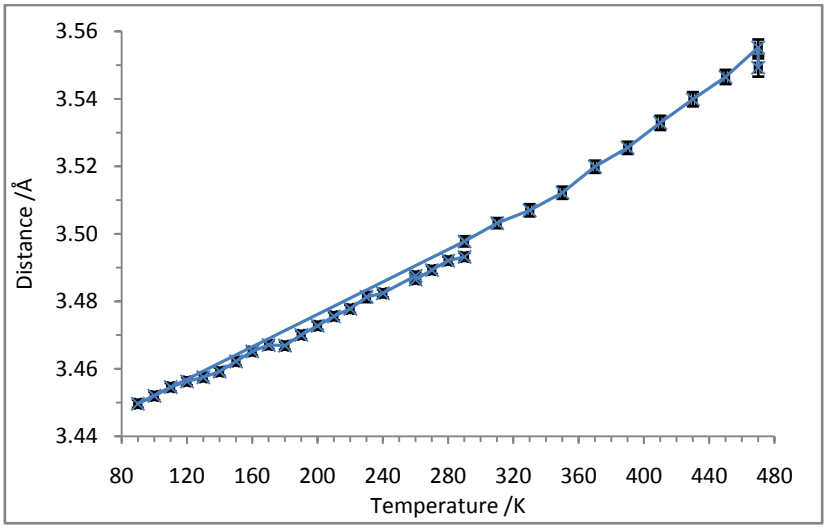



**Figure 34** The effects of temperature on the intradimer Pd1···Pd1_#2 separation in β-**1** (symmetry code #2 = −*x*, 1 − *y*, −*z*).

The Pd−S bond lengths are unchanged within the precision of the experiment. The more apparent changes in the Pd−Cl bond lengths (Fig. 35) are attributed to their greater vibrational freedom as terminal atoms, evidenced in their anisotropic displacement parameters. The contractions are consequently artefacts of the experiment and librational correction (Hirshfeld, 1976; Spek, 2009) calculates the Pd−Cl bonds as instead increasing by 0.006 Å from 90 to 470 K.

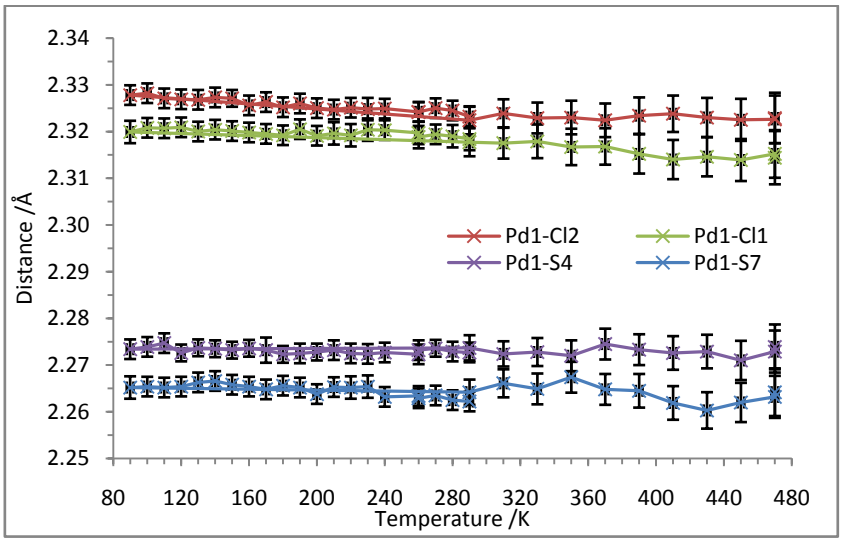



**Figure 35** The effects of temperature on the coordination bond lengths in β-**1**.

The bending of the *trans* S7−Pd1−Cl1 angle appears to be relaxed by increased temperature (Fig. 36), an observation which can be rationalised by the same argument as for its pressure-dependent behaviour and is again reflected in the behaviour of *cis* S4−Pd1−Cl1 (Fig. 37). In this regard, an increase in temperature can be considered as having a similar effect as might 'low pressure'.

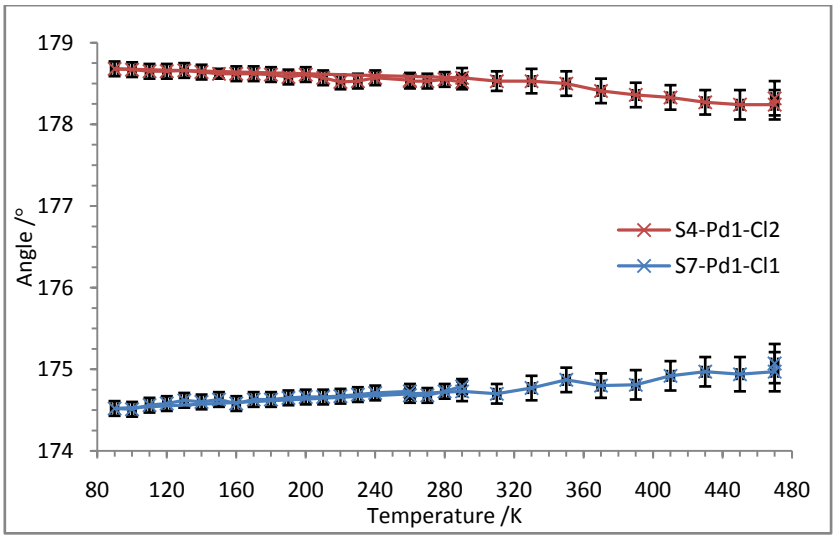



**Figure 36** The effects of temperature on the *trans* coordination bond angles in β-**1**.

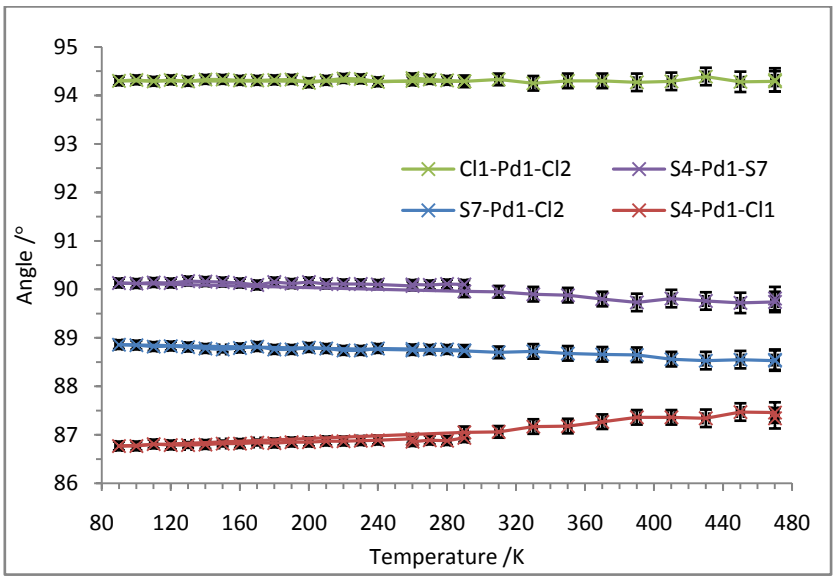



**Figure 37** The effects of temperature on the *cis* coordination bond angles in β-**1**.

### 3.7.3. γ-[$PdCl_2$([9]ane$S_2O$)]

Between 99 and 488 K the intermolecular chain-forming interaction Pd1···O1_#3 (symmetry code #3 = 0.5 − *x*, −0.5 + *y*, 1.5 − *z*) varies linearly by a total of 0.067(5) Å (Fig. 38). Cooling from 290 to 99 K results in a contraction of 0.035(5) Å, corresponding to the effects of *ca*. 4 kbar. The effect of temperature of the Pd−Cl and Pd−S bond lengths was similar to that of β-**1** (Fig. 39).

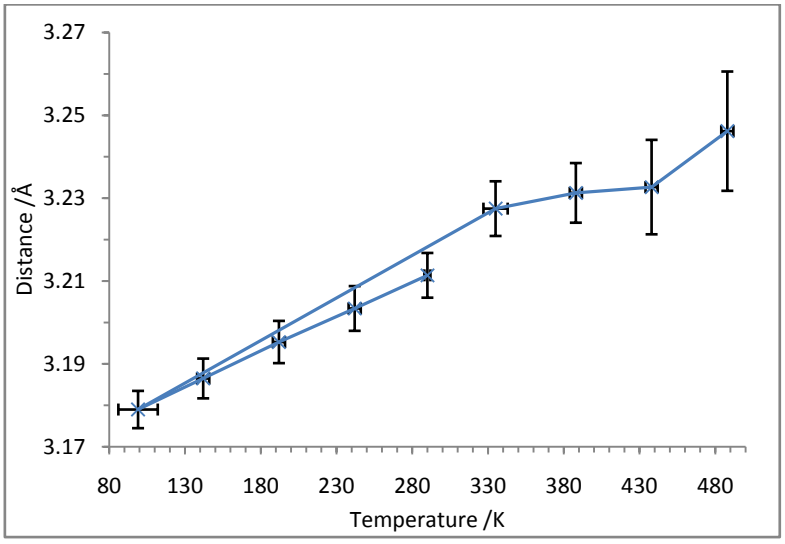



**Figure 38** The effects of temperature on the intermolecular chain-forming interaction Pd1···O1_#3 (symmetry code #3 = 0.5 − *x*, −0.5 + *y*, 1.5 − *z*) in γ-**1**.

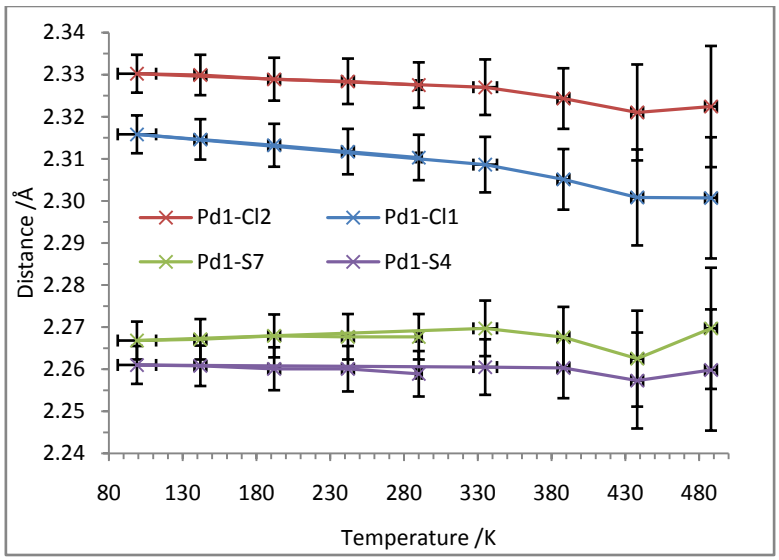



**Figure 39** The effects of temperature on the coordination bonds in γ-**1**.

Variation of the temperature has little effect on the relative positions of Pd1, Cl1, S4 and S7 (Fig. 40). In contrast, geometric parameters involving Cl2 all deviate in complimentary manners towards 90 °. This appears to come about *via* increased temperature decreasing the packing density, so reducing the contacts described in Section 3.5.4 that cause the atom to reside out of an idealised position. This is most apparent in the *trans* coordination angles (Fig. 41).

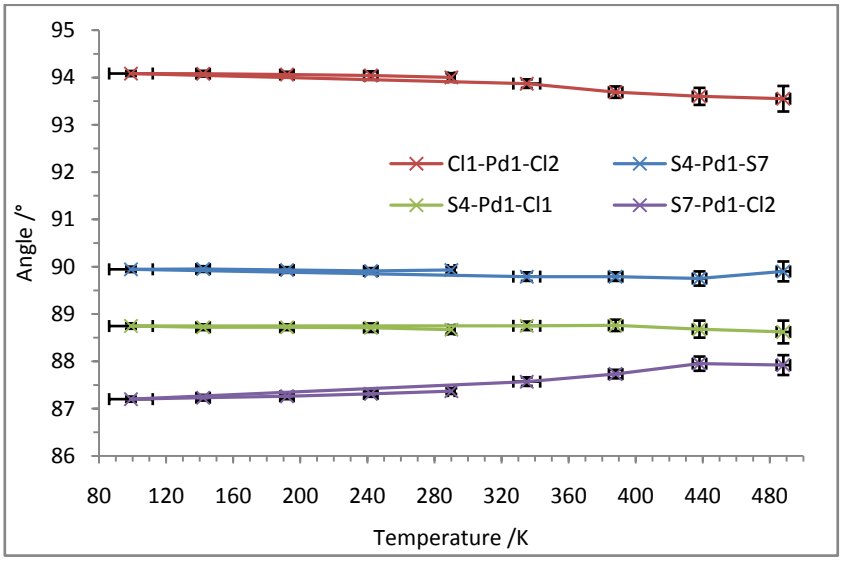



**Figure 40** The effects of temperature on the *cis* coordination angles in γ-**1**.

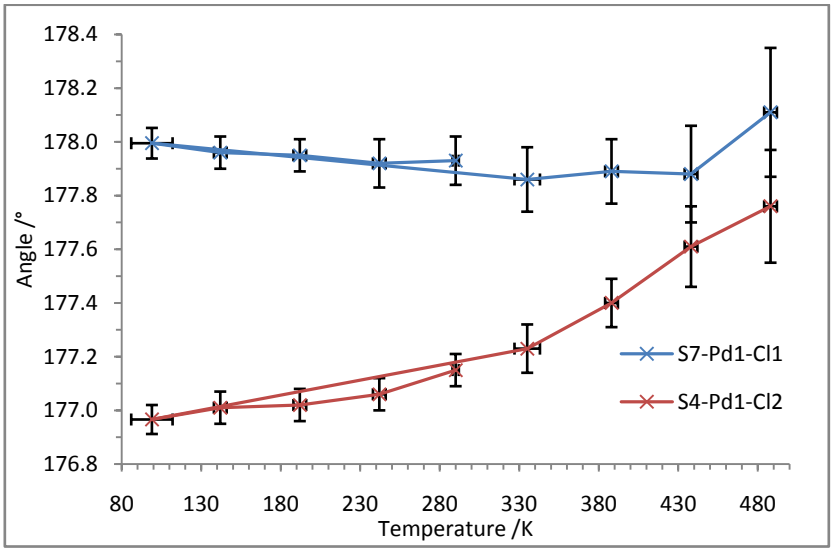



**Figure 41** The effects of temperature on the *trans* coordination angles in γ-**1**.

### 3.8. Calculated energies and bond orders

Density functional theory calculations were carried out on two-molecule fragments of each experimentally-determined high-pressure crystal structure using the Amsterdam Density Functional suite (Fonseca-Guerra *et al.*, 1998; Te Velde *et al.*, 2001). These were carried out to obtain a quantitative estimation of the effect of pressure on the bond orders of Pd···Pd, Pd···O and Pd−*L*, and on the relative energies of the fragments considered.

The following energies discussed herein correspond to the total bonding energy ($\Delta E_{\text{bond}}$) of the fragments considered in each calculation. This is calculated as the sum of the repulsive total steric interaction energy ($\Delta E_{\text{steric}}$) and attractive total orbital interactions ($\Delta E_{\text{OI}}$). The total steric interaction energy can be further reduced to the sum of the Pauli repulsion ($\Delta E_{\text{Pauli}}$) and electrostatic interactions ($\Delta E_{\text{EI}}$):

$$\Delta E_{\text{bond}} = \Delta E_{\text{OI}} + \Delta E_{\text{Pauli}} + \Delta E_{\text{EI}}$$

The effect of pressure on the total bonding energy in the considered fragments is exceedingly similar in the three ambient-pressure phases (Fig. 42), all increasing linearly at a rate of *ca.* 0.9 kJmol$^{-1}$ kbar$^{-1}$. The transformation of β-**1** to β'-**1** brings an increase in energy in all three resulting dimers. As with the derived structural parameters, there is a disparity in the energies of the corresponding disordered sites denoted "@Pd1,2" and "@Pd1A,2A" immediately after the phase transition but by 71 kbar these have approximately converged in energy.

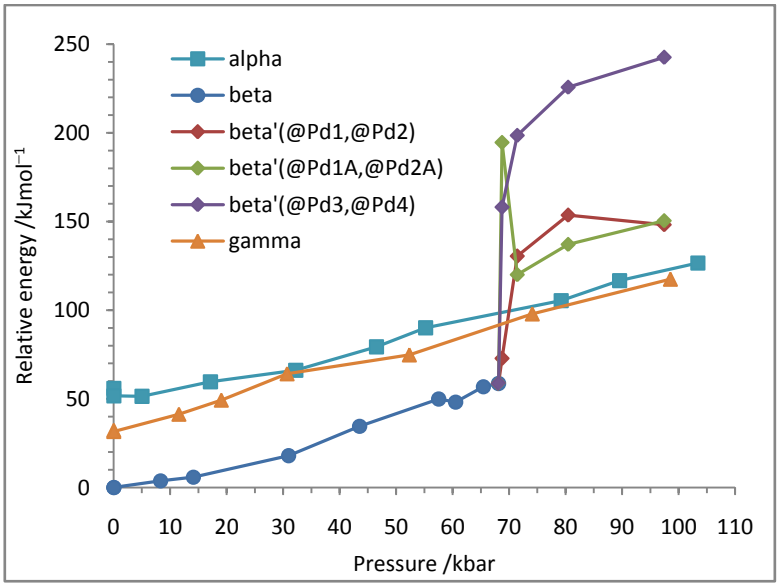



**Figure 42** The calculated bonding energy for the two-molecule fragments described in Section 2.3 for α-**1** (squares), β-**1** (circles), β'-**1** (diamonds) and γ-**1** (triangles); metal centres of specific dimers specified in the case of β'-**1**. Pressures are subject to *ca.* ±1.2 kbar uncertainty.

There is a substantial increase in total bonding energy of all resulting dimer fragments corresponding to an average increase of *ca.* 90 kJ $mol^{-1}$ between 68.1 and 71.4 kbar. This increase in energy is over twenty times greater than the energy released by the change in volume [4.4 kJ $mol^{-1}$ with respect to dimer fragments]. The substantial difference between these values is indicative of the transformation being a response to packing effects that are not considered in these calculations, lending weight to the rationalisation that the phenomenon is a response to the C−H···H−C contact described in Section 3.4.3.

### 3.8.1. α-[$PdCl_2$([9]ane$S_2O$)]

Calculations were carried out on a fragment comprising one dimer as described in Section 3.1.1. Despite having similar values at ambient pressure, the bond orders

of the axial Pd···O and Pd···Pd interactions showed different but smooth increases from 0.070 to 0.101 and 0.067 to 0.180, respectively, (Fig. 43) corresponding to relative increases of 45% and 167% , respectively, by 103.4 kbar. The equivalent ratios for the contraction of the interaction distances are 7% and 17%, respectively. Clearly, the Pd(II) centre shows preference for axial interaction from another Pd(II) rather than from an ether oxygen donor. The Mayer bond order for the Pd···Pd interaction exceeds that for the intermolecular axial *M*···S interactions investigated in our previous study of [$MX_2$([9]ane$S_3$)] (*M* = Pd, Pt; *X* = Cl, Br, I) (Allan *et al*., 2014) which lie in the range 0.044±0.02 at ambient pressure and do not exceed 0.117 within the same pressure range. This is accompanied by only a marginal decrease of 0.01−0.02 in bond order for the equatorial donor set by 103.4 kbar (Fig. 44).

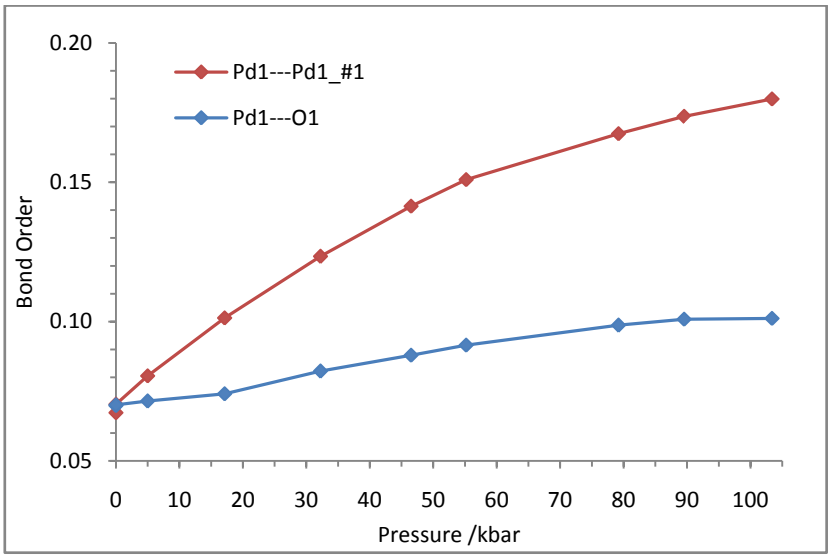



**Figure 43** The calculated Mayer bond orders as a function of pressure for axial interactions in α-**1**. Pressures are subject to *ca*. ±1.2 kbar uncertainty.

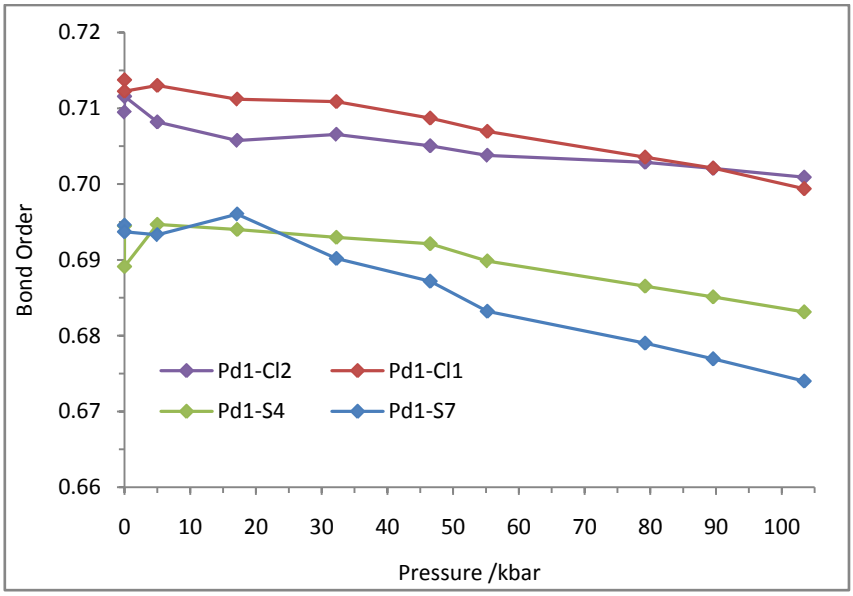



**Figure 44** The calculated Mayer bond orders as a function of pressure in α-**1**. Pressures are subject to *ca*. ±1.2 kbar uncertainty.

In conjunction with analysis of the corresponding bond orders in β-**1** (*vide infra*) this would not appear to be linked to the deviation of the Pd(II) centre out of the $Cl_2S_2$ plane and associated geometric distortion of the coordination sphere. Instead, the trends observed in each interaction appear to map to the compression of the interaction *trans* to it (Fig. 45). It would therefore appear that the increase in electron density at the metal centre associated with the compression of a given interaction serves to decrease the bond order of the interaction paired *trans* to it. It would therefore appear that the more distinct features present in the data, for example those around 17 kbar for Pd1−Cl2 and Pd1−S7, arise from the calculated geometric parameters being less precise than at other pressures.

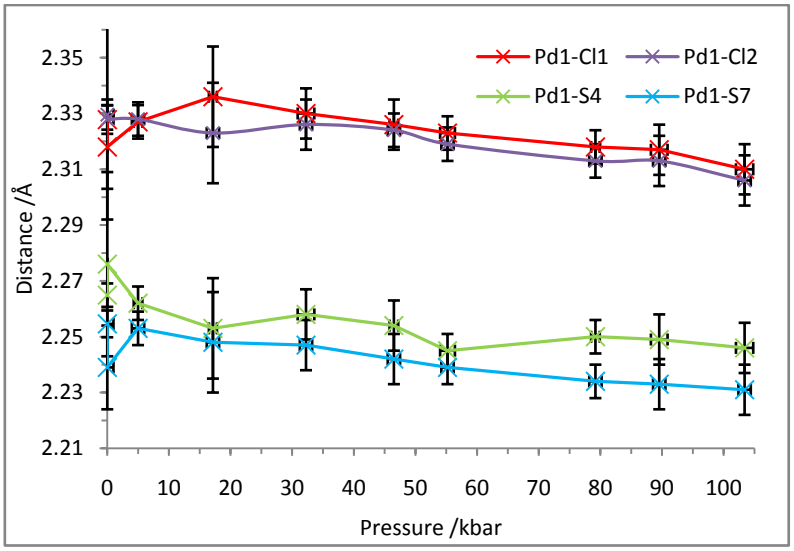



**Figure 45** The effect of pressure on the coordination bonds in α-**1**.

### 3.8.2. β-[$PdCl_2$([9]ane$S_2O$)] and β'-[$PdCl_2$([9]ane$S_2O$)]

For β-**1**, calculations were run on a fragment in the form of one dimer as described in Section 3.1.2.For β'-**1**, calculations were run on fragments corresponding to each of the three unique dimer combinations in the form of one dimer as described in Section 3.4.2.

Up to 68.1 kbar, the Pd···Pd bond order in β-**1** increases from 0.12 to 0.20 (Fig. S49), exceeding at *ca.* 35 kbar the maximum order reached in α-**1** at 103.4 kbar. If the bond orders are instead considered as a function of bond distance then the difference between the two phases is markedly reduced (Fig. 46). The remaining difference between the calculated bond orders of the β and α phases and also between the dimers within β'-**1** is then intuitively rationalised by the difference in slip between the coordination planes of the molecules within the dimers, *i.e.*, an increase in slip decreases the bond order for a given separation of square planar Pd(II) centres. This is supported by the interaction between molecules at Pd1 and Pd2 showing a similar plateau as for the other interactions in the β series but at a

maximum bond order more consistent with the data calculated for α-**1**, with the centroid-centroid slippage in the specified dimer having tended towards a value also reminiscent of that found in the α phase [slip = *ca.* 1.2 and 0.9 Å for α and specified β'-**1** dimer, respectively].

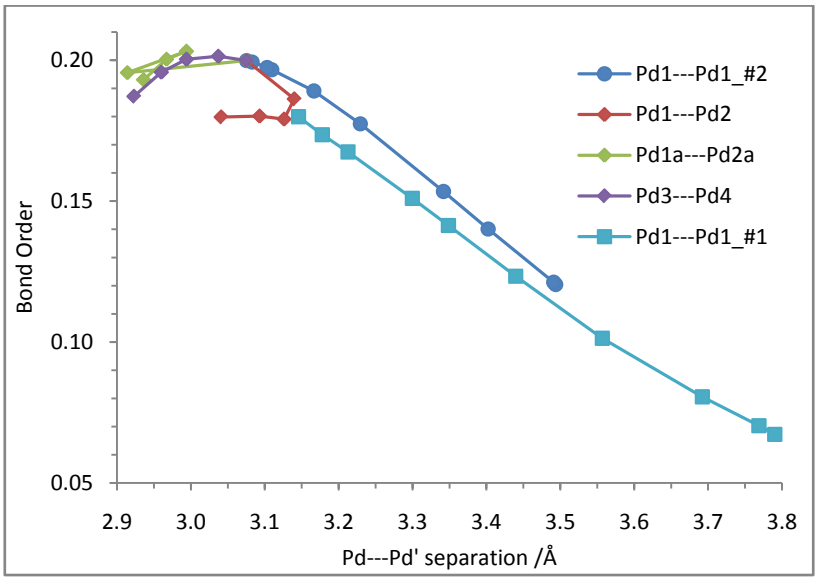



**Figure 46** The calculated Mayer bond orders as a function of the interatomic separation for the intradimer Pd···Pd interactions in α-**1** (squares), β-**1** (circles) and β'-**1** (diamonds). Symmetry code #1 = −*x*, 2 − *y*, −*z*; #2 = −*x*, 1 − *y*, −*z*.

A bond order of 0.20 represents a maximum in this study and defines a plateau for Pd···Pd separations *ca.* 2.98−3.08 Å and a centroid-centroid slippage of *ca.* 0.5 Å in the case of dimers comprising molecules at Pd1a and Pd2a, and at Pd3 and Pd4 (*cf.* Fig. 24). After this point, the bond order for these interactions decreases, despite continued contractions in the Pd···Pd separations (see Section 3.5.2). This is indicative of the interaction entering a regime increasingly dominated by, for example, repulsive steric interactions between the two atoms. A search of the Cambridge Structural Database (CSD; Nov. 2015 release plus one update; Groom *et al.*, 2016) for the separation between two four coordinate Pd centres excluding

intramolecular contacts connected by fewer than 6 bonds shows that this distance indeed represents a limit for intermolecular interactions of this nature (Fig. 47): below this limit intramolecular Pd···Pd contacts dominate. As the maximum bond order for the Pd···Pd interaction is coincident with the phase transition, this interaction may be involved along with the close H···H contact in bringing about the full range of changes observed across the phase transition: the increase in repulsion in the Pd···Pd interaction may assist in the phase transition by, for example, promoting increased slippage in the untransformed dimer such that the separation between the metal centres increases.

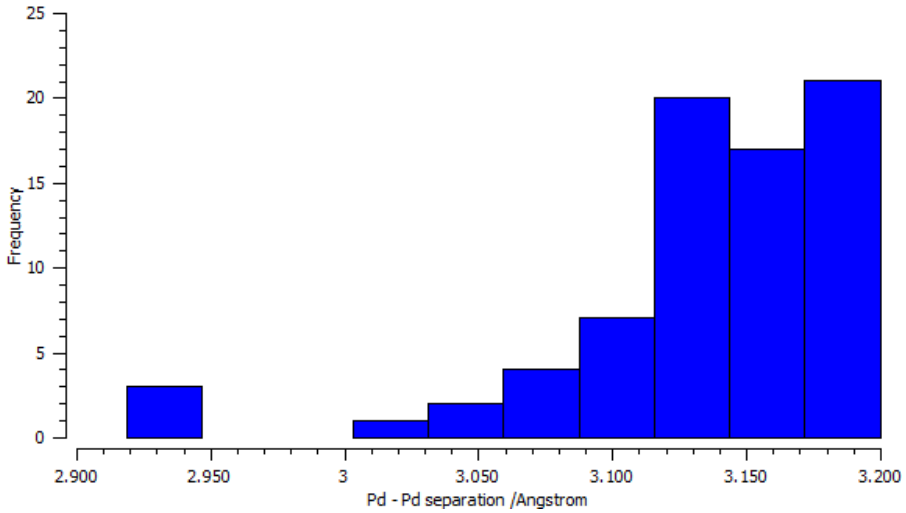



**Figure 47** Distribution of the Pd···Pd separations found in the CSD for four-coordinate Pd centres, excluding intramolecular contacts connected by fewer than 6 bonds (Nov. 2015 release plus one update; Groom *et al.*, 2016).

Additionally, the transformation brings about a decrease in repulsive steric interaction within all of the resulting dimers (Fig. 46). In the case of the transformed dimers, it is likely that this is owed to reduction of the S7···Cl1 contacts brought about by the lifting of S7 away from Cl1. In the case of the untransformed dimer, the increase in centroid-centroid slippage (*cf.* Fig. 24) serves

to reduce all S···Cl contacts, which would also appear to explain the data. It may therefore be concluded that intradimer interactions between coordination planes are involved in bringing about the full range of changes observed across the phase transition and follow as effects of the conformational rearrangement.

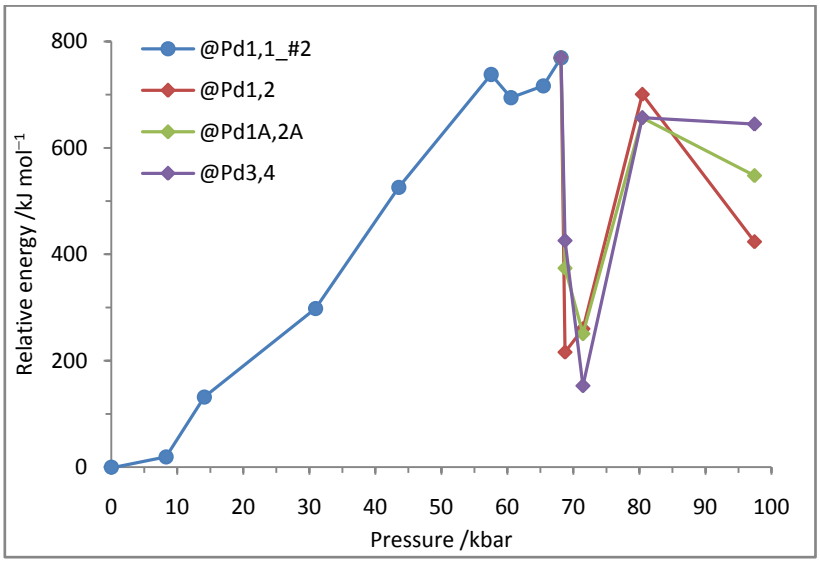



**Figure 48** The calculated total steric interaction relative to the ambient pressure state for the two-molecule fragments described in Section 2.3 for β-**1** (circles) and β'-**1** (diamonds). Symmetry code #2 = −*x*, 1 − *y*, −*z*. Pressures are subject to *ca*. ±1.2 kbar uncertainty.

Up to the phase transition there is again a steady decrease in the bond order for the coordination bonds, but with Pd1−Cl2 being significantly more weakened than the other three (Fig. 49). Deformation of the coordination geometry again seems to have little direct effect on the calculated bond order as it is Cl1 which is pushed out of the coordination plane, not Cl2, and this behaves very similarly to the two S donors. Furthermore, the rationale given for the behaviour of the α-**1** coordination and the Pd···Pd interaction bond orders does not hold here as there is negligible difference in the behaviour of the two Pd−S bonds under pressure.

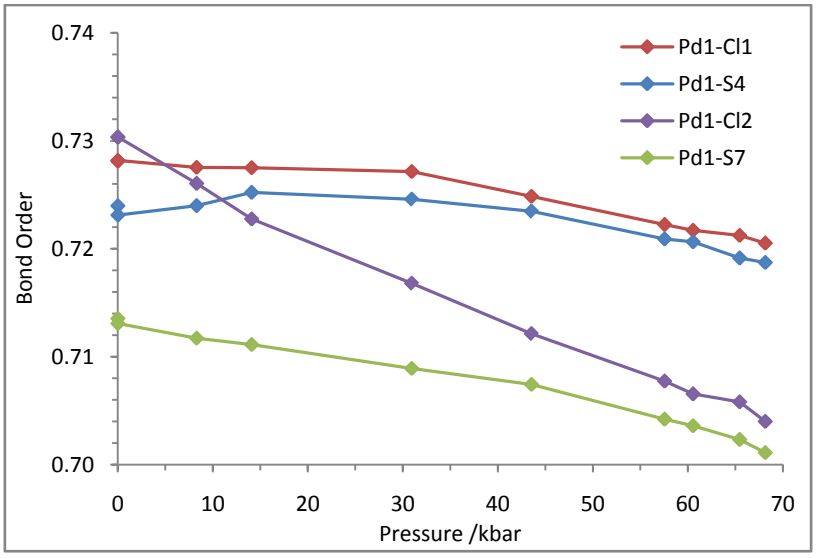



**Figure 49** The calculated Mayer bond orders as a function of pressure for the coordination bonds in β-**1**. Pressures are subject to *ca*. ±1.2 kbar uncertainty.

The next most obvious consideration included in the calculations is that of the close contact between the Cl2 of one molecule and S4 of the other in the dimer. It is possible that one effect of this interaction is to weaken the bonding between the Cl donor and the metal centre. If this were the case, one might expect to also see a similar, mutual weakening of the Pd−S4 bond, but no such complementary effect is observed, perhaps because the S donor is part of a more extensive network that in some way mitigates any effect on it. In such a case, a difference in behaviour of the S−C bond orders would be expected, supposing that the Cl donor might donate electron density into the S4−C3 σ* orbital. While this bond order decreases with pressure, the decrease is similar to that for the other S−C bond orders (Fig. 50).

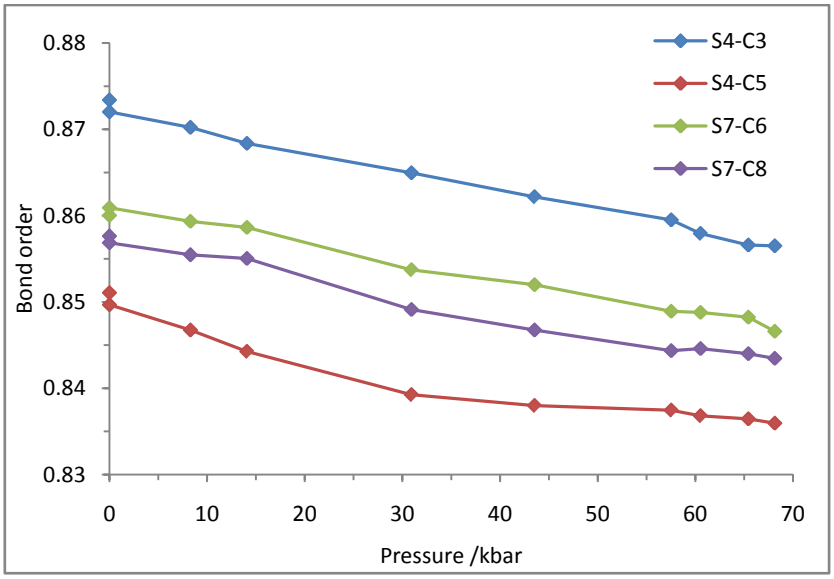



**Figure 50** The calculated Mayer bonders as a function of pressure for S−C interactions in β-**1**. Pressures are subject to *ca*. ±1.2 kbar uncertainty.

After the phase transition, in β'-**1**, a significant increase in uncertainty is associated with coordination bond parameters and therefore also with the relevant calculated bond orders. For this reason, discussion of these parameters is omitted.

### 3.8.3. γ-[$PdCl_2$([9]ane$S_2O$)]

Calculations were run on a fragment in the form of two molecules from a single chain as described in Section 3.1.3.

The calculated bond order for the intermolecular Pd1···O1_#3 (symmetry code #3 = 0.5 − *x*, −0.5 + *y*, 1.5 − *z*) interaction increases steadily with pressure with a profile that appears to directly follow the effect of pressure on this interaction (Fig. S51) and a linear dependence of bond order on atomic separation (Fig. 51). Comparison of this with the bond order of the intramolecular Pd···O interaction in α-**1** shows these to be similar in nature, albeit with α-**1** exhibiting a slightly stronger dependence on atomic separation. This could be an effect of the

concomitant compression of the Pd···Pd interaction in α-**1** that is not present in γ-**1**. The presence of another region of positive charge nearby to the metal centre in α-**1** may further polarise the metal centre and increase the strength of the interaction with the O donor. This complimentary effect would increase with pressure and so explain the continued deviation of the bond orders from one another as atomic separation is decreased.

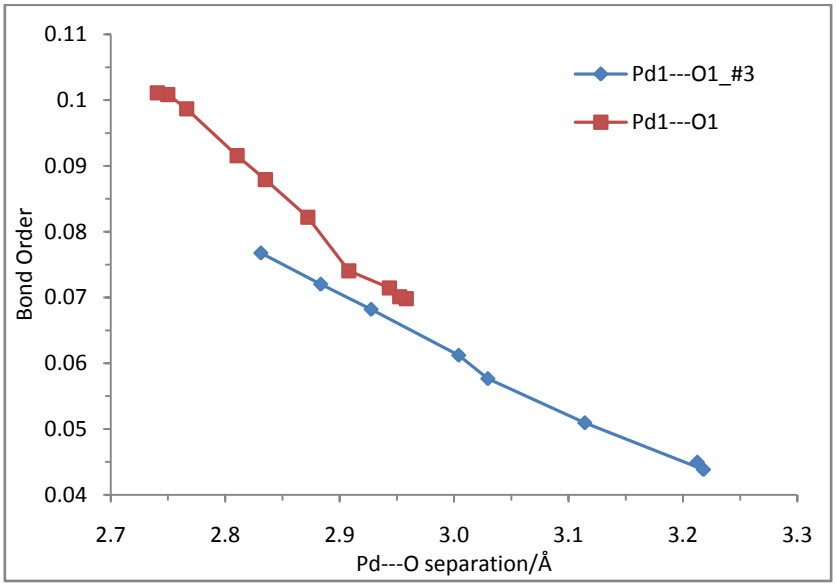



**Figure 51** The calculated Mayer bond-orders as a function of atomic separation for the intermolecular chain-forming Pd···O interaction γ-**1** (diamonds) and in α-**1** (squares) (symmetry code #3 = 0.5 − *x*, −0.5 + *y*, 1.5 − *z*).

The calculated bond orders for the coordination bonds in this phase are similar to those in the other two phases (Fig. 52). The application of pressure brings about small decreases in bond order, except for Pd1−Cl1 where a minor increase is observed. The small maxima in the Pd−S bond orders at *ca*. 20 kbar resemble equivalent features in the compression of the Pd−Cl interactions. While we cannot fully exclude the possibility that these phenomena may only reflect artefacts in the refined structural model, the data do appear to indicate that compression of the

Pd−Cl bonds weakens the Pd−S bonds, in agreement with the corresponding discussion given in the case of α-**1**.

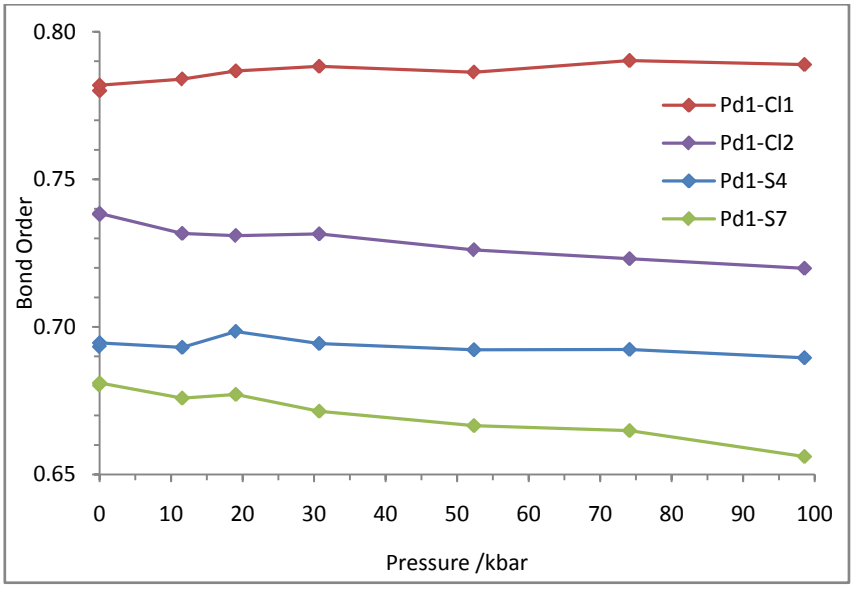



**Figure 52** The calculated Mayer bond orders as a function of pressure for the coordination bonds in γ-**1**.

## 4. Conclusions

Three phases of [$PdCl_2$([9]ane$S_2O$)] (**1**) were each studied up to pressures exceeding 90 kbar using high-pressure single-crystal X-ray diffraction. The differences in overall compressibility were attributed to the difference in void space volume and distribution: the most compressible γ-**1** phase had a relatively high degree of void space located between complimentary chain-like macromolecular structures, whereas the least compressible α-**1** phase contained the least void space, located in comparatively distinct and inaccessible pockets. β-**1** comprised a similar volume of void space distributed across two distinct regions: one region being that between neighbouring dimers and was found to be highly compressible, the other located between sheets of dimers, residing amongst the aliphatic regions of the macrocycle and was both less compressible and less

accessible than the former. This second region contained a pocket of particularly inaccessible void space which ultimately allowed for a conformational rearrangement of the macrocycle and phase transition. In all cases, the equatorial donor-sets were found to be largely incompressible.

For α-**1**, $B_0$ =14.4(8) GPa and $B'_0$ = 7.8(6). Compression brought smooth compression of unit cell and geometric parameters up to 103.4 kbar. The apical Pd1···O1 interaction was compressed from 2.958(4) to 2.741(3) Å and the intradimer Pd1···Pd1_#1 (symmetry code #1 = −*x*, 2 − *y*, −*z*) separation from 3.7903(10) to 3.1456(16) Å. This interaction exhibited lower resistance to compression compared to the corresponding compression between donor sets within dimers; the metal centre was displaced from the $Cl_2S_2$ least squares mean plane from 0.0128(10) to 0.0656(8) Å in the direction away from the apical oxygen. This affects simultaneous bending of the *trans* coordination bonds by 2.19(10) °.

For β-**1**, $B_0$ = 12.8(8) and $B'_0$ = 7.4(7) up to 68.1 kbar. Up to this pressure, smooth compression of unit cell and geometric parameters was observed. The intradimer Pd1···Pd1_#2 (symmetry code #2 = −*x*, 1 − *y*, −*z*) separation is compressed from 3.4937(6) to 3.0752(9) Å and remains in position with relation to the $ClS_2$ least squares mean plane defined by donors Cl2, S4 and S7, whereas Cl1 is pushed out of the plane in the direction away from the incoming molecule with which the dimer is formed. This appears to happen so as to alleviate the formation of an otherwise close contact with S4_#2, the donor able to move slightly owing to the location of a persistent region of void space above it that offers little comparable resistance.

Between 68.1 and 68.7 kbar a reversible phase transition was observed to a phase designated β'-**1**. This involved a tripling of the unit cell and a partial conformational rearrangement of the macrocycle at two of the three resulting unique sites to result in an extensively disordered structure. The root of this transformation was attributed to a persistent region of void space residing directly behind a carbon of the macrocycle associated with a close C−H···H−C approach about an inversion centre. The directionality of the resulting force causes one of the $CH_2$ moieties in question to rotate such that this contact is negated and the void space filled. This results in a [135] conformation by Dale analysis. In the rearranged molecules, the equivalent donors to S7 (*i.e.*, S27A and S47) are lifted up, out of the coordination plane, away from the neighbouring molecule in the dimer, in turn releasing the pressure on the corresponding Cl1_#2 donors (*i.e.*, Cl13 and Cl31) and alleviating the bending of the relevant *trans*- coordination angle. Intradimer Pd···Pd interactions continue to compress after the phase transition, but across the phase transition the separation in dimers that undergo the rearrangement decreases and diverges from that of the remaining disorder component which is instead subject to an increase in this parameter. This is attributed to a decrease in slip between molecules within dimers affected by the conformational rearrangement and an increase in the dimer that is not.

For γ-**1**, $B_0$ =7.6(6) GPa and $B'_0$ = 13.0(11)**.** The chain forming intermolecular interaction Pd1···O1_#3 (symmetry code #3 = 0.5 − *x*, −0.5 + *y*, 1.5 − *z*) is compressed smoothly from 3.213(3) to 2.831(8) Å. As with the β-**1**, the metal centre remains in the coordination plane along with the donors Cl1, S4 and S7, while Cl2 is pushed up, out of the plane and away from the incoming O donor.

This appears to happen as an effect of a number of close contacts surrounding the donor except in the direction in which it is deviated, in which place resides a small region of void.

Temperature was found to be largely inconsequential to the three phases. In each case, cooling from 290 to 90 K brought about similar effects as the application of 4-5 kbar pressure, an observation similar to that elsewhere in the literature, for example in the case of $[(CH_3)_2NH(CH_2)_2NH_3][SbCl_5]$ (Bujak& Angel, 2006) and a pair of iron(II) N-2'-pyridylmethylene complexes (Guionneau *et al.*, 2001). Minor deviations to the geometries of the coordination planes were observed, typically as an effect of thermal expansion decreasing the strain of close contacts.

DFT calculations showed a similar increase in total bonding energy with pressure for the two molecule fragments used for all three ambient phases. Across the $\beta \rightarrow \beta'$ phase transition, an average increase of 90 kJ $mol^{-1}$ is observed in the resulting dimers between 68.1 and 71.4 kbar. This data clearly suggests that the transition is as a consequence of packing effects not considered in the calculation and serves to support the earlier given rationale.

A linear dependence of bond order with interaction distance was calculated for both Pd···O interactions investigated in this study. The interaction in α-**1** showed a stronger dependence on separation, potentially owed to an additional polarizing effect of the Pd(II) centre of the neighbouring molecule in the dimer. A linear dependence of bond order on atomic separation was calculated for the Pd···Pd interaction in α-**1** which increased from 0.067 to 0.180. In β-**1** an approximately linear dependence was also observed down to 3.0752(9) Å at 68.1 kbar, corresponding to a bond order of 0.200. After this point, coincident with the

β → β’ phase transition, plateaus were observed for the following *ca.* 0.1 Å of compression before the bond orders then appeared to decrease as compression continued. This separation of *ca.* 3 Å also shows itself as a limit for ambient intermolecular Pd···Pd separation through analysis of the CSD. This appears to provide a potential cause for the extensive changes observed across the phase transition, wherein an increase in Pd···Pd repulsion may promote, for example, an increase in slip of the coordination planes in the untransformed dimer. With regards to the $Cl_2S_2$ donor sets, bond order analysis suggests that compression serves only to marginally weaken these interactions by an order of 0.01−0.03 and an interdependence of the bond order of one interaction with that of the interaction *trans* to it.

## References


Agilent (2014). *CrysAlis$^{PRO}$*. Agilent Technologies, Yarnton, England.

Allan, D. R.; Blake, A. J.; Huang, D.; Prior, T. J.; Schröder, M. (2006). *Chem. Commun.*, 4081-4083.

Allan, D. R.; Bailey, D.; Bird, N.; Blake, A. J.; Champness, N. R.; Huang, D.; Keane, C. P.; McMaster, J.; Prior, T. J.; Tidey, J. P.; Schröder, M. (2014). *Acta Crystallogr., Sect. B*, **70**, 469-486.

Angel, R. J.; Gonzalez-Platas, J.; Alvaro, M. (2014). *Z. Kristallogr.* **229**, 405-419.

Ballaran, T. B.; Kurnosov, A.; Trots, D. (2013). *High Pressure Res.* **33**, 3, 453-465.

Barnett, J. D.; Block, S.; Piermarini, G. J. (1973). *Rev. Sci. Instrum.* **44**, 1-9.

Becke, A. D. (1988). *Phys. Rev. A*, **38**, 3098-3100.

Blake, A. J.; Roberts, Y. V.; Schröder, M. (1996). *Dalton Trans*. 1885-1895

Bondi, A. J. (1964). *J. Phys. Chem.***68**, 441-451.

Bruker (2001). *SADABS.* Bruker AXS Inc., Madison, Wisconsin, USA.

Bruker (2007). *SAINT.* Bruker AXS Inc., Madison, Wisconsin, USA.

Bujak, M.; Angel, R. J. (2006). *J. Phys. Chem. B*, **110**, 10322-10331.

Byrne, P. J.; Richardson, P. J.; Chang, J.; Kusmartseva, A. F.; Allan, D. R.; Jones, A. C.; Kamenev, K. V.; Tasker, P. A.; Parsons, S. (2012). *Chem. Eur. J.* **18**, 7738-7748.

Cairns, A. B.; Thompson, A. L.; Tucker, M. G.; Haines, J.; Goodwin, A. L. (2012). *J. Am. Chem. Soc.* **134**, 4454-4456.

Clark, R. C.; Reid, J. S. (1995). *Acta Crystallogr., Sect A*, **51**, 887–897.

Connor, L. E.; Delori, A.; Hutchison, I. B.; Daeid, N. N.; Sutcliffe, O. B.; Oswald, I. D. H. (2015). *Acta Crystallogr., Sect. B*, **71**, 3-9.

Cosier, J.; Glazer, A. M. (1986). *J. Appl. Crystallogr.* **19**, 105-107.

Dale, J. (1973). *Acta Chem. Scand.* **27**, 1115-1129.

Dolomanov, O.V.; Bourhis, L.J.; Gildea, R.J.; Howard, J.A.K.; Puschmann, H. (2009). *J. Appl. Cryst.* **42**, 339-341.

Fabbiani, F. P. A.; Allan, D. R.; David, W. I. F.; Davidson, A. J.; Lennie, A. R.; Parsons, S.; Pulham., C. R.; Warren, J. E. (2007). *Cryst. Growth Des.* **7**, 6, 1115-1124.

Fonseca-Guerra, C.; Snijders , J. G.; Te Velde, G.; Baerends, E. J. (1998). *Theor. Chem. Acc.* **99**, 391-403.

Galloway, K. W.; Moggach, S. A.; Parois, P.; Lennie, A. R.; Warren, J. E.; Brechin, E. K.; Peacock, R. D.; Valiente, R.; González, J.; Rodríguez, F.; Parsons, S.; Murrie, M. (2010). *CrystEngComm*, **12**, 2516-2519.

Gould, J.A.; Rosseinsky, M. J.; Moggach, S. A. (2012). *Dalton Trans.* **41**, 5464-5467.

Guionneau, P.; Brigouleix, C.; Barrans, Y.; Goeta, A. E.; Létard, J.-F.; Howard, J. A. K.; Gaultier, J.; Chasseau, D. (2001). *Acad. Sci., Ser. IIc: Chim.* **4**, 161-171.

Groom, C. R.; Bruno, I. J.; Lightfoot, M. P.; Ward, S.C. (2016). *Acta Crystallogr., Sect. B*, **72**, 171–179.

Hirshfeld, F. L. (1976). *Acta Crystallogr., Sect. A*, **32**, 239-244.

Holzapfel, W. B. (2003). *J. Appl. Phys.* **93**, 1813-1818.

Katrusiak, A.; Dauter, Z. (1996). *Acta Crystallogr., Sect. D*, **52**, 607-608.

Klotz, S.; Chervin, J.-C.; Munsch, P.; Le Marchand, G. (2009). *J. Phys. D: Appl. Phys.***42**, 075413/1- 075413/7.

Konno, M.; Okamoto, T.; Shirotani, I. (1989). *Acta Crystallogr., Sect. B*, **45**, 142-147.

Lucas, C. R.; Liang, W.; Miller, D. O.; Bridson, J. N. (1996). *Inorg. Chem.***36**, 4508-4513.

Macrae, C. F.; Edgington, P. R.; McCabe, P.; Pidcock, E.; Shields, G. P.; Taylor, R.; Towler, M.; van de Streek, J. (2006). *J. Appl. Cryst.* **39**, 453-457.

Macrae, C. F.; Bruno, I. J.; Chisholm, J. A.; Edgington, P. R.; McCabe, P.; Pidcock, E.; Rodriguez-Monge, L.; Taylor, R.; van de Streek, J.; Wood, P. A. (2008). *J. Appl. Cryst.* **41**, 466-470.

Moggach, S. A.; Parson, S.; Wood, P. A. (2008). *Crystallogr. Rev.* **14**, 2, 143-184.

Okano, Y.; Adachi, T.; Narymbetov, B.; Kobayashi, H.; Zhou, B.; Kobayashi, A. (2004). *Chem. Lett.* **33**, 938-939.

Park, J. K.; Cho, Y. G.; Lee, S. S.; Kim, B. G. (2004). *Bull. Korean Chem. Soc.* **25**, 1, 85-89.

Parois, P.; Moggach, S. A.; Sanchez-Benitez, J.; Kamenev, K. V.; Lennie, A. R.; Warren, J. E.; Brechin, E. U.; Parsons, S.; Murrie, M. (2010). *Chem. Commun.***46**, 1881-1883.

Perdew, J. (1986). *Phys. Rev. B*, **33**, 8822-8824.

Piermarini, G. J.; Block, S.; Barnett, J. D. (1973). *J. Appl. Phys.* **44**, 5377-5382.

Prescimone, A.; Milios, C. J.;Sanchez-Benitez, J.; Kamenev, K. V.; Loose, C., Kortus, J.;Moggach, S. A.; Murrie, M.; Warren, J. E.; Lennie, A. R.; Parsons, S.; Brechin, E. U. (2009). *Dalton Trans.* 4858-4867.

Prescimone, A.; Sanchez-Benitez, J.; Kamenev, K. V.; Moggach, S. A.; Warren, J. E.; Lennie, A. R.; Murrie, M.; Parsons, S.; Brechin, E. U. (2010). *Dalton Trans.* **39**, 113-123.

Satthaphut, N.; Sutcliffe, O. B.; Oswald, I. D. H. (2014). *Z. Kristallogr.* **229**, 101-111.

Schmidtmann, M.; Coster, P.; Henry, P. F.; Ting, V. P.; Weller, M. T.; Wilson, C. C. (2014). *CrystEngComm*. **16**, 1232-1236.

Sheldrick, G. M. (1996). *SADABS*. University of Göttingen, Germany.

Sheldrick, G. M. (2008). *Acta Crystallogr., Sect. A*, **64**, 112-122.

Sheldrick, G. M. (2015). *Acta Crystallogr., Sect. C*, **71**, 3-8.

Shepherd, H. J.; Rosa, P.; Vendier, L.; Casati, N.; Létard, J.-F.; Bousseksou, A.; Guionneau, P.; Molnár, G. (2012). *Phys. Chem. Chem. Phys.* **14**, 5265-5271.

Spek, A. L. (2009). *Acta Crystallogr., Sect. D*, **65**, 148-155.

Takeda, K.; Hayashi, J.; Shirotani, I.; Fukuda, H.; Yakushi, K. (2006). *Mol. Cryst. Liq. Cryst.* **460**, 131-144.

Te Velde, G.; Bickelhaupt, F. M.; Baerends, E. J.; Fonseca-Guerra, C.; van Gisbergen, S. J. A.; Snijders, J. G.; Ziegler, T. (2001). *J. Comput. Chem.* **22**, 931-967.

Tidey, J. P. (2012). *University of Nottingham*. MSci dissertation: “High Pressure Crystallographic Study of Macrocyclic Platinum Group Complexes”.

Tidey, J. P.; Wong, H. L. S.; Schröder, M.; Blake, A. J. (2014). *Coord. Chem. Rev.* **277-278**, 187-207.

Tidey, J. P.; O’Connor, A. E.; Markevich, A.; Bitchoutskaia, E.; Cavan, J. J. P.; Lawrence, G. A.; Wong, H. L. S.; McMaster, J.; Schröder, M.; Blake, A. J. (2015). *Cryst. Growth Des.* **15**, 115-123.

Tidey, J. P.; Wong, H. L. S.; McMaster, J.; Schröder, M.; Blake, A. J. (2016). *Acta Crystallogr., Sect. B*, **72**, 3, 357-371.

Turner, M. J.; McKinnon, J. J.; Jayatilaka, D.; Spackman, M. A. (2011). *CrystEngComm*. **13**, 1804-1813.

Vosko, S. H.; Wilk, L.; Nusair, M. (1980). *Can. J. Phys.*, **58**, 1200-1211.

Wolff, S. K.; Grimwood, D. J.; McKinnon, J. J.; Turner, M. J.; Jayatilaka, D.; Spackman, M. A. (2012). *CrystalExplorer* version 3.1, University of Western Australia, Australia.

Wong, H. L. S.; Allan, D. R.; Champness, N. R.; McMaster, J.; Schröder, M.; Blake, A. J. (2013). *Angew. Chem. Int. Ed.* **52**, 5093-5095.

Wong, H. L. S. (2014). *University of Nottingham*. PhD thesis: "High Pressure Crystallography of Palladium Thioether Complexes".

Woodall, C. H.; Beavers, C. M.; Christensen, J.; Hatcher, L. E.; Intissar, M.; Parlett, A.; Teat, S. J.; Reber, C.; Raithby, P. R. (2013). *Angew. Chem. Int. Ed.* **52**, 9691-9694.

Yamada, H.; Nagae, T.; Watanabe, N. (2015). *Acta Crystallogr., Sect. D*, **71**, 724-753.

# Chapter 4

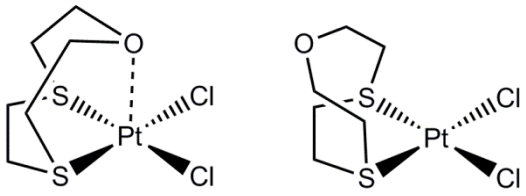
## High-Pressure Studies of Two Polymorphs of a Platinum(II) Macrocycle Complex

## 1. Introduction

The work in this chapter continues directly from that of the previous two. In Chapter 2, three phases of [$PdCl_2$([9]ane$S_2O$)] (**1**) were reported, α-**1**, β-**1** and γ-**1**, and a further two phases of the analogous Pt(II) complex, [$PtCl_2$([9]ane$S_2O$)] (**2**), α-**2** and β-**2** which were isomorphous and isostructural with the correspondingly named phases of **1**. Their phase behaviour was rationalised in accordance with experimental observations and DFT calculations, while in Chapter 3 the high pressure behaviour of the Pd(II) complex was studied. Those studies showed γ-**1** to be significantly more compressible than the other two phases, rationalised by a favourable spread of void space between the supramolecular chain motifs which could interdigitate under pressure, while the other two phases contained much less accessible void space. The major result of that study was a phase transition in β-**1** which tripled the unit cell volume, seemingly in response to an approximately linear close C−H···H−C contact, at the termini of which were highly persistent pockets of void that allowed for one $CH_2$ moiety to rotate and so alleviate the contact. This gave rise to a heavily disordered system containing an unprecedented [135] conformation of the macrocycle and was in contrast to the incomplete and destructive β → α phase transition observed with anisotropic pressure, such as when cutting the crystal.

Having studied the three phases of **1** and obtained such a result with the β phase, it followed that an investigation of the corresponding Pt(II) complex should be undertaken. While palladium and platinum have similar chemistry, they of course have their differences, with platinum being the larger metal and softer acid, so further decreasing its affinity towards hard $R_2O$ donors (Pearson, 1968). In our study of [$MX_2$([9]ane$S_3$)] ($M$ = Pd, Pt; $X$ = Cl, Br, I) it was notably only for $M$ = Pd

and *X* = Cl that a phase transition was observed (Allan *et al*., 2014). Given the marginally greater stability of β-**2** and that no β → α phase transition was observed in cut crystals as reported and discussed in Chapter 2, and that the full range of changes seen in the β → β' transition may be dependent on intradimer interactions (Chapter 3; Tidey *et al.*, 2016), the question stood of whether or not β-**2** would behave in the same way as β-**1** under pressure.




**Scheme 1** Scheme showing *endodentate* (left) and *exodentate* (right) conformers of $[PtCl_2([9]aneS_2O)]$.

## 2. Experimental

### 2.1. Synthesis

Complex **2** was prepared as described in Chapter 2 and by Tidey *et al*. (2015). Crystals of α-**2** were obtained by diffusion of $Et_2O$ vapour into a solution of the complex in $CH_3NO_2$ at 20 °C. Crystals of β-**2** were obtained by diffusion of $Et_2O$ vapour into a solution of the complex in $CH_3NO_2$ at 35 °C.

### 2.2. Crystallography

#### 2.2.1. High-pressure crystallography

For α-**2**, two crystals were studied to give the full range of data reported: a single crystal of dimensions 0.09 × 0.06 × 0.05 $mm^3$ (crystal 1) was studied at 0.001, 2.0, 15.7, 30.0 and 43.0 kbar; a second single crystal of dimensions 0.09 × 0.05 × 0.05

$mm^3$ (crystal 2) was studied at 0.001, 66.7, 81.8, 90.1 and 95.7 kbar, and decompressed to collect data at 68.6 kbar.

For β-**2**, five crystals were studied: a single crystal of dimensions 0.11 × 0.04 × 0.02 $mm^3$ (crystal 1) was studied at 9.1, 15.0, 21.9, 34.1, 50.5, 69.9, 100.1 and 119.7 kbar; a single crystal of dimensions 0.05 × 0.04 × 0.02 $mm^3$ (crystal 2) was studied at 9.0, 36.7, 47.7 and 58.4 kbar; a single crystal of dimensions 0.09 × 0.08 × 0.07 $mm^3$ (crystal 3) was studied at 4.7, 38.5 and 50.5 kbar; a single crystal of dimensions 0.14 × 0.06 × 0.04 $mm^3$ (crystal 4) was studied at 5.2, 32.6, 46.6, 53.7, 62.4 and 65.2 kbar; and a final single crystal of dimensions 0.04 × 0.02 × 0.01 $mm^3$ (crystal 5) was studied at 38.4, 71.5, 74.2, 78.1, 87.2 and 99.3 kbar.

The sample chamber of a Merrill-Bassett diamond anvil cell (DAC) was formed by the 600 μm culet faces of the Boehler-Almax diamonds and by laser-cut tungsten sheet (Goodfellow Metals, thickness 200 μm) indented to either a thickness of *ca.*80 μm (for crystals 1 and 2 of α-**2**, and crystals 1 and 5 of β-**2**) or a thickness of *ca.* 130 μm (for crystals 2, 3 and 4 of β-**2**) with a gasket hole of diameter 200 μm drilled using a BETSA electric discharge machine. In each case, the sample crystal was fixed to one culet face by means of silicone grease, alongside a ruby sphere which allowed pressure measurement using the ruby fluorescence method (Barnett *et al.*, 1973). Methanol/ethanol (4:1*v*/*v*) was used as the pressure transmitting medium (PTM), except in the case of ambient-pressure in-cell data collections for which no PTM was used. After each pressure ramp, the pressure inside the DAC was allowed to equilibrate for a minimum of 16 hours before data collection was initiated except in the case of data collected at Diamond Light Source. In this instance, the reduced collection time permitted a rest period in the order of 2 hours.

Pressure measurements were taken immediately before and after each collection and the pressure reported is the average of these. The average uncertainty in pressure across this study is ±1.1 kbar with specific error bars drawn on figures as ±0.5 times the magnitude of the drift plus 0.5 kbar attributed to the inherent uncertainty of the ruby fluorescence method (Holzapfel, 2003).

Data for β-**2** at pressures of 32.6, 46.6, 53.7, 62.4 and 65.2 kbar were collected on Beamline I19, Experimental Hutch 2, of Diamond Light Source using silicon double-crystal monochromated synchrotron radiation (λ = 0.6889 Å) detected at a Pilatus 300K hybrid pixel array detector. All other data were collected using a Rigaku SuperNovaII diffractometer equipped with a microfocus sealed-tube source focussing mirror-monochromated Mo-*K*α radiation (λ = 0.71073 Å) detected at an Eos CCD area detector. Cell refinement and data reduction was performed using *CrysAlis*$^{PRO}$ (Agilent, 2014).

For ambient temperature (293 K) and pressure collections collected outside the cell, crystals were mounted using silicon grease on MiTeGen MicroMounts$^{TM}$ and numerical absorption corrections based on Gaussian integration over a multifaceted crystal model were applied. For all other data, multi-scan absorption corrections were applied with an empirical absorption correction using spherical harmonics, implemented in SCALE3 ABSPACK scaling algorithm (Clark & Reid, 1995) through *CrysAlis*$^{PRO}$ (Agilent, 2014). Structure solution was undertaken using *SHELXS*14 direct methods (Sheldrick, 2008) for the ambient pressure structures. All other structures were solved by isomorphous replacement with an appropriate model. Structures were refined to convergence using *SHELXL*14 (Sheldrick, 2015). Solution and refinement were implemented through *Olex2* (Dolomanov *et al*.,

2009). Specific refinement details are embedded in the relevant CIFs which can be found along with the experimental tables in the supplementary information.

### 2.2.2. Variable temperature crystallography

For α-**2**, a single crystal of dimensions 0.11 × 0.07 × 0.06 $mm^3$ was mounted in a Fomblin film on a MiTeGen MicroMount$^{TM}$ and data collected at 290, 240, 190, 90, 290, 340, 390, 440 and 490 K with a ramp rate of 120 K $hr^{-1}$ and a standing time of 5 mins prior to each collection.

For β-**2**, two crystals were studied: the first, crystal T0, was a single crystal of dimensions 0.06 × 0.05 × 0.02 $mm^3$, mounted in a Fomblin film on a MiTeGen MicroMount$^{TM}$ and data were collected first from 290 to 90 K at 10 K intervals, then again from 290 to 480 K at 10 K intervals, inclusively, with a ramp rate of 60 K $hr^{-1}$ and a standing time of 5 mins prior to each collection. The second, crystal T1, was a single crystal of dimensions 0.22 × 0.18 × 0.09 $mm^3$, mounted in a Fomblin film on a MiTeGen MicroMount$^{TM}$ and data were collected at 290, 300, 310, 320, 330, 340, 460, 470, 480, 490, 470, 450, 330, 310, 290, 280, 270, 260, 250, 112, 100, 90, 110, 90, 110, 130, 260, 290, 300, 310, 320, 330, 340, 490, 310, 290, 270, 250, 270, 290, 310, 330, 290, 350 and 290 K with a ramp rate of 240 K $hr^{-1}$ and a standing time of 2 mins prior to each collection.

Data were collected using a Rigaku SuperNovaII diffractometer equipped with a microfocus sealed-tube source focussing mirror-monochromated Cu-*K*α radiation (λ = 1.5418 Å) detected at an Atlas CCD area detector. Cell refinement and data reduction was performed using *CrysAlis$^{PRO}$* (Agilent, 2014) and numerical absorption corrections based on Gaussian integration over a multifaceted crystal

model were applied. Temperature was regulated using Oxford Cryostreams open-flow cryostats (Cosier & Glazer, 1986), and structures were solved by isomorphous replacement with an appropriate model and refined to convergence using *SHELXL*14 (Sheldrick, 2015). Solution and refinement were implemented through *Olex2* (Dolomanov *et al*., 2009). Specific refinement details are embedded in the relevant CIFs which can be found along with the experimental tables in the supplementary information.

### 2.3. Density functional theory calculations

Single-point density functional theory (DFT) calculations were carried out on models derived directly from the experimentally obtained crystal structures using the Amsterdam Density Functional suit version 2014.02 (*ADF*; Fonseca-Guerra *et al.*, 1998; Te Velde *et al.*, 2001). Slater-type orbital triple-ζ-plus double polarisation basis sets were used from the ZORA/TZP2 database of the *ADF* suite: for Pt, a frozen core approximation up to and including 4*f* was used; for S and Cl, up to and including 2*p*; for C and O, only including 1*s*. Scalar relativistic approaches were used within the ZORA Hamiltonian and the local density approximation with correlation potential due to Vosko *et al.* (1980) were used in all calculations. Gradient corrections were performed using the functionals of Becke (1988) and Perdew *et al.* (1986). For α-**2**, DFT calculations were carried out on a dimer fragment as described in Section 3.1.1. For β-**2**, DFT calculations were carried out on a dimer fragment as described in Section 3.1.2. In the case of β-**2** at pressures of 69.9 kbar and higher, DFT calculations were carried out on fragments corresponding to dimers formed by the three possible combinations of the two possible conformers.

## 3. Results and discussion

### 3.1. Structures at ambient pressure and temperature

Structures for the ambient pressure phases are fully reported in Chapter 2 but it is pertinent to highlight certain features for the sake of discussion. Details of the unit cell parameters at ambient temperature and pressure for the phases discussed in this chapter are given in Table 1.

**Table 1** Unit cell parameters for the two reported phases of **2** at ambient temperature and pressure. In both phases, $Z = 4$.

| Phase | Space group | $a$ / Å | $b$ / Å | $c$ / Å | β/ ° | $V$ / Å$^3$ |
|---|---|---|---|---|---|---|
| α-**2** | $P2_1/n$ | 8.4580(2) | 12.2793(3) | 10.3572(3) | 105.531(2) | 1036.40(5) |
| β-**2** | $P2_1/c$ | 9.41666(18) | 12.6646(2) | 9.0376(16) | 91.5297(17) | 1077.43(3) |

#### 3.1.1. α-[$PtCl_2$([9]ane$S_2O$)]

α-**2** is isomorphous and isostructural to α-**1**. The Pt(II) centre is bound in a square plane by two mutually *cis* chloride donors [Pt−Cl = 2.3328(17) and 2.3322(17) Å] and two macrocyclic sulfur donors [Pt−S = 2.2403(16) and 2.2456(17) Å] (Fig. 1). The macrocycle binds in an *endodentate* configuration providing a distant apical oxygen donor [Pt1···O1 = 3.084(4) Å] within the sum of the van der Waals radii [$\Sigma_{vdW}$ = 3.27 Å (Bondi, 1964)] to form a [4+1] square based pyramidal geometry at the metal. The mononuclear units pack base-to-base (Fig. 2) with the coordination planes parallel to each other to form dimeric units [Pt1···Pt1_#1 = 3.8253(5) Å; symmetry code #1 = $-x$, $2 - y$, $-z$]. This value lies significantly outside the sum of the relevant van der Waals radii [$\Sigma_{vdW}$ = 3.50 Å (Bondi, 1964)]. The perpendicular separation of the $Cl_2S_2Pt$ least squares planes is 3.6827(14) Å and the centroid-centroid shift is 1.123(2) Å. These dimers form ABAB alternating sheets

in the *bc* plane, generating a herringbone-like motif when viewed along the *a* axis (Fig. 2).

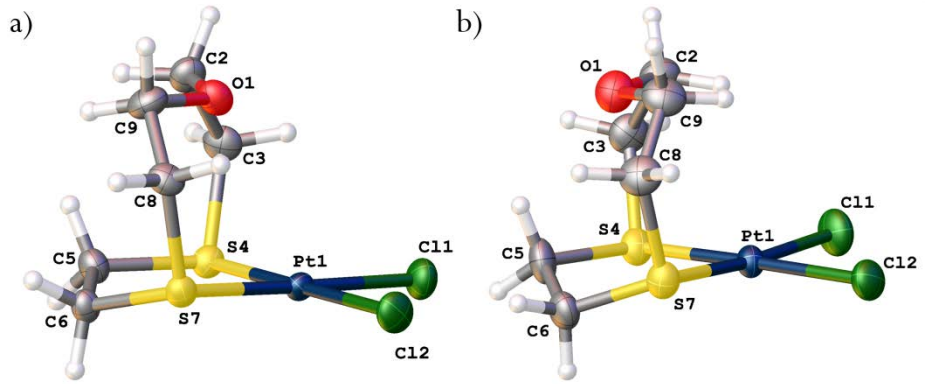



**Figure 1** View of complex **2** in the a) α and b) β phases. Non-H atoms are labelled in accordance with text and anisotropic displacement parameters are drawn at 50 % probability.

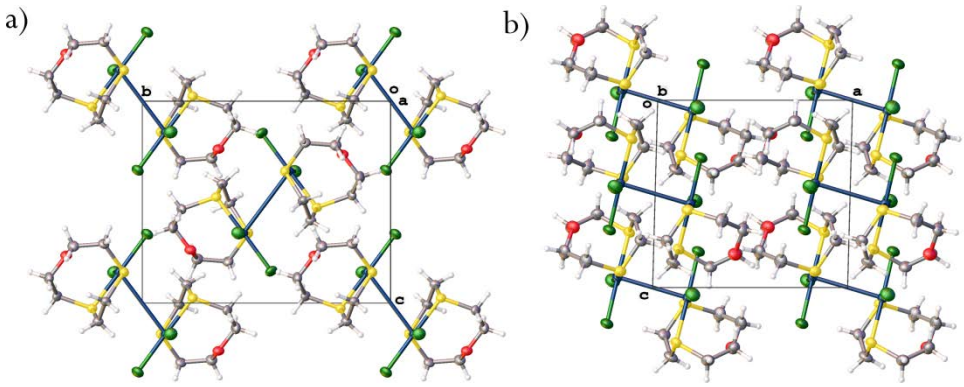



**Figure 2** a) View of herringbone packing of α-**2** viewed along the *a* axis; Pt···Pt interactions within dimeric units are highlighted by an additional blue bond. b) Layered packing of β-**2** viewed along the *b* axis; Pt···Pt interactions within dimeric units are highlighted by an additional blue bond. Anisotropic displacement parameters are drawn at 50 % probability.

### 3.1.2. β-[$PtCl_2$([9]ane$S_2O$)]

β-**2** is isomorphous and isostructural to β-**1**. The Pt(II) centre is bound in a square plane by two mutually *cis* chloride donors [Pt−Cl = 2.3220(8) and 2.3266(8) Å]

and two macrocyclic sulfur donors [Pt−S = 2.2729(10) and 2.2605(10) Å] (Fig. 1). The macrocycle binds in an *exodentate* fashion with the oxygen donor atom directed away from the metal centre [Pt1···O1 = 3.445(2) Å] with the result that no apical interaction supplements the square planar geometry at the metal. Similar to the α phase, these units pack base-to-base (Fig. 2) with the coordination planes parallel to each other to form dimeric units [Pt1···Pt1_#2 = 3.5294(2) Å; symmetry code #2 = $-x$, $1-y$, $-z$]. This value again lies significantly outside the sum of the relevant van der Waals radii [$\Sigma_{vdW}$ = 3.50 Å (Bondi, 1964)]. The perpendicular separation of the $Cl_2S_2Pt$ least squares planes is 3.5471(6) Å and the centroid-centroid shift is 0.4003(11) Å. These dimers form sheets in the *bc* plane with intradimer vectors aligned approximately parallel to the *a* axis, generating alternating hydrophobic and hydrophilic layers (Fig. 2).

### 3.2. Pressure limits of studies

As with the study of the Pd(II) phases, α-**2** and β-**2** were each studied in a PTM of methanol/ethanol (4:1 *v/v*), which is reported as having a hydrostatic limit of 105 kbar (Klotz *et al.*, 2009). It was again the case that the limit posed by the PTM was below that of what the crystals appeared to be able to handle. For β-**2**, data is reported to 100.1 kbar but a further collection was made at 119.7 kbar and, although non-hydrostatic conditions had evidently had a detrimental effect on the system, the crystal was still diffracting well. This data is, nevertheless, omitted entirely. Similarly, a crystal of α-**2** was taken to 95.7 kbar with no significant loss of crystallinity, though no higher collections were made so to allow for data collection on decompression without the crystal becoming subject to a non-hydrostatic pressure regime. Despite this, some parameters indicate that the system

had already entered a non-hydrostatic regime at 95.7 kbar, while the data at 90.1 kbar remain consistent with the behaviour at lower pressures. Under the assumption that other factors in the experiments were consistent, such as the accuracy of pressure calibration or contamination of the PTM, this would suggest one of two cases. The first is that either α-**1** or α-**2** moderated the hydrostatic limit of the PTM slightly, perhaps by a small amount dissolving. This seems unlikely given the low solubility of either complex in the PTM. The second is that the absorbed water content of the PTM used in the two experiments differed, altering the hydrostatic limits. This appears more likely, as it has been shown that the presence of *ca.* 5 % water to 4:1 MeOH/EtOH increases the hydrostatic limit from 92 to 105 kbar (Angel *et al.*, 2007). In the case of crystals 2, 3 and 4 of β-**2**, the deeper gaskets used were found to fail at around 60 kbar.

### 3.3. Pressure dependence of cell parameters

#### 3.3.1. α-[$PtCl_2$([9]ane$S_2O$)]

Between ambient pressure and 95.7 kbar, smooth contractions of 7, 10, 9 and 23 % were observed for *a*, *b*, *c* and *V*, respectively (Fig. 3; compression of cell parameters shown in Fig. S1). For the third-order Birch-Murnaghan (BM) equation of state (EoS) calculated using *EoSFit7c* (Angel, 2014), $B_0$ = 11.8(5) GPa, $B'_0$= 9.4(6) and $V_0$ = 1036.41(6) $Å^3$. In contrast to the Pd(II) analogue, α-**2** was not found to be more resistant to compression than β-**2**.

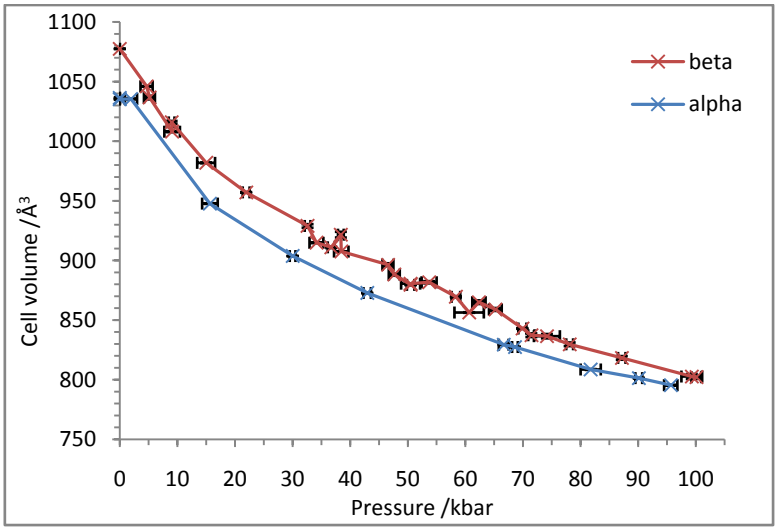



**Figure 3** The effects of pressure on the average molecular volume, *V*/*Z*, for the two phases investigated.

### 3.5.2. β-[$PtCl_2$([9]ane$S_2O$)]

Between ambient pressure and 100.1 kbar, smooth contractions of 9, 9, 10 and 26 % were observed for *a*, *b*, *c* and *V*, respectively (Fig. 3; compression of cell parameters shown in Fig. S2). For the third-order BM EoS, $B_0$ = 13.5(5) GPa, $B'_0$ = 6.3(4) and $V_0$ = 1077.44(7) $Å^3$ for all data, making it marginally less compressible than the α phase.

Between 65.2 and 69.9 kbar, a similar transformation as seen for β-**1** was observed in the material but without the corresponding phase transition. It is likely that this occurs with a small discontinuity in compression, but inconsistency between data collected using different instruments prevents this being conclusively stated.

### 3.3.3. Relative compressibility and void space analysis

An overview of the pressure dependence of the three ambient phases is given in Figure 3. As observed for **1**, the bulk compressibility of both α-**2** and β-**2** are very much typical for molecular crystals of coordination complexes. While it is again

unsurprising that the two phases are similarly compressible given the similarities in packing between them, it is interesting to note that it is the β phase which is calculated as having the greater bulk modulus, rather than the α phase as seen in the equivalent phases of **1**. That said, the difference is not statistically significant in either case, with the difference between the bulk moduli of the two phases being 1.7(7) GPa for α-**2** and β-**2**, and 1.6(11) for α-**1** and β-**1**. Another comment that can be made is that the relative compressibility of the β phases appears more similar than do the α phases (Δ = 0.7(9) and 2.2(10) GPa, respectively), though these differences are again not statistically significant. In either case, the variations seen in the data between crystals of β-**2** serve to convolute this discussion.

Depletion of the void space in the two phases of **2** greatly resembled the depletion of void space in the corresponding phases of **1**, and Fig. 4 maps the void space present in each structure as a function of pressure, calculated with a 0.002 e $Å^{-3}$ isovalue using *CrystalExplorer* (Turner *et al*., 2011; Wolff *et al*., 2012).

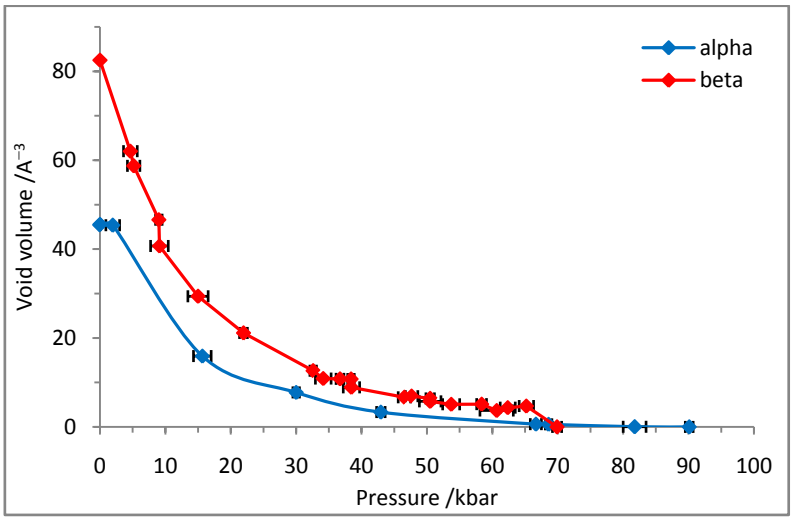



**Figure 4** The effect of pressure on the void volume in each phase, calculated using *CrystalExplorer* (Turner *et al*., 2011; Wolff *et al*., 2012) at 0.002 e $Å^{-3}$.

The α phase, which is the densest of the two phases, contains only 4.4 % void space under ambient conditions, corresponding to a difference of 2 $Å^3$ per unit cell less than the corresponding α-**1** phase. This void space is distributed in the same way as in α-**1** and located in pockets around the dimers (Fig. 5), again giving rise to a relatively hard phase as the void space is depleted very slowly and compression relies first on the compression of other much closer intermolecular contacts and of the molecules themselves.

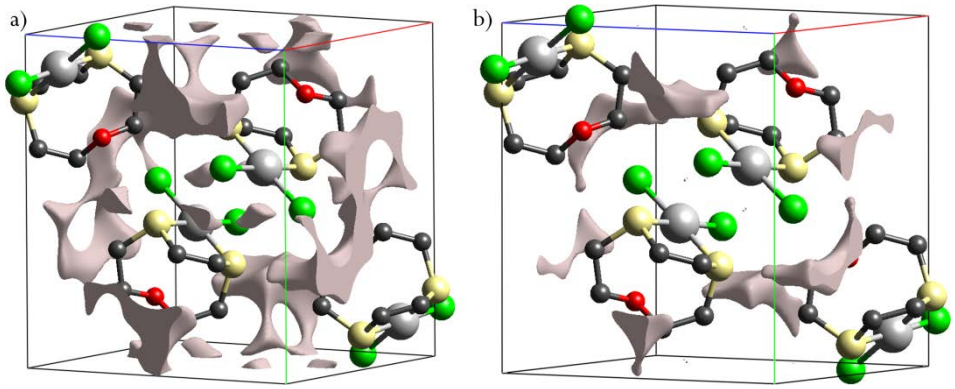



**Figure 5** The distribution of void space in α-**2** at a) ambient pressure and b) 15.7 kbar calculated using *CrystalExplorer* (Turner *et al*., 2011; Wolff *et al*., 2012) at 0.002 e $Å^{-3}$. Hydrogen atoms omitted for clarity; *a* axis in red, *b* axis in green, *c* axis in blue.

The β phase is again calculated as having nearly twice the proportion of void space under ambient conditions as the α phase (7.7 %) which is again distributed in two distinctly different regions: partially between neighbouring dimers within layers and more prominently in the region between dimer layers (Fig. 6). The graph depicting the depletion of this space as a function of pressure accordingly shows distinct regions as the first, more compressible region is rapidly depleted over the first *ca.* 10 kbar of compression with the bulk of the remaining space between dimer layers depleting more slowly and over a larger pressure range. There are again highly persistent pockets of void that remain unfilled across the entire

pressure range in which the ambient conformation alone is maintained (Figs. 4 & 6). This is indicative of both the higher resistance of C−H···H−C interactions to compression compared to C−H···*X* interactions and of an inefficient packing between dimer sheets.

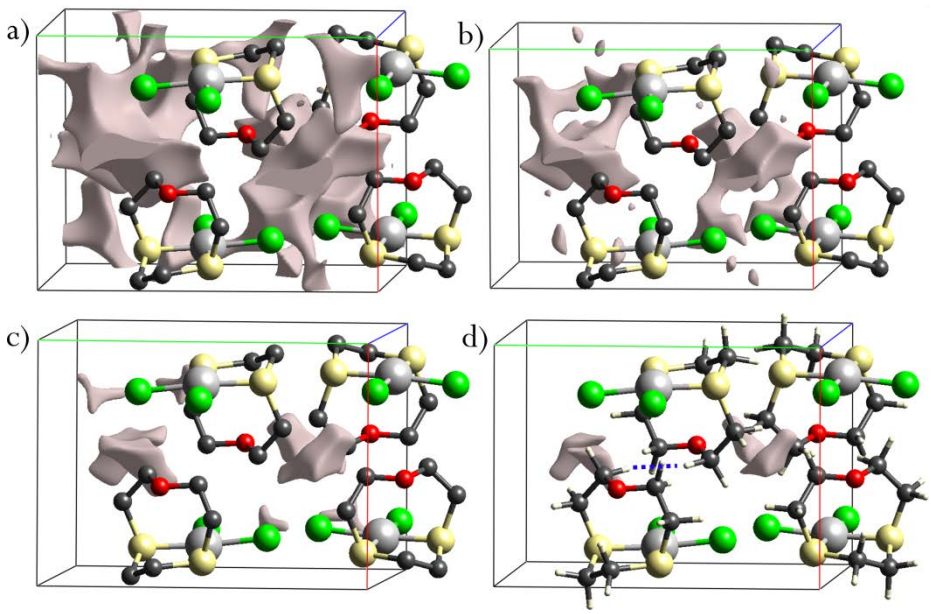



**Figure 6** The distribution of void space in β-**2** at a) ambient pressure, b) 15.0 kbar, c) 34.1kbar and d) 60.7 kbar calculated using *CrystalExplorer* (Turner *et al*., 2011; Wolff *et al*., 2012) at 0.002 e $Å^{-3}$. Hydrogen atoms omitted for clarity except at 60.7 kbar where the close C−H···H−C approach described in Section 3.4.3 is highlighted by the addition of a dashed blue line; *a* axis in red, *b* axis in green, *c* axis in blue.

### 3.4. Conformational rearrangement in β-[$PtCl_2$([9]ane$S_2$O)]

#### 3.4.1. Overview

The effects of pressure on the α phase were smooth and continuous across the entire pressure range interrogated. Although no phase transition was observed in β-**2** as was the case for β-**1**, the phase exhibited the same incomplete and disordered conformational rearrangement of the macrocycle at a similar pressure (between 65.2 and 69.9 kbar). While it is not formally a different phase, the high pressure modification of β-**2** shall henceforth be referred to as β”-**2** so as to

distinguish it from both β-**2** and β'-**1**. This absence of a comparable phase transition for β-**2** as in β-**1** is discussed in Section 3.8.

Data quality beyond the conformational rearrangement was again diminished with increased standard uncertainties on geometric parameters. A range of structural models were explored, seeking the one most compatible with both the diffraction data and the chemistry. The extensively disordered model reported at 69.9 and 100.1 kbar was unstable to refinement in the case of the slightly weaker and lower resolution data collected from 71.5 to 99.3 kbar and numerous atoms had to be refined with constrained identical coordinates and anisotropic displacement parameters. Nevertheless, the model obtained for 69.9 and 100.1 kbar is believed to be the most accurate description of β"-**2**.

Much as in the case of β-**1**, the discussion of the pressure dependence of the structure of β-**2** and β"-**2** will therefore involve the behaviour of the form found at ambient pressure, which is ordered and subject to standard uncertainties of similar magnitude as the other phases, and of the modified form above 65.2 kbar, for which the magnitude of the standard uncertainties place more limitations on the extent of the discussion and comparisons possible.

### 3.4.2. Description of the structure at high-pressure

The conformational rearrangement that ensues in the β-**2** → β"-**2** transformation does not alter the *exodentate* coordination mode and the Pt(II) centres remain bound by $Cl_2S_2$ donor sets and the supramolecular layered motif of dimers persists. The resulting conformation of the macrocycle in the affected molecules is the same [135] conformation as seen in β'-**1** (Fig. 7, *cf.* Chapter 3, Section 3.4.2, Fig. 12).

The conformationally transformed component of the structure refines to an occupancy of *ca.* 30 %. Considered alongside the arrangement of molecules seen in β'-**1**, this would imply that the crystal comprises a similar 2:1 mixture of dimers comprising one transformed molecule and one in the ambient conformation, and entirely of the ambient form, respectively. While the possibility of a dimer comprising two molecules in the modified form cannot be completely ruled out from the crystallography alone, this is at the very least statistically unlikely. Naming of the unchanged molecule is carried forth from β-**2** while atoms of the transformed molecules are given the suffix "A", as shown in Fig. 7.

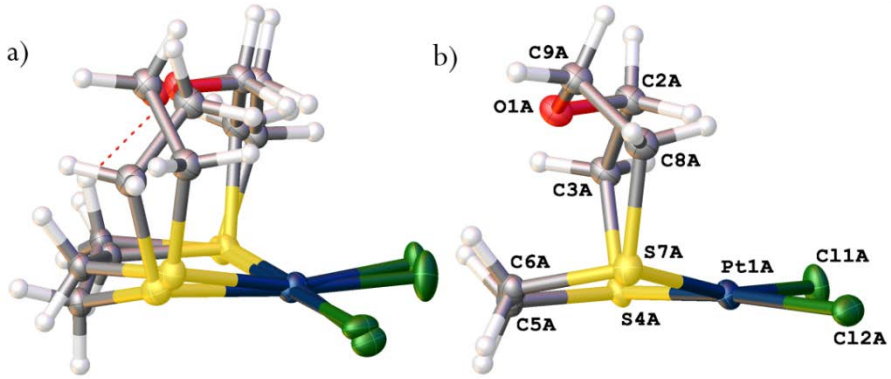



**Figure 7** a) View of disordered asymmetric unit in β"-**2** at 69.9 kbar. b) View of the [135] conformation of the macrocycle in the molecule in β"-**2** at 69.9 kbar with atoms numbered in accordance with the text. Anisotropic displacement parameters drawn at 50 % probability level.

### 3.4.3. Rationalisation of the transformation

In the same way that the application of pressure to β-**1** results in the near-linear approach of two C−H moieties, so too is the case for β-**2**, while beyond the terminal carbons of this approach there again lies a persistent region of void space, as described in Section 3.3.3 (Fig. 6). While the data for this approach appear anomalously higher prior to the transformation than was the case for β-**1**, the

uncertainty on these parameters is also clearly greater, implicitly displayed by the uncertainty for the approaching carbon atoms on which the hydrogen positions are based (Fig. 8; *cf.* Chapter 3,Section 3.4.3, Fig. 13). Therefore, it is better to rely on the prediction of a line of best fit to establish the approximate distance prior to the transition. By this method, it can be seen that raising the pressure to, for example, 67.6 kbar brings this interaction close to the sum of the relevant van der Waals radii [H9b···H9b_#4 = *ca.* 2.65 Å; $\Sigma_{vdW}$ = 2.4 Å (Bondi, 1964)]. Just as in β-**1**, at about this distance the repulsion between the hydrogen atoms overcomes the strain of the macrocycle and other pressures exerted on the molecule within the crystal and results in the moiety rearranging to occupy the region of void beyond the termini of the interaction, alleviating this repulsive contact. While this separation appears clearly outside the sum of the van der Waals radii, treatment of the hydrogen atoms followed the same routine as in β-**1**. Consequently, the C−H bond length is fixed at the X-ray crystallographic standard of 0.97 Å. If the bond length was selected to be more reminiscent of those obtained from neutron studies (see Schmidtmann *et al.*, 2014) then this separation would be around 0.2 Å lower and the repulsive contact more apparent.

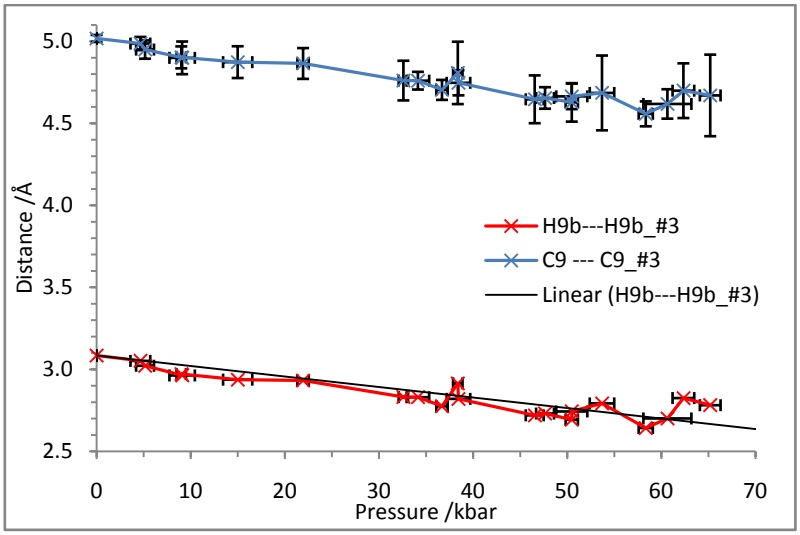



**Figure 8** The effect of pressure on the approximately linear approach of C9−H9b···H9b_#3−C9_#3 (symmetry code #3 = 1 − *x*, 1 − *y*, −*z*) in β-**2**. C−H bond lengths are constrained at 0.97 Å.

Being isomorphous with β-**1**, two additional sets of relevant close contacts could be expected and are indeed formed. Up to the transformation, close S···Cl contacts are formed between the bases of molecules within dimers, as too are contacts between H6a and the two chloride donors of the paired molecule (Fig. 9). The rearrangement serves to alleviate one of the S···Cl contacts by lifting the affected sulfur donor from the plane, alongside a simultaneous flattening of the S4−C6−C6−S7 torsion angle. This in turn relieves the close contact between H6a and the chloride donors of the neighbouring molecule. While these two interactions are not presented as primary drivers of the transformation, their effects on the macrocycle would assist conformational rearrangement.

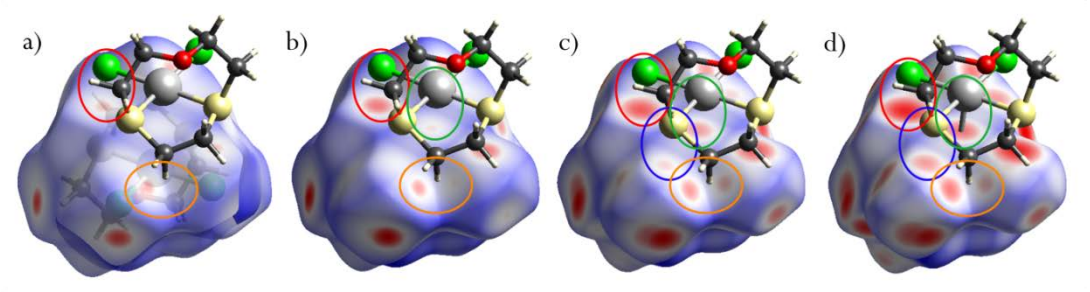



**Figure 9** Hirshfeld surfaces (Spackman & Jayatilaka, 2009) for β-**2** at a) ambient pressure, b) 9.1 kbar, c) 34.1 kbar and d) 65.2 kbar showing the effect of pressure on intradimer intermolecular contacts at the base of the molecule. Note the swift development of red spots at one pair of Cl and S donors (Cl2 and S4; circled in red, symmetry equivalent contacts not circled) compared to the other pair (Cl1 and S7; circled in blue, symmetry equivalent contacts not circled). H6a···Cl1/2 contacts circled in orange and Pt···Pt contact circled in green.

### 3.5. Pressure dependence of the coordination sphere

#### 3.5.1. α-[$PtCl_2$([9]ane$S_2O$)]

A pressure of 95.7 kbar leads to slightly differing compression of the equatorial donor set, with the Pt−Cl interactions compressing by twice that of the Pt−S interactions [ΔPt1−Cl1, ΔPt1−Cl2 = −0.021(4), −0.021(3) Å, and ΔPt1−S4, ΔPt1-S7 = −0.013(3), −0.009(4) Å, respectively] (*cf.* Fig. 33). The apical Pt···O interaction undergoes significantly greater compression across this pressure range and contracts linearly down to *ca.* 65 kbar, at which point compression appears to slow slightly (Fig. 10). By 95.7 kbar, this interaction has reached a final length of 2.897(9) Å, a total contraction of 0.187(10) Å. This is only marginally less than the total compression of the equivalent Pd···O interaction in α-**1**, which undergoes a contraction of 0.217(5) Å under 103.4 kbar pressure.

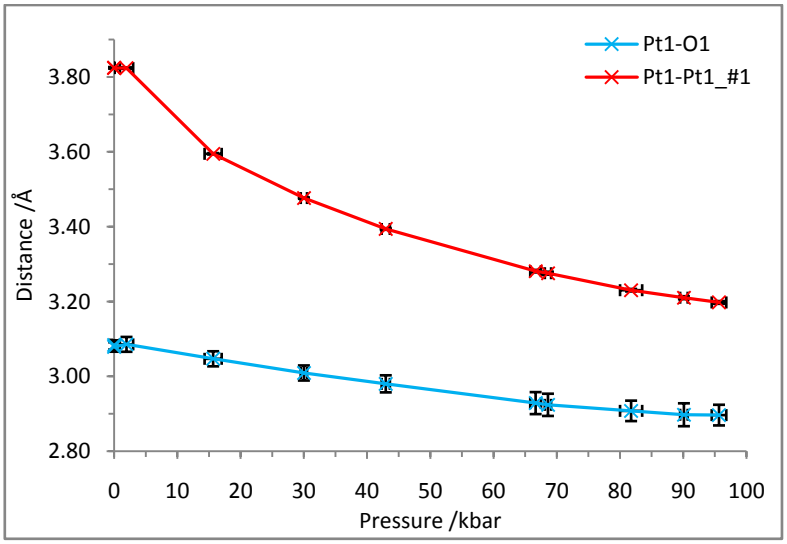



**Figure 10** The effects of pressure on the axial parameters of α-**2**. Symmetry code #1 = −*x*, 2 − *y*, −*z*.

The compression observed in the intradimer Pt···Pt interaction is greater still, with a smooth contraction of 0.6275(13) Å over 95.7 kbar to a final length of 3.1978(12) Å. This is compared to 0.6447(19) Å over 103.4 kbar for the equivalent Pd···Pd interaction in α-**1**. Nevertheless, this interaction falls below the sum of the van der Waals radii [$\Sigma_{vdW}$ = 3.50 Å (Bondi, 1964)] at a much lower pressure of *ca.* 27 kbar, *cf.* 66 kbar in α-**1**. Throughout this contraction, the general arrangement of the dimer remains stable and the centroid-centroid slippage of the two least squares planes defined by the $Cl_2S_2$ donor sets is unchanged at *ca.* 1.125 Å. Although the Pt···Pt interaction is marginally longer than the corresponding Pd···Pd interaction, the difference is not directly reminiscent of the differing van der Waals radii of the two metals. Equally, the greater size of the Pt(II) centre does not appear to further hinder the compression of this interaction and the pressure dependence of the two *M*···*M* interactions appears almost identical. Thus, it seems that the significantly lower pressure at which the Pt···Pt interaction crosses to within the sum of the van der Waals radii compared to the Pd···Pd interaction in α-**1** is owed simply to the

larger van der Waals radii of Pt. Rather than the interaction being significantly softer in α-**2** than in α-**1**, compression of the *M*···*M* interaction in both phases is limited primarily by compression of the less favourable intradimer S···Cl contacts.

Simultaneous to these apical contractions is an approximately symmetrical distortion of the coordination plane whereby the *trans* coordination angles deviate further from 180 ° (Fig. 11). The Pt(II) centre moves steadily out of the $Cl_2S_2$ plane and away from the incoming O donor [Δ = 0.051(2) Å at 95.7 kbar] while the RMS deviation of the defining atoms from the plane tends towards zero (Fig. 12).

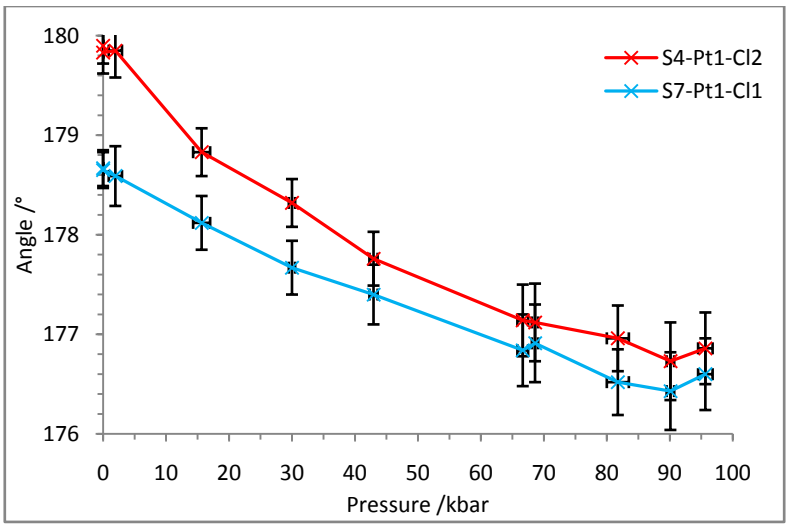



**Figure 11** The effect of pressure on the *trans* coordination angles in α-**2**.

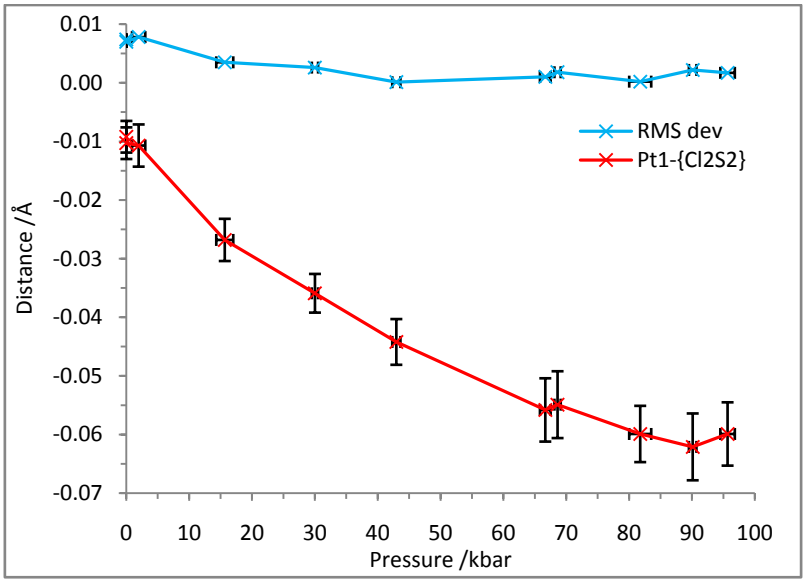



**Figure 12** The deviation of the Pt(II) centre from the least squares mean plane defined by the $Cl_2S_2$ donor set in α-**2**.

The deformation of the coordination plane in α-**2** is almost identical in comparison to that of α-**1** and occurs for the same reasons. Although the S···Cl interactions form contacts at a similar range as does the Pt···Pt interaction (Fig. 13), this phenomenon further shows that they offer significantly greater resistance to compression. Additionally, that the Pt···O interaction is similarly resistant to compression as the Pd···O interaction and again more so than the corresponding *M*···*M* interaction. Consequently, as the base of the two molecules within the dimer are brought together, the $Cl_2S_2$ donor sets resist compression while the O donors exert an additional force on the Pt···Pt interaction. This results in the observed deviation of the metal centre from the mean square plane defined by the donor atoms. Given that the deformation in the two phases is almost exactly the same, in the range of pressure and separation interrogated for these two phases, the two coordination planes can be described as equally deformable.

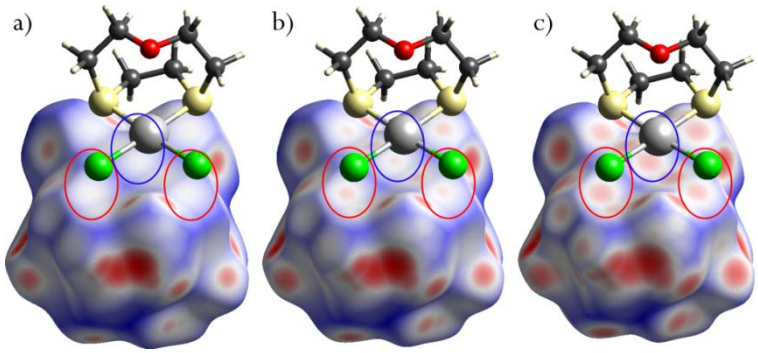



**Figure 13** Hirshfeld surfaces (Spackman & Jayatilaka, 2009) for α-**2** showing the base of the molecule within the dimer at a) 30.0 kbar, b) 43.0 kbar and c) 66.7 kbar. Note the generation of red spots between the Cl and S donors (circled in red; symmetry equivalents not circled) at a similar rate as between Pt(II) centres (circled in blue).

### 3.5.2. β-[$PtCl_2$([9]ane$S_2O$)]

The effects of pressures on the equatorial donor set in β-**2** are obscured by the uncertainties in the derived parameters, even at low pressures, and little detailed discussion can be made (Fig. 14). The data collected for crystal 3 at 60.1 kbar provides the highest pressure data point where the ESUs do not fully obscure the trend and from this it can be calculated that the Pt−S bonds are compressed by 0.029(4) and 0.027(3) Å and the Pt−Cl bonds by 0.025(3) and 0.013(4) Å.

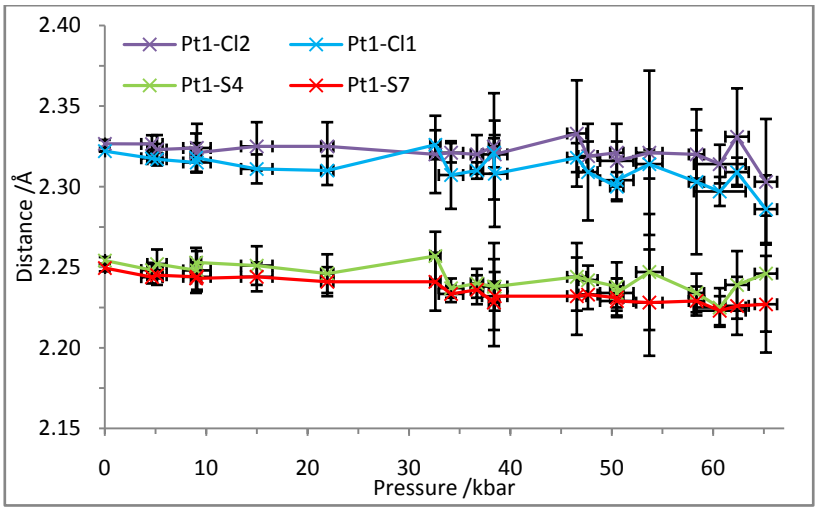



**Figure 14** The effects of pressure on the coordination plane in β-**2**.

Just as with the equivalent phases of compound **1**, this compression of the coordination plane of β-**2** is greater than to total compression observed in the α phase. This difference is perhaps reflective of the greater resistance to compression of the aliphatic region between sheets of dimers in the β phases resulting in a greater pressure being exerted elsewhere throughout the crystal. In addition, H contacts to the Cl and S donors are in general shorter in β-**2** than α-**2** even at ambient pressure, as can be seen using fingerprint plots (Fig. 15), and so the coordination bonds are more readily affected by pressure.

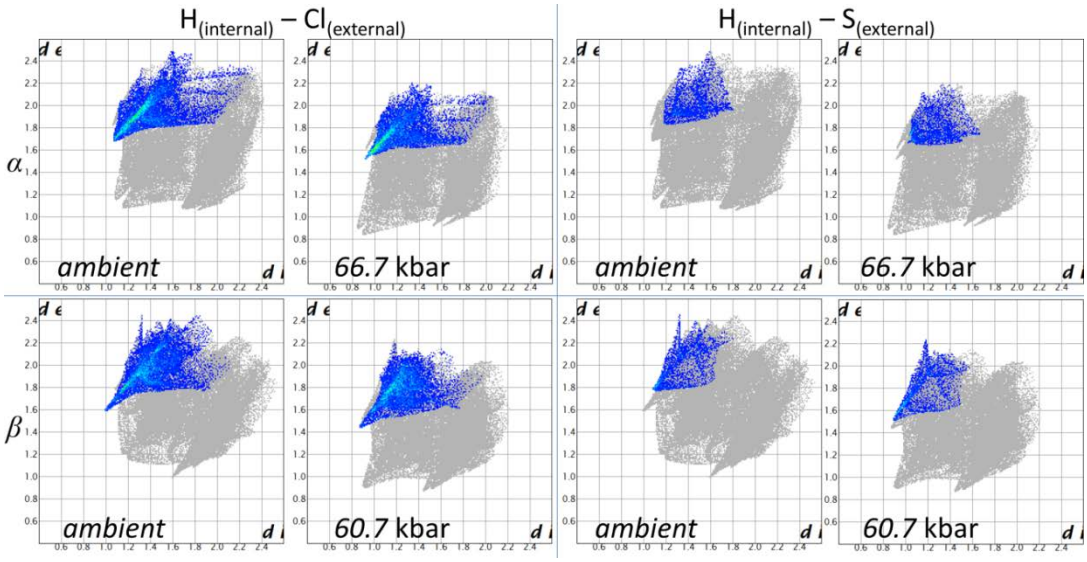



**Figure 15** Fingerprint plots (Spackman & McKinnon, 2002) generated for intermolecular contacts in the α (top) and β (bottom) phases at ambient pressure at 66.7 kbar; H−Cl (left) and H−S (right) contacts highlighted in blue. Note that given contacts are closer for β-**2** than for α-**2**.

As seen for the α phase, the length of the Pt···Pt interaction in the β-**2** form is significantly affected by pressure and by 65.2 kbar has fallen by 0.416(8) Å to 3.1139(8) Å. The magnitude of this contraction is almost identical to the corresponding contraction in β-**1**, while the separation achieved remains ca. 0.04 Å greater. In contrast to α-**2**, it takes less than 5 kbar to compress the Pt···Pt distance

below the sum of the van der Waals radii [$\Sigma_{vdW}$ = 3.50 Å (Bondi, 1964)] and, similarly as in the case of compound **1**, by *ca*.45 kbar it has already reached the minimum distance observed for α-**2** at 95.7 kbar (Fig. 16, *cf*. Fig. 10).

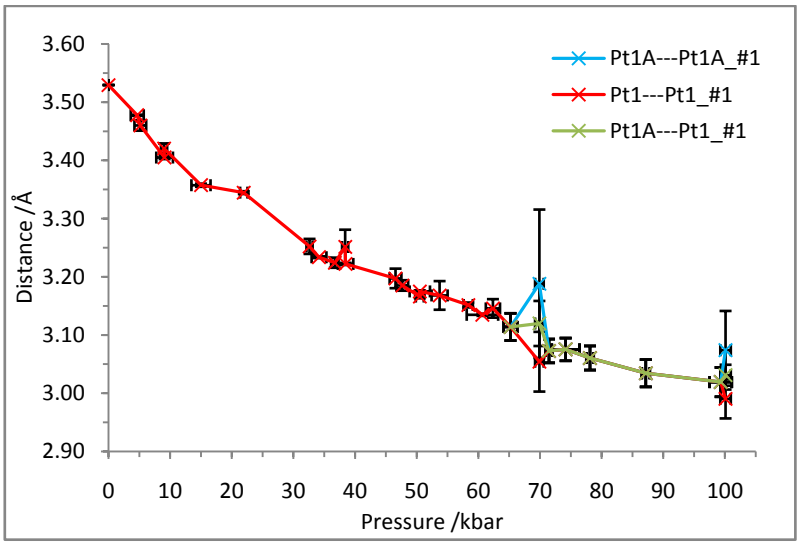



**Figure 16** The effects of pressure on the Pt···Pt interactions in β-**2** and β"-**2**. Symmetry code #1 = −*x*, 2 − *y*, −*z* in β-**2**.

The most prominent effect of pressure on the coordination plane of the molecule is the deviation of the *trans* S7−Pt1−Cl1 angle from 180 ° (Fig. 17), the result of Cl1 moving out of the plane away from the other molecule in the dimeric motif. Of the *cis* angles, those involving Cl1 are the most deformed by pressure (Fig.18). There is no reason to suggest this behaviour arises by any different means than those described as for the equivalent behaviour in β-**1**: the close contacts shown on the Hirshfeld surfaces (Fig. 9), distribution of void space (Fig. 6) and magnitude of the deviation in the angles all match well with the corresponding data described in Chapter 3 (*cf*. Chapter 3, Figs. 14, 6 and 20-21, respectively).

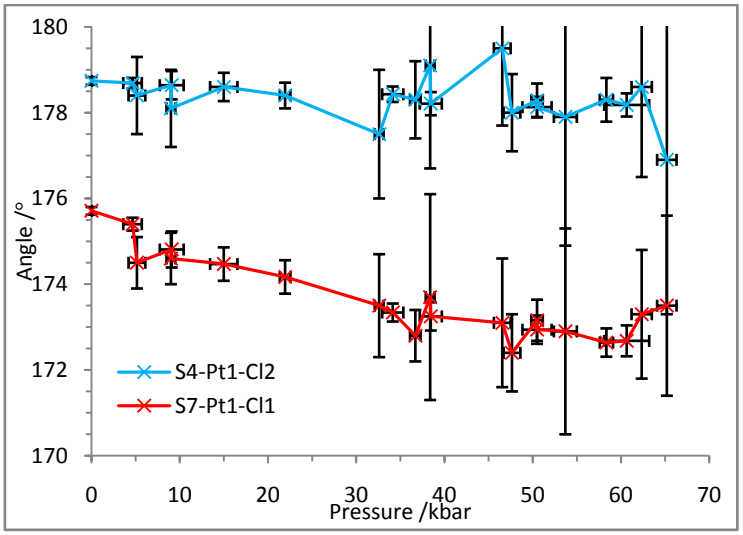



**Figure 17** The effects of pressure on the *trans* angles in the coordination plane of β-**2**.

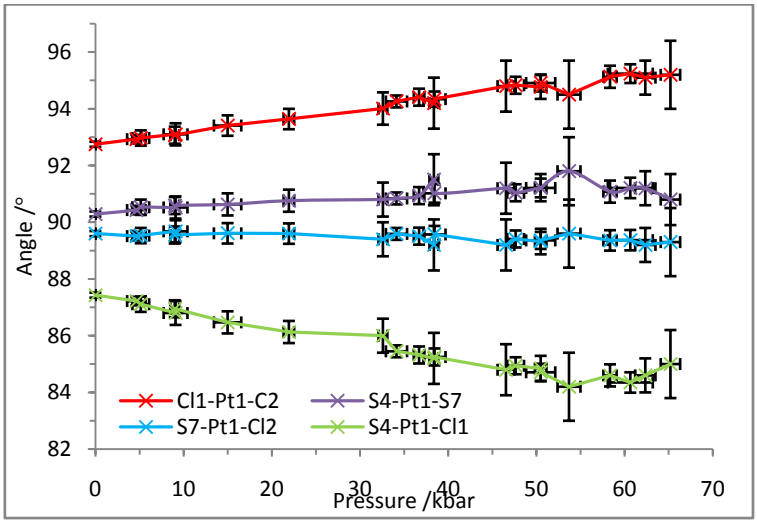



**Figure 18** The effects of pressure on the *cis* angles in the coordination plane of β-**2**.

In light of the changing position of Cl1 relative to the other donors, the mean plane of the coordination environment is again chosen as that formed by S4, S7 and Cl2, just as with β-**1**. As discussed above, Cl1 deviates from the plane of the molecule in the opposite direction from the other molecule in the dimeric motif, though the precision of the data obscures any clear description of how this proceeds as a function of pressure (Fig. 19). Just was observed in β-**1** there is almost no

movement of the metal centre with respect to this plane. This behaviour lends further support to the earlier contention that the incoming O donor gives rise to the deviation of the metal centre from the plane in the α phases.

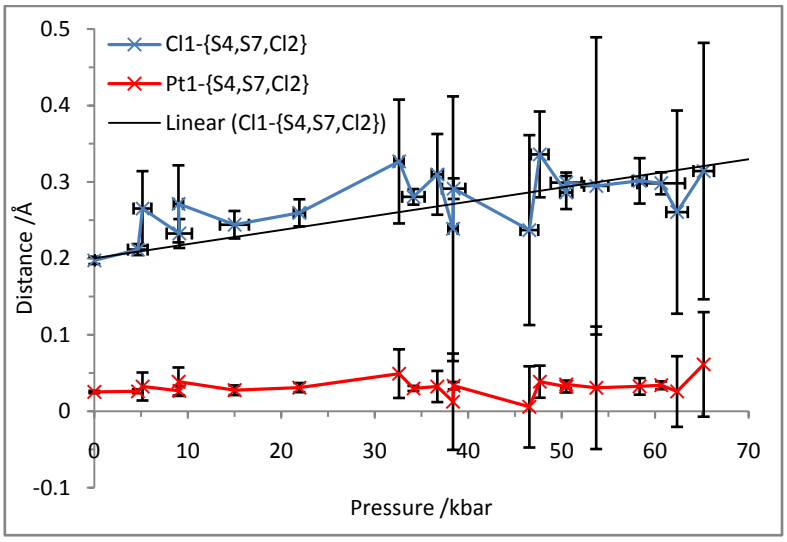



**Figure 19** The effects of pressure on the position of Pt1 and Cl1 with regards to the plane defined by S4, S7 and Cl2 in β-**2**. A linear line of best fit is added to the data for Cl1 to help highlight the general trend.

### 3.5.3. β"-[$PtCl_2$([9]ane$S_2$O)]

The disorder brought about by the conformational rearrangement and the stress exerted on the crystal by the transformation result in the data for β"-**2** being similarly poor as the data for β'-**1**. Analysis of the effects of pressure on the different resulting coordination interactions is further limited by the inability to fully separate the different disorder components in the majority of solutions obtained for this regime. As a consequence of this, these data are subject to even greater uncertainties than the corresponding β'-**1** data. Nevertheless, trends in the derived values for the compression and deformation of the coordination plane map well to those seen in β'-**1** so, although the accuracy of the values is certainly in question, it is still relevant to highlight these.

While the ESUs serve to entirely preclude numerical analysis in the case of the pressure dependence of the angles in the coordination plane, the general trends in these parameters for the two resulting conformers in β”-**2** precisely follow those seen for β’-**1** (Fig. 20, *cf*. Chapter 3, Section 3.5.3, Fig. 23). This reflects the similarity of the transformation between the two phases: again it appears that S7A is lifted out of the coordination plane and away from the paired molecule of the dimer (Fig. 20). The torsion across S4−C5−C6−S7 is again flattened towards an angle of zero (Fig. 21) and C6−H6a is rotated to point less directly at the chloride donors. The untransformed molecule (*i.e.*, that corresponding to Pt1) is seemingly subject to a marginal relief of the bending of Cl1−Pt1−S7, indicative of the refined atoms comprising components owed to molecules that form dimer pairs with transformed molecules: a relief of Cl1−Pt1−S7 is expected when the corresponding molecule in the dimer pair is subject to the conformational rearrangement (*cf*. Chapter 3, Section 3.5.3).

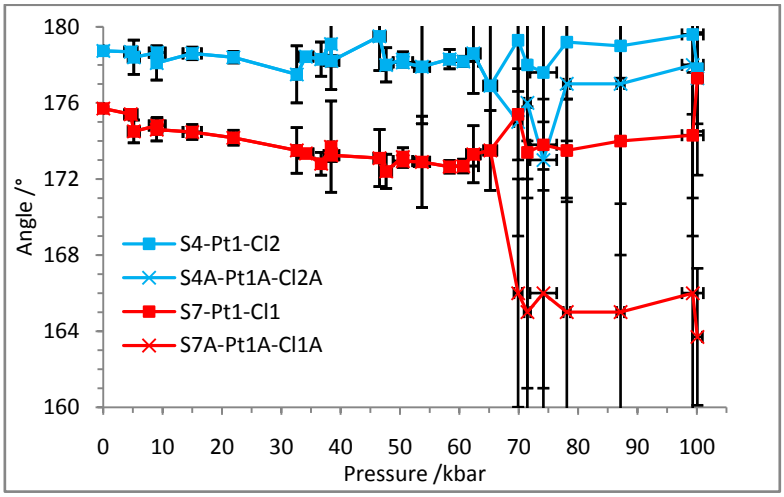



**Figure 20** The effects of the β → β” transformation on the *trans* coordination angles for molecules at Pt1 and Pt1A dimer wherein the macrocycle bound to Pt1A has undergone conformational rearrangement.

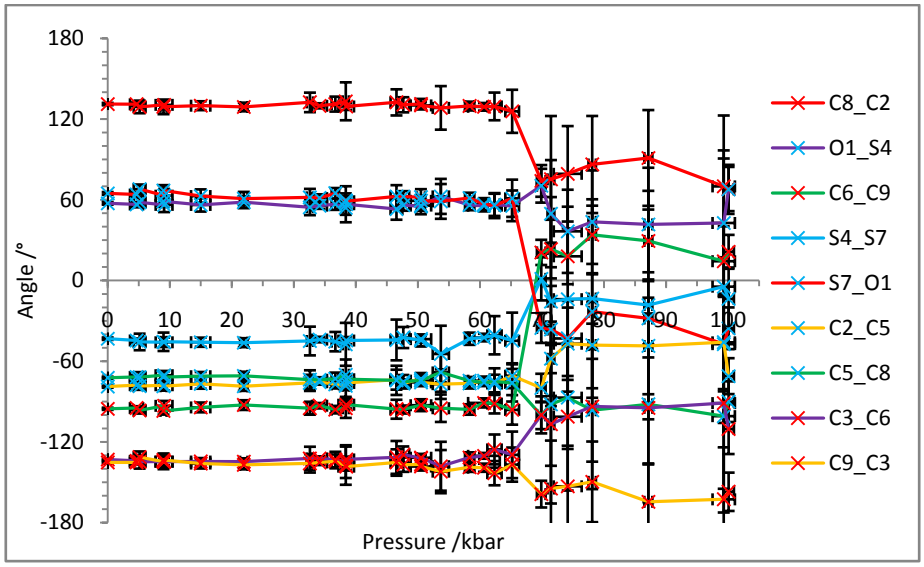



**Figure 21** The effects of pressure on the torsional angles for the macrocycle bound to Pt1A in β"-**2** (>67 kbar) relative to the macrocycle in β-**2** (<67 kbar).

The transformation produces three possible unique Pt···Pt combinations though the two unique metal sites could only be refined separately at 69.9 and 100.1 kbar, being constrained to occupy the same site otherwise. Consequently, a detailed extrapolation of discontinuity or divergence in the compression of these interactions is not possible. It can, however, be stated that the interactions continue to compress much as in the same way as prior to the transformation (Fig. 16), and the final Pt···Pt separations at 100.1 kbar are 2.990(11) Å in a dimer of untransformed molecules, 3.031(6) Å in the mixed dimer and 3.07(2) Å in the possible case of a dimer comprising only transformed molecules.

While the uncertainties in the data continue to preclude accurate discussion, the effect of pressure on the slippage of the least squares planes in the supramolecular dimeric motif (Fig. 22) appears to resemble that of the corresponding phases of compound **1**. The data suggest that the transformation results in a decrease in slippage in dimers directly affected while those not subject to it appear to plateau.

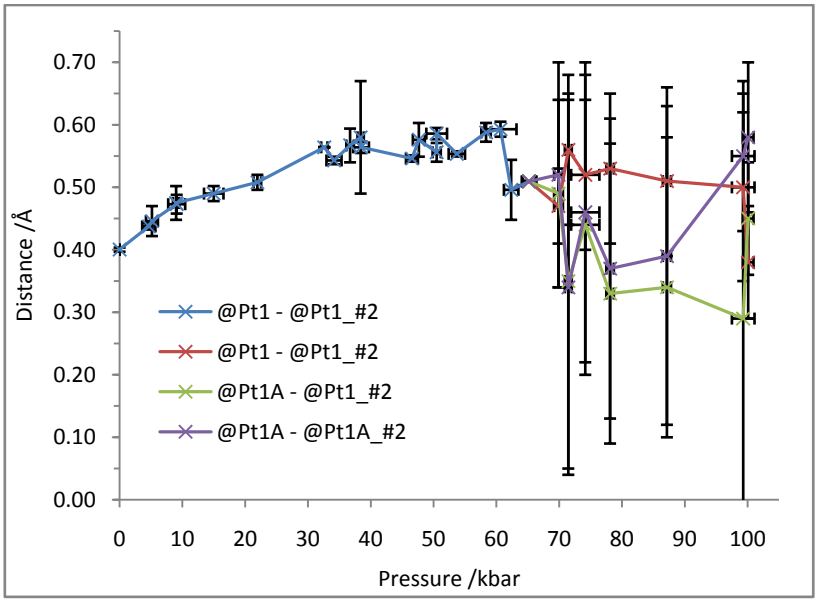



**Figure 22** The effect of pressure on the centroid-centroid slippage for the $Cl_2S_2Pt$ least squares planes within dimers in β-**2** (blue) and β”-**2** (red, green, purple). @Pt1 corresponds to the molecule not subject to the transformation and @Pt1A corresponds to that which was.

### 3.6. Pressure dependence of the macrocyclic conformation

Throughout this study there are no notable changes to the conformation of the macrocycles in α-**2** (Fig. 23). As discussed in Section 3.4.3, this is not the case for β-**2** (Fig. 21) which undergoes an incomplete conformational rearrangement to give rise to a disordered arrangement involving the same [135] conformation as arose across the β → β’ transformation detailed in Chapter 3. This is described by a switching of the torsion across S7−C8−C9−O1 and a flattening of S4−C5−C6−S7.

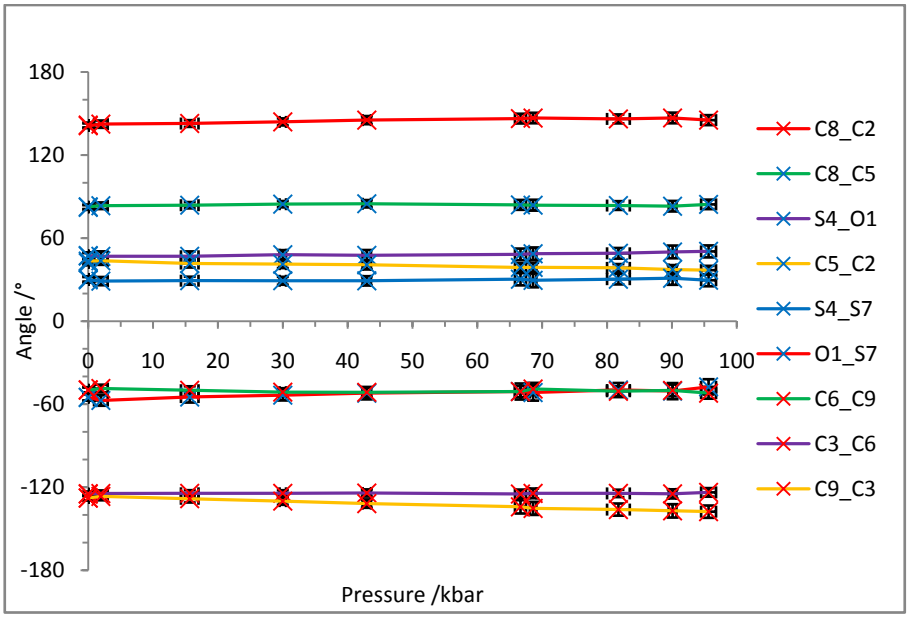



**Figure 23** The effects of pressure on the torsional angles for the macrocycle bound to Pt1 in α-**2**.

### 3.7. Temperature-dependent studies

Variable-temperature single-crystal X-ray diffraction studies were carried out in the ranges 90−490 K for both the α and β phases as described in Section 2.2.2. In the case of crystal T0 for β-**2**, *ca.* 1 % discrepancy is observed when comparing the cell volume at 290 K as-synthesised with those later collected after the cooling cycle (Fig. 24), similar to the artefacts observed in the corresponding data collected on compound **1**. The data were recollected at a higher ramp-rate which gave no such artefacts. Additionally, the data for the α phase which was collected at an intermediary ramp rate compared to the two collections for β-**2** also lacks this anomaly. This data would indicate that these are associated to an insufficiently fast ramp rate, with the ramping process and temperature regulation of the equipment appearing to become unreliable between 120 and 60 K $hr^{-1}$. Consequently, data for crystal T0 of β-**2** will not be discussed any further.

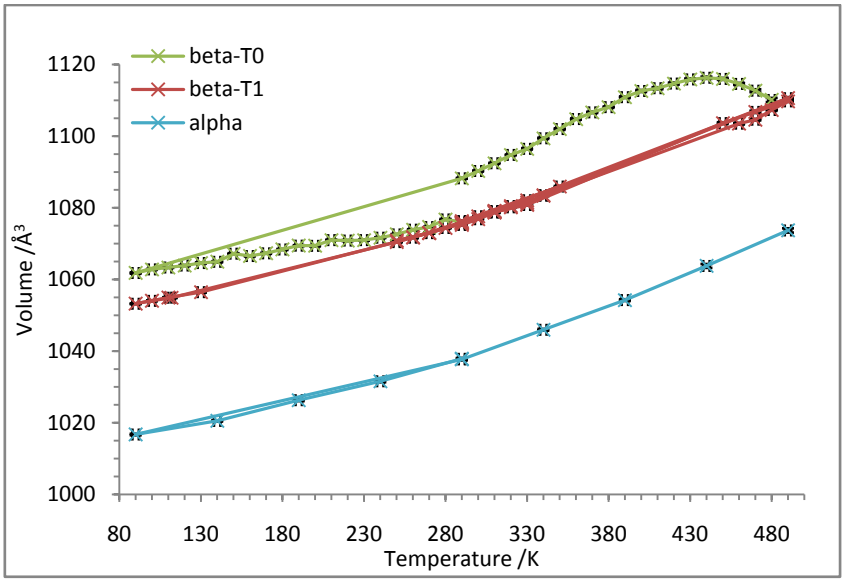



**Figure 24** The effects of temperature on the cell volume for the two phases of **2**. "beta-T*x*" corresponds to crystal 'T*x*' (*x* = 0, 1) of the β phase. Note that the anomalous trace for "beta-T0" is most likely owed to equipment problems and experimental design.

The temperature dependence of the cell unit cell volume of the three experiments performed on the two phases is given in Figure 24. Smooth positive thermal expansion was observed in all phases, with no indication of any thermally induced phenomena. In each of the graphs in this Section, the lines track the progress of the experiments, each starting at 290 K.

### 3.7.1. α-[$PtCl_2$([9]ane$S_2O$)]

The length of the apical Pt1···O1 interaction in α-**2** is almost invariant across the temperature range investigated and expands by a total of 0.010(7) Å between 90 and 490 K (Fig. 25), notably lower than the effect seen in α-**1** between 90 and 390 K [ΔPd1···O1 =0.022(3) Å]. In contrast, the effect of temperature on the separation of Pt1···Pt1_#1 (symmetry code #1 = −*x*, 2 − *y*, −*z*) is found to be directly comparable to the analogous Pd1···Pd1_#1 interaction in α-**1**, and the total

expansion between 90 and 490 K was 0.1967(8) Å. The effect of cooling from 290 to 90 K was again equivalent to the application of c*a.* 5 kbar with a contraction of 0.0737(6) Å observed.

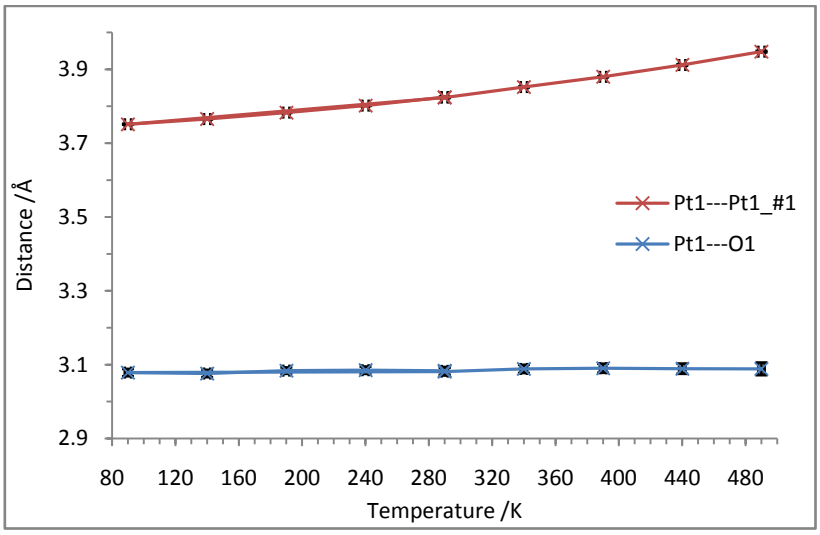



**Figure 25** The effects of temperature on the apical interactions to Pt1 in α-**2**. Symmetry code #1 = −*x*, 2 − *y*, −*z*.

Although the Pt-Cl interactions appear to be contracted by heating (Fig. 26), the libration corrected values for Pt1−Cl1 and Pt1−Cl2 at 90 K are calculated as being 2.3368 and 2.3408 Å while at 490 they are calculated as being 2.3387 and 2.3390 Å, respectively (Hirshfeld, 1976; Spek, 2009). Variation of temperature does not exert significant effects on the other intramolecular parameters over the range studied (Fig. S3-S4).

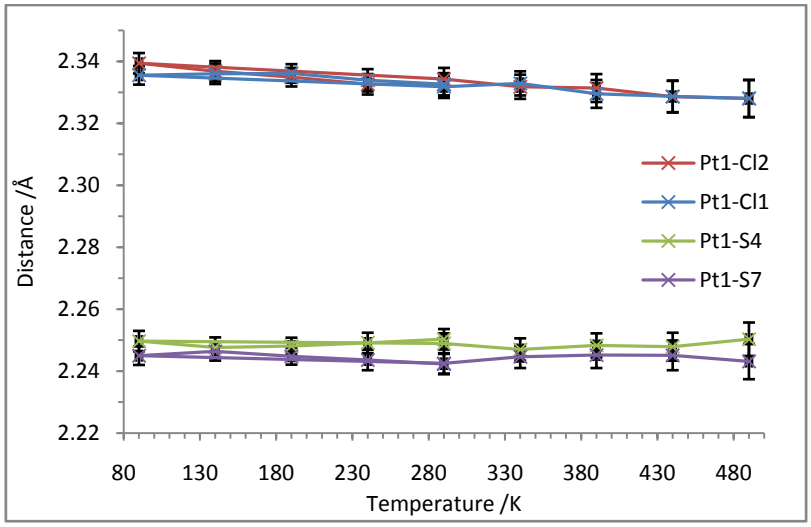



**Figure 26** The effects of temperature on the coordination bonds to Pt1 in α-**2**.

### 3.7.2. β-[$PtCl_2$([9]ane$S_2O$)]

Variation of the temperature from 90 to 490 K has little effect on the main structural parameters in β-**2** and does not bring about the transformation seen in the pressure dependant experiments. Between 90 and 490 K the intradimer Pt1···Pt1_#2 (symmetry code #2 = −*x*, 1 − *y*, −*z*) separation varies linearly by a total of 0.1173(8) Å (Fig. 27). Cooling from 290 to 90 K gives a contraction of 0.0513(4) Å, equivalent to the compression associated with *ca.* 5 kbar pressure.

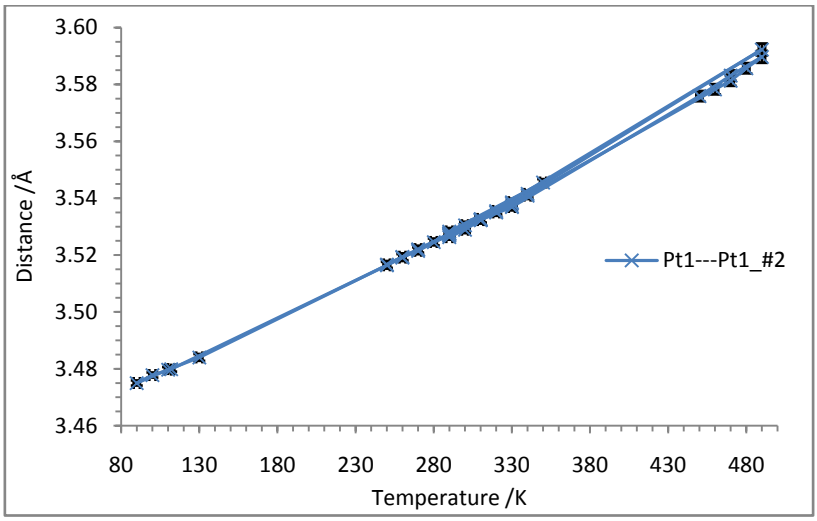



**Figure 27** The effects of temperature on the intradimer Pt1···Pt1_#2 separation in β-**2**. Symmetry code #2 = −*x*, 1 − *y*, −*z*.

It remains the case the temperature exerts negligible effect on the coordination plane of the molecule and the coordination bond lengths are effectively unchanged (Fig. S5). The bending of the *trans* S7−Pt1−Cl1 angle appears to be relaxed by increased temperature (Fig. 28), an observation which can be rationalised by the thermal expansion of the crystal reducing the contacts that otherwise cause the bending. The behaviour is again reflected in the behaviour of *cis* S4−Pt1−Cl1 which relaxes towards 90 ° (Fig. 29).

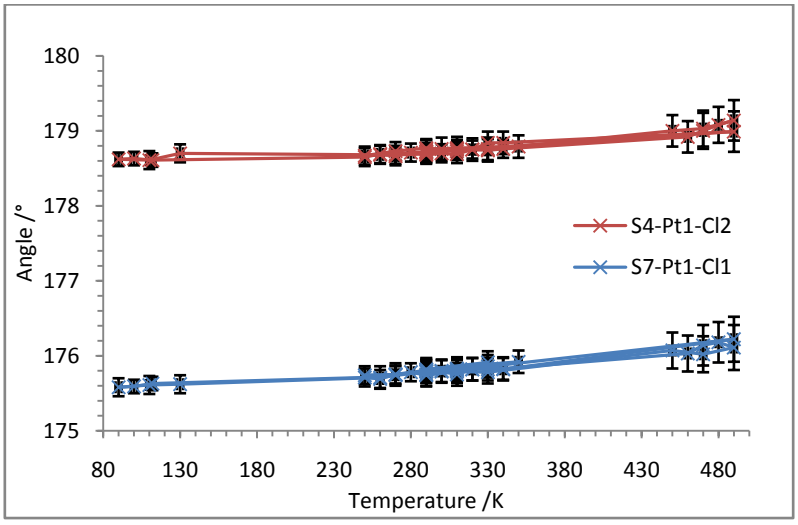



**Figure 28** The effects of temperature on the *trans* coordination bond angles in β-**2**.

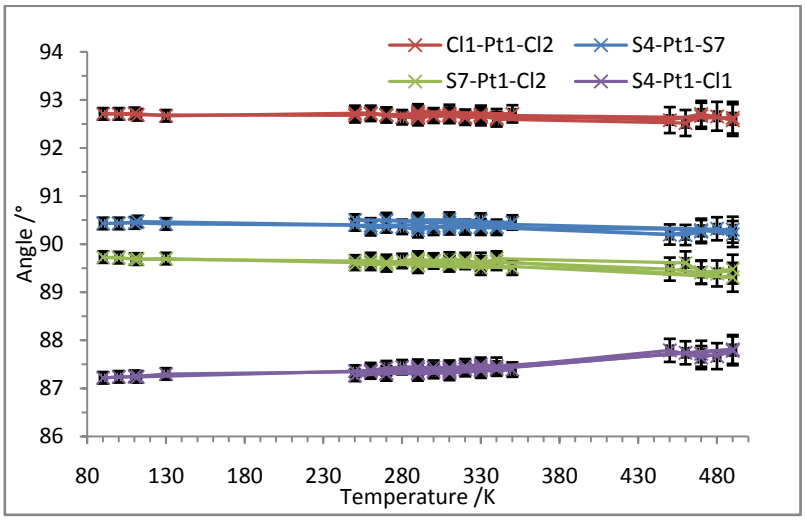



**Figure 29** The effects of temperature on the *cis* coordination bond angles in β-**2**.

### 3.8. Calculated energies and bond orders

Density functional theory calculations were carried out on two-molecule fragments of each experimentally-determined high-pressure crystal structure using the Amsterdam Density Functional suite (Fonseca-Guerra *et al.*, 1998; Te Velde *et al.*, 2001). These were carried out to obtain a quantitative estimation of the effect of pressure on the bond orders of Pt···Pt, Pt···O and Pd–*L* interactions and on the relative energies of the fragments considered. The energies discussed herein correspond to the total bonding energy ($\Delta E_{bond}$) of the fragments considered in each calculation. This is calculated as the sum of the repulsive total steric interaction energy ($\Delta E_{steric}$) and attractive total orbital interactions ($\Delta E_{OI}$) where the total steric interaction energy is calculated as the sum of the Pauli repulsion ($\Delta E_{Pauli}$) and electrostatic interactions ($\Delta E_{EI}$):

$$\Delta E_{bond} = \Delta E_{OI} + \Delta E_{Pauli} + \Delta E_{EI}$$

The effect of pressure on the total bonding energy in the considered fragments of the α and β phases and also the unmodified dimer in β”-**2** is exceedingly similar, all increasing at a rate of *ca.*1.5 kJ mol$^{-1}$ kbar$^{-1}$ per dimer fragment after *ca.* 35 kbar (Fig. 30). Prior to this pressure, the calculated rate of increase in total bonding energy is *ca.* 0.2 and 0.5 kJ mol$^{-1}$ kbar$^{-1}$ per dimer fragment for the α and β phases, respectively. Such a lag in the onset of an increase in energy was not observed in the equivalent phases of **1**. Where structural parameters between isostructural phases of the differing compounds are so similar, this lag is likely attributed to a difference in the interactions between / at the metal centres.

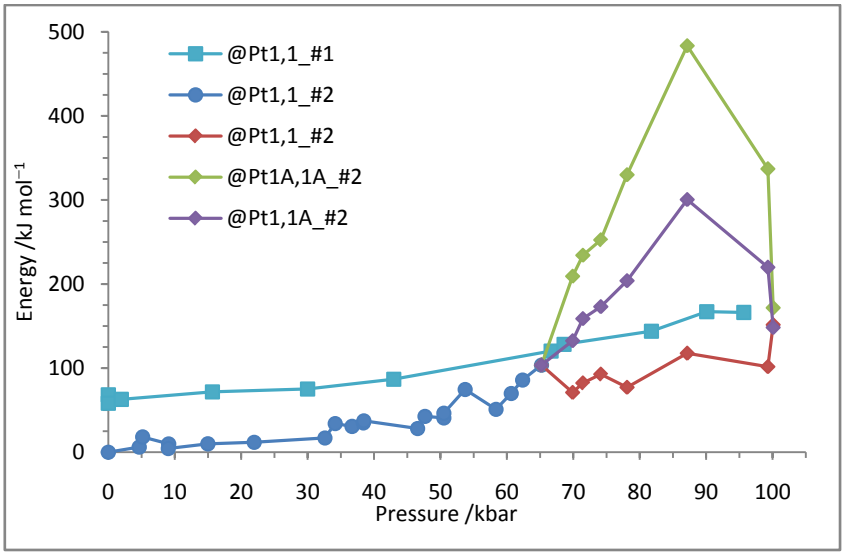



**Figure 30** The calculated bonding energy for the two-molecule fragments described in Section 2.3 for α-**2** (squares), β-**2** (circles) and β”-**2** (diamonds). Symmetry code #1 = −*x*, 2 − *y*, −*z*; #2 = −*x*, 1 − *y*, −*z*.

In the case of a dimer in β”-**2** comprising two transformed molecules, pressure appears to have a significantly greater effect on the total bonding energy which would initially suggest that it is increasingly unlikely to be present. However, with the exception of the data at 69.9 and 100.1 kbar, these calculations were based on structures for which the refinement of the metal and chloride sites are constrained to occupy the same site as the corresponding atoms of the untransformed component which itself dominates the diffraction. Consequently, these numbers are likely erroneously high as the geometry of the fragments presumably deviate significantly from the true form. This potential error is corroborated by the results for calculations on the data at 69.9 and 100.1 kbar both being the lowest in energy in this series and only marginally deviating from one another and the overall trend of the rest of the data.

It is interesting to note that, while in β’-**1** all dimeric motifs experience a significant increase in total bonding energy, no such increase is calculated in the

case of the untransformed dimers of β”-**2** and only a small increase is calculated for the likely dimers at 69.9 and 100.1 kbar. It can therefore be inferred that there is either a greater resistance to deformation of the ambient dimeric motif in β-**2** or that β-**1** possesses an additional promoting factor not present in β-**2**. In the case that β-**2** resisted deformation to the dimeric motif more than β-**1** then it might be expected to have a greater cohesive energy, indicating that the molecule is bound more strongly in the crystal, but instead this parameter was found to be identical for the two phases at ambient pressure (*cf*. Chapter 2, Section3.5, Table 15). The likelihood of an additional promoting factor in β-**1** being lacked by β-**2** is therefore probable and will be returned to in Section 3.8.2.

### 3.8.1. α-[$PtCl_2$([9]ane$S_2O$)]

Calculations were run on a fragment in the form of one dimer as described in Section 3.1.1. As was the case for α-**1**, the apical *M*···O and *M*···*M* interactions are calculated as having similar bond orders at ambient pressure but show differing smooth increases with the application of pressure. The apical Pt···O interaction rises from 0.034 at ambient pressure to 0.051 (Fig. 31), maintaining a bond order half that as found for the Pd···O interaction in α-**1** throughout the study. In contrast, the intradimer Pt···Pt interaction rises from a bond order of 0.042 to 0.145, corresponding to an increase of only 0.01 less than that observed for the equivalent Pd···Pd interaction in α-**1**. As expected, the resistance to apical bonding with $R_2O$ donors is even stronger in the case of Pt(II) than Pd(II) while the malleability of the *M*···*M* interactions is very similar in this range.

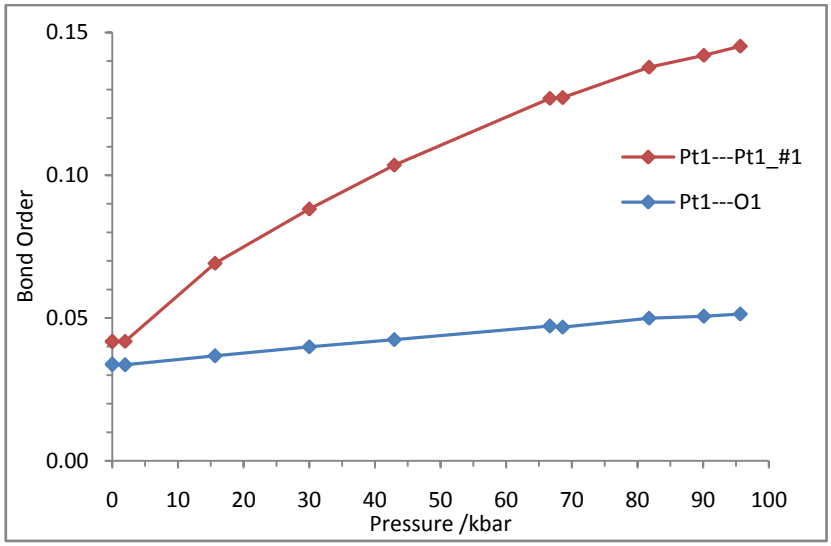



**Figure 31** The calculated Mayer bond orders as a function of pressure for the axial interactions in α-**2**.

The behaviour of the calculated Mayer bond orders for the coordination plane is predictably unremarkable with the general effect of pressure being a reduction in the bond orders by a value of *ca*. 0.01−0.02 (Fig. 32). These deviations appear more related to the corresponding bond lengths themselves (Fig. 33) than to compression of the bonds *trans* to them, as was the case for the Pd(II) analogue (*cf*. Chapter 3, Section 3.8.1). What is noteworthy is that the Pt−Cl bond orders are very similar to their Pd−Cl counterparts, whereas the Pt−S bonds are calculated as being *ca*. 0.2 higher in bond order than the Pd−S bonds of α-**1**. This stronger Pt−S bond may explain the slight resistance they exhibit to compression when compared to the Pt−Cl bonds.

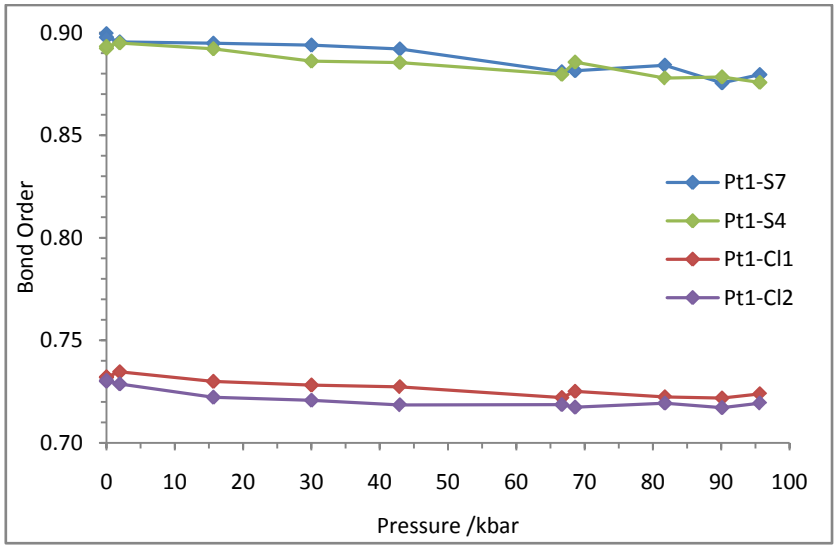



**Figure 32** The calculated Mayer bond orders as a function of pressure for the coordination bonds in α-**2**.

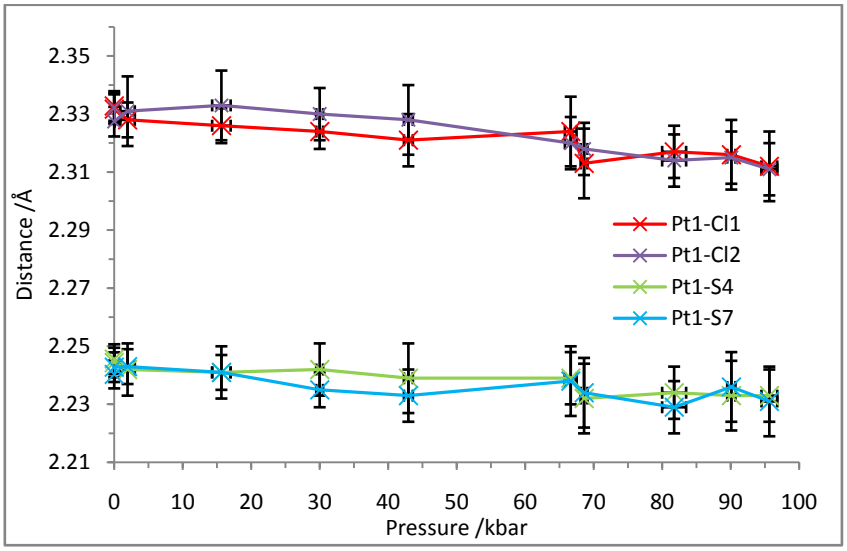



**Figure 33** The effects of pressure on the coordination bonds in α-**2**.

### 3.8.2. β-[$PtCl_2$([9]ane$S_2O$)] and β”-[$PtCl_2$([9]ane$S_2O$)]

For β-**2**, calculations were run on a fragment in the form of one dimer as described in Section 3.1.2. For β”-**2**, calculations were run on dimer fragments corresponding to each of the three potential combinations of conformers as described in Section 3.4.2.

Up to 65.2 kbar, the Pt···Pt bond order in β-**2** increases from 0.090 to 0.184 in a manner equally similar to the Pd(II) analogue, exceeding at *ca.* 30 kbar the maximum order reached in α-**2** at 95.7 kbar. Considering the bond order as a function of atomic separation then the difference between the two phases is again markedly reduced (Fig. 34) and the plot is similar to the equivalent plot for compound **1** (Chapter 3, Section 3.8.2, Fig. 46). Thus, it is likely that the difference between the calculated bond orders at a given *M*···*M* separation for the β and α phases is in the same way rationalised by the difference in slippage of the coordination planes of the molecules within the dimers.

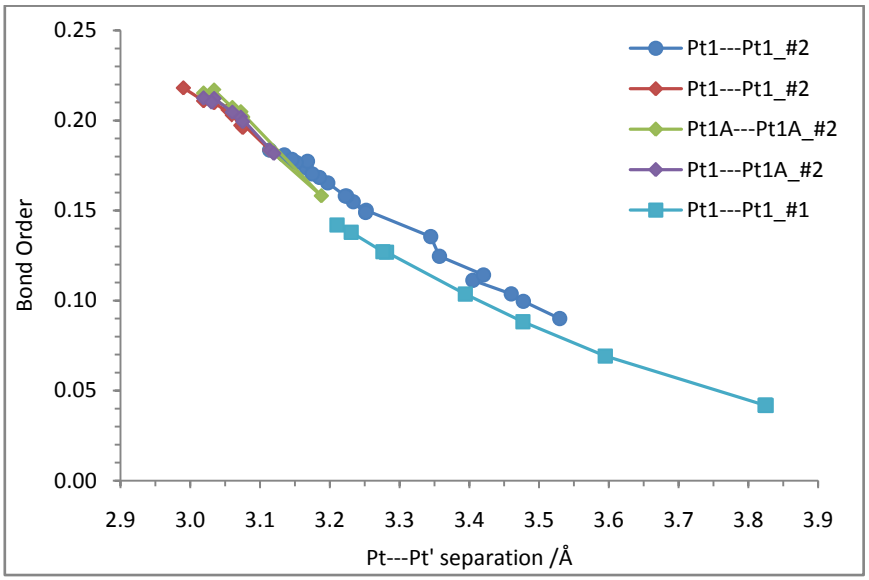



**Figure 34** The calculated Mayer bond orders as a function of the interatomic separation for the intradimer Pt···Pt interactions in α-**2** (squares), β-**2** (circles) and β”-**2** (diamonds). Symmetry codes #1 = −*x*, 2 − *y*, −*z*; #2 = −*x*, 1 − *y*, −*z*.

A distinct difference between the study of compound **1** and compound **2** is that a maximum was found in the plot of bond order against separation for the *M*···*M* interaction in the case of β/β’-**1** but not for β/β”-**2**. In the case of **1**, a bond order of *ca.* 0.20 was found to present a limit with the observation of a plateau at this value for Pd···Pd separations of *ca.* 2.98−3.08 Å, with the bond orders at lower

separations calculated as decreasing (*cf.* Chapter 3, Section 3.8.2, Fig. 46). In contrast, no such limit was observed in the case of β/β”-**2** and the trend shows no significant indication of changing towards a plateau. Given that the maximum is reached in β-**1** at the phase transition and that no corresponding phase transition is observed in the case of β-**2**, this difference could well be significant in explaining why β-**2** does not undergo the same transition despite their extensive similarity: it is likely that the full phase transition seen in β-**1** came about as a result of the Pd···Pd and C−H···H−C contacts acting together. It is entirely possible that if β”-**2** was compressed in search of a corresponding limit for the Pt···Pt interactions, a phase corresponding to β’-**1** might be attained. Nevertheless, this is by no means a certainty as a significant portion of the driving force to overcome any energy barrier may well have been released in the disordered conformational rearrangement.

Just as for the α phases, the *M*−Cl bond orders in β-**2** were calculated as being very much the same as in β-**1**, whereas the *M*−S bond orders were calculated as being significantly higher. Up to the conformational rearrangement there is again a steady decrease in the bond order for the coordination bonds, with Pt1−S7 being less affected than the other three (Fig. 35). The observation given for the behaviour of α-**2** that the bond orders follow their compression profiles appears to hold here also. After the rearrangement, in β”-**2**, a significant increase in uncertainty is associated with coordination bond parameters and therefore also with the relevant calculated bond orders, which show no significant trends. For this reason, discussion of these parameters is omitted.

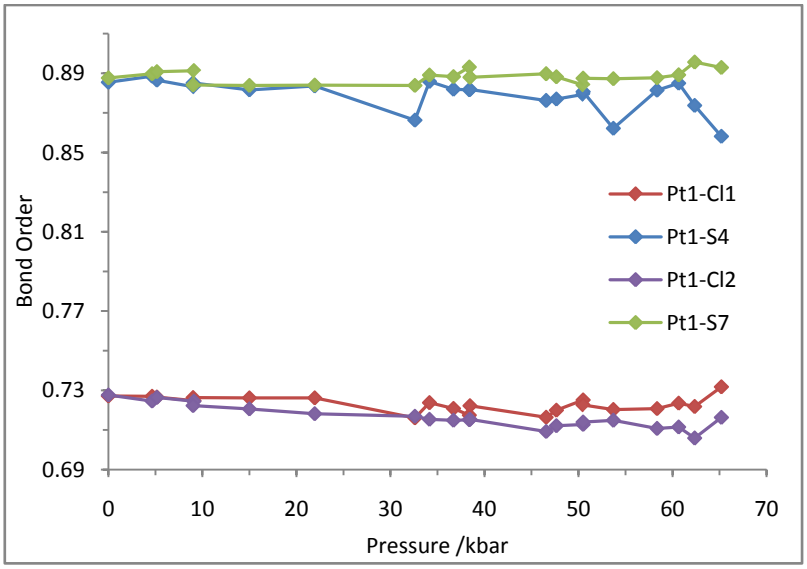



**Figure 35** The calculated Mayer bond orders as a function of pressure for the coordination bonds in β-**2**.

## 4. Conclusions

Two phases of [$PtCl_2$([9]ane$S_2O$)] (**2**) were each studied up to pressures exceeding 90 kbar using high-pressure single-crystal X-ray diffraction, showing many similarities to the study of the analogous phases of [$PdCl_2$([9]ane$S_2O$)] (**1**) detailed in Chapter 3 and by Tidey *et al.* (2016). As was the case for compound **1**, α-**2** and β-**2** exhibited similar overall compressibility, while the specific order of compressibility was calculated as reversed, *i.e.*, α-**2** was more compressible than β-**2**: for the third-order BM EoS, $B_0$ = 11.8(5) GPa, $B'_0$= 9.4(6) and $V_0$ = 1036.41(6) Å$^3$ for α-**2**; $B_0$ = 13.5(5) GPa, $B'_0$ = 6.3(4) and $V_0$ = 1077.44(7) Å$^3$ for β-**2**, calculated across the full range of pressures studied. The root of this slight difference between the two α and two β phases is not clear, but it should be noted that neither pair-wise difference exceeds the three sigma confidence bound. Being isomorphous and isostructural to β-**1**, β-**2** contained a pocket of particularly inaccessible void space between layers of dimers which ultimately allowed for the

same conformational rearrangement of the macrocycle but without the occurrence of a corresponding phase transition as was the case with β-**1**. This was the major crystallographic difference in the high pressure studies of these two phases. In all cases, the equatorial donor-sets were found to be largely incompressible.

For α-**2**, pressure brought smooth compression of unit cell and geometric parameters up to 95.7 kbar. The apical Pt1···O1 interaction was compressed from 3.084(4) to 2.897(8) Å, showing a marginal resistance to compression compared to the corresponding Pd1···O1 of α-**1**. The intradimer Pt1···Pt1_#1 separation (symmetry code #1 = −*x*, 2 − *y*, −*z*) was compressed by 0.6275(13) Å from 3.8523(5) to 3.1978(12) Å, proving marginally more compressible than the corresponding Pd1···Pd1_#1 separation, perhaps to account for the reduction in compression of the molecular volume brought about by the additional resistance in the Pt···O interaction. The metal centre was displaced from the $Cl_2S_2$ least squares mean plane from 0.0092(9) to 0.0599(18) Å in the direction away from the apical oxygen, again a similar deformation to that of α-**1**. This affects simultaneous bending of the *trans* S7−Pt1−Cl1 and S4−Pt1−Cl2 coordination bonds by 2.07(13) and 3.04(13) °, respectively.

For β-**2**, 65.2 kbar brought smooth compression of unit cell and geometric parameters within the variation of the different data collected on different crystals either in house or at Diamond Light Source. The intradimer Pt1···Pt1_#2 (symmetry code #2 = −*x*, 1 − *y*, −*z*) separation is compressed from 3.5294(2) to 3.114(8) Å, almost identical to the compression seen for β-**1**, and is not further deviated from the $ClS_2$ least squares mean plane defined by donors Cl2, S4 and S7. Cl1 is pushed out of the plane in the direction away from the incoming molecule

with which the dimer is formed, affecting a bending of S7−Pt1−Cl1 from 175.71(3) to 173.5(7) °, similar to that of β-**1**.

Between 65.2 and 69.9 kbar, covering the range in which the reversible phase transition was observed in β-**1**, β-**2** undergoes the same conformational rearrangement to the macrocycle but without the accompanying phase transition. Hence, this resulted in a single disordered site comprising the transformed and ambient form of the molecule. The root of this rearrangement was again attributed to a persistent region of void space residing directly beyond the carbon of the macrocycle associated with a close C−H···H−C approach about an inversion centre. The directionality of the resulting force causes one of the $CH_2$ moieties in question to rotate such that this contact is negated and the void space filled. The resulting macrocycle adopts the same [135] conformation by Dale analysis as in β'-**1**. The intradimer Pt···Pt interactions continue to compress after the transition to final values of 2.990(11), 3.031(6) and 3.07(2) Å for dimers comprising the untransformed molecules only, both forms, and the rearranged form only, respectively. Notably, these contractions came without the same stepwise contractions and divergence observed for β'-**1**. This may or may not be a consequence of the data not allowing the resulting range of interactions produced to be fully resolved. The data at 69.9 kbar, in which the two conformers of the molecule could be fully discriminated from one other, there is evidence of a comparable stepwise contraction [Δ = 0.060(19) Å] in the dimer not subject to the conformational rearrangement.

Temperature of the range 90−490 K was again found to be largely inconsequential to the phases studied. Data collected for β-**2** indicated that the anomalous

behaviour of β-**1** and γ-**1** was owed to limitations in the equipment and an insufficiently fast temperature ramp rate. In both phases, cooling from 290 to 90 K brought about similar effects as the application of 4−5 kbar pressure. Minor deviations to the geometries of the coordination planes were observed, most likely as an effect of thermal expansion decreasing the strain of close contacts. It is perhaps notable that the apical Pt···O interaction in α-**2** showed no temperature dependence across the range studied.

DFT calculations showed a similar increase in total bonding energy with pressure for the dimer fragments used for both ambient phases, albeit with a *ca*. 35 kbar lag in pressure bringing notable increase to these energies. This lag is likely owed to differences in the nature of the *M*···*M* interactions between compounds. For β-**2**, no stepwise increase in energy is observed across the conformational rearrangement for the dimer fragments comprising molecules in the ambient conformation. This is in contrast to an average *ca.* 90 kJ $mol^{-1}$ increase in energy calculated for dimer fragments across the β-**1** → β'-**1** phase transition in compound **1**. A steep increase in total bonding energy was calculated for a dimer comprising only the transformed form of the molecule in β-**2**, corroborating the inference made based on the occupancies of the two parts and on the dimers present in β'-**1** that it likely does not exist in reality.

With regards to the $Cl_2S_2$ donor sets, bond order analysis suggests that compression serves only to marginally weaken these interactions by an order of 0.01−0.03. It appeared that these deviations were linked directly to compression of the particular in question. An approximately linear dependence of bond order with interaction distance was calculated for Pt···O interaction in α-**2**. This interaction

showed a lesser dependence on separation than the corresponding Pd···O interaction in α-**1**, indicative of the reduced affinity of Pt(II) centres to bonding with ether O donors compared to Pd(II). An approximately linear dependence of bond order on atomic separation was calculated for the Pt···Pt interaction in both α-**2** and β/β”-**2**. In the case of α-**2**, this interaction increased from 0.042 to 0.145 at 95.7 kbar. In β-**2**, a continuous increase from 0.090 to 0.218 was calculated for the Pt···Pt bond order between ambient pressure and 100.1 kbar with no evidence of a plateau and maximum as seen in the corresponding Pd···Pd interactions of β/β’-**1** at the point of the phase transition. This corroborates the hypothesis that the *M*···*M* interactions have a role in bringing about the more extensive changes in β’-**1** that were not seen in β”-**2**.

## References


Agilent (2014). *CrysAlis$^{PRO}$*. Agilent Technologies, Yarnton, England.

Allan, D. R.; Blake, A. J.; Huang, D.; Prior, T. J.; Schröder, M. (2006). *Chem. Commun.*, 4081-4083.

Allan, D. R.; Bailey, D.; Bird, N.; Blake, A. J.; Champness, N. R.; Huang, D.; Keane, C. P.; McMaster, J.; Prior, T. J.; Tidey, J. P.; Schröder, M. (2014). *Acta Crystallogr., Sect. B*, **70**, 469-486.

Angel, R. J.; Bujak, M.; Zhao, J.; Gatta, G. D.; Jacobsen, S. D. (2007). *J. Appl. Cryst.* **40**, 26-32.

Angel, R. J.; Gonzalez-Platas, J.; Alvaro, M. (2014). *Z. Kristallogr.* **229**, 405-419.

Ballaran, T. B.; Kurnosov, A.; Trots, D. (2013). *High Pressure Res.* **33**, 3, 453-465.

Barnett, J. D.; Block, S.; Piermarini, G. J. (1973). *Rev. Sci. Instrum.* **44**, 1-9.

Becke, A. D. (1988). *Phys. Rev. A*, **38**, 3098-3100.

Blake, A. J.; Roberts, Y. V.; Schröder, M. (1996). *Dalton Trans*. 1885-1895

Bondi, A. J. (1964). *J. Phys. Chem.* **68**, 441-451.

Bruker (2001). *SADABS.* Bruker AXS Inc., Madison, Wisconsin, USA.

Bruker (2007). *SAINT.* Bruker AXS Inc., Madison, Wisconsin, USA.

Bujak, M.; Angel, R. J. (2006). *J. Phys. Chem. B*, **110**, 10322-10331.

Byrne, P. J.; Richardson, P. J.; Chang, J.; Kusmartseva, A. F.; Allan, D. R.; Jones, A. C.; Kamenev, K. V.; Tasker, P. A.; Parsons, S. (2012). *Chem. Eur. J.* **18**, 7738-7748.

Cairns, A. B.; Thompson, A. L.; Tucker, M. G.; Haines, J.; Goodwin, A. L. (2012). *J. Am. Chem. Soc.* **134**, 4454-4456.

Clark, R. C.; Reid, J. S. (1995). *Acta Crystallogr., Sect A*, **51**, 887–897.

Connor, L. E.; Delori, A.; Hutchison, I. B.; Daeid, N. N.; Sutcliffe, O. B.; Oswald, I. D. H. (2015). *Acta Crystallogr., Sect. B*, **71**, 3-9.

Cosier, J.; Glazer, A. M. (1986). *J. Appl. Cryst.* **19**, 105-107.

Dale, J. (1973). *Acta Chem. Scand.* **27**, 1115-1129.

Dolomanov, O. V.; Bourhis, L. J.; Gildea, R. J.; Howard, J. A. K.; Puschmann, H. (2009). *J. Appl. Cryst.* **42**, 339-341.

Fabbiani, F. P. A.; Allan, D. R.; David, W. I. F.; Davidson, A. J.; Lennie, A. R.; Parsons, S.; Pulham., C. R.; Warren, J. E. (2007). *Cryst. Growth Des.* **7**, 6, 1115-1124.

Fonseca-Guerra, C.; Snijders, J. G.; Te Velde, G.; Baerends, E. J. (1998). *Theor. Chem. Acc.* **99**, 391-403.

Galloway, K. W.; Moggach, S. A.; Parois, P.; Lennie, A. R.; Warren, J. E.; Brechin, E. K.; Peacock, R. D.; Valiente, R.; González, J.; Rodríguez, F.; Parsons, S.; Murrie, M. (2010). *CrystEngComm*, **12**, 2516-2519.

Gould, J. A.; Rosseinsky, M. J.; Moggach, S. A. (2012). *Dalton Trans.* **41**, 5464-5467.

Guionneau, P.; Brigouleix, C.; Barrans, Y.; Goeta, A. E.; Létard, J.-F.; Howard, J. A. K.; Gaultier, J.; Chasseau, D. (2001). *Acad. Sci., Ser. IIc: Chim.* **4**, 161-171.

Hirshfeld, F. L. (1976). *Acta Crystallogr., Sect. A*, **32**, 239-244.

Holzapfel, W. B. (2003). *J. Appl. Phys.* **93**, 1813-1818.

Katrusiak, A.; Dauter, Z. (1996). *Acta Crystallogr., Sect. D*, **52**, 607-608.

Klotz, S.; Chervin, J.-C.; Munsch, P.; Le Marchand, G. (2009). *J. Phys. D: Appl. Phys.* **42**, 075413/1- 075413/7.

Konno, M.; Okamoto, T.; Shirotani, I. (1989). *Acta Crystallogr., Sect. B*, **45**, 142-147.

Lucas, C. R.; Liang, W.; Miller, D. O.; Bridson, J. N. (1996). *Inorg. Chem.* **36**, 4508-4513.

Macrae, C. F.; Edgington, P. R.; McCabe, P.; Pidcock, E.; Shields, G. P.; Taylor, R.; Towler, M.; van de Streek, J. (2006). *J. Appl. Cryst.* **39**, 453-457.

Macrae, C. F.; Bruno, I. J.; Chisholm, J. A.; Edgington, P. R.; McCabe, P.; Pidcock, E.; Rodriguez-Monge, L.; Taylor, R.; van de Streek, J.; Wood, P. A. (2008). *J. Appl. Cryst.* **41**, 466-470.

Moggach, S. A.; Parson, S.; Wood, P. A. (2008). *Crystallogr. Rev.* **14**, 2, 143-184.

Okano, Y.; Adachi, T.; Narymbetov, B.; Kobayashi, H.; Zhou, B.; Kobayashi, A. (2004). *Chem. Lett.* **33**, 938-939.

Park, J. K.; Cho, Y. G.; Lee, S. S.; Kim, B. G. (2004). *Bull. Korean Chem. Soc.* **25**, 1, 85-89.

Parois, P.; Moggach, S. A.; Sanchez-Benitez, J.; Kamenev, K. V.; Lennie, A. R.; Warren, J. E.; Brechin, E. U.; Parsons, S.; Murrie, M. (2010). *Chem. Commun.* **46**, 1881-1883.

Pearson, R. G. (1968). *J. Chem. Educ.* **45**, 581-587.

Perdew, J. (1986). *Phys. Rev. B*, **33**, 8822-8824.

Piermarini, G. J.; Block, S.; Barnett, J. D. (1973). *J. Appl. Phys.* **44**, 5377-5382.

Prescimone, A.; Milios, C. J.; Sanchez-Benitez, J.; Kamenev, K. V.; Loose, C., Kortus, J.; Moggach, S. A.; Murrie, M.; Warren, J. E.; Lennie, A. R.; Parsons, S.; Brechin, E. U. (2009). *Dalton Trans.* 4858-4867.

Prescimone, A.; Sanchez-Benitez, J.; Kamenev, K. V.; Moggach, S. A.; Warren, J. E.; Lennie, A. R.; Murrie, M.; Parsons, S.; Brechin, E. U. (2010). *Dalton Trans.* **39**, 113-123.

Schmidtmann, M.; Coster, P.; Henry, P. F.; Ting, V. P.; Weller, M. T.; Wilson, C. C. (2014). *CrystEngComm*. **16**, 1232-1236.

Sheldrick, G. M. (1996). *SADABS*. University of Göttingen, Germany.

Sheldrick, G. M. (2008). *Acta Crystallogr., Sect. A*, **64**, 112-122.

Sheldrick, G. M. (2015). *Acta Crystallogr., Sect. C*, **71**, 3-8.

Shepherd, H. J.; Rosa, P.; Vendier, L.; Casati, N.; Létard, J.-F.; Bousseksou, A.; Guionneau, P.; Molnár, G. (2012). *Phys. Chem. Chem. Phys.* **14**, 5265-5271.

Spackman, M. A.; McKinnon, J. J. (2002). *CrystEngComm*, **4**, 378-392.

Spackman, M. A.; Jayatilaka, D. (2009). *CrystEngComm*, **11**, 19-32.

Spek, A. L. (2009). *Acta Crystallogr., Sect. D*, **65**, 148-155.

Takeda, K.; Hayashi, J.; Shirotani, I.; Fukuda, H.; Yakushi, K. (2006). *Mol. Cryst. Liq. Cryst.* **460**, 131-144.

Te Velde, G.; Bickelhaupt, F. M.; Baerends, E. J.; Fonseca-Guerra, C.; van Gisbergen, S. J. A.; Snijders, J. G.; Ziegler, T. (2001). *J. Comput. Chem.* **22**, 931-967.

Tidey, J. P.; Wong, H. L. S.; Schröder, M.; Blake, A. J. (2014). *Coord. Chem. Rev.* **277-278**, 187-207.

Tidey, J. P.; O'Connor, A. E.; Markevich, A.; Bitchoutskaia, E.; Cavan, J. J. P.; Lawrence, G. A.; Wong, H. L. S.; McMaster, J.; Schröder, M.; Blake, A. J. (2015). *Cryst. Growth Des.* **15**, 115-123.

Tidey, J. P.; Wong, H. L. S.; McMaster, J.; Schröder, M.; Blake, A. J. (2016). *Acta Crystallogr., Sect. B*, **72**, 3, 357-371.

Turner, M. J.; McKinnon, J. J.; Jayatilaka, D.; Spackman, M. A. (2011). *CrystEngComm*. **13**, 1804-1813.

Vosko, S. H.; Wilk, L.; Nusair, M. (1980). *Can. J. Phys.* **58**, 1200-1211.

Wolff, S. K.; Grimwood, D. J.; McKinnon, J. J.; Turner, M. J.; Jayatilaka, D.; Spackman, M. A. (2012). *CrystalExplorer* version 3.1, University of Western Australia, Australia.

Wong, H. L. S.; Allan, D. R.; Champness, N. R.; McMaster, J.; Schröder, M.; Blake, A. J. (2013). *Angew. Chem. Int. Ed.* **52**, 5093-5095.

Woodall, C. H.; Beavers, C. M.; Christensen, J.; Hatcher, L. E.; Intissar, M.; Parlett, A.; Teat, S. J.; Reber, C.; Raithby, P. R. (2013). *Angew. Chem. Int. Ed.* **52**, 9691-9694.

Yamada, H.; Nagae, T.; Watanabe, N. (2015). *Acta Crystallogr., Sect. D*, **71**, 724-753.

# Chapter 5

## Reversible Piezochromism in a Palladium(II) Macrocycle Complex

## 1. Introduction

Piezochromism is a change in the electronic spectrum of a given compound with pressure and in the context of coordination complexes is a well-described phenomenon (Grey & Butler, 2001). Since the electronic structure and orbital energies dictate the colour of the complex, any rationalisation of piezochromism requires an understanding of what may affect these. High-pressure crystallography offers a powerful tool towards interrogating their various possible mechanisms. For example, the literature contains examples of piezochromic coordination complexes where the colour is dependent on modulation of the molecular conformation (Woodall *et al*., 2013), coordination number (Allan *et al*., 2014) and coordination geometry (Galloway *et al.*, 2010). In all such cases, and in the case of simple compression of the coordination sphere (*vide infra*), the energy levels of the molecular orbitals involved in absorption and/or emission processes are altered by the perturbations brought by pressure. This in turn alters the energy of the transitions and hence the spectra of the materials.

Despite providing a comprehensive view of the structural changes that may contribute to the phenomenon, without further assistance from, for example, computational modelling it is easily possible to draw false conclusions. Red-shifting piezochromism has been observed in glyoximato and related complexes of nickel, palladium and platinum (Zahner & Drickamer, 1960; Takagi, 2004) and can be attributed to compression of axial $M\cdots M$ interactions, corroborated in the work of Nagakura *et al*. (1970). As the metal centres approach one another, the positive charges lower the energy of vacant $p_z$ orbitals while orbitals in the *xy* plane remain relatively unaffected. This results in a decrease in the energy of the absorption. In their combined crystallographic and computation study of two nickel

salicylaldoximato complexes, Byrne *et al.*(2012) report blue-shifting piezochromism which they associate with compression of equatorial interactions, thereby increasing the crystal field energy. This behaviour was in stark contrast to that of the glyoximato complexes and, where the *M*−*L* compression is small compared to compression of the axial *M*···*M* interactions, the conclusion might easily have been overlooked in absence of guiding computational work.

The complex $[Pd([9]aneS_3)_2](PF_6)_2$ (**3**) is reported as forming crystalline solvate phases with water (Wieghardt *et al.*, 1986) and acetonitrile (Stephen *et al.*, 2012) as well as existing as a solvent-free phase (Blake *et al.*, 1987). Furthermore, we have long known it to form a solvate with nitromethane (*vide infra*). Notably, these phases are not all the same colour, and while most are slightly differing shades of blue, the non-solvate is a dull green colour. In work carried out at the Daresbury Laboratory Synchrotron Radiation Source several years before the work of this chapter, the nitromethane bisolvate $[Pd([9]aneS_3)_2](PF_6)_2{\cdot}2CH_3NO_2$ (**3a**) was found to exhibit piezochromism from blue, through green, to a dark orange colour. Unfortunately, no crystallographic data could be collected to complement those observations. Alongside **3a**, the corresponding acetonitrile bisolvate $[Pd([9]aneS_3)_2](PF_6)_2{\cdot}2CH_3CN$ was shown not to exhibit any piezochromic response (Blake, 2014). Wieghardt *et al.*(1986) suggested that the colour of these different phases was both dependent on the length of the axial Pd···S interaction, which potentially modulates the position of an absorption band at the edge of the UV/vis region, and on packing effects altering the strength of the absorption. In this case, the presence of piezochromism in one phase but not the other is very much unexpected. As the axial interaction is expected to be highly compressible, piezochromism would be expected to some degree in all such phases if the

wavelength of the excitations which dictate the colour of the chromophore were dependent on it. This raised the suggestion that the chromophore is indeed particularly susceptible to outer-sphere contacts. The work presented herein details the study of **3a** by high-pressure single-crystal X-ray diffraction, high-pressure solid-state UV/vis and employing complementary computational studies to better clarify the nature of the piezochromism and investigate its origins.

## 2. Experimental

Reagents were used as received from Sigma-Aldrich and Fischer Industries. NMR spectroscopy was carried out at 400 MHz using Bruker AV400 spectrometer. ESI mass spectrometry was undertaken using a Bruker Daltonics microTOF electrospray mass spectrometer

### 2.1. Synthesis of $[Pd([9]aneS_3)_2](PF_6)_2$

*Bis*-acetonitrile palladium chloride (43.8 mg, 0.169 mmol) and 1,4,7-trithiacyclononane (60 mg, 0.333 mmol) were added to methanol/ethanol (2:1 *v/v*, 35 $cm^3$) and heated at reflux (70 °C) for 1 hour. The solution was hot filtered and excess ammonium hexafluorophosphate (100 mg) was added and the solution stirred for a further 15 minutes. The solution was cooled in an ice bath and the resulting precipitate collected by filtration and washed with diethyl ether (3 x 15 $cm^3$) to give a fine green crystalline powder (81.8 mg, 79 %). Mass spectrometry (ESI, $CH_3CN$): 242 $[Pd([9]aneS_3)_2]^{2+}$; 613$[Pd([9]aneS_3)_2](PF_6)^+$. $^1H$ NMR $\delta_H$/ppm (400 MHz; $CD_3CN$): 2.22 (2H, s, C$H_2$), 3.31 (10H, s, C$H_2$). $^{13}C$ NMR $\delta_c$/ppm (400 MHz; $CD_3CN$): 34.95 ($sp^3C$).

Crystals of **3**·2$CH_3NO_2$ (**3a**) were obtained by diffusion of $Et_2O$ vapour into a solution of the complex in nitromethane at room temperature. Crystals of **3**·2$(CH_3)_2CO$ (**3b**) were obtained by diffusion of $Et_2O$ vapour into a solution of the complex in $(CH_3)_2CO$ at room temperature. Crystals of **3**·2$CH_3CN$ (**3c-I** and **3c-II**) were obtained by diffusion of $Et_2O$ vapour into a solution of the complex in $CH_3CN$ at room temperature. Reddish crystals were obtained by diffusion of $Et_2O$ vapour into a solution of the complex in MeOH at room temperature but no crystal of sufficient quality for X-ray diffraction experiments was obtained.

### 2.2. Crystallography

For ambient temperature (293 K) and pressure collection of **3a**, a crystal of dimensions 0.26 × 0.16 × 0.13 $mm^3$ (crystal 0) was mounted on a MiTeGen MicroMount™ using silicon grease. Data were collected using a Rigaku Oxford Diffraction SuperNovaII diffractometer equipped with a microfocus sealed-tube source focussing mirror-monochromated Mo-*K*α radiation (λ = 0.71073 Å) detected at an Eos CCD area detector. For ambient pressure, low temperature collection of **3b** and **3c-II**, crystals of dimensions 0.39 × 0.22 × 0.06 and 0.13 × 0.08 × 0.06 $mm^3$, respectively, were mounted in a Fomblin film on MiTeGen MicroMounts™ and data collected at 120(2) K using an Oxford Cryostreams open-flow cryostat (Cosier & Glazer, 1986). Data were collected using Rigaku Oxford Diffraction SuperNovaII diffractometers equipped with a microfocus sealed-tube sources focussing mirror-monochromated Cu-*K*α radiation (λ = 1.5418 Å) detected at TitanS2 (**3b**) or Atlas (**3c-II**) CCD area detectors. Cell refinement and data reduction were performed using *CrysAlis*$^{PRO}$ (Agilent, 2014) and numerical

absorption corrections based on Gaussian integration over a multifaceted crystal model were applied.

For high-pressure data collections of **3a**, crystals of dimensions 0.07 × 0.04 × 0.03 $mm^3$ (crystal 1), 0.07 × 0.06 × 0.01 $mm^3$ (crystal 2) and 0.09 × 0.05 × 0.03 $mm^3$ (crystal 3) were studied using methanol/ethanol/nitromethane (80:20:1 *v*/*v*/*v*) as the pressure transmitting medium (PTM). For crystal 1, data were collected at 1.2, 16.4, 23.9, 41.5, 49.3, 74.8, 79.4, 84.9, 89.0 and 104.3 kbar, and decompressed to collect at 58.0 and 49.2 kbar. Further decompression between 49.2 and 36 kbar resulted in the crystal dissolving before data could be collected. For crystal 2, data were collected at 5.7, 35.2, 52.5 and 59.0 kbar, and decompressed to collect at 45.0 kbar; a further unit cell determination was carried out at 37.9 kbar. For crystal 3, data were collected at 36.1, 39.4 and 51.0 kbar, and decompressed to obtain unit cell dimensions at 40.7, 37.4 and 34.1 kbar. For the in-house high pressure structure of **3c-II**, a crystal of dimensions 0.05 × 0.03 × 0.02 $mm^3$ was studied using RS3000 as the PTM and data collected at 1.2 kbar.

Each crystal was individually loaded into the sample chamber of a Merrill-Bassett diamond anvil cell (DAC) formed by the 600 μm culet faces of the Boehler-Almax diamonds and by laser-cut tungsten sheet (Goodfellow Metals, thickness 200 μm) indented to a thickness of *ca*.80 μm with a gasket hole of diameter 200 μm drilled using a BETSA electric discharge machine. In each case, the sample crystal was fixed to one culet face by means of high-molecular-weight silicone grease, alongside a ruby sphere which allowed pressure measurement using the ruby fluorescence method (Barnett *et al.*, 1973). After each pressure ramp, the pressure inside the DAC was allowed to equilibrate for a minimum of 16 hours before data

collection was initiated. Pressure measurements were taken immediately before and after each collection and the pressure reported is the average of these. The average uncertainty in pressure across this study is ±1.0 kbar with individual error bars on figures representing 0.5 times the magnitude of the drift plus 0.5 kbar attributed to the inherent uncertainty of the ruby fluorescence method (Holzapfel, 2003). Data were collected using a Rigaku Oxford Diffraction SuperNovaII diffractometer equipped with a microfocus sealed-tube source focussing mirror-monochromated Mo-*K*α radiation (λ = 0.71073 Å) detected at an Eos CCD area detector. Cell refinement and data reduction was performed using *CrysAlis*$^{PRO}$ (Agilent, 2014). For all data, multi-scan absorption corrections were applied with an empirical absorption correction using spherical harmonics, implemented in SCALE3 ABSPACK scaling algorithm (Clark& Reid, 1995) through *CrysAlis*$^{PRO}$ (Agilent, 2014).

Structure solution was undertaken using *SHELXS*14 direct methods (Sheldrick, 2008) for the ambient pressure structures and for structures obtained at 62.9and 1.2 kbar for **3a** and **3c-II**, respectively. All other structures were solved by isomorphous replacement with an appropriate model. Structures were refined to convergence using *SHELXL*14 (Sheldrick, 2015). Structure solution and refinement were implemented through *Olex2* (Dolomanov *et al*., 2009). Specific refinement details are embedded in the relevant CIFs which can be found along with the experimental tables in the supplementary information.

## 2.3. UV/Vis experiments

A sample crystal of **3a** was mounted in a DAC by the same method as detailed for high-pressure crystallographic experiments. The DAC was mounted on a custom built rig (Fig. 1) and Ocean Optics P200-2 transmission fibre optic cables were used to deliver the light from an Ocean Optics DT-MINI-2-GS light source to an Ocean Optics USB2000+UV-VIS-ES spectrometer at which the absorbance of the sample was measured. Data were collected every 0.37 nm between 301.07 and 876.26 nm as the average of five 60 ms scans and are reported as the moving average of five data points.

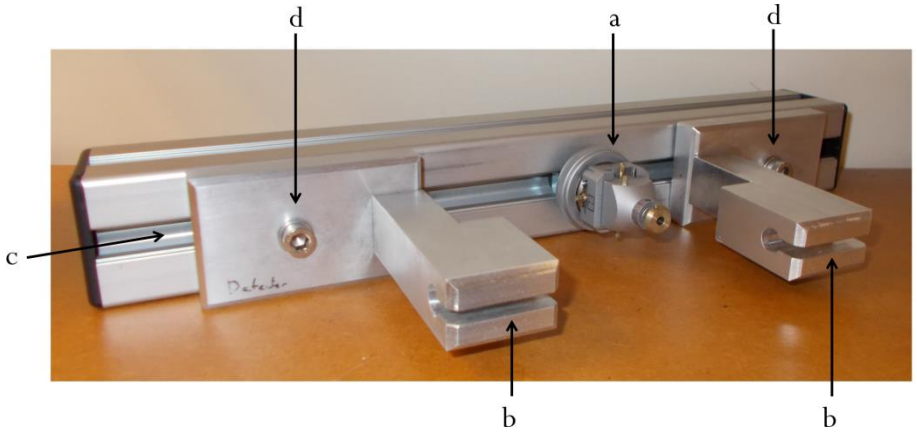



**Figure 1** Photographs of the rig used to mount the equipment used to carry out UV/Vis experiments: DAC is mounted on the IUCr standard goniometer mount at (a) which allows for fine tuning of the alignment; fibre optics are slotted into holes in the stages at (b); these stages can be moved along the path of (c) to deliver the fibre optics to the face of the DAC, and tightened in place using screws at (d).

## 2.4. Density functional theory calculations

Single-point density functional theory (DFT) calculations were carried out without geometry optimisation on models derived from the experimentally obtained crystal structures using the Amsterdam Density Functional suite version 2014.02 (*ADF*; Fonseca-Guerra *et al.*, 1998; Te Velde *et al.*, 2001). Slater-type orbital double-ζ-

plus single polarisation all-electron basis sets were used from the ZORA/DZP database of the *ADF* suite for all atoms except Pd, for which the triple-ζ-plus single polarisation all-electron basis set was used from the ZORA/TZP database. For Pd, a frozen core approximation up to and including 4*p* was used; for S, up to and including 2*p*; and for C only including 1*s*. Scalar relativistic approaches used within the ZORA Hamiltonian and the local density approximation with correlation potential due to Vosko *et al.* (1980) were used in all calculations. Gradient corrections were performed using the functionals of Becke (1988) and Perdew *et al.* (1986). Calculations were carried out individually on fragments corresponding to each unique cation obtained in the study of **3a** and **3a'**.

## 3. Results and discussion

### 3.1. Structures at ambient pressure

#### 3.1.1. $[Pd([9]aneS_3)_2](PF_6)_2 \cdot 2CH_3NO_2$ - 3a

$[Pd([9]aneS_3)_2](PF_6)_2 \cdot 2CH_3NO_2$ (**3a**) is isomorphous and isostructural to the Pt(II) analogue reported by Grant *et al.* (2005). At ambient temperature and pressure, **3a** crystallises in the monoclinic space group $P2_1/c$ with $a$ = 10.1059(3) Å, $b$ = 15.4680(4) Å, $c$ = 10.0013(2) Å, β = 99.777(2) °, $V$ = 1540.67(7) Å$^3$ and $Z$ = 2. Crystals of **3a** are blue in colour. It was found that the crystals gradually degrade and turn reddish-purple if left in the mother liquors for a period of weeks-months but these could not be crystallographically characterised. The Pd(II) centre in **3a** resides on an inversion centre and is bound in a square plane by four sulfur donors with each macrocycle providing two of these [Pd−S4 = 2.3076(10) Å; Pd−S7 = 2.3129(10) Å; S4−Pd−S7 = 89.01(3) °]. Each macrocycle adopts a [333] conformation following Dale (1973) analysis and binds in an *endodentate*

configuration, providing distant apical sulfur donors to the metal centre [Pd···S1 = 2.9808(10) Å; S1···Pd–S4 = 84.85(3) °; S1···Pd–S7 = 83.23(3) °] (Fig. 2) within the sum of the van der Waals radii [$\Sigma_{vdW}$ = 3.43 Å (Bondi, 1964)] to form a [4+2] distorted octahedral geometry at the metal centre.

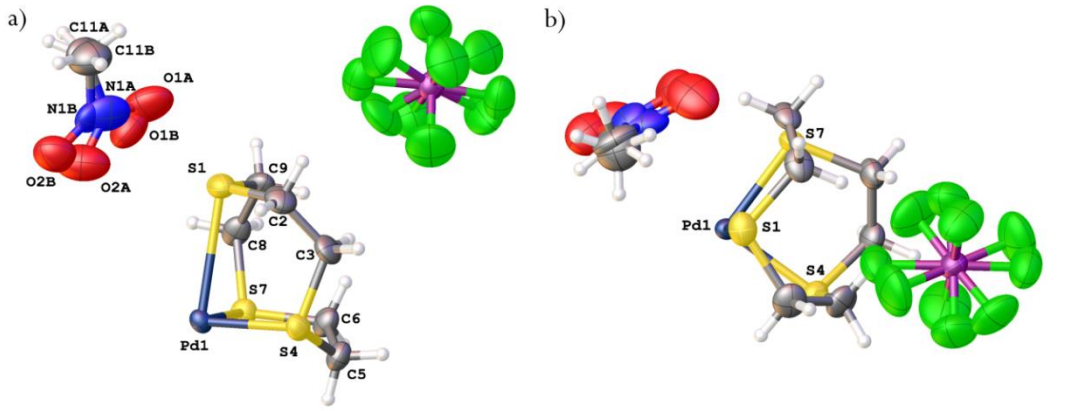



**Figure 2** View of the asymmetric unit of **3a** viewed from a) the side and b) the top. Selected atoms labelled in accordance with the text; P atoms in purple, F atoms in green and H atoms in white; anisotropic displacement parameters are drawn at 50 % probability level.

The mononuclear cations in **3a** form sheets perpendicular to the *a* axis within the elongated axis approximately aligned in the *b* axis (Fig. 3). Cations within sheets can be described as interacting *via* C–H···S hydrogen bonds between C9(H9A) and equatorial S7_#1 [for *D*–H = 0.97 Å: H···*A* = 3.04 Å; *D*···*A* = 3.907(4) Å; *D*–H···*A* = 149.8 °] and C2(H2A) and apical S1_#2 [for *D*–H = 0.97 Å: H···*A* = 3.24 Å; *D*···*A* = 4.028(4) Å; *D*–H···*A* = 139.1 °] (symmetry code #1 = +*x*, 0.5 − *y*, 0.5 + *z*; #2 = 2 − *x*, −*y*, 1 − *z*). Each cation is accompanied by two $PF_6^-$ moieties and two $CH_3NO_2$ solvent molecules which reside in the region between cationic sheets and the solvent molecules occupy positions in proximity with the sulfur donors. At ambient temperature and pressure, both solvent molecule and anion appear dynamically disordered and were each refined over two positions; the

closest S···O separations are 3.37(5) Å between apical S1 and O1A, and 3.26(3) Å between equatorial S4 and O1A_#3 (symmetry code #3 = 2 − *x*, −0.5 + *y*, 0.5 − *z*).

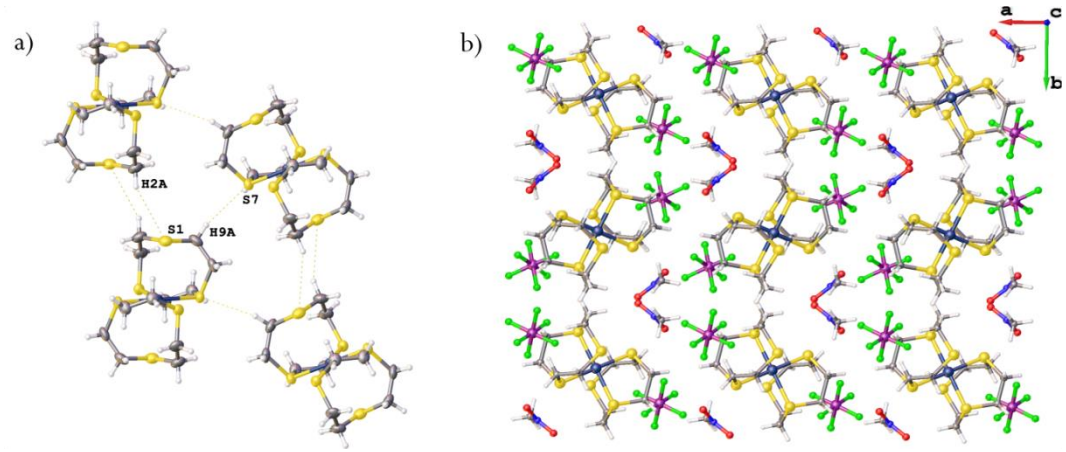



**Figure 3** a) View of the hydrogen bonding between cations and b) ball-and-stick image of the layered packing as viewed along the *c* axis in **3a**. Selected atoms labelled in accordance with the text; Pd atoms in dark blue, S in yellow, P in purple, F in green, O in red, N in light blue, C in grey and H in white; anisotropic displacement parameters are drawn at 50 % probability level.

### 3.1.2. $[Pd([9]aneS_3)_2](PF_6)_2 \cdot 2(CH_3)_2CO$ - 3b

At ambient pressure and 120 K, $[Pd([9]aneS_3)_2](PF_6)_2 \cdot 2(CH_3)_2CO$ (**3b**) crystallises in the orthorhombic space group *Pbca* with *a* = 15.4566(6) Å, *b* = 10.1354(4) Å, *c* = 19.9753(11) Å, *V* = 3129.3(3) Å$^3$ and *Z* = 4; crystals of **3b** are blue in colour. The Pd(II) centre in **3b** resides on an inversion centre and is bound in a square plane by four sulfur donors with each macrocycle providing two of these [Pd−S4 = 2.3142(10) Å; Pd−S7 = 2.3014(11) Å; S4−Pd−S7 = 89.54(4) °]. Each macrocycle adopts a [333] conformation following Dale (1973) analysis and binds in an *endodentate* configuration, providing distant apical sulfur donors to the metal centre [Pd···S1 = 2.9798(10) Å; S1···Pd−S4 = 82.88(3) °; S1···Pd−S7 =

85.04(3) °] (Fig. 4) within the sum of the van der Waals radii [$\Sigma_{vdW}$ = 3.43 Å (Bondi, 1964)] to form a [4+2] distorted octahedral geometry at the metal centre.

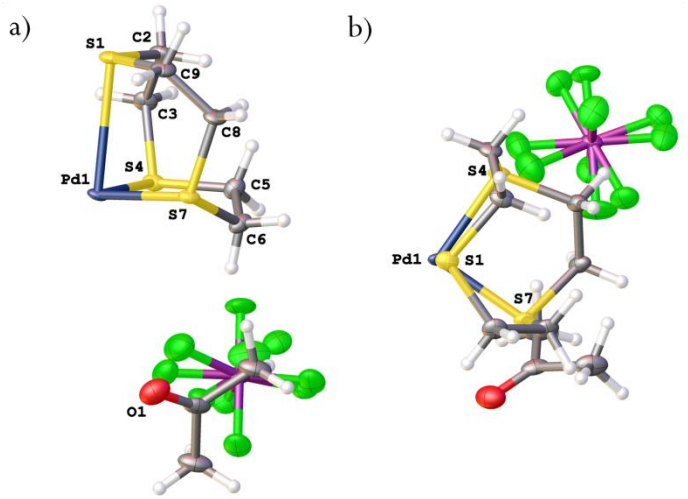



**Figure 4** View of the asymmetric unit of **3b** viewed from a) the side and b) the top. Selected atoms labelled in accordance with the text; P atoms in purple, F atoms in green and H atoms in white; anisotropic displacement parameters are drawn at 50 % probability level.

Similarly to **3a**, the mononuclear cations in **3b** form sheets perpendicular to the *c* axis with the elongated axis approximately aligned in the *a* axis (Fig. 5). Cations within sheets can be described as interacting *via* C–H···S hydrogen bonds between C2(H2A) and equatorial S4_#4 [for *D*–H = 0.97 Å: H···*A* = 3.13 Å; *D*···*A* = 4.027(4) Å; *D*–H···*A* = 151.4 °] and C9(H9A) and apical S1_#5 [for *D*–*H* = 0.97 Å: H···*A* = 3.31 Å; *D*···*A* = 4.119(4) Å; *D*–H···*A* = 140.5 °] (symmetry code #4 = 1.5 − *x*, −0.5 + *y*, +*z*; #5 = 1 − *x*, −*y*, 1 − *z*). Each cation is accompanied by two $PF_6^-$ moieties and two $(CH_3)_2CO$ solvent molecules which reside in the region between cationic sheets and the solvent molecules again occupy positions in proximity to the sulfur donors. At ambient pressure and 120 K, only the anion appears dynamically disordered and was refined over two positions; the closest S···O separations are 3.505(4) Å between apical S1 and O1_#6, and 3.371(4) Å

between equatorial S7 and O1_#7 (symmetry code #6 = 1 − *x*, 1 − *y*, 1 − *z*; symmetry code #7 = 0.5 − *x*, −0.5 + *y*, +*z*).

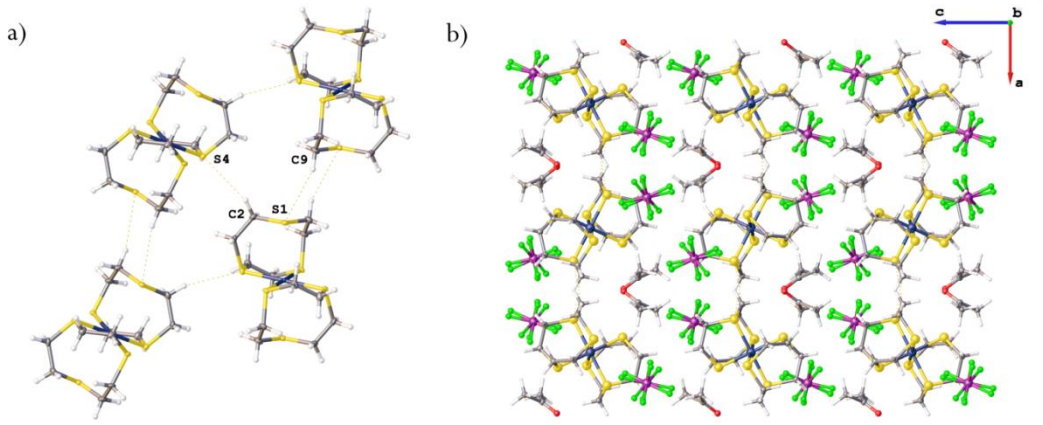



**Figure 5** a) View of the hydrogen bonding between cations and b) ball-and-stick image of the layered packing as viewed along the *c* axis. Selected atoms labelled in accordance with the text; Pd atoms in dark blue, S in yellow, P in purple, F in green, O in red, C in grey and H in white; anisotropic displacement parameters are drawn at 50 % probability level.

### 3.1.3. II-[Pd([9]aneS$_3$)$_2$](PF$_6$)$_2$·2CH$_3$CN- 3c-II

At ambient pressure and 120 K, [Pd([9]aneS$_3$)$_2$](PF$_6$)$_2$·2CH$_3$CN (**3c-II**) crystallises in the orthorhombic space group *Pbca* with *a* = 15.1991(2) Å, *b* = 9.74074(15) Å, *c* = 20.4782(3) Å, *V* = 3031.80(8) Å$^3$ and *Z* = 4. Crystals of **3c-II** are more greenish-blue in colour compared to **3a** and **3b** and the phase differs from the acetonitrile solvate of [Pd([9]aneS$_3$)$_2$](PF$_6$)$_2$ already reported in the literature (Stephen *et al.*, 2012; **3c-I**). The Pd(II) centre in **3c-II** resides on an inversion centre and is bound in a square plane by four macrocycle sulfur donors of two macrocycles [Pd−S4 = 2.3122(5) Å; Pd−S7 = 2.3096(5) Å; S4−Pd−S7 = 89.016(19) °]. Each macrocycle adopts a [333] conformation following Dale (1973) analysis and binds in an *endodentate* configuration, providing distant apical sulfur donors to the metal centre [Pd···S1 = 2.9388(6) Å; S1···Pd−S4 =

84.069(18) °; S1···Pd−S7 = 85.798(19) °] (Fig. 6) within the sum of the van der Waals radii [$\Sigma_{vdW}$ = 3.43 Å (Bondi, 1964)] to form a [4+2] distorted octahedral geometry at the metal centre.

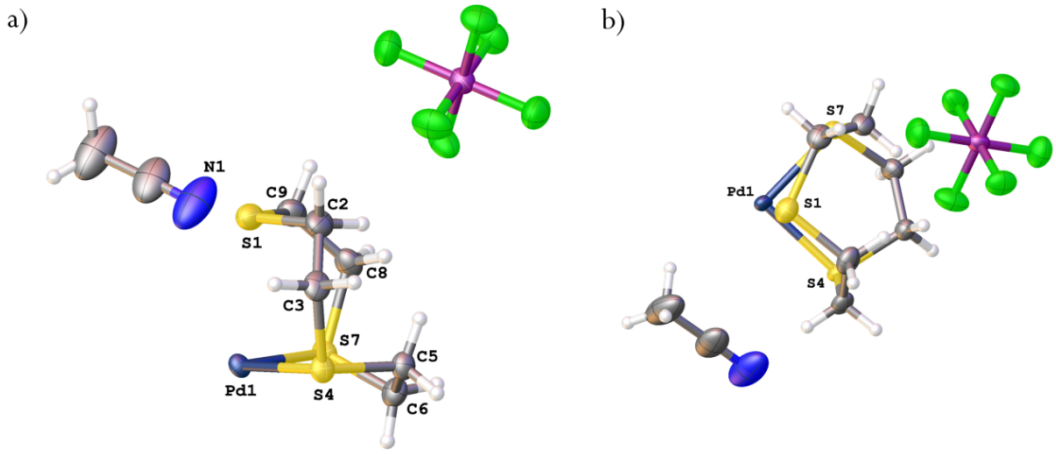



**Figure 6** View of the asymmetric unit of **3c** viewed from a) the side and b) the top with selected atoms labelled in accordance with the text. P atoms in purple, F atoms in green and H atoms in white; anisotropic displacement parameters are drawn at 50 % probability level.

Similarly to both **3a** and **3b**, the mononuclear cations in **3c-II** form sheets perpendicular to the *c* axis with the elongated axis approximately aligned in the *a* axis (Fig. 7). Cations within sheets can be described as interacting *via* C−H···S hydrogen bonds between C2(H2A) and equatorial S4_#8 [for *D*−H = 0.97 Å: H···*A* = 2.80 Å; *D*···*A* = 3.679(2) Å; *D*−H···*A* = 151.0 °] and C9(H9A) and apical S1_#9 [for *D*−H = 0.97 Å: H···*A* = 3.28 Å; *D*···*A* = 3.962(3) Å; *D*−H···*A* = 129.2 °] (symmetry code #8 = 1.5 − *x*, 0.5 + *y*, +*z*; #9 = 1 − *x*, 2 − *y*, 1 − *z*). Each cation is accompanied by two $PF_6$ moieties and two $CH_3CN$ solvent molecules which reside in the region between cationic sheets and the solvent molecules again occupy positions in proximity to the sulfur donors. The closest S···N separations

are 3.750(4) Å between apical S1 and N1, and 3.461(4) Å between S7 and N1_#10 (symmetry code #10 = −0.5 + *x*, 1.5 − *y*, 1 − *z*).

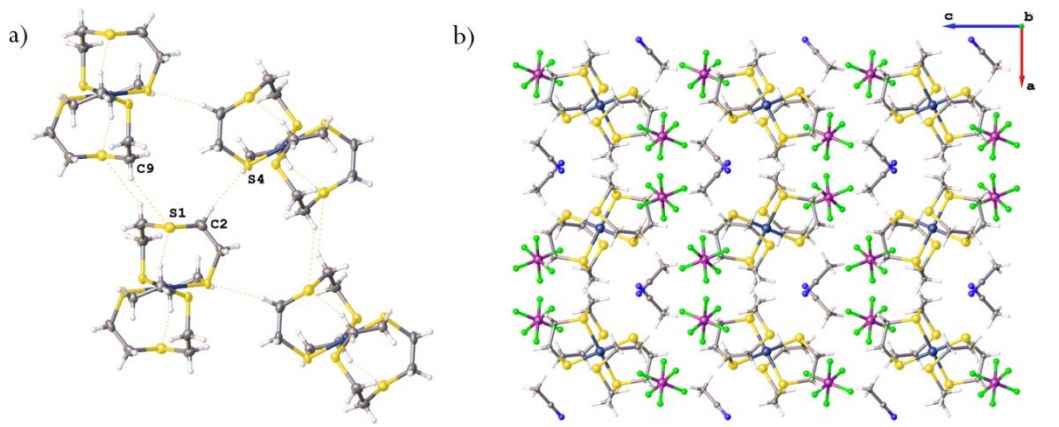



**Figure 7** a) View of the hydrogen bonding between cations and b) ball-and-stick image of the layered packing as viewed along the *c* axis in **3c**. Selected atoms labelled in accordance with the text; Pd atoms in dark blue, S in yellow, P in purple, F in green, N in light blue, C in grey and H in white; anisotropic displacement parameters are drawn at 50 % probability level.

### 3.2. Pressure transmitting medium

Crystals of **3a** were found to be unstable in the usual 4:1 methanol/ethanol solution used as a PTM, appearing to degrade in the order of seconds. This degradation appeared similar to the slower degradation which occurred as a result of desolvation in air. The addition of a small quantity of nitromethane to the PTM was consequently tested and found to stabilise the crystals. Consequently, the sample was studied using a solution of methanol/ethanol/nitromethane (80:20:1 *v/v/v*) as the PTM. This in turn necessitated a higher-molecular-weight silicone grease to keep the sample in place. Crystals of **3c-II** were found to be similarly unstable to methanol/ethanol solution, but could not be stabilised by

addition of $CH_3CN$ to the solution up to 5%. The experiments studying **3c-II** were carried out in RS3000.

It was unknown how the addition of nitromethane to the solution would affect the hydrostatic limit of the PTM and rigorous investigation has not been carried out. The maximum pressure any sample of **3a** was taken to was 104.3 kbar which is at the limit of the hydrostatic window for a 4:1 (*v/v*) solution of methanol/ethanol (Klotz *et al.*, 2009). The data appears to behave in accordance with hydrostatic conditions within this range, as indicated by the cell parameters (Fig. 8) and other geometric parameters (*vide infra*).

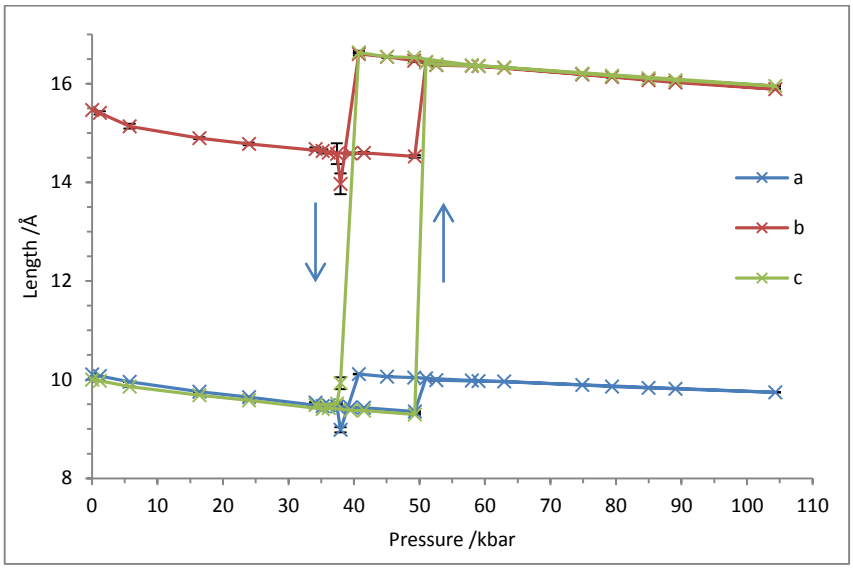



**Figure 8** The effects of pressure on the cell parameters of **3a** with decompression through the metastable region for the high-pressure phase shown. Lines added to guide the eyes with arrows added to show the transition on compression (↑) and decompression (↓).

### 3.3. Summary of high-pressure studies on 3a and 3c

Only **3a** was studied extensively under pressure. The phase showed significant and smooth compression of unit cell parameters up to 49.3 kbar, where *a*, *b* and *c* were compressed by 7, 6 and 7 %, respectively, resulting in a total compression of 20 %

to the unit cell volume. For the third-order Birch-Murnaghan equation of state calculated using *EoSFit7c* (Angel, 2014), $B_0$ = 10.1(9) GPa, $B'_0$ = 7.6(12) and $V_0$ = 1540.68(7) Å$^3$ between 0.001 and 49.3 kbar. Thus the phase is relatively soft for a molecular crystal, likely a combined effect of both the compressible cation and multiple smaller, more labile anions and solvent molecules allowing flexibility of space filling. The compression of **3a** is accompanied by a gradual piezochromic response from sky blue to a dull green (Fig. 9).

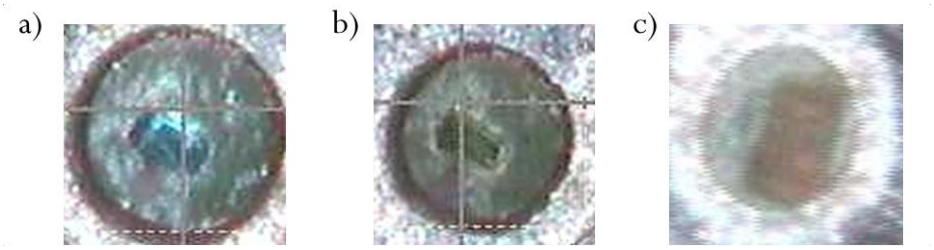



**Figure 9** Photographs of crystals of **3a** in the DAC at a) 1.2 and b) 49.3 kbar, and c) of **3a'** at 51.0 kbar.

Between 49.3 and 51.0 kbar, a $P2_1/c \rightarrow P1$ phase transition takes place with doubling of the unit cell volume in accordance with the transformation matrix [1 0 0 / 0 1 1 / 0 1 1] and resulting in four inequivalent molecules in the unit cell. The high pressure phase was subject to twinning by the matrix [1 0 0 / 0 0 1 / 0 1 0]. The transition was accompanied by a discontinuous compression [1.7 %] (Fig. 10) and piezochromic response from dull green to orange (Fig. 9). Statistically meaningful data for the third-order Birch-Murnaghan equation of state could not be obtained for the high pressure phase, and the total compression brought by 104.3 kbar to *V*/*Z* was 28 %. The crystal showed hysteresis with respect to the reverse phase transition upon decompression which occurred between 40.7 and 37.9 kbar. Decompression through the metastable pressure range resulted in the crystal

becoming unstable in the PTM and slowly dissolving if not cycled to the ambient phase sufficiently quickly. This placed limits on the data available around the return transition and consequently decompression below 45 kbar is only characterised by cell parameters.

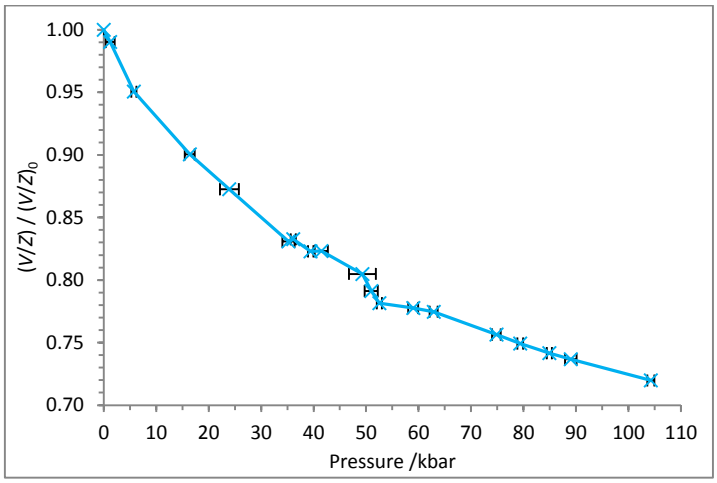



**Figure 10** The effects of pressure upon compression on the normalised *V*/*Z*.

A high pressure study of **3c** was also attempted, employing RS3000 as the PTM, but gave extremely limited data. Data collected in-house showed a *Pbca* → $P2_1/c$ phase transition according to the matrix [0 0 $^1/_2$ / 1 0 0 / 0 0 1] under the pressure of closing the cell (1.2 kbar) described by cell parameters $a$ = 10.398(14) Å, $b$ = 15.0082(16) Å, $c$ = 9.7888(16), β = 100.22(5) °, $V$ = 1503(2) Å$^3$ and $Z$ = 2. A second crystal was studied on Experimental Hutch 2 of Diamond Light Source which revealed a *Pbca* → $P2_1/c$ phase transition between 7.8 and 14.0 kbar to a different monoclinic phase described by cell parameters $a$ = 19.84(10) Å, $b$ = 15.014(7) Å, $c$ = 9.471(5) Å, β = 92.87(11) °, $V$ = 2818(14) Å$^3$. The β angle of this cell readily opened further to 100.10(14) ° up to 29.2 kbar, but the data are of distinctly low quality and no structure solution could be obtained.

### 3.3.1. High-pressure phase of $[Pd([9]aneS_3)_2](PF_6)_2 \cdot 2CH_3NO_2$ - 3a'

At 51.0 kbar, $[Pd([9]aneS_3)_2](PF_6)_2.2MeNO_2$ crystallises in the triclinic space group *P*1 with *a* = 10.0301(7) Å, *b* = 16.431(2) Å, *c* = 16.442(4) Å, α = 114.621(18) °, β = 94.153(11) °, γ = 94.716(11) °, *V* = 2437.9(7) $Å^3$ and *Z* = 4, designated **3a'**. The cations of **3a'** remain on centres of inversion and thus there are four unique cations represented in the asymmetric unit (Fig. 11). Structural parameters will be discussed in detail in sections detailing the specific response of **3a** to pressure. The primary difference of **3a'** to **3a** is that two of the four inequivalent cations have undergone a rearrangement of the coordination sphere such that the axial donors are switched with equatorial donors (Fig. 11, *cf.* Fig. 3). This results in a denser packing of cations within the sheet motif (Fig. 12) and directs the elongated axial interactions of Pd1 and Pd3 into the region of anions and solvent molecules. The reoriented axes displace the anion and solvent molecules from their positions at lower pressures (Fig. 12) and result in significantly closer S···O contacts (*vide infra*). The reorientation of the coordination axes also results in a stepwise expansion of the *a* axis (Fig. 8). Coupled to the reorientation is a stepwise contraction of the axial Pd···S interactions that remain aligned as in the preceding phase (*vide infra*).

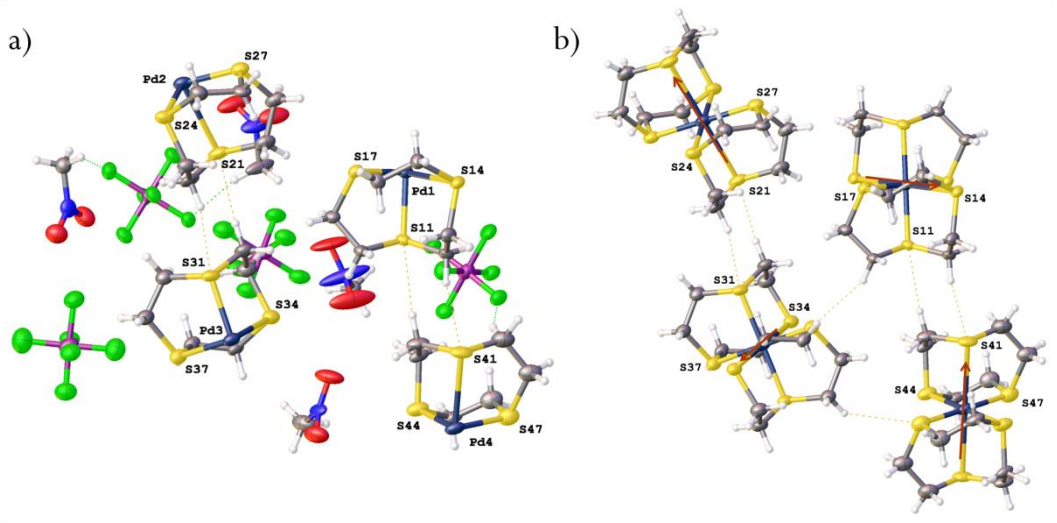



**Figure 11** Image depicting a) the asymmetric unit and b) the relative orientation of the axial interactions in the cations of **3a'** at 51.0 kbar with selected atoms. Pd atoms in green/blue, S in yellow, P in orange, F in green, O in red, N in light blue, C in dark grey; anisotropic displacement parameters drawn at 50 % probability level.

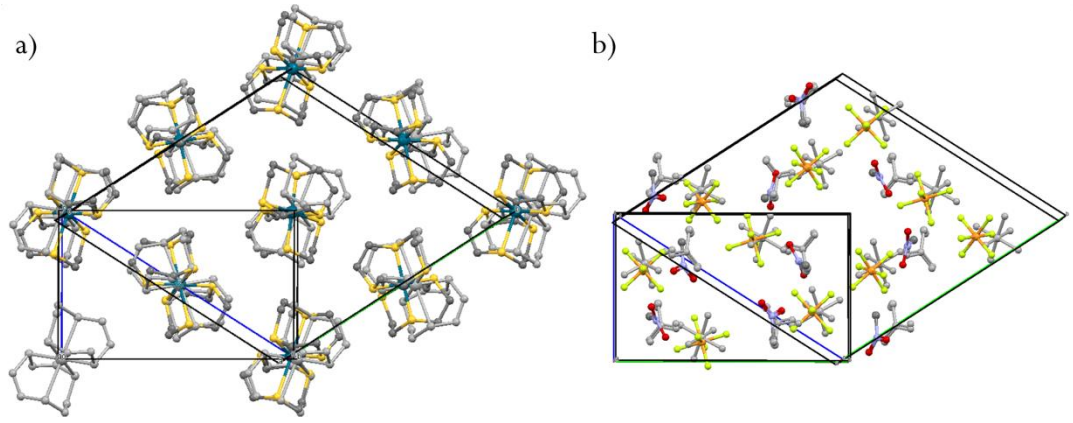



**Figure 12** Overlay image of the packing of a) cations and b)the anions and solvent molecules in phases **3a** at 49.3 kbar (grey) and **3a'** at 51.0 kbar (coloured) as viewed along the *a* axis of **3a**. Pd atoms in green/blue, S in yellow, P in orange, F in green, O in red, N in light blue, C in dark grey; H atoms omitted for clarity; the larger unit cell corresponds to the high-pressure phase.

### 3.3.2. High-pressure phase of $[Pd([9]aneS_3)_2](PF_6)_2 \cdot 2CH_3CN$ - 3c-II'

At 1.2 kbar, $[Pd([9]aneS_3)_2](PF_6)_2 \cdot 2CH_3CN$ crystallises in the monoclinic space group $P2_1/c$ with $a$ = 10.402(4) Å, $b$ = 14.9604(8) Å, $c$ = 9.7726(6) Å, β =

100.158(13) °, $V$ = 1497.0(5) Å$^3$ and $Z$ = 2 (**3c-II'**). The structure of **3c-II'** is essentially isomorphous to **3a** with the exception of the differing solvent molecules and slight rotation of $PF_6$ anions (Fig. 13). The Pd(II) centre in **3c-II'** resides on an inversion centre and is bound in a square plane by four macrocycle sulfur donors of two macrocycles [Pd−S4 = 2.318(12) Å; Pd−S7 = 2.310(9) Å; S4−Pd−S7 = 88.6(4) °]. Each macrocycle adopts a [333] conformation following Dale (1973) analysis and binds in an *endodentate* configuration, providing distant apical sulfur donors to the metal centre [Pd···S1 = 2.937(5) Å; S1···Pd−S4 = 83.5(2) °; S1···Pd−S7 = 84.9(3) °] within the sum of the van der Waals radii [$\Sigma_{vdW}$ = 3.43 Å (Bondi, 1964)] to form a [4+2] distorted octahedral geometry at the metal centre.

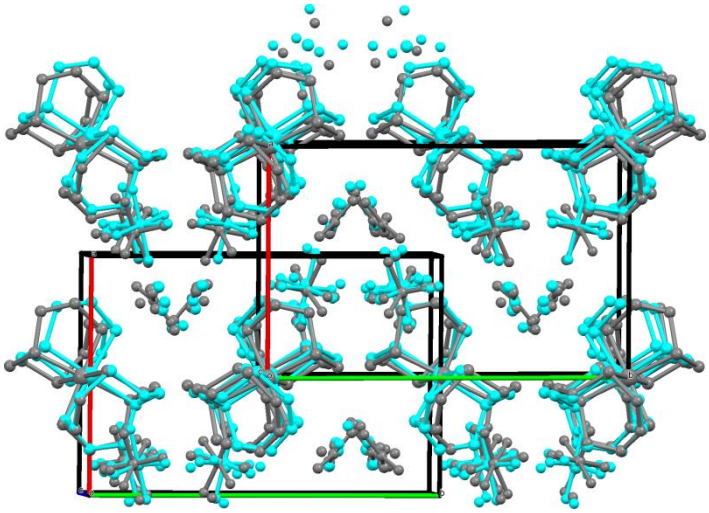


**Figure 13** Structure overlay of phases **3a** (grey) and **3c-II'** (cyan) showing the striking similarity in their packing.

Cations within sheets can be described as interacting *via* C−H···S hydrogen bonds between C2(H2A) and equatorial S4_#11 [for *D*−H = 0.97 Å: H···*A* = 3.12 Å; *D*···*A* = 3.966(16) Å; *D*−H···*A* = 147.2 °] and C9(H9A) and apical S1_#12 [for *D*−H = 0.97 Å: H···*A* = 2.93 Å; *D*···*A* = 3.77(2) Å; *D*−H···*A* = 145.6 °] (symmetry code #11 = +*x*, 0.5 − *y*, −0.5 + *z*; #12 = 1 − *x*, 1 − *y*, −*z*). Each cation is

accompanied by two $PF_6^-$ moieties and two $CH_3CN$ solvent molecules which reside in the region between cationic sheets and the solvent molecules again occupy positions in proximity to the sulfur donors. Both the anion and solvent molecules appear disordered and are refined over two positions; the closest S···N separations are 3.30(9) Å between apical S1 and N1A, and 3.49(9) Å between equatorial S7 and N1A_#12 (symmetry code #12 = 1 − *x*, 0.5 + *y*, 0.5 − *z*).

### 3.4. High-pressure X-ray studies of 3a/3a'

#### 3.4.1. Compression of the coordination sphere

The application of pressure to **3a** results in significant linear compression of the apical Pd···S interaction such that 49.3 kbar brings a contraction of 0.113(3) Å [Pd1···S1 = 2.868(3) Å] (Fig. 14 & 15). The same pressure brings about contractions of 0.025(3) and 0.034(6) Å to the equatorial Pd1−S4 and Pd1−S7 interactions, respectively. While the equatorial donors are expectedly much less compressible than the softer apical interaction, this compression is significantly more than in the complexes [*M*$Cl_2$([9]ane$S_2$O)] (*M* = Pd, Pt) described in Chapters 3 and 4. This comparably high compression is attributed to the supramolecular sheet motif in which the cations reside, providing C−H···S interactions at S1 and S7. S4 is directed into the layers of anion and solvent molecules to form close contacts with both species.

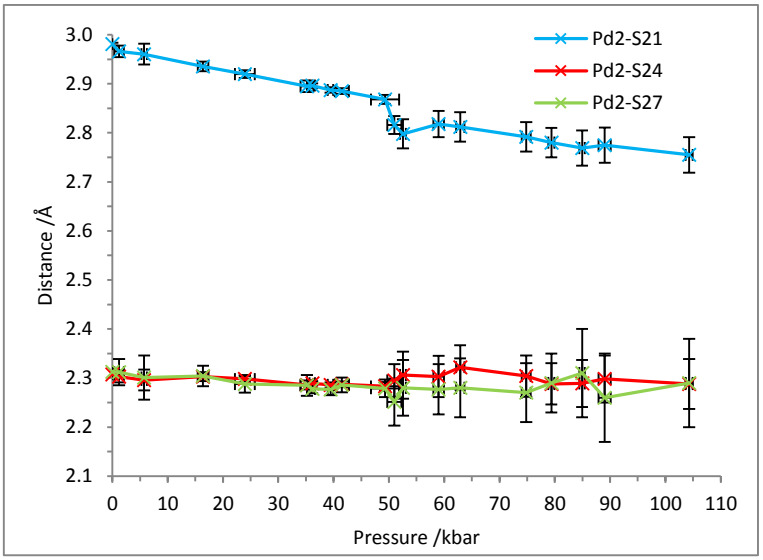



**Figure 14** The effects of pressure on the coordination bonds in the ambient phase and in the high-pressure phase at Pd2. The cation in **3a'** is not subject to a reorientation of its coordination axes over the phase transition.

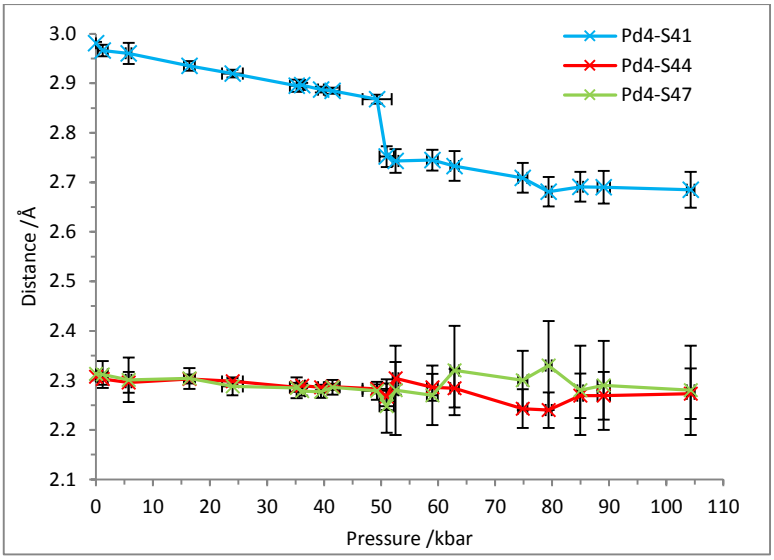



**Figure 15** The effects of pressure on the coordination bonds in the ambient phase and in the high-pressure phase at Pd4. The cation in **3a'** is not subject to a reorientation of its coordination axes over the phase transition.

Between 49.3 and 51.0 kbar, **3a** was observed to undergo a $P2_1/c \rightarrow P1$ phase transition, doubling the unit cell and resulting in four inequivalent cations in the asymmetric unit. The transition is most prominently characterised by the apparent

reorientation of the coordination axes in two of the four resulting inequivalent cations, specifically those corresponding to Pd1 and Pd3 of **3a'** (*cf.* Fig. 11). To the two cations which are not reoriented, the phase transition affects a stepwise compression to the axial Pd···S interactions, and between 49.3 and 51.0 kbar, Pd2···S21 and Pd4···S41 contract by 0.052(7) and 0.116(8) Å (Fig. 14 & 15), respectively. In both cases, the axial interaction remains similarly compressible as prior to the phase transition and distances of 2.755(12) and 2.685(12) Å are obtained for Pd2···S21 and Pd4···S41, respectively, with the latter corresponding to the maximum compression of this type of interaction in the study. While it appears that compression of the equatorial interactions continues in a similar manner as prior to the transition, the standard uncertainties coupled to them are larger still in the high pressure phase and do not allow for accurate discussion.

Across the phase transition, the axial interactions of the reoriented cations undergo a stepwise contraction to a length reminiscent of an equatorial interaction (Fig. 16 & 17). Concomitant to this, a pair of opposing equatorial interactions expands to adopt the length of elongated axial interactions. The resulting axial interactions direct into the region of the more labile solvent / anion moieties, rather than at another cation. The use of the term 'reoriented' thus does not refer to the entire molecule rotating, a process which would incur a massive energy penalty, but to the relative orientation of the coordination axes.

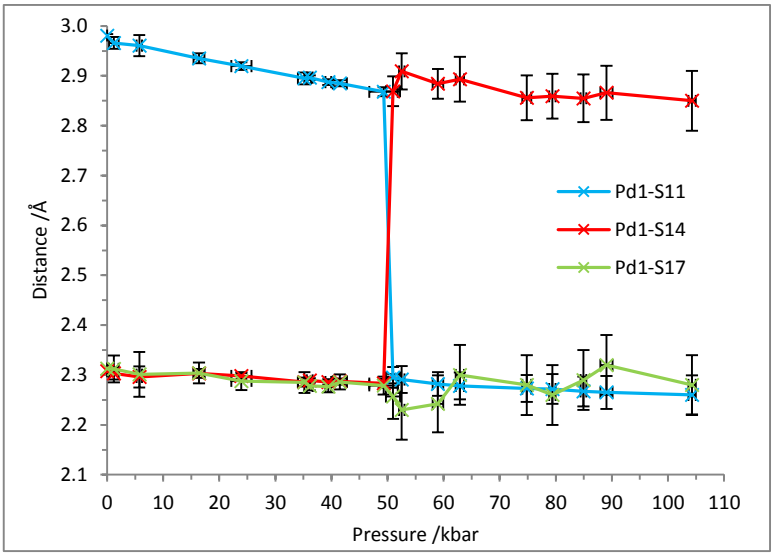



**Figure 16** The effects of pressure on the coordination bonds in the ambient phase and in the high-pressure phase at Pd1. The cation in **3a'** is subject to a reorientation of its coordination axes over the phase transition.

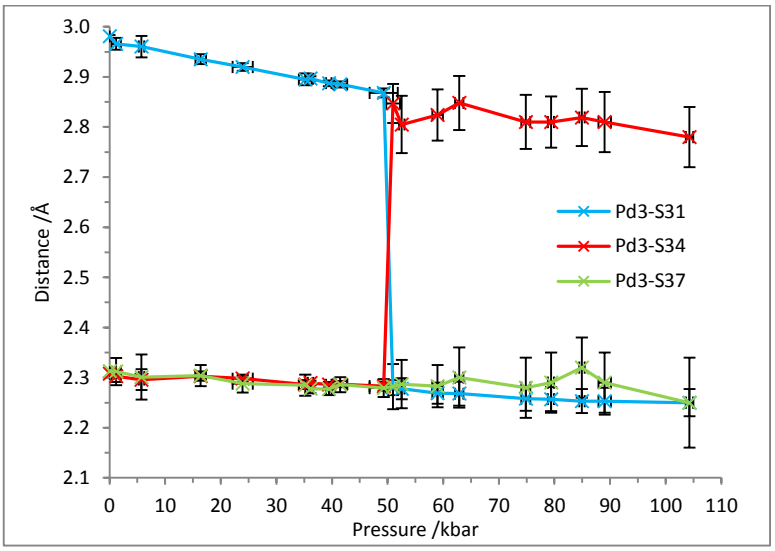



**Figure 17** The effects of pressure on the coordination bonds in the ambient phase and in the high-pressure phase at Pd3. The cation in **3a'** is subject to a reorientation of its coordination axes over the phase transition.

While the ESUs on the interaction are significantly increased, between 49.3 and 52.5 kbar, the axial interaction at Pd1 is observed as increasing from 2.868(3) Å at

49.3 kbar in **3a** to 2.909(12) Å at 52.5 kbar. Over the same pressure, the axial interaction at Pd3 appears to be smoothly and sharply compressed to 2.847(13) Å. This compression is then seemingly relaxed over the following *ca.* 10 kbar to a value that would instead match the projected compression of the interaction based on the low pressure data. Whether or not these deviations are real remains debateable; the increased uncertainty on these axial interactions in the high pressure phase makes description of their behaviour less clear. In contrast, the reorientation of one of the equatorial donors gives rise to a greater degree of certainty in its length and suggests that compression of these interactions also continues at a similar rate as to before the phase transition.

The application of pressure up to 49.3 kbar to **3a** serves to bring the coordination geometry at the metal centre closer to that of a more ideal octahedron (Fig. 18). As S1 is compressed in towards the metal centre it adopts a more central position and angles subtended at the metal between S1 and the two equatorial donors open up by *ca*. 3 °. Simultaneously, S4−Pd1−S7 is also opened with pressure and rises from 89.01(3) to 90.86(16) ° between ambient pressure and 49.3 kbar.

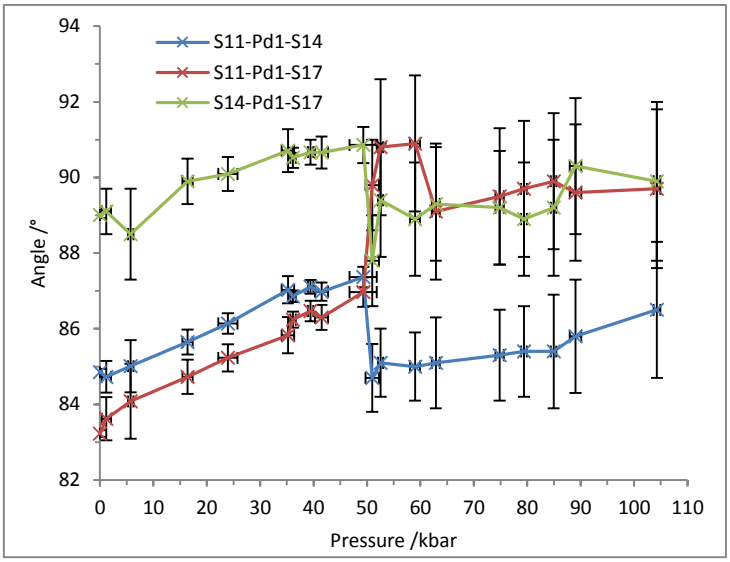



**Figure 18** The effects of pressure on the coordination geometry in the ambient phase and in the high-pressure phase at Pd1. The cation in **3a'** is subject to a reorientation of its coordination axes over the phase transition.

The effect of the phase transition on the coordination geometry of the cations is as varied as the effect on the axial interaction and the uncertainties associated to the parameters are also significantly increased. As a general observation, in the reoriented cations the transition results in narrower angles for those corresponding to S1−Pd1−S4 of **3a**, *i.e.* including the axial donors before and after the reorientation (Fig. 18 & 19). At the same time, angles corresponding to S1−Pd1−S7 of **3a** where both sulfurs form equatorial donors in **3a'**, are opened towards that of the angle between equatorial donors prior to the transition. S4−Pd1−S7 is closed similarly in both cations back to angles reminiscent of the value at ambient pressure.

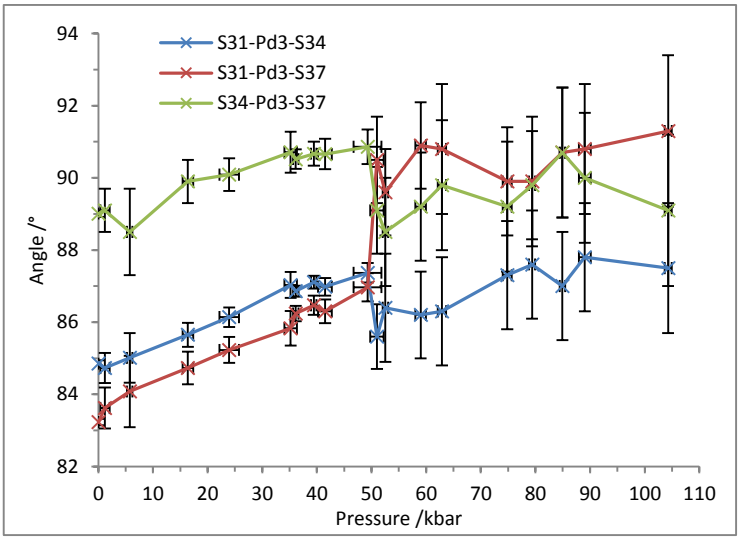



**Figure 19** The effects of pressure on the coordination geometry in the ambient phase and in the high-pressure phase at Pd3. The cation in **3a'** is subject to a reorientation of its coordination axes over the phase transition.

Compression of the coordination geometry in the cations not subject to reorientation is notably different to those that are. The stepwise compression of the axial interactions is accompanied by an expansion to the angle corresponding to S1−Pd1−S4 of **3a** that is much greater at Pd4 than Pd2 (Fig. 20 & 21, respectively), where Pd4−S41 was also subject to the greatest compression. Angles relating to S1−Pd1−S7 only appear to be affected to a similar degree as would be expected by continued compression of **3a**. The remaining angles all appear slightly closed by the transition.

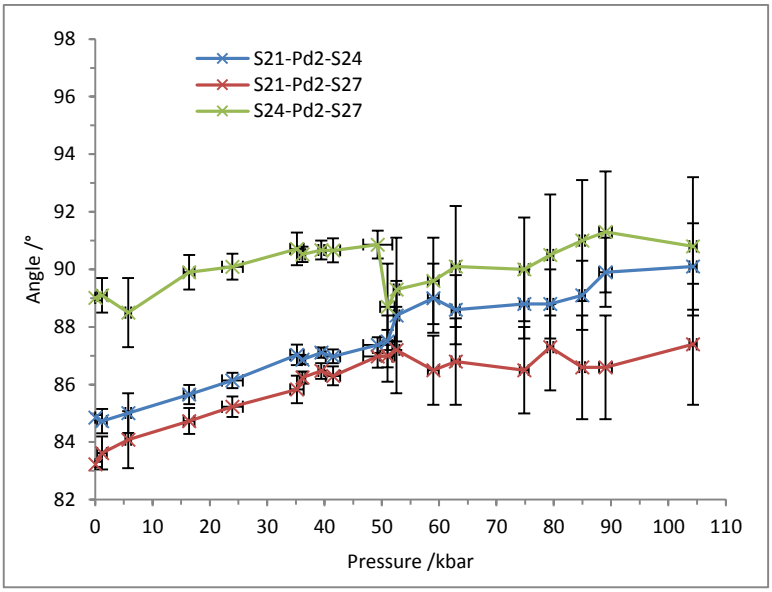



**Figure 20** The effects of pressure on the coordination geometry in the ambient phase and in the high-pressure phase at Pd2. The cation in **3a'** is not subject to a reorientation of its coordination axes over the phase transition.

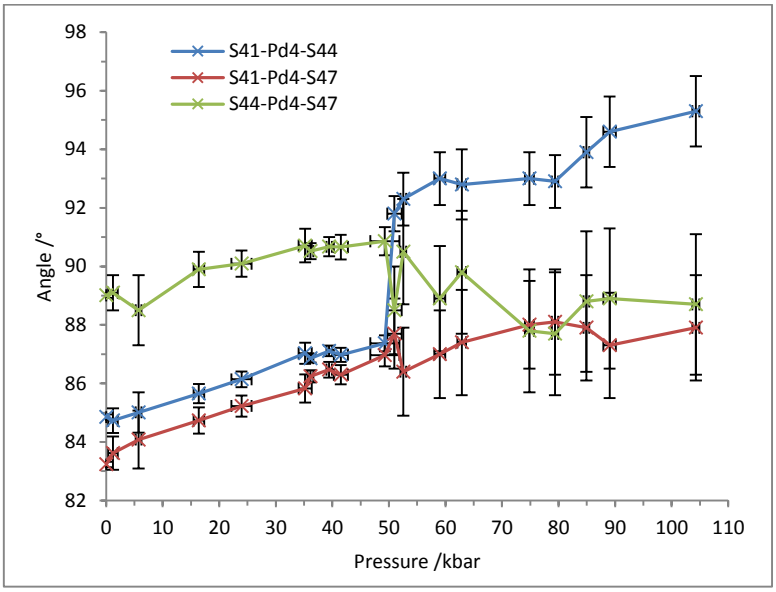



**Figure 21** The effects of pressure on the coordination geometry in the ambient phase and in the high-pressure phase at Pd4. The cation in **3a'** is not subject to a reorientation of its coordination axes over the phase transition.

### 3.4.2. Compression of intermolecular interactions

Under ambient conditions, the contact C9−H9A···S7_#1 (symmetry code #1 = +*x*, 0.5 − *y*, 0.5 + *z*) is already at the edge of the sum of the relevant van der Waals radii [for *D*−H = 0.97 Å: H···*A* = 3.04 Å; $\Sigma_{vdW}$ = 3.00 Å (Bondi, 1964)] and 49.3 kbar is calculated as compressing this to 2.48 Å [for *D*−H = 0.97 Å: *D*···*A* = 3.338(13) Å; *D*−H···*A* = 147.9 °] (Fig. 22). Although the contact to S1 is comparatively longer at ambient pressure [for *D*−H = 0.97 Å; H···*A* = 3.24 Å], C2−H2A···S1_#2 (symmetry code #2 = 2 − *x*, −*y*, 1 − *z*) is compressed to within the sum of the van der Waals radii at *ca.* 25 kbar and reaches 2.82 Å by 49.3 kbar [for *D*−H = 0.97 Å: *D*···*A* = 3.574(7) Å; *D*−H···*A* = 135.6 °] (Fig. 23). While these contacts are not as highly repulsive as, for example, close H···H contacts, at these distances they would certainly exert a significant force on their respective Pd−S interactions.

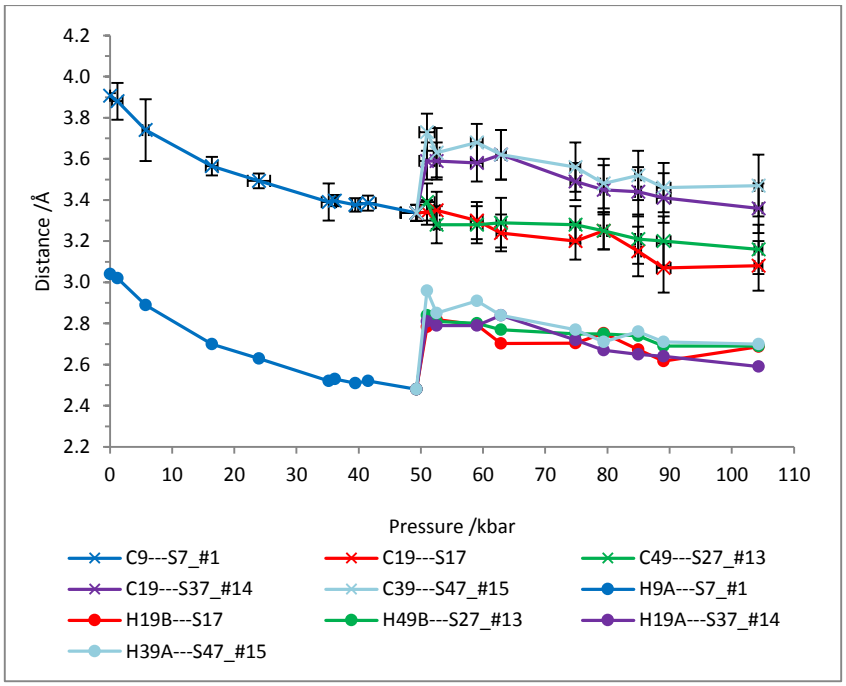



**Figure 22** Effects of pressure on the intermolecular hydrogen bonding at donors corresponding to S7 of **3a**. Symmetry codes: #1 = +*x*, 0.5 − *y*, 0.5 +*z*; #13 = −*x*, 1 − *y*, 2 − *z*; #14 = −*x*, 1 − *y*, 1 − *z*; #15 = +*x*, 1 + *y*, +*z*.

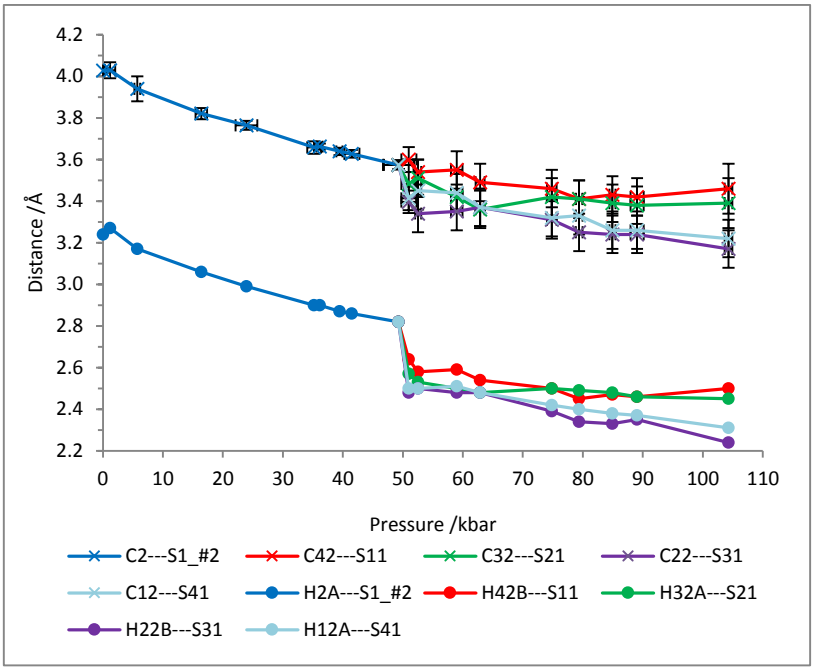



**Figure 23** Effects of pressure on the intermolecular hydrogen bonding at donors corresponding to S1 of **3a**. Symmetry code #2 = 2 − *x*, −*y*, 1 − *z*.

The phase transition brings a distinct and stepwise switching in the interaction distances within the hydrogen bonding motif. The ordered rearrangement of the coordination axes at half of the cations allows for considerably closer packing within their sheets. Switching of the affected axial interactions with equatorial interactions that direct out from the cationic sheets allows the complexes to slip relative to one another. This slipping of cations within sheets gives rise to closer contacts at the donors equivalent to S1 of **3a** (Fig. 22). This motion, along with the movement of the relevant $CH_2$ moieties brought about by the simultaneous expansion and contraction of coordination bonds, results in the relief of the contacts at donors equivalent to S7 of **3a** (Fig. 23). In this process, the relative lengths of the hydrogen bonding contacts at donors equivalent to S1 and S7 of **3a** are almost exactly switched (Fig. 22 & 23). As would be expected, the continued application of pressure results in further compression of both sets of interactions.

Coupled to the switching of their lengths, the phase transition has significant effect on the angles in the hydrogen bonding motifs. Between 49.3 and 51.0 kbar, the angles associated with the pair-wise interaction at the previously designated axial sulfurs (equivalent to S1 of **3a**) increase from 136 ° to between 155 and 170 °, whereas the angles remain relatively unaffected by pressure both before and after the transition (Fig. 24). Coupled to this, the *D*–H···*A* angles that were described as at equatorial sulfurs (equivalent to S7 of **3a**) contract from 148 ° to either *ca.* 116 or 137 ° (Fig. 25) while again being relatively stable prior to and beyond the transition. These discrete deviations are indicative of the slippage of the molecules over one another across the transition.

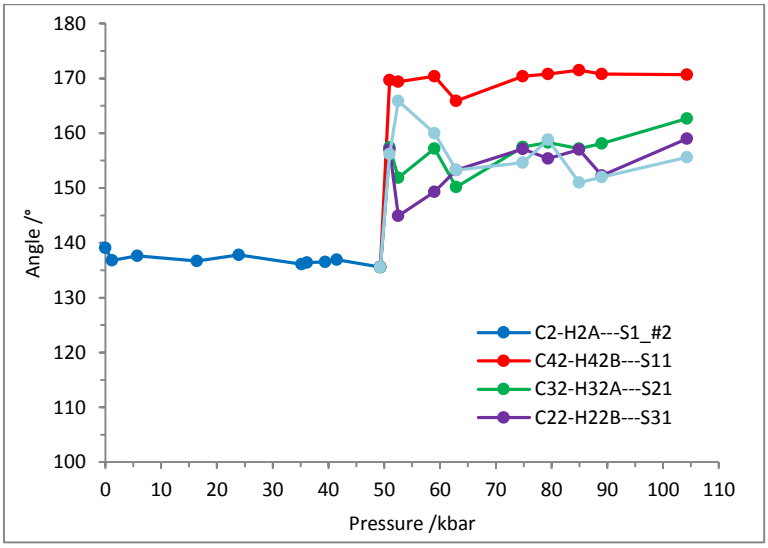



**Figure 24** Effect of pressure on the *D*–H···*A* angles in the ambient phase and in the high-pressure phase at donors corresponding to S1 of **3a**. Symmetry code #2 = 2 − *x*, −*y*, 1 − *z*.

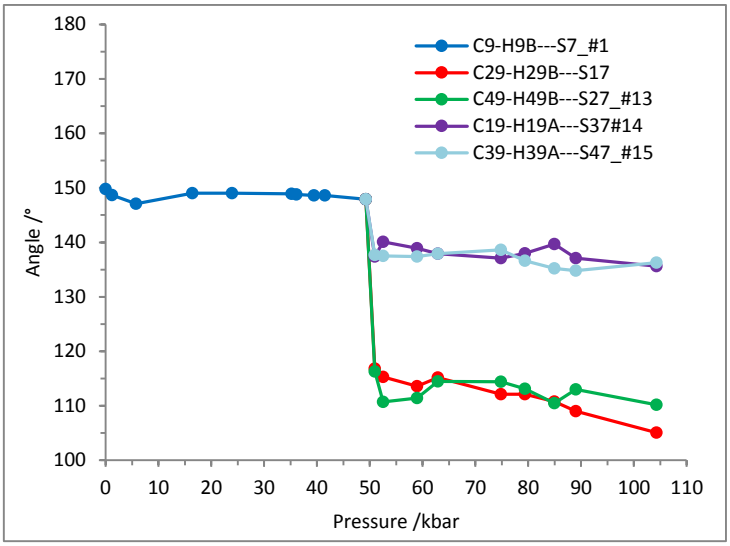



**Figure 25** Effect of pressure on the *D*–H···*A* angles in the ambient phase and in the high-pressure phase at donors corresponding to S7 of **3a**. Symmetry codes: #1 = +*x*, 0.5 − *y*, 0.5 + *z*; #13 = −*x*, 1 − *y*, 2 − *z*; #14 = −*x*, 1 − *y*, 1 − *z*; #15 = +*x*, 1 + *y*, +*z*.

Further close contacts are formed to S4 and S1 by the neighbouring nitromethane solvent molecules. Under ambient conditions, the small molecules in the solvent/anion layers are less hindered than the cations as these layers harbour the majority of the void space in the crystal. The application of 35 kbar serves to rapidly reduce the void space from 186 to 23 Å$^3$, reflected in compression in the *b* axis being rapid for the first *ca.* 20 kbar before notably slowing (Fig. 8). Consequently, the contacts between sulfur donors and nitromethane solvent molecules are rapidly compressed so that they fall within the sum of the relevant van der Waals radii (Fig. 26). The effects of the phase transition on the S···O contacts are clear with respect to the donors equivalent to S1 of **3a**, and in three of the four cases a stepwise compression of 0.1−0.2 Å is observed. In the cases of sulfur donors equivalent to S4 of **3a**, the effects are more varied and the protrusion of certain donors into these layers associated with the reorientation of the coordination axes at Pd1 and Pd3 allows for other contacts to become significant.

To broadly surmise, these contacts fall into two ranges after the phase transition, from which they are all similarly compressed: one set in the range 2.8−2.9 Å and another in the range 3.1−3.3 Å.

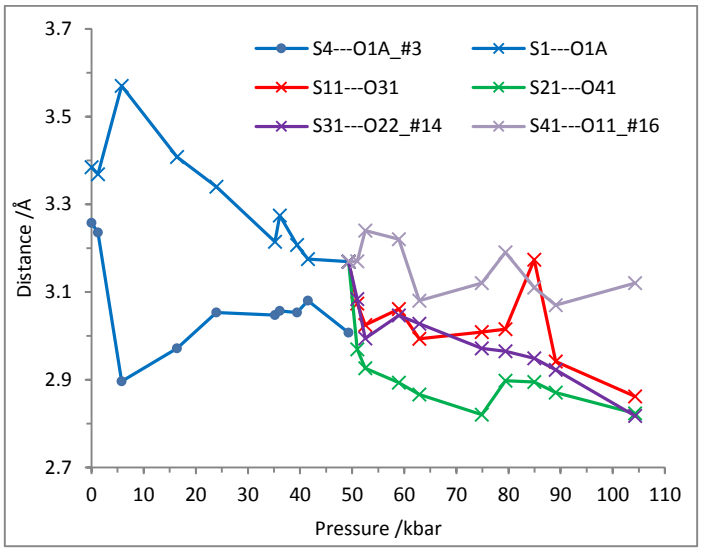



**Figure 26** Effect of pressure on the various intermolecular S···O contacts in **3a'** at the donor atom corresponding to S1 of **3a** and also at S4 in **3a** only (circles). Error bars are suppressed for clarity but are similar throughout: average value of 3σ in $y$ = ±0.16 Å; average error in $x$ = ±0.9 kbar. $\Sigma_{vdW}$S,O = 3.32 Å (Bondi, 1964).

### 3.4.3. Pressure dependence of the macrocyclic conformation

Throughout this study there were no notable changes in the macrocycle, which accommodates rearrangement of the coordination sphere without any necessity for conformational rearrangement: the [333] conformation is maintained across the entire pressure range studied.

### 3.4.4. Calculated bond orders

Analysis of the Mayer bond orders for the axial Pd···S interactions as a function of distance shows a distinct linear increase with compression (Fig. 27). This is indicative of no significant change in the nature of the bonding interaction with

pressure, both over the stepwise compression of the axes which remain aligned as in **3a** and in those which are reoriented. This would indicate that the phase transition is not primarily a response to the axial Pd···S interactions reaching an unstable length, as seen for the binuclear Cu(II) complex [guH][$Cu_2$(OH)(cit)(gu)$_2$] ($cit^{4-}$ = citrate; gu = guanidine; Moggach *et al.*, 2009). Compression of the equatorial interactions in the range of those observed in this study has no significant or systematic effect on the bond orders.

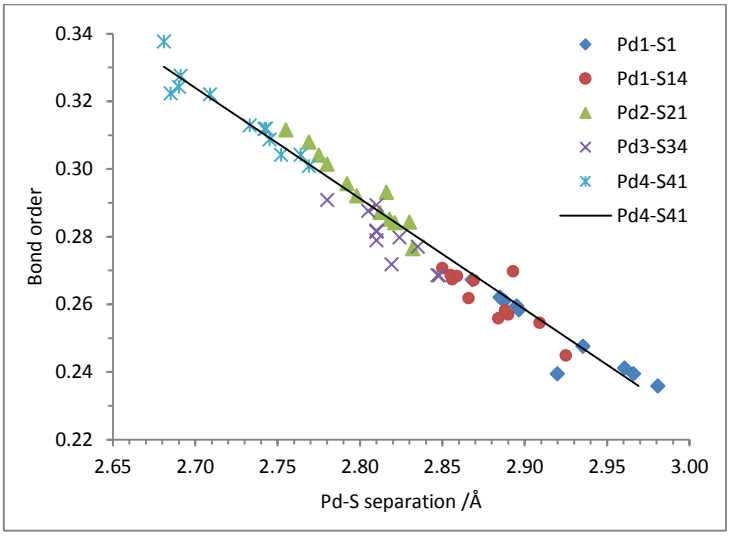



**Figure 27** Calculated Mayer bond orders for the axial Pd···S interactions as a function of interaction length. The linear trend-line for Pd4−S41 is extrapolated to show the agreement of the data.

### 3.4.5. Rationalisation of 3a → 3a' phase transition

As described in Section 3.1.1, the cations in **3a** form sheets *via* C−H···S interactions between one another, with longer pair-wise interactions at the axial sulfurs and shorter singular interactions at equatorial S7. The application of pressure rapidly compresses these to form much closer contacts than those described at low pressure (*cf.* Section 3.4.2, Fig. 23 & 22, respectively). The closer of these interactions is relieved from 2.48 Å to *ca.* 2.8 Å by the phase transition

while also being significantly bent away from linearity (*cf.* Fig. 25). In contrast, the longer, pair-wise C−H···S interactions at the axial sulfurs of **3a** are compressed across the transition from 2.82 to *ca.* 2.5−2.6 Å while also becoming more linear (*cf.* Fig. 24) as a consequence of the complexes slipping relative to one another. This in turn allows for denser packing within the cationic sheets and, despite the slight expansion of 0.6757(8) Å in the *a* axis, gives rise to a stepwise reduction of 10.5 $Å^3$ in *V*/*Z*. This stepwise contraction corresponds to an energy of 32.2 kJ $mol^{-1}$ at 50.14 kbar, *ca.* 25 times greater than that calculated for the β-**1** → β'-**1** transition reported for complex **1** which was rationalised as primarily an effect of highly repulsive, near linear C−H···H−C contacts (*cf.* Chapter 3, Section 3.4.3; Tidey *et al*., 2016). In the case of the **3a** → **3a'** transition, there is an apparent absence of the relief of any such contacts over the transition without incurring costly compression to others. Furthermore, there is a lack of any indication of changes in the nature of the bonding in the DFT to explain the reorientation of the coordination axes, as seen in Chapter 6 for $[Ag([18]aneS_6)]I_7$. Given such absence of cause, this significantly higher effect on the *PV* term of the Gibbs free energy may suggest that the transition occurs simply as a mode by which the system can decrease the volume and thus total energy. This decrease in energy is comparable to that associated with the phase transitions observed in the compression of 4-methylmethcathinone (Satthaphut *et al*., 204), where the authors reach much the same conclusions. The compound undergoes phase transitions at 8.8 and 48 kbar, with decreases in the *PV* term of 18 and 43 kJ $mol^{-1}$, respectively. In a similar fashion as in this study, the authors find that neither phase transition conclusively reduces the strain of a given parameter without resulting in yet more highly strained close contacts. They conclude that the reduction in volume and its

effect on the *PV* term of the Gibbs free energy is the driving force of the transitions.

### 3.4.6. Decompression and hysteresis

Decompression revealed a hysteresis loop of *ca.* 10 kbar with respect to the phase transition (Fig. 28). Across this pressure range, the response of the structural parameters corresponds to what is expected from extrapolation of the results. These parameters have been omitted from discussion for clarity but the behaviour of select parameters are included in the supplementary information (Section S1). It follows that if the phase transition upon compression provides a significant release in energy then the return transition upon decompression comes at a significant energy penalty: between 40.7 and 37.4 kbar the energy associated to the *PV* term is calculated as increasing by 39.4 kJ $mol^{-1}$ ($\Delta V/Z$ = 16.5 $Å^3$, calculated at 39.1 kbar). While transformation to a less dense phase would result in a net relief of intermolecular interactions and compression of the coordination sphere, the expansion that this brings to the sample favours lower pressures. In addition, the pressure of close and highly directed C−H···S contacts greatly resists the necessary expansion of Pd1−S11 and Pd3−S31, likely also favouring lower pressures.

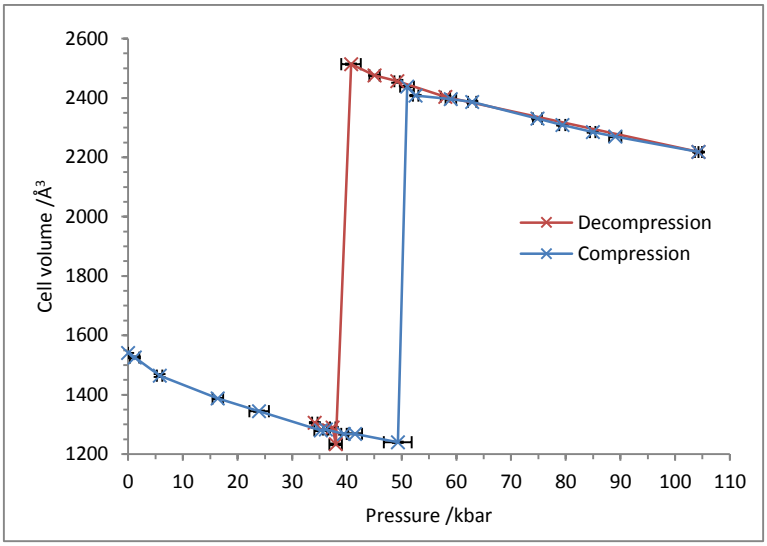



**Figure 28** Effects of pressure on the unit cell volume of $[Pd([9]aneS_3)_2](PF_6)_2 \cdot 2CH_3NO_2$ with compression and decompression.

### 3.5. UV/vis absorption studies

#### 3.5.1. Experimental high-pressure solid-state UV/vis spectra

A rig was designed and constructed which delivered the fibre-optic cables of an Ocean Optics UV/vis spectrometer to the sample within the DAC with stable and reproducible alignment (Fig. 1). Despite this, there was still a large degree of variability in the apparent baseline between scans and peak position was the only information that can reasonably be compared between spectra. Solid state UV/vis spectra were recorded upon compression at intervals of *ca.* 5 kbar up to 76.5 kbar before recording upon decompression to 13.2 kbar with particular focus on pressures between 42.5 and 33.8 kbar. The phase transition upon compression was visually monitored using an optical microscope and the crystal was observed changing in colour from dull green to orange. The colour change commenced in two adjacent corners and proceeded as straight fronts of colour moving diagonally across the crystal to meet in the middle, thereby explaining the occurrence of

twinning in the phase. The phase transition upon decompression on this occasion was highly destructive and shattered the crystal into many pieces, but this was not the case in the crystallographic experiments. The pressures found for the phase transition both with compression and decompression were lower than those found in the crystallographic study by *ca*. 3−5 kbar. The difference in this case may be related to the very differing rates of pressure ramping between the crystallographic and spectroscopic experiments, perhaps by affecting the precise location of the more labile anions or solvent molecules. Other possible causes include slightly differing degrees of solvation or defects in the crystal. This highlights the point that the precise pressure at which a particular phenomenon in a molecular crystal occurs can only be determined by studies of multiple crystals.

Solid-state UV/vis studies reveal the gradual migration of a band in the UV region into the visible region with increasing pressure up to the phase transition (Fig. 29; see supplementary information, Section S2 for all individual spectra). Across the transition, absorption in the 400−500 nm range is significantly increased and appears broad. It is likely that this is an effect of the phase transition generating four unique cations, each with differing coordination bond lengths and contacts to the sulfur donors, causing the absorption band to migrate by differing degrees in each case. The absorption band at *ca*. 630 nm is essentially unaffected by the phase transition.

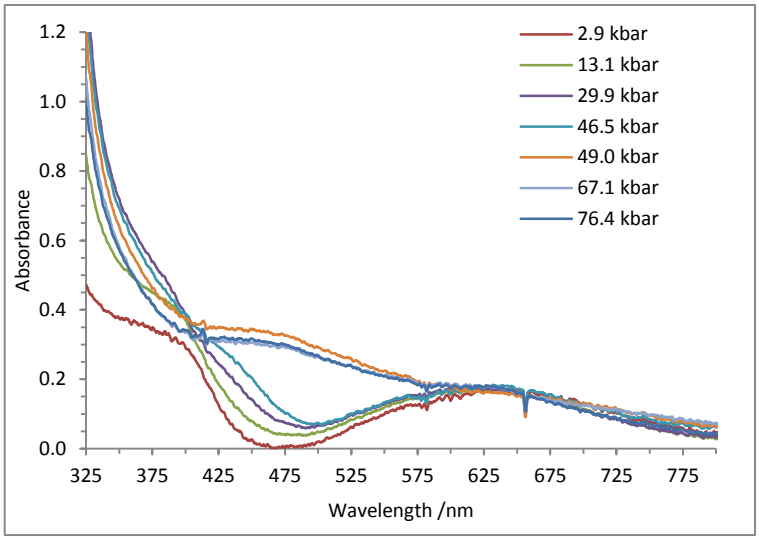



**Figure 29** Effect of pressure on the solid-state UV/vis spectra of **3a** / **3a'**. Spectra have been approximately normalised to one another at 630 nm to account for clarity and to account for the variable baseline, mentioned at the head of Section 3.5.1. The feature at *ca.* 655 nm is an instrumental artefact.

### 3.5.2. Computational gas-phase UV/vis spectra

In addition to the experimentally obtained spectra, the UV/vis excitations were calculated for each individual cation as part of the *ADF* DFT calculations. In doing so, spectra could be generated that represented compression of the coordination sphere in the absence of any outer-sphere interactions. Given the possibility of the complex being sensitive to these and not just inherently piezochromic, such calculations are of immense value in the absence of detailed systematic study of other solvates and non-solvates.

The relative intensity of each excitation was calculated as varying significantly from cation to cation, but the peak positions of the excitations were more consistent. Three absorptions were revealed and the results were in moderate agreement with the solid-state spectra collected, showing migration of a band at the edge of the UV region into the visible region in such a way as to produce the

observed piezochromic response (Fig. 30; see also Fig. 31). However, a significant shift calculated for the $^1A_g$ transition is not observed in the experimental spectra. Furthermore, the positions of these excitations do not precisely match those of the experimental spectra, implying that the outer coordination environment certainly has bearing on their precise energies.

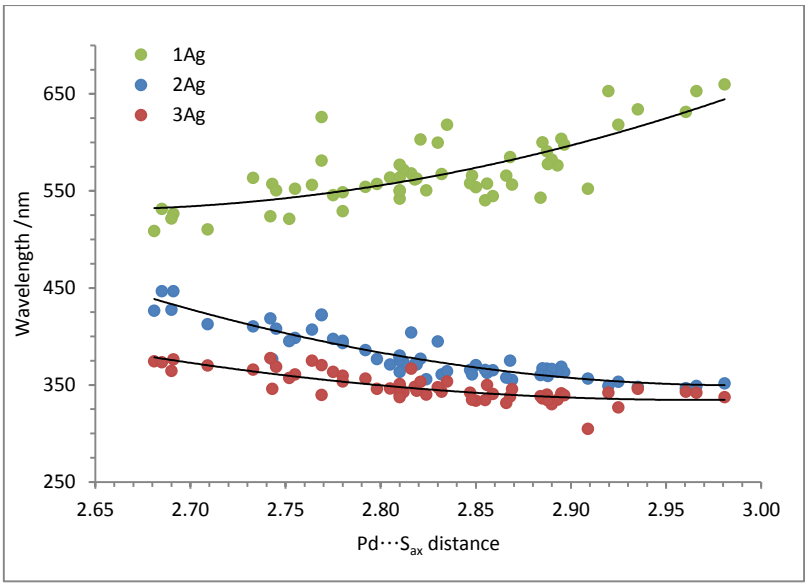



**Figure 30** The effect of compression of the Pd···$S_{ax}$ interactions on the calculated excitation wavelengths for the cations observed in the high-pressure crystallographic experiments.

Plotting the wavelength of the calculated excitations against the various structural parameters shows dependence of the $^2A_g$ and $^3A_g$ excitations on compression of the Pd···$S_{ax}$ interaction (Fig. 30) but not on compression of the Pd−$S_{eq}$ interactions (Fig. 31). In contrast, the $^1A_g$ excitation appears to depend on both the axial and the equatorial bond lengths.

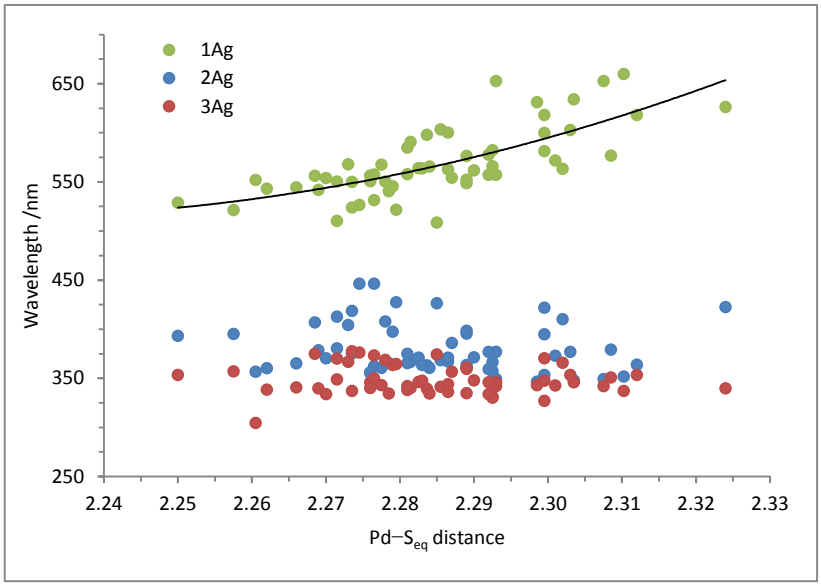



**Figure 31** The effect of compression of the Pd–$S_{eq}$ (right) interactions on the calculated excitation wavelengths for the cations observed in the high-pressure crystallographic experiments.

### 3.5.3. Rationalisation of piezochromic response

Compression of the distances between the sulfur donors and either the oxygen atoms of the solvent or the fluorine atoms of the anions was not considered as these could not be included using the software available. Given the similar migration of the $^2A_g$ band in the experimental and calculated spectra, it is valid to associate this band with the Pd···$S_{ax}$ interaction. However, the discrepancy between the experimental and calculated spectra for the $^1A_g$ band suggests that either the calculations and functionals employed are flawed, or that intermolecular, outer-sphere effects play a considerable role in negating this migration. Fig. 32 shows the primary molecular orbitals involved in the three excitations calculated for **3a**. It is clear that the close S···H–C and S···O outer-sphere contacts may well modulate the excitations given the protrusion of large orbital components from the sulfur donors. It is unsurprising, therefore, that the omission of packing considerations

would result in discrepancies between the calculated and experimental spectra. While the observable piezochromism is a response to simple compression of the axial interactions, the true extent of the piezochromic response in this cation is reduced by the compression of intermolecular contacts.

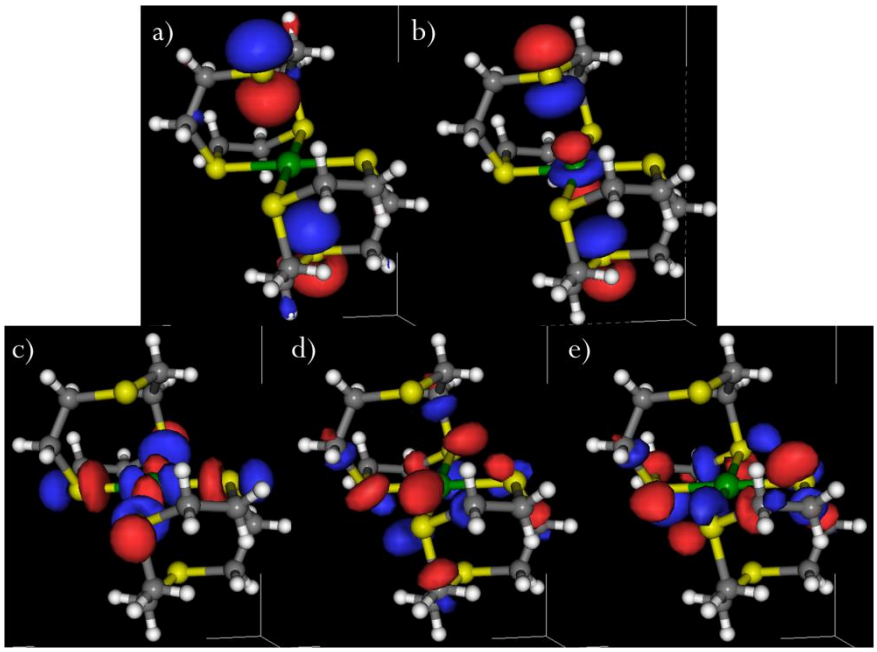



**Figure 32** Images of the electron density surfaces for the molecular orbitals which comprise the major components of the excitations calculated. a) HOMO-1, b) HOMO, c) LUMO, d) LUMO+2, e) LUMO+3; $^{1}A_{g}$excitation corresponds to the transition between the HOMO−1 and LUMO; $^{2}A_{g}$ excitation corresponds to the transition between the HOMO and LUMO+2; $^{3}A_{g}$ excitation corresponds to the transition between the HOMO and LUMO+3.

### 3.6. Further comments - ambient phases

In Section 3.1, three previously unreported solvates of **3** are reported, along with two high-pressure phases in Section 3.3. Table 1 lists the cell the cell parameters for these and for the other reported phases of $[Pd([9]aneS_3)_2](PF_6)_2$. With reference to the aforementioned table and relevant sections, it is clear that the solvates and high-pressure phases described in this chapter are all very closely related. Indeed,

given the similarity of **3b** and **3c-II**, and of **3c-II'** and **3a**, it could be expected that if high-pressure crystallographic study were carried out on **3b**or**3c-II** then they would follow the phase path *Pbca* → $P2_1/c$ → *P*1. Furthermore, given the conclusion that the piezochromism is mediated through compression of the axial Pd···S interactions, similar piezochromism should be observed in such studies. Characterisation of this may well prove invaluable in further elucidating the true effect of outer-sphere contacts on the chromophore.

**Table 1** List of cell parameters for all known phases of $[Pd([9]aneS_3)_2](PF_6)_2$. Codes refer either to this chapter (bold) or Cambridge Structural Database Ref Codes (italics; Groom *et al.*, 2016); modification **DLS** corresponds to **3c-II** studied at Diamond Light Source; parameter values have been rounded for ease of comparison.

| **Modification** | **Space group** | ***a*** | ***b*** | ***c*** | **α** | **β** | **γ** | ***V*** | ***Z*** |
|---|---|---|---|---|---|---|---|---|---|
| $2(CH_3)_2CO$; **3b** | *Pbca* | 15.5 | 10.1 | 20.0 | 90 | 90 | 90 | 3129 | 4 |
| $2CH_3CN$; **3c-II** | *Pbca* | 15.2 | 9.7 | 20.5 | 90 | 90 | 90 | 3032 | 2 |
| $2CH_3CN$; **3c-II'** | $P2_1/c$ | 10.4 | 15.0 | 9.8 | 90 | 100 | 90 | 1503 | 2 |
| $2CH_3CN$; **DLS** | $P2_1/c$ | 19.8 | 15.0 | 9.5 | 90 | >93 | 90 | 2818 | N/A |
| $2CH_3NO_2$; **3a** | $P2_1/c$ | 10.1 | 15.5 | 10.0 | 90 | 100 | 90 | 1541 | 2 |
| $2CH_3NO_2$; **3a'** | *P*1 | 10.0 | 16.4 | 16.4 | 115 | 94 | 95 | 1503 | 4 |
| $2CH_3CN$; **3c-I** *DAPTUL* | *Pccn* | 11.9 | 21.7 | 11.4 | 90 | 90 | 90 | 2948 | 2 |
| $2H_2O$; *FAPBED* | $P2_1/c$ | 10.5 | 11.6 | 11.6 | 90 | 112 | 90 | 1301 | 2 |
| Non-solvate; *FAPBAZ* | $C2/c$ | 17.9 | 15.7 | 11.5 | 90 | 126 | 90 | 2611 | 4 |

It is interesting that piezochromism was not observed in the preliminary study of **3c**. Given that the relevant diffraction data are no longer available, it is not possible to say why this is, but in the light of the current work it may be the case that the phase studied was the known solvate, **3c-I**, which differs in some significant ways from those newly reported within. Although the phase still comprises a layered

packing motif of alternating cationic and solvent/anionic regions, the packing of the cations within the sheets differs significantly. Instead of being approximately aligned, the coordination axes of the cations in **3c-I** are rotated by 90 ° in the *ac* plane and the packing does not give rise to any similar C−H···S hydrogen bonding interactions which would readily compress the axial interactions (Fig. 33). Instead, axial sulfur donors are directed into the open side of neighbouring cations, between equatorial sulfurs, and cations are afforded more room in which to rotate. Nevertheless, with the axial interaction being the softest of all intramolecular interactions in the phase, once the van der Waals space had been compressed this interaction could then be compressed sufficiently to give a notable colour change. Therefore, even if it was the known form of **3c** that was studied, *i.e.*, **3c-I**, and it was taken to moderately high pressures, a piezochromic response would be expected. Thus, outer-sphere effects must be considered as relevant to the chromophore. However, this remains speculation in the absence of the original data.

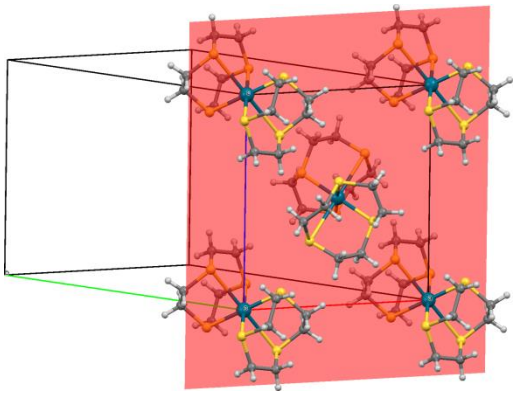


**Figure 33** Ball-and-stick image of the packing of cations within the cationic sheets of the reported form of $[Pd([9]aneS_3)_2](PF_6)_2 \cdot 2CH_3CN$. Cell axes shown; [101] plane added in red as depth marker.

## 4. Conclusions

The *bis*-nitromethane solvate of $[Pd([9]aneS_3)_2](PF_6)_2$ (**3a**) was studied by high-pressure single-crystal X-ray diffraction, variable-pressure solid-state UV/vis spectroscopy and employing complementary single-point density functional theory calculations. In the X-ray studies, it was found that the complex exhibited gradual sky-blue to dull green piezochromism between ambient pressure and 49.3 kbar along with linear compression of the axial Pd···S interaction from 2.9808(10) to 2.868(3) Å. Between 49.3 and 51.0 kbar, a $P2_1/c \rightarrow P1$ phase transition was observed with doubling of the unit cell volume by the transformation matrix [1 0 0 / 0 1 1 / 0 1 1] to a phase twinned by the matrix [1 0 0 / 0 0 1 / 0 1 0]. The phase transition was accompanied by a piezochromic response from dull-green to orange, with reorientation of the coordination axes at two of the four resulting unique cations. In addition, stepwise compression of the axial interactions that were not redirected was observed in the order of 0.1 Å while compression of the reoriented axial bond-lengths appears relaxed. Increased standard uncertainties preclude more detailed discussion of these parameters. The transition is followed by seemingly reduced compression of the axial interactions and cell volume for *ca.* 10 kbar, after which compression of the high pressure phase (**3a'**) continues similarly as before the transition. The four resulting axial interactions continue to compress at a similar rate after this period of lag and reach values ranging 2.686(12) to 2.85(2) Å at 104.3 kbar. There was little clear cause found for the phase transition in the behaviour of intra- or intermolecular parameters. Instead, it appears to be related to the considerable stepwise compression associated with it [$\Delta V/Z$ = 10.5 Å$^3$] and the large release of energy that this brings [$\Delta PV$ = 32.2 kJ mol$^{-1}$].

In the introduction it was noted that preliminary studies showed the same piezochromism reported herein for **3a** while no such piezochromism was observed for the acetonitrile solvate. This raised questions over the mechanism of piezochromism and solvatochromism in the complex. UV/vis spectra were calculated using the Amsterdam Density Functional suite (Fonseca-Guerra *et al.*, 1998; Te Velde *et al.*, 2001) for each experimentally determined cation of **3a** and **3a'** while it was not possible to extend the calculations to include the presence of neighbouring cations or surrounding anions or solvent molecules. The calculations gave reasonable agreement with the experimentally determined solid-state spectra. Correlation of the calculated spectra with the length of the axial and equatorial bond lengths revealed the strong appearance of a relationship between compression of the axial interaction and energy of each of the three excitations revealed. An additional dependence of the excitation at *ca*. 650 nm on compression of the equatorial interactions was also calculated. While this would initially appear to dispel the hypothesis that the piezochromism in **3a** is a response to outer-sphere contacts, the experimentally determined spectra only showed shifts in the two higher-energy excitations. It is hence reasonable to suggest that outer-sphere interactions not included in the calculations modulate the effects of compression on the lower energy excitation at *ca*. 650 nm.

Understanding how outer-sphere effects modulate the piezochromism of **3** requires significant further study. To investigate the effect of the solvate, the newly reported acetone and acetonitrile solvates presented in this chapter would provide isolation of the cationic network. Further study of the reported acetonitrile (Stephen *et al*., 2012) and non-solvate (Blake *et al*., 1987) phases would expand that investigation to interrogating the effect of cation···cation interactions.

## References


Agilent (2014). *CrysAlis$^{PRO}$*. Agilent Technologies, Yarnton, England.

Allan, D. R.; Bailey, D.; Bird, N.; Blake, A. J.; Champness, N. R.; Huang, D.; Keane, C. P.; McMaster, J.; Prior, T. J.; Tidey, J. P.; Schröder, M. (2014). *Acta Crystallogr., Sect. B*, **70**, 469-486.

Angel, R. J.; Gonzalez-Platas, J.; Alvaro, M. (2014). *Z. Kristallogr.* **229**, 405-419.

Barnett, J. D.; Block, S.; Piermarini, G. J. (1973). *Rev. Sci. Instrum.* **44**, 1-9.

Becke, A. D. (1988). *Phys. Rev. A*, **38**, 3098-3100.

Blake, A. J.; Holder, A. J.; Hyde, T. I.; Roberts, Y. V.; Lavery, A. J.; Schröder, M. (1987). *J. Organomet. Chem.* **323**, 261-270.

Blake, A. J. (2014). *Private communication.*

Bondi, A. J. (1964). *J. Phys. Chem.* **68**, 441-451.

Clark, R. C.; Reid, J. S. (1995). *Acta Crystallogr., Sect A*, **51**, 887–897.

Cosier, J.; Glazer, A. M. (1986). *J. Appl. Crystallogr.* **19**, 105-107.

Dale, J. (1973). *Acta Chem. Scand.* **27**, 1115-1129.

Dolomanov, O. V.; Bourhis, L. J.; Gildea, R. J.; Howard, J. A. K.; Puschmann, H. (2009). *J. Appl. Cryst.* **42**, 339-341.

Fonseca-Guerra, C.; Snijders, J. G.; Te Velde, G.; Baerends, E. J. (1998). *Theor. Chem. Acc.* **99**, 391-403.

Galloway, K. W.; Moggach, S. A.; Parois, P.; Lennie, A. R.; Warren, J. E.; Brechin, E. K.; Peacock, R. D.; Valiente, R.; González, J.; Rodríguez, F.; Parsons, S.; Murrie, M. (2010). *CrystEngComm*, **12**, 2516-2519.

Grant, G. J.; Chen, W.; Goforth, A. M.; Baucom, C. L.; Patel, K.; Repovic, P.; VanDerveer, D. G.; Pennington, W. T. (2005). *Eur. J. Inorg. Chem.* 479-485.

Grey, J. K.; Butler, I. S. (2001). *Coord. Chem. Rev.* **219-221**, 713-759.

Groom, C. R.; Bruno, I. J.; Lightfoot, M. P.; Ward, S.C. (2016). *Acta Crystallogr., Sect. B*, **72**, 171–179.

Holzapfel, W. B. (2003). *J. Appl. Phys.* **93**, 1813-1818.

Klotz, S.; Chervin, J.-C.; Munsch, P.; Le Marchand, G. (2009). *J. Phys. D: Appl. Phys.* **42**, 075413/1- 075413/7.

Moggach, S. A.; Galloway, K. W.; Lennie, A. R.; Parois, P.; Rowantree, N.; Brechin, E. K.; Warren, J. E.; Murrie, M.; Parsons, S. (2009). *CrystEngComm*, **11**, 2601-2604.

Nagakura, S.; Ohashi, Y.; Hanazaki, I. (1970). *Inorg. Chem.* **9**, 2551-2556.

Perdew, J. (1986). *Phys. Rev. B*, **33**, 8822-8824.

Satthaphut, N.; Sutcliffe, O. B.; Oswald, I. D. H. (2014). *Z. Kristallogr.* **229**, 101-111.

Sheldrick, G. M. (2008). *Acta Crystallogr., Sect. A*, **64**, 112-122.

Sheldrick, G. M. (2015). *Acta Crystallogr., Sect. C*, **71**, 3-8.

Stephen, E.; Blake, A. J.; Carter, E.; Collison, D.; Davies, E. S.; Edge, R.; Lewis, W.; Murphy, D. M.; Wilson, C.; Gould, R. O.; Holder, A. J.; McMaster, J.; Schröder, M. (2012). *Inorg. Chem.* **51**, 1450-1461.

Takagi, H. D.; Noda, K.; Itoh, S. (2004). *Platinum Met. Rev*. **48**, 117-124.

Te Velde, G.; Bickelhaupt, F. M.; Baerends, E. J.; Fonseca-Guerra, C.; van Gisbergen, S. J. A.; Snijders, J. G.; Ziegler, T. (2001). *J. Comput. Chem.* **22**, 931-967.

Tidey, J. P.; Wong, H. L. S.; McMaster, J.; Schröder, M.; Blake, A. J. (2016). *Acta Crystallogr., Sect. B*, **72**, 3, 357-371.

Vosko, S. H.; Wilk, L.; Nusair, M. (1980). *Can. J. Phys.* **58**, 1200-1211.

Wieghardt, K.; Kuppers, H.-J.; Raabe, E.; Kruger, C. (1986). *Angew. Chem., Int. Ed.* **25**, 1101-1103

Woodall, C. H.; Beavers, C. M.; Christensen, J.; Hatcher, L. E.; Intissar, M.; Parlett, A.; Teat, S. J.; Reber, C.; Raithby, P. R. (2013). *Angew. Chem. Int. Ed.* **52**, 9691-9694.

Wu, L.-C.; Overgaard, J.; Madsen, S. R.; Schmoekel, M. S.; Iverson, B. B. (2013). *J. Chin. Chem. Soc.* **60**, 929-934.

Wu., L.-C.; Nielsen, M. B.; Bremholm, M.; Madsen, S. R.; Overgaard, J.; Newville, M.; Chen, Y.-S.; Iversen, B. B. (2015). *Chem. Commun.* **51**, 8868-8871.

Zahner, J. C.; Drickamer, H. G. (1960). *J. Chem. Phys.* **33**, 1625-1628.

# Chapter 6

## Compression Studies of a Templated Polyiodide Network

## 1. Introduction

The catenation of larger halides is a well-established field of chemical research with polyiodides receiving a high amount of interest since they find application in a range of areas including optics (Kahr *et al*., 2009), solar energy (Grätzel, 2009) and energy storage (Li *et al.*, 2015). A huge range of polyiodide catenation has been reported, comprehensively covering $I_3^-$ to $I_{14}^-$ with examples as high as $I_{29}^{3-}$ (Tebbe & Buchem, 1997), and Svensson & Kloo (2003) report a still very relevant review of these. In the vast majority of cases, the polyiodide motif can be described as comprising $I^-$and $I_3^-$ ions solvated by $I_2$ molecules, though often the inclusion of $I_5^-$ ions as a constituent component is employed. Thus, a number of bonding modes arise and bond lengths in polyiodides vary greatly, from that of diiodine to the very edge of the van der Waals radii (Fig. 1).

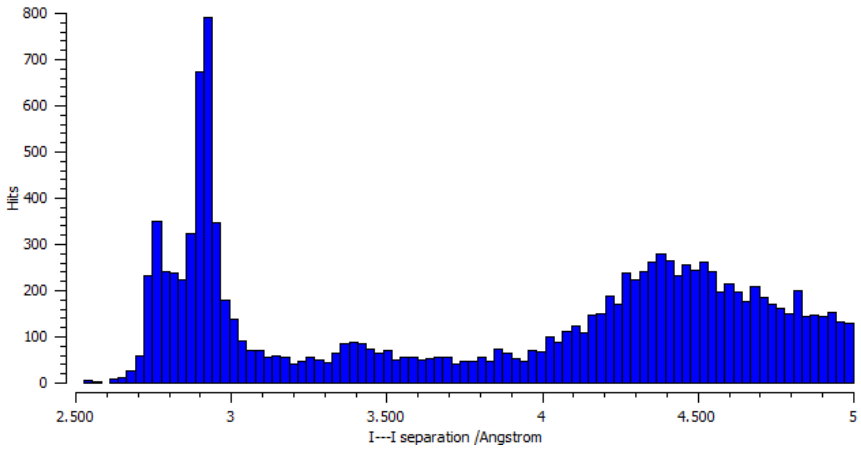



**Figure 1** Search results for the separation of an iodine/iodide residing 2.5−5.0 Å from an $I_2$ moiety of unspecified bond length from the Cambridge Structural Database, 2016 release plus two updates (Groom *et al.*, 2016).

The distribution of bond lengths for I···I interactions found in the Cambridge Structural Database is found to be distinctly tri-modal (2016 release plus two updates; Groom *et al.*, 2016), with the preferred intramolecular separation either

being *ca.* 2.7-2.8 Å, that of the diiodine bond, or more typically slightly longer at *ca.* 2.9-2.95 Å, corresponding to the elongated bond in $I_3^-$ moieties. Additionally, there is a broad maximum corresponding to interactions reminiscent of van der Waals contacts at *ca.* 4.5 Å. Notably, the entire region between these modal averages is very evenly populated, perhaps with the appearance of a small, fourth maximum at *ca.* 3.4 Å. Interactions of the3−4 Å length are typically referred to as 'secondary bonds', with the cut-off therein depending on the intention of the author. Given the uniform and significant population throughout this range it is deemed somewhat arbitrary, however, to assign a cut-off between what constitutes a 'bond' and what constitutes only a 'contact'.

Kloo *et al*. (2002) report an enlightening computational study of polyiodide bonding across the entire range of these interactions and beyond. The study focussed on bonding between $I^-$ ions and $I_2$ moieties, showing that electrostatic interactions dominate at separations greater than 5 Å as $I^-$ ions polarise neighbouring $I_2$ moieties to give rise to attractive partial charges. Covalent interactions remained significant well beyond the sum of the van der Waals radii, extending up to almost 5 Å. The onset of orbital overlap implicit to this gives rise to charge transfer effects which cause the electrostatic interactions to go from attractive to repulsive in nature as they cross below *ca.* 4.7 Å in length, reported by the same authors as *ca*. 4.5 Å in their review of the field which included this work in 2003 (Svensson & Kloo). Nevertheless, the covalent interactions compensate and interactions that can be considered as covalent intramolecular bonds certainly exist right up to the edge of the secondary bond region. This matter corroborates with the inference taken from the statistical data that it is wrong to attribute a cut-off for what constitutes a 'secondary bond' within the 3-4 Å region.

By way of geometry, I−I−I angles are typically found to closely favour linearity or, far less strictly, 90 ° (Fig. 2; CSD search employing 2016 release plus two updates; Groom *et al.*, 2016), indicative of their tendency to bond *via* 5p orbitals (Wiebenga & Kracht, 1969). Consequently, linear geometry is preferred for $I_3^-$ ions where the bonding is that of a 3-centre, 4-electron (3c, 4e) bond. Increasing the complexity to pentaiodides results in either linear or V/L shapes as the form taken is either that of a 5c, 6e bond or one describable as a resonance of terminal $I^-$ sharing triiodide ions, respectively (Hach & Rundle, 1951). For higher polyiodides, the geometry is typically reflective of their being constructed from the aforementioned building blocks, and heptaiodides are no exception to the rule.

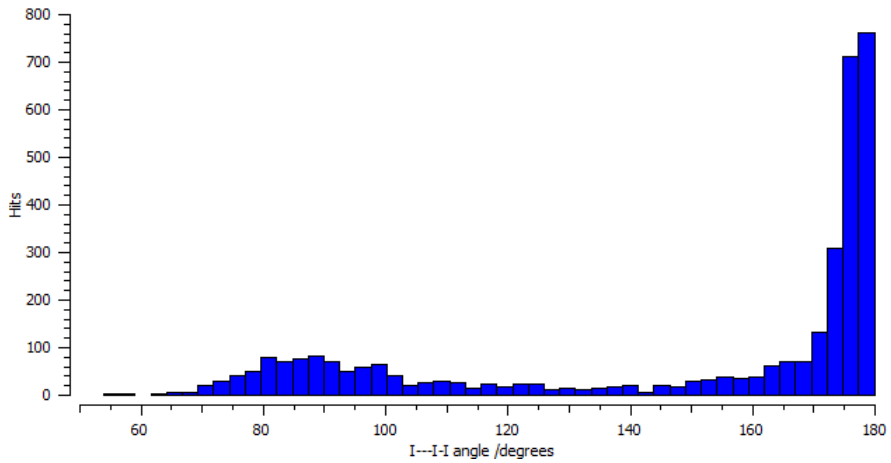



**Figure 2** Search results for the angle at the central atom of an iodine/iodide residing 2.5−4.0 Å from an $I_2$ moiety of unspecified bond length from the Cambridge Structural Database, 2016 release plus two update (Groom *et al.*, 2016).

As one might expect, the literature favours the lower polyiodides and tends to comprise only select examples at the upper bounds, an observation corroborated by Wang *et al.* (2014) who find that the greater the degree of polymerisation, the lower the stability of the polyiodide. The use of larger cations to template the more elaborate and less stable networks of higher-order polyiodide systems is well

established, and complexes of crown ethers (Fiolka *et al.*, 2015) and thioether macrocycles (Blake *et al.*, 1998) are very effective to this end.

With an increase in the number of fundamental building blocks there is an increase in the number of potential viable conformations. Consequently, the $I_7^-$ ion is seen in a number of forms in the literature, though these mostly reduce down to Z and trigonal pyramidal shapes. The literature would indicate that it is around this stoichiometry of iodine, *i.e.*, 3:1 $I_2/I^-$, that the proportion of iodine 'linkers' becomes sufficiently high as to make the formation of extended motifs a commonality: the formation of networks is far more common than distinct molecular anions for heptaiodides. For example, one dimensional chains motifs (Demartin *et al.*, 1993; Tebbe & Gilles, 1996; Tebbe & Loukili, 1998), two dimensional sheets (Tebbe & Farida, 1995) and three-dimensional networks (Tebbe & Nagel, 1996) have all been observed.

Despite extensive and combined structural and computational study, the high-pressure investigation of such systems is almost entirely novel. High-pressure study of iodine containing compounds has been almost entirely limited to the study of simple halocarbons, and those which include I···I contacts appear only to comprise studies of methyliodide (Podsiadlo & Katrusiak,2009), diiodomethane (Podsiadlo & Katrusiak,2006; 2008a; 2008b) and the study of iodoform by Bertolotti *et al.* (2013). Across these studies, compression of intermolecular I···I contacts is commonly brought significantly within the sum of the van der Waals radii by only very moderate pressure and, for example, 8.0 kbar results in an I···I contact of 3.738(4) Å in iodoform. Elemental iodine has also been studied using high-pressure X-ray diffraction, finding an intermediary phase to coexists with

phase I between 125 and 235 kbar (Zeng *et al.*, 2008) before the onset of phase V and metallic iodine is formed (Takemura *et al.*, 1980).

Similar studies of iodinated coordination complexes are seemingly limited to that of our own paper on [$MX_2$([9]ane$S_3$)] (*M* = Pd, Pt; *X* = Cl, Br, I; Allan *et al.*, 2014) wherein the study of complexes *M* = Pd, Pt where *X* = I are included. It was found that intermolecular iodide-iodide contacts were formed and able to compress well beyond the sum of the relevant van der Waals radii at notably low pressures (*ca.* 17 kbar). The corresponding bromides required significantly higher pressures (*ca.* 57 kbar) to catenate and the chlorides did not do so at all within the range studied.

This chapter reports the high-pressure study of the templated polyiodide [Ag([18]ane$S_6$)]$I_7$ ([18]ane$S_6$ = 1,4,7,10,13,16-hexathiacyclooctadecane; **4**). The macrocyclic complex serves to template an extended, distorted cubic array of diiodine molecules connecting two iodide nodes in a highly symmetric $^3_\infty[I^-\cdot(I_2)_{6/2}]$ network (Blake *et al.*, 1995). The high symmetry of the system makes it fortuitously ideal for high-pressure crystallography and the long six-fold arrangement of $I^-\cdots I_2$ interactions were expected to provide a sensitive probe to the effect of pressure on iodine/iodide catenation and polyiodide systems. The coordination complex cations were not, in this case, the primary interest.

## 2. Experimental

### 2.1. Synthesis

Reagents were used as received from Acros Organics, Alfa Aesar, Fischer Industries, Merck Schuchardt and Sigma-Aldrich. NMR spectroscopy was carried out at 270 MHz using a JEOL EX270 spectrometer ($^{13}$C) or at 100.61 MHz on a

Bruker AV400 spectrometer ($^1$H). IR spectroscopy was carried out using a Thermoscientific Nicolet 6700 FTIR spectrometer with a Specac supercritical fluid Golden Gate ATR attachment. Mass spectrometry was carried out using a Bruker Daltonics microTOF electrospray mass spectrometer. Elemental analysis was carried out using a model CE-440 Elemental Analyser.

### 2.1.1. Synthesis of [18]ane$S_6$

The reaction was carried out under anhydrous conditions in an Ar atmosphere. Sodium (1.379 g, 60 mmol) was added to a solution of 2,2'-thiodiethanethiol (4.629 g, 3.9 cm$^3$, 30 mmol) in methanol (400 cm$^3$) and the solution stirred until it had fully dissolved. 1,2-dibromoethane (5.636 g, 2.6 cm$^3$, 30 mmol) in methanol (18 cm$^3$) was added to this at a rate of 60 cm$^3$ hr$^{-1}$ with vigorous stirring for 50 minutes at 60 °C and a precipitate formed. The solution was allowed to cool before being filtered and the solids washed with dichloromethane (2 × 10 cm$^3$). The solvent was removed *in vacuo* and the resulting white solid extracted into dichloromethane (130 cm$^3$), washed with water (2 × 50 cm$^3$, 4 × 100 cm$^3$) and dried over magnesium sulfate. The solvent was removed *in vacuo* to give a white solid (720.1 mg) which was purified *via* column chromatography using an eluent of 25:1 (*v*/*v*) petroleum ether/ethyl acetate, $R_f$ = 0.16. The product was characterised as [18]ane$S_6$ (yield = 173.1 mg, 0.48 mmol, 3.2%). Mass spectrometry (ESI): 383 $[M+Na]^+$. $^1$H NMR $\delta_H$ (DMSO): 2.8 (24H, s, *CH*$_2$). $^{13}$C NMR $\delta_c$ (DMSO): 32.06 (*sp*$^3$*C*). Anal. Calcd for $C_{12}H_{24}S_6$: C=41.34% H=3.47%, N=0%. Found: C=39.39%, H=6.62%, N=0%. IR *v*/cm$^{-1}$ (ATR): 2956 (w), 2924 (w), 2853 (w), 1418 (s), 1259 (m), 1216 (w), 1193 (s), 1149 (m), 1125 (w), 1026

(w) 969 (w), 928 (w), 877 (w), 864 (w), 842 (m), 742.5 (w), 730 (w), 713 (m), 699 (m), 682 (s), 658.38 (m), 623 (w).

### 2.1.2. Synthesis of $[Ag([18]aneS_6)]I_7$

Synthesis followed that reported in the literature (Blake *et al.*, 1995). Silver tetrafluoroborate (27 mg, 0.14 mmol) in nitromethane (3 ml) was added to a solution of [18]ane$S_6$ (50 mg, 0.14 mmol) in chloroform (3.5 $cm^3$) and stirred for 15 minutes at room temperature. Diiodine (106 mg, 0.42 mmol) in chloroform (3 ml) was added drop-wise to this, causing the solution to immediately turn purple and discolour over time to a reddish brown. The solvent was removed *in vacuo* to give a dark green solid of $[Ag([18]aneS_6)]I_x$. The target was obtained alongside crystals of the triiodide by dissolving this in the minimum quantity of hot acetonitrile and allowing the solution to evaporate in a petri dish; the product was identified by single-crystal X-ray diffraction.

### 2.2. Crystallography

For the low temperature (120(2) K), ambient pressure collection outside of the DAC, a crystal of dimensions 0.086 × 0.031 × 0.009 $mm^3$ was mounted in a Fomblin film on a MiTeGen MicroMount™ and data collected using a Rigaku SuperNovaII diffractometer equipped with a microfocus sealed-tube source focussing mirror-monochromated Cu-*K*α radiation (λ = 1.54184 Å) detected at an Atlas CCD area detector. Cell refinement and data reduction was performed using *CrysAlis*$^{PRO}$ (Agilent, 2014) and numerical absorption corrections based on Gaussian integration over a multifaceted crystal model were applied. Temperature

was regulated using Oxford Cryostreams open-flow cryostats (Cosier & Glazer, 1986).

For high pressure experiments, data were collected on two crystals: crystal A was of dimensions 0.10 × 0.07 × 0.02 $mm^3$ and crystal B was of dimensions 0.10 × 0.07 × 0.03 $mm^3$. Both crystals were irregular plates cut from larger crystals and were a dark green/brown colour of metallic lustre. For crystal A, data were collected at 0.001, 2.5, 6.5, 9.8, 10.4, 20.3, 24.5, 30.0, 36.3, 41.0 and 45.8 kbar. For crystal B, data were collected at 0.001, 4.1, 7.0, 13.9, 11.7, 24.0, 31.4, 40.5 and 42.9 kbar. The sample was then decompressed and data collected at 39.1, 38.1, 38.2, 28.8, 13.0, 13.1 and 12.4 kbar.

The sample chamber of a Merrill-Bassett diamond anvil cell (DAC) was formed by the 600 μm culet faces of the Boehler-Almax diamonds and by laser-cut tungsten sheet (Goodfellow Metals, thickness 200 μm) indented to a thickness of *ca.* 80 μm with a gasket hole of diameter 200 μm drilled using a BETSA electric discharge machine. In each case, the sample crystal was fixed to one culet face by means of high-molecular-weight silicone grease alongside a ruby sphere which allowed pressure measurement using the ruby fluorescence method (Barnett *et al.*, 1973). The pressure transmitting medium (PTM) employed was RS3000, an oil for which the hydrostatic limit was determined in-house as being *ca.* 50 kbar (O'Connor, 2014); no PTM was used for the in-cell data collections at ambient pressure. After each pressure ramp, the pressure inside the DAC was allowed to equilibrate for a minimum of 24 hours before data collection was initiated. Pressure measurements were taken immediately before and after each collection and the pressure reported is the average of these. The average uncertainty in pressure across this study is ±0.8 kbar with specific error bars drawn on Figures as 0.5 times the magnitude of

the drift plus 0.5 kbar attributed to the inherent uncertainty of the ruby fluorescence method (Holzapfel, 2003).

High pressure data were collected using a Rigaku SuperNovaII diffractometer equipped with a microfocus sealed-tube source focussing mirror-monochromated Mo-*K*α radiation (λ = 0.71073 Å) detected at an Eos CCD area detector. Cell refinement and data reduction was performed using *CrysAlis*$^{PRO}$ (Agilent, 2014). For all data, multi-scan absorption corrections were applied with an empirical absorption correction using spherical harmonics, implemented in SCALE3 ABSPACK scaling algorithm (Clark & Reid, 1995) through *CrysAlis*$^{PRO}$.

Structure solution was undertaken using *SHELXS*14 direct methods (Sheldrick, 2008) for the ambient pressure structure and for the structures obtained at 20.3 and 41.0 kbar for Crystal 'a' and at 40.5 kbar for Crystal 'b'. All other structures were solved by isomorphous replacement using an appropriate model. Structures were refined to convergence using *SHELXL*14 (Sheldrick, 2015). Structure solution and refinement were implemented through *Olex2* (Dolomanov *et al*., 2009). Specific refinement details are embedded in the relevant CIFs which can be found along with the experimental tables in the supplementary information.

### 2.3. Density functional theory calculations

Single-point density functional theory (DFT) calculations were carried out on models derived from the experimentally obtained crystal structures using the Amsterdam Density Functional suite version 2014.02 (*ADF*; Fonseca-Guerra *et al.*, 1998; Te Velde *et al.*, 2001). Slater-type orbital triple-ζ-plus double polarisation basis sets were used from the ZORA/TZ2P database of the *ADF* suite. A frozen

core approximation up to and including 4*p* was used or I, 3*d* for Ag, 2*p* for S, and 1*s* for C. Scalar relativistic approaches were used within the ZORA Hamiltonian and the local density approximation with correlation potential due to Vosko *et al.* (1980) were used in all calculations. Gradient corrections were performed using the functionals of Becke (1988) and Perdew (1986). DFT calculations were carried out on sections of the polyiodide network which can be described as one central $I_7^-$ moiety with three $I_7^-$ moieties binding *via* terminal iodine atoms to the central iodide of the central unit, along with a further $I_7^-$moiety located at each terminal iodine of the central unit (Fig. 3).

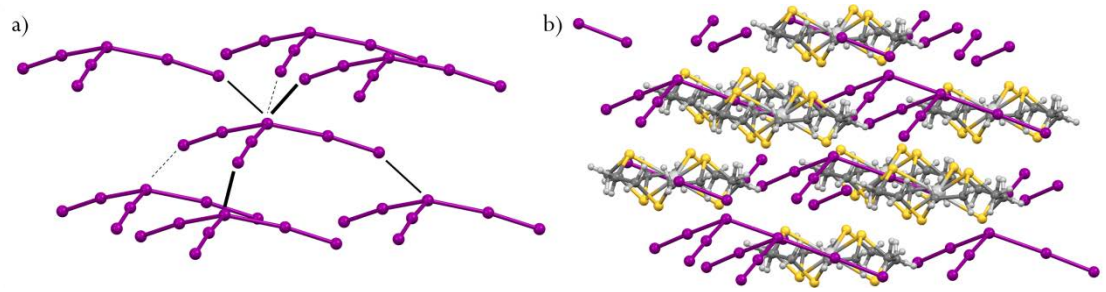



**Figure 3** Images depicting example fragments employed in a) calculations on polyiodide network only, and b) centrosymmetric, cation inclusive calculations. Black lines in (a) added to better illustrate bonding.

These calculations were correlated against larger calculations employing the same polyiodide network plus inclusion of the eight nearest cations to the central iodide node: owing to their computational expense, these calculations were performed only on data at ambient pressure & low temperature*, at 2.5,10.4*, 20.3 and 36.3 kbar for crystal A, and at4.1*,6.5*, 13.9*and 42.9* kbar for crystal B. For the calculations marked by asterisks, there was the further addition of eighteen diiodine moieties at the existing six outer iodide nodes such as to model a centrosymmetric phase (Fig. 3).

## 3. Results and discussion

### 3.1. Complex 4 at ambient pressure and 120 K: phase 1

Phase 1 has been previously reported (Blake *et al.*, 1995). At ambient pressure and 120(2) K, complex **4** crystallises in the trigonal space group $R\bar{3}m$ with $a = b =$ 14.8902(10) Å, $c$ = 11.9450(10) Å, $V$ = 2293.5(4) Å$^3$ and $Z$ = 3. The metal centre and iodide node both occupy sites of inversion symmetry. The metal centre is bound to six equivalent sulfur atoms of a single macrocycle [Ag1−S1 = 2.7542(14) Å] and the macrocycle adopts a disordered conformation that cannot be directly assigned (*vide infra*). The singular inequivalent carbon is disordered over two sites which were freely refined; C1 and C1A were found to have occupancies of 0.60(2) and 0.40(2), respectively. The geometry of the cation can be described as a distorted octahedron where *trans* ligation angles are constrained to 180 ° and the two *cis* angles are 78.95(4) and 101.05(4) ° (Fig. 4). Iodide nodes are catenated to six equivalent iodine atoms [I1−I2 = 3.3632(4) Å] of equivalent diiodine molecules [I2−I2_#1 = 2.7545(6) Å; symmetry code #1 = 4/3 − $x$, 2/3 − $x$ + $y$, 2/3 − $z$] which link the iodide nodes to form an extended $^3_\infty[I^-\cdot(I_2)_{6/2}]$ network about the cation (Fig. 4).

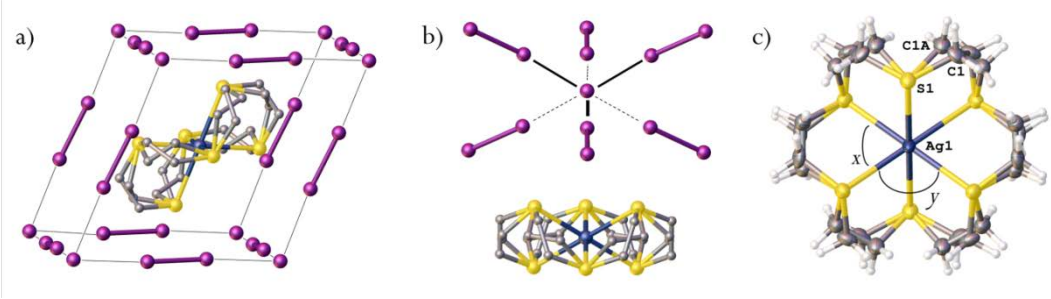



**Figure 4** Ball-and-stick representations of a) the polyiodide cage surrounding the complex and b) the arrangement at the iodide node above the metal centre. c) Image of the cation labelled in accordance with the text: $x$ = 78.95(4) °, $y$ = 101.04(4) °. Iodine/iodide atoms are coloured as purple, silver in blue, sulfur in yellow, carbon in grey; hydrogen atoms omitted from a) and b) for clarity and coloured white in c); both disorder components of macrocycle shown in all cases.

### 3.2. High-pressure summary

Crystals of **4** were studied using perfluoroether RS3000 as the PTM. This was determined by in-house studies to give hydrostatic conditions up to *ca*. 50 kbar (O'Connor, 2014). Two crystals were studied in the experiment reported herein: crystal A was studied up to 45.8 kbar and crystal B was taken to 42.9 kbar before also being studied on decompression. In neither case did the crystals cease to diffract within the pressure ranges studied, although the second phase transition and both occurring on decompression all served to decrease the quality of diffraction. Both crystals exhibited smooth compression which appeared to accelerate up to *ca*. 11 kbar, above which pressure a reversible $R\bar{3}m \rightarrow R3m$ phase transition was observed with retention of the unit cell axes (Figs. 5 & 6). The ambient pressure phase will herein be referred to as phase 1.

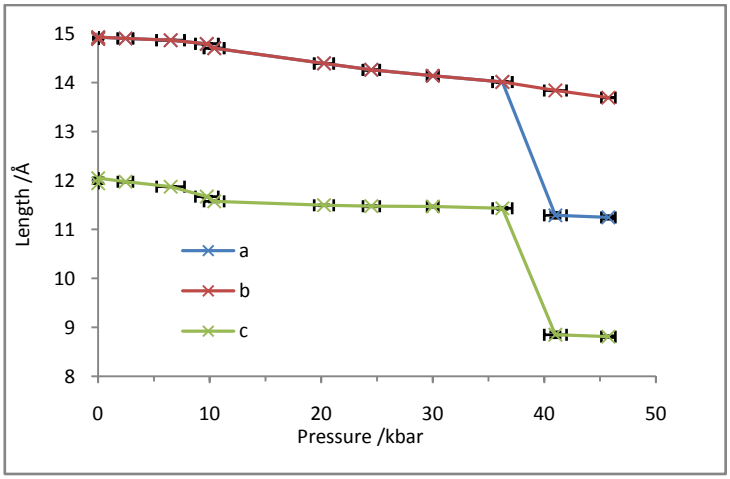



**Figure 5** The effects of pressure on the cell parameters for crystal A. Lines track the progression of the experiment.

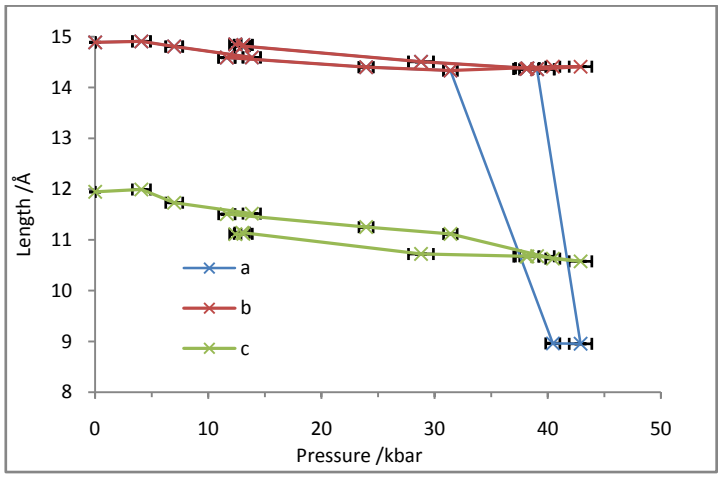



**Figure 6** The effects of pressure on the cell parameters for crystal B. Lines track the progression of the experiment .

The phase transition at *ca*. 11 kbar was associated with a collapse of the extended polyiodide network towards formation of discrete $I_7^-$ units and resulted in possible merohedral twinning of the crystals (twin law = [0 1 0 / 1 0 0 / 0 0 $\bar{1}$]). This transformation would result in a distinct change in the polarisation of the diiodine moieties. Furthermore, the $I_7^-$ units are aligned in the resulting phase so as to give a crystal that can be regarded as polar. In the centrosymmetric phase 1, neither the

diiodine moieties nor the phase as a whole has any dipole. Thus, the 1 → 2 transition appears to constitute a ferroelectric phase transition. The resulting phase, designated phase 2, persisted for the majority of the hydrostatic window of the PTM but with the two crystals exhibiting notably differing compression of unit cell axes and key parameters. In the case of crystal A, additional compression was served to the *a* and *b* axes (Fig. 5) while in crystal B there was instead additional compression of the *c* axis (Fig. 6). At *ca*. 40 kbar, both crystals underwent a trigonal → monoclinic phase transition that in each case most affected the cations therein, but with specifics of this transformation differing between crystals. Crystal A was subject to an *R*3*m* → *Cm* transformation with inversion of the *b* axis while the *a* and c axes were redefined by the transformation matrix [$-^{2}/_{3}$ $-^{1}/_{3}$ $^{2}/_{3}$ / 0 $\bar{1}$ 0 / $^{2}/_{3}$ $^{1}/_{3}$ $^{1}/_{3}$]. The resulting phase comprised a less symmetric, distorted cation bound to an ordered macrocycle. Crystal B underwent a similar yet differing transition that required the employment of the non-standard space group setting *Im* to retain comparable axes with crystal A. In this phase, the cation remains relatively symmetrical compared to the equivalent phase of crystal A. The macrocycle remains seemingly disordered in the same way as in the two lower pressure phases. An overlay of these two phases shows the relation of their unit cells (Fig. 7). This transformation occurred with inversion of the *b* and *c* axes while the *a* axis was redefined by the transformation matrix [$^{2}/_{3}$ $^{1}/_{3}$ $^{1}/_{3}$ / 0 $\bar{1}$ 0 / 0 0 $\bar{1}$]. It should be noted that the solution of phase 2 was carried out so as to be isomorphous between crystals while this transformation matrix and the refinement data indicate that the major component of phase 2 for crystal B is the inverted form of that in crystal A.

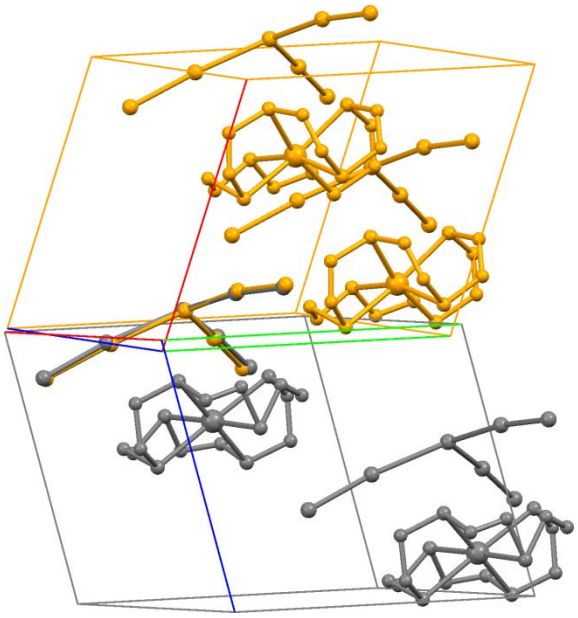


**Figure 7** Overlay of the two differing third phases of crystal A (orange) and crystal B (grey) showing their distinct similarity and the relationship between cell axes. Cell axes coloured as *a* in red, *b* in green and *c* in blue. H atoms and additional disorder of crystal B omitted for clarity.

While hysteresis was not conclusively observed in either transition, decompression of crystal B showed significant reverse hysteresis in the expansion of certain structural parameters throughout the intermediary high-pressure phase. For the purpose of discussion, the various phases of the two crystals shall be referred to by the phase identifier and then by the crystal identifier, *e.g.*, phase 2 of crystal A is specifically referred to as phase 2A.

### 3.2.1. First high-pressure phase: phase 2

Phase 2 crystallises in the trigonal space group *R*3*m* and cell parameters are given in Table 1 while specific bonding parameters are discussed later in this chapter. Phase 2 is neither isomorphous nor strictly isostructural to phase 1 despite their significant similarity. The cation remains relatively unchanged from that found in

phase 1 and *Z* remains 3; the loss of inversion symmetry results in two inequivalent Ag−S interactions (Ag1−S1 and Ag1−S4) and two inequivalent carbons (C2 and C3) disordered over two sites. The macrocycle maintains the same disordered appearance as seen in phase 1. Phase 2 is most notably characterised by the collapse of the extended polyiodide network towards distinct $I_7^-$ moieties, though the termini of these remain within sufficient proximity of the central iodide nodes of the neighbouring units for the system to be described as comprising a catenated $^3_\infty[I_7^-]$ network (Fig. 8).

**Table 1** Cell parameters for each of the phases outlined in this study. Data reported for 1 at ambient pressure and 120 K; for 2A at 20.3 kbar and 293 K; for 2B at 13.9 kbar and 293 K; for 3A at 41.0 kbar and 293 K; and for 3B at 40.5 kbar and 293 K.

| Phase | Space Group | *Z* | *a* | *b* | *c* | β | *V* |
|---|---|---|---|---|---|---|---|
| 1 | $R\bar{3}m$ | 3 | 14.8902(10) | 14.8902(10) | 11.9445(10) | 90 | 2293.5(4) |
| 2A | *R*3*m* | 3 | 14.3897(6) | 14.3897(6) | 11.494(3) | 90 | 2061.2(6) |
| 2B | *R*3*m* | 3 | 14.5935(6) | 14.5935(6) | 11.5181(9) | 90 | 2124.4(2) |
| 3A | *Cm* | 2 | 11.29(2) | 13.838(2) | 8.85(2) | 112.6(3) | 1276(5) |
| 3B | *Im* | 2 | 8.962(2) | 14.4092(5) | 10.631(2) | 112.22(3) | 1270.9(5) |

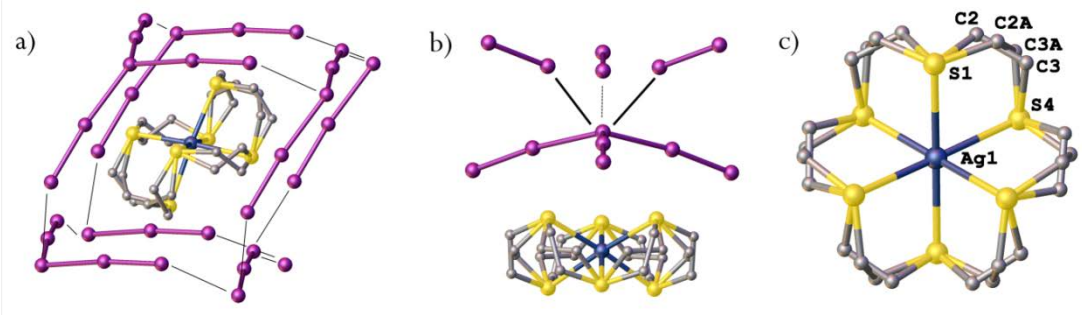



**Figure 8** Ball and stick figures depicting a) the distorted polyiodide cage surrounding the complex and b) the arrangement at the iodide node above the metal centre. c) Image of cation, labelled in accordance with the text. Iodine/iodide atoms are coloured as purple, silver in blue, sulfur in yellow, carbon in grey; hydrogen atoms omitted for clarity; both

disorder components of macrocycle shown in all cases; images specifically depict phase 2A at 30.0 kbar.

### 3.2.2. Second high-pressure phase for crystal A: phase 3A

Phase 3A crystallises in the monoclinic space group *Cm* and cell parameters are given in Table 1 while specific bonding parameters are discussed later in this chapter. The silver centre remains bound by six macrocyclic S donors, of which 4 are inequivalent as the cation now resides across only a mirror plane; $Z = 2$. The macrocycle does not adopt a disordered conformation in this phase and instead adopts an [84114] conformation according to Dale (1973) analysis which significantly distorts the geometry of the coordination sphere (Fig.9). Although the conformation is not one reported in the literature, it bears similarity to that found in the same cation by Pickardt *et al*. (2004). The polyiodide network is further desymmetrised but the motif remains without significant change.

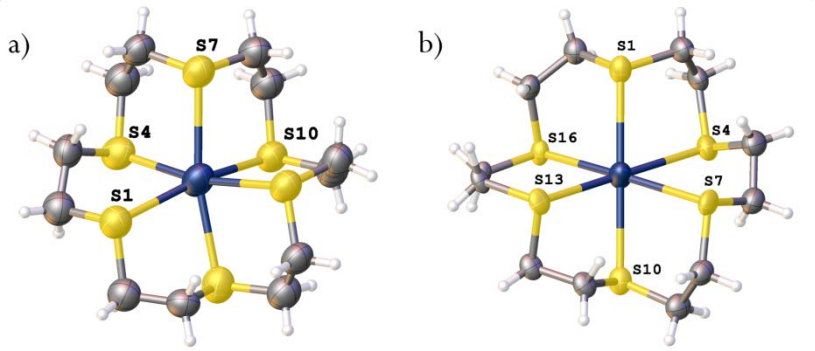



**Figure 9** Image of a) the deformed, ordered cation in phase 3A at 41.0 kbar and b) the comparatively symmetrical cation in phase 3B at 40.5 kbar. The cation of 3B is disordered across the mirror-plane which bisects the molecule through S1-Ag1-S10 and the disorder component is suppressed for clarity. Sulfur atoms labelled according to text. In each case, silver atoms are coloured as blue, sulfur in yellow, carbon in grey and hydrogen in white; anisotropic displacement parameters are shown at 50% probability level.

### 3.2.3. Second high-pressure phase for crystal B: phase 3B

Phase 3B crystallises in space group *Im* and cell parameters are given in Table 1 while specific bonding parameters are discussed later in this chapter. Similarly to phase 3A, the silver centre remains bound by six macrocyclic S donors but is disordered across the mirror plane and hence all are inequivalent; $Z = 2$. The geometry of the coordination sphere is largely undistorted from that of phases 1 and 2 when compared to that of phase 3A (Fig. 9, *cf.* Figs. 4 & 8, respectively). Occupancy of the two disorder components appear to be strictly one half and are consequently constrained as such, the conformation tentatively assigned [333333] according to Dale (1973) analysis, discussed further in Section 3.4.1. The polyiodide network is further released from symmetry constraints but undergoes a lesser degree of desymmetrisation compared to 3A and the bonding motif remains without significant change.

### 3.3. Experimental considerations

#### 3.3.1. Pressure ramping: RS3000 as a PTM

The use of RS3000 as a PTM is currently novel to the literature and to our knowledge limited only to recent studies in the group. Additionally, with the exception of this and the limited study of $[Pd([9]aneS_3)_2](PF_6)_2{\cdot}2CH_3CN$, detailed in Chapter 5, all such studies have been on the investigation of framework materials. In light of this, it is pertinent to discuss the observed nuances in the behaviour of the PTM to aid in assessing its worth for future experiments.

A larger degree of closing pressure was required to bring the sample above ambient pressure than for samples studied in, for example, 4:1 MeOH/EtOH. The pressure would typically be increased by 2−3 kbar and steadily decompress back to ambient pressure, requiring a significantly larger degree of closing turns of the

Allen screws than compared to when using other, non-oil PTMs. This was assumed to be an effect of the viscous oil being slowly forced out from between the anvils and gasket material until such a time as it is finally truly sealed. It could also/instead be related to a further observation given in the following paragraph. If the closing was attempted in one go, this effect appeared to be limited and a much higher pressure than expected would be reached. Consequently, it appears to be a worthwhile use of time to undertake this step progressively and carefully, whereas with other fluids such an approach would result in an emptying of the cell and the need to refill with PTM.

Another phenomenon observed with RS3000 was that it appeared to resist compression at first but then relax a little over the settling period, in contrast to the more common response of an increasing drift in pressure. Similarly, there appeared to be significant lag in decompression of the sample chamber. It is usual for decompression of samples housed in a Merrill-Bassett diamond anvil cell to require very careful and gradual release of pressure. Nevertheless, once the sample has begun decompressing it is typical that further loosening of the screws certainly results in further decompression. This was not the case when studying decompression of crystal B. It was found that a significant amount more backlash needed to be overcome. Furthermore, sample pressure was observed to increase across five of the thirteen recorded periods in which it was either settling or on the diffractometer under scrutiny during the decompression study, requiring the further removal of backlash thereafter. This behaviour would imply that the fluid is slow to reorganise in response to changes in pressure. This made accurate pressure control with this fluid particularly challenging and required a longer period of rest

for the cell to equilibrate than when using, for example, 4:1 MeOH/EtOH solution as the PTM.

### 3.3.2. Specific refinement details: twinning

The solution and refinement of the phases obtained in this study required that certain bond lengths be restrained, either a set value or to one another, while anisotropic displacement parameters were either restrained as similar within a given radius or/and by use of rigid bond restraints. In addition to this, desymmetrisation from centrosymmetric $R\bar{3}m$ to non-centrosymmetric $R3m$ gave the possibility and indication of merohedral twinning. In the highly symmetric environment of phase 1 there is no clear cause for the desymmetrisation to occur one way or the other. However, it is expected that a cascade should occur once a given node undergoes the transition and so a domain form. Thus, the use of the twin law [0 1 0 / 1 0 0 / 0 0 $\bar{1}$] was employed and the batch scale factor (BASF) allowed to freely refine, typically adopting a value of *ca*. 0.70(13). Refinements carried out without this twin law served a minor increase to the $R_1$ of the final structure. In the non-twinned refinements for crystal A, Flack parameters of *ca.* 0.60-0.70(3) were typical, corroborating the employment of said twin law. In the case of crystal B, standard uncertainties in these parameters were generally around four times greater. In both cases, these numbers indicate that the refinements correspond to inversion of the major component, an issue also overcome by the inclusion of the twin matrix and in either case one that appears to give no detrimental effect to the outcome of the refinement. In the event that phase 2 is twinned, it is likely that the twinning is carried across into phase 3. Flack parameters in this instance were of the order 0.20(13) for 2B and 0.28(4) for 3B

and the twin law [$\bar{1}$ 0 0 / 0 1 0 / 0 0 $\bar{1}$] was included but in all cases the BASF was not found to be significant and neither did the inclusion of the law affect the $R_1$. Phase 3A and 3B being inverted to one another supports the observation that phase 2A and 2B are likely also inverted forms.

### 3.4. Macrocycle conformation and disorder

The carbon atoms of the macrocycle are disordered over two sites in all phases except phase 3A. In the case of phase 1, competitive refinement consistently gave occupancies *ca.* 60:40. This steadily decreased over the course of phase 2 and tended towards 50:50 prior to the second phase transition (Fig. 10). The estimated standard uncertainty in occupancies was around 4% and only reduced to 2% in the complete data collection at ambient pressure and 120 K. This manner of refinement was only found to provide an $R_1$ of a few tenths of a percent lower than a fixed occupancy of 2:1 or 1:1, as found in the literature (Blake *et al.*, 1995). Despite this, owing to the clear trend and corroboration between the two phases, this data will be considered as valid in its deviation from 50:50. The final refinement chosen was, therefore, one wherein the occupancies of the two sites have been competitively refined in the compression stages of phases 1 and 2 until phase 3 brings ordering to both crystals. This point of difference was settled upon following a number of considerations, discussed herein and including the above noted competitive refinement. It is also important to note that the parts assigned for phases 1 and 2 do not depict the likely conformation of the macrocycle upon the generation of symmetry equivalents and, given the symmetry of the site in each

case, no model that would is possible for phases 1 and 2. The occupancy of parts is strongly believed to be 50:50 in phase 3B.

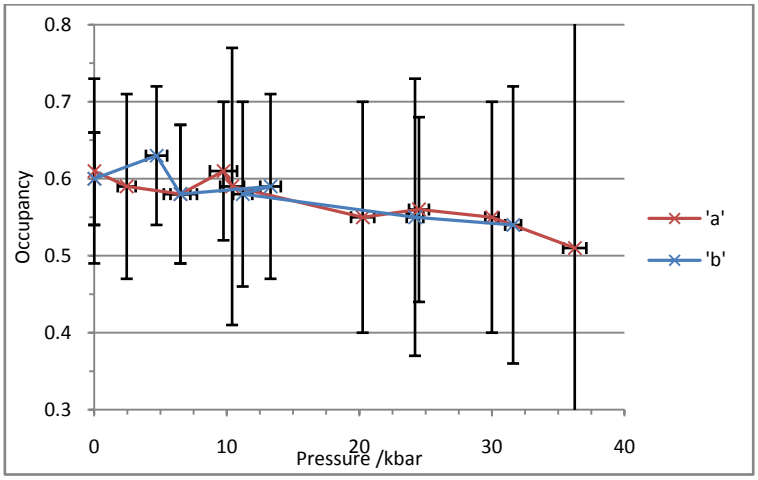



**Figure 10** The effects of compression on the occupancy of sites corresponding to C1 of phase 1 over the first two phases for crystal A and B. Lines track the progress of each experiment.

### 3.4.1. Conformation upon compression

Assuming the macrocycle to adopt the [5454] conformation that is common for complexes of [18]ane$S_6$ in the literature (*i.e.*, the conformation seen the same cation in [Ag([18]ane$S_6$)]$I_3$ (Blake *et al*., 1995; Fig. 11)), occupancies of precisely 2/3 and 1/3 would be expected for a cation of the same symmetry as those found for the trigonal phases. Given the threefold site symmetry and two-fold point symmetry of such a cation, this would suitably explain the disorder in the refined structure, even without disorder from one site to another as the diffraction pattern is so dominated by the rest of the structure. However, where the contact between cations through windows in the framework is comprised of two major components of such a cation, pair-wise close C−H···H−C contacts are formed even at ambient pressure (Fig. 11), a case which this conformation must give rise to.

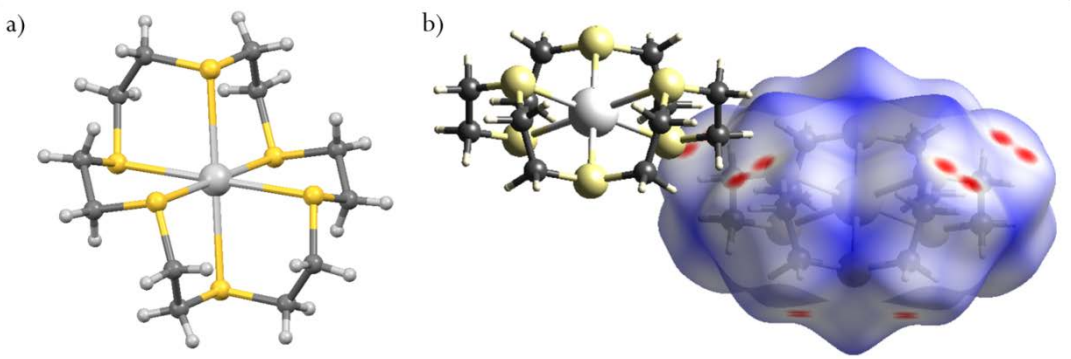



**Figure 11** a) Ball-and-stick representation of the [5454] conformation of the macrocycle as found in [Ag([18]aneS$_6$)]I$_3$. b) Image of the Hirshfeld surface at ambient pressure and 120 K, calculated using solely the major component of the macrocycle, corresponding to the carbon atoms occupying only the C1 site of phase 1; note the close contacts formed between cations, shown as red spots.

For the case of site occupancies being 50:50, the most probable conformation corresponds to the [333333] conformation which is also observed in the literature, for example in [Pd([18]aneS$_6$)](PPh$_4$)$_2$ (Blake *et al.*, 1986). This is the conformation assigned to the macrocycle in phase 3B (*cf.* Fig. 9). In this case, it is entirely possible for the close contacts between neighbouring cations to be decreased. However, the occurrence of the [5454] conformation in the CSD is *ca.* four times that of the [333333] conformation, excluding structures that appear disordered as phase 1 (CSD, Nov 2015 release plus 2 updates; Groom *et al.*, 2016). This would imply that the [5454] conformation is favoured over the [333333] conformation at ambient pressure. As there is no single conformation of the macrocycle corresponding to 60:40 occupation of these sites, it is likely that the crystal comprises a mixture of [333333] and [5454] conformations under ambient conditions, with an energetic trade-off between the favourability of the [5454] conformation against the close contacts it would give rise to. The increase in close

contacts between cations as pressure is applied would then alter this balance, serving to explain why occupancies tend towards 50:50 at higher pressures.

It is only in phase 3A that the macrocycle and cation become ordered from the perspective of the refinement. In this case, an [84114] conformation is adopted which would correspond to a 2:1 ratio of occupancies if found the lower pressure phases and is not otherwise observed in the literature. Assuming the cation to be in the above suggested [5454] conformation prior to the phase transition, might correspond to the switching of only two consecutive regions of the macrocycle; if the [333333] conformation was present, a far more extensive rearrangement would be necessitated. In either case, the rearrangement results in a significant decrease in the number of the ultra-close contacts between cations described for the [5454] conformation. This in turn allows the phase to pack more densely. It is likely that this relief of close contacts is the cause for the 2A → 3A phase transition.

In the case of 3B, the macrocycle appears at first glance to comprise the same disordered form as in the lower pressure phases. Given the occurrence of a phase transition at the same pressure for crystal A that heavily impacted the macrocycle, along with the same potential for highly repulsive C−H···H−C contacts, this is unlikely. Phase 3B differs from phase 3A: the centring of the unit cell is different for a similar assignment of cell dimensions while the cation adopts a less distorted structure (Fig. 9). In addition, specific interatomic parameters differ significantly within the polyiodide network while inequivalent interactions therein are less divergent than in 3A (*vide infra*). This serves to suggest that the macrocycle, which templates the polyiodide network, retains a greater symmetry in 3B than in 3A. Furthermore, competitive refinement of the various carbon sites indicates a 50:50

ratio of occupancies, consistent with the trends observed prior to the formation of this phase. Constraining this to be the case serves a 0.15% benefit to the $R_1$ over a 2:1 ratio corresponding to an [84114] conformation. Furthermore, if it is assumed that the 2B → 3B phase transition also happens to reduce contacts between cations, as the conformation is clearly not that seen in phase 3A, it is reasonable to suggest that the conformation is in fact [333333]. This provides the likelihood of an ordered disorder between neighbouring cations that would also reduce the ultra-close contacts between cations. The carbon site occupancies are consequently constrained to one half and the macrocycle is modelled as disordered across the mirror plane which bisects the cation.

While the steady trend in carbon site occupancies across phase 2B suggests a gradual change towards the [333333] conformation, the cause of the 2B → 3B phase transition appears to be the macroscopic ordering of disorder components. Up to *ca.* 40 kbar, where both crystals undergo a second phase transitions, conformational rearrangement is localised. As this pressure is reached, cations order macroscopically to minimise the remaining highly repulsive C−H···H−C contacts. This in turn affects an ordered distortion on the polyiodide network, albeit small, and the phase transition is observed.

### 3.4.2. Conformation upon decompression - crystal B

The 50:50 occupancy of the two carbon sites in crystal B appears to be held throughout decompression, suggesting that the macrocycle remains in the form found in phase 3B once it has adopted this conformation. This is highly likely as there is no significant force on the cation to overcome the barrier to rearrangement

upon decompression: return to a mixture of [5454] and [333333] conformations would increase close contacts between cations. This also necessitates that the conformation is not so strained as to be unstable in the relaxation of the forces which caused it, as was the case for the high-pressure macrocycle conformations of β'-[$PdCl_2$([9]ane$S_2O$)] (Tidey *et al*., 2016; Chapter 3) and [$PdCl_2$([9]ane$S_3$)] (Allan *et al*., 2014). This serves to add weight to the assignment of the [333333] conformation for phase 3B. Retention of this ordering of the conformation of the macrocycle upon decompression would alter the limit to compression posed by the contacts and give a slight change in the specific C−H···I contacts that affect the precise arrangement of the polyiodide network. Thus, it could be expected that, if the macroscopically ordered [333333] conformation was retained, decompression behaviour would not directly mimic that of compression. This was indeed found to be case (*vide infra*). With this in mind, it is not clear whether decompression of phase 3A would result in differing behaviour to that of its compression.

### 3.5. Compression of the coordination sphere

The coordination bonds remain incompressible for the duration of phase 1A compared to other interactions in the crystal, but in phase 2A appear to differentiate with Ag1−S1 continuing to resist the effects of pressure while Ag1−S4 is more compressed (Fig. 12). In this case, S4 is the sulfur directed slightly towards to the newly-formed $I_7^-$ moiety and the iodide which has 'collapsed' toward the cation. Despite this, there is essentially no difference throughout phase 2 in the distance between S4 or S1 and the nearest iodine atoms to them. Additionally, contacts between cations which occur through windows in the polyiodide network occur mutually between S1 and S4 regions: there is no

clear explanation for the extra compression of Ag1−S4 compared to Ag1−S1. In the case of phase 1B, Ag1−S1 is slightly compressed up to the phase transformation and no such anisotropy in the compression of the inequivalent Ag−S interactions is observed in phase 2B (Fig. 13).

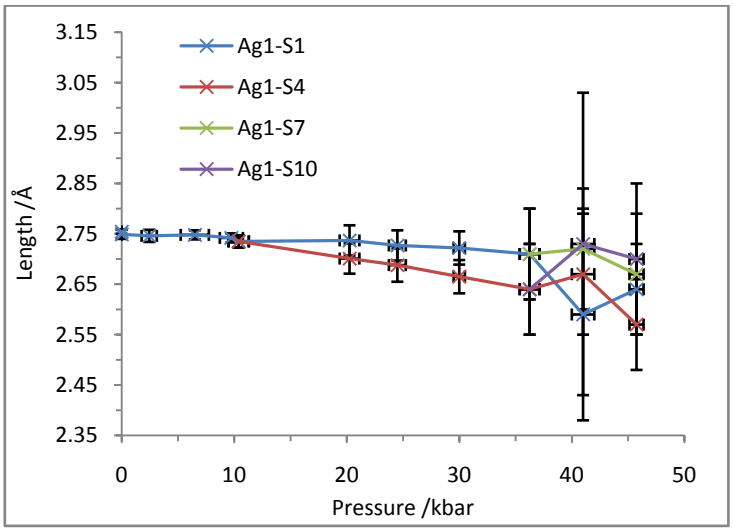



**Figure 12** The effects of pressure on the coordination bond lengths in crystal A. Lines track the progression of the experiment.

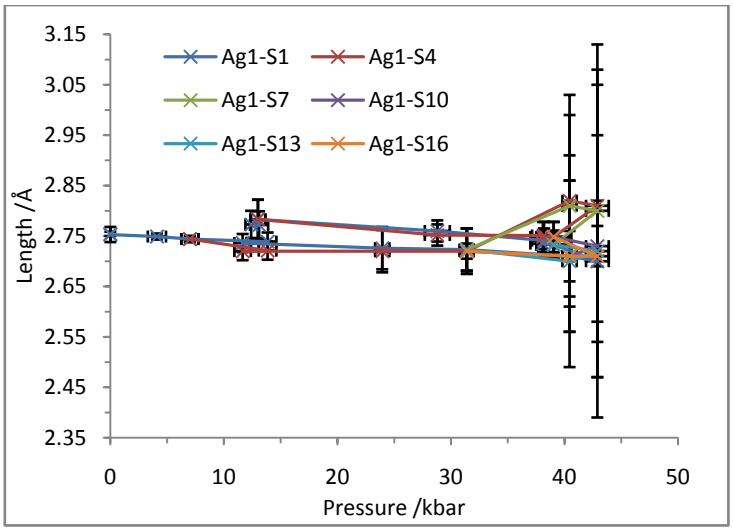



**Figure 13** The effects of pressure on the coordination bond lengths in crystal B. Lines track the progression of the experiment.

For both crystals, phase 3 results in significantly higher standard uncertainties associated to the Ag−S bond lengths. Bond lengths for phase 3B adopt either *ca*. 2.71 or 2.80, whereas the spread is more uniform in 3A and vary between *ca*. 2.59−2.73 Å. This is a reflection of the less symmetric and more highly strained macrocycle in the latter. While seeming resistant to compression when compared to, for example, the catenated iodide−iodine interactions, the compression served by 10.4 kbar to Ag1−S1 in phase 1A [$\Delta = -0.019(4)$ Å] is comparable to the total compression seen in metal−ligand bonds over *ca.* 100 kbar to [*M*$Cl_2$([9]ane$S_2$O)] (*M* = Pd, Pt; *cf.* Chapters 3 and 4, respectively). This is likely owed to the matter of the Ag−S bond lengths found in the cation being notably toward the longer end of those found for Ag(I) complexes (Fig. 14), a restriction presumably imposed by the size of the macrocycle. The additional compression seen in phases 2A and 3A is indicative of the potentially differing conformations of the macrocycle between crystals. Similarly, the apparent relaxation of Ag−S bonds upon decompression from 3B back to 1B is suggestive of retention of the [333333] pressure induced conformation in phase 3B through this period.

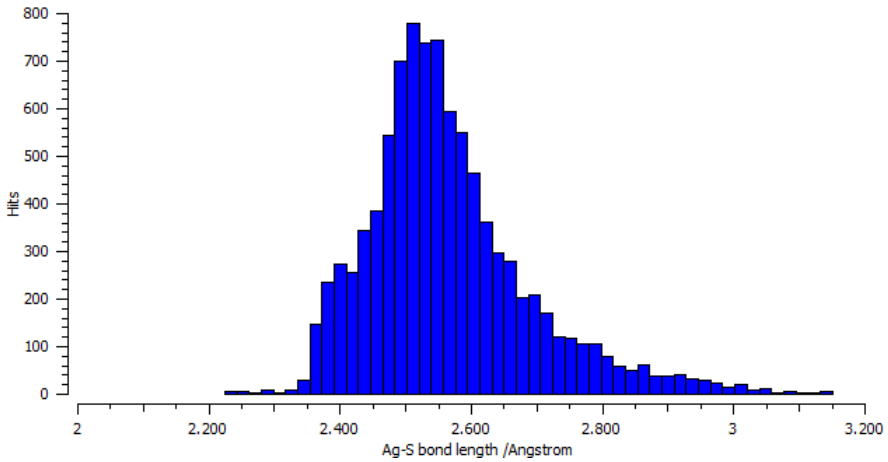



**Figure 14** Search results for the Ag−S bond length between 2.0 and 3.2 Å from the Cambridge Structural Database, 2016 release plus two update (Groom *et al.*, 2016).

The geometry of the coordination sphere is invariant with pressure for the duration of phase 1 in both crystals and the maximum deviation in any S−Ag−S angle is 0.54(18) ° between ambient pressure and 10.4 kbar for S1−Ag1−S1_#1 (symmetry code #1 = 4/3 − *x*, 2/3 − *x* + *y*, 2/3 − *z*) in phase 1A (Figs. 15 & 16). As previously mentioned, the two crystals behave differently with the application of pressure across phase 2. In both cases, the geometry of the cation is marginally more affected by pressure than across phase 1 given the loss of inversion symmetry. In phase 1, *trans* S−Ag−S interactions are constrained to linearity but in phase 2 the constraint is relaxed and the angle deviates smoothly in phase 2A by 4.5(6) ° to 30 kbar (measurements at 36.3 kbar associated to prohibitively large ESUs; Fig. 15). The smaller of the two *cis* angles continues to widen at the same rate as prior to the transformation in crystal A and reaches 80.6(3) ° at the same pressure. The phase transition results in two inequivalent interactions corresponding to the wider of the *cis* angles: in phase 2A, these have mutually diverged by *ca*. ±2.5 ° by 20.3 kbar but are not significantly affected by pressure thereafter.

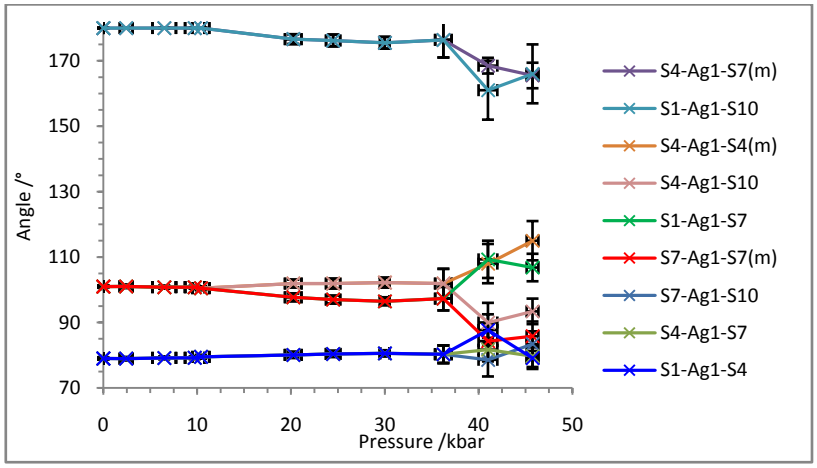



**Figure 15** The effects of pressure on the geometry of the coordination sphere in crystal A. Lines track the progression of the experiment. Atoms labelled in accordance to phase 3 where S1 additionally corresponds to S1 of phases 1 and 2, and S4 to S4 of phase 2; atoms generated by the mirror plane in phase 3A denoted by "(m)".

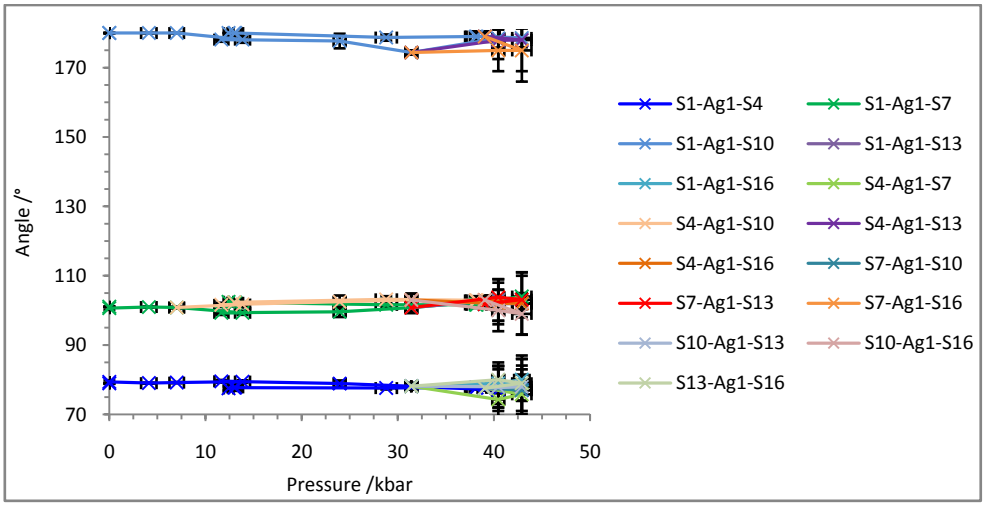



**Figure 16** The effects of pressure on the geometry of the coordination sphere in crystal B. Lines track the progression of the experiment such that decompression is clearly distinguished from compression in the case of B. Atoms labelled in accordance to phase 3 where S1 additionally corresponds to S1 of phases 1 and 2, and S4 to S4 of phase 2.

In phase 2B the observed deviation in the *trans* S−Ag−S angle is smaller than for 2A and the uncertainties associated make it indistinguishable from linearity (Fig. 16). Although the smaller *cis* angle of phase 1B behaved similarly to that of phase 1A, it is steadily compressed in phase 2B to 78.1(3) ° by 31.4 kbar, contrary to the steady opening in phase 2A. The larger *cis* angles in phase 2B diverge by a lesser degree [*ca*. 1 °] and are both seemingly marginally opened by compression. This difference serves to corroborate the hypothesis that the specific change in conformation of the macrocycle across phase 2 for the two crystals differs.

The differing response of the two crystals to pressure is most evident in phase 3. The cation of 3B is similar to the cation found at lower pressures and remains a relatively symmetric distorted octahedron: the three inequivalent *trans* S−Ag−S angles both take values that do not significantly differ from linearity, the three smaller *cis* angles approximate 77.5 ° and the three larger *cis* angles adopt values around 102.5 °. The cation of phase 3A is, however, markedly different from any

other found in this study and is far less symmetric than the phase 3B counterpart. At 41.0 kbar, the two unique *trans* S−Ag−S angles are found to be 161(3) and 168.5(8) ° at 41.0 kbar; the smaller form of *cis* angles range 78−88 °, albeit with large ESUs. The two larger *cis* angles from phase 2A each comprise two inequivalent angles which in both cases diverge. The two that are closed each contract to *ca*. 87 ° while the two that open adopt values of *ca*. 109 °. The differences between the coordination geometry of the cations in phase 3 are attributed directly to the different conformations of the macrocycle therein.

### 3.6. Compression of the polyiodide network

The polyiodide network is a highly symmetrical, extended array comprising only two inequivalent sites under ambient conditions. Consequently, to properly discuss it we must first define the parameters of interest in each phase, which is formally done in Table 2 with reference to Fig. 17. In the high pressure phases, the extended $^{3}_{\infty}[I^{-}\cdot(I_2)_{6/2}]$ framework collapses towards one of interconnected $I_7^{-}$ moieties, and thus one where there is a distinction between intramolecular and intermolecular interactions. While this is not strictly true for the ambient modification, this distinction shall be loosely held to facilitate discussion.

**Table 2** Table defining the parameters referred to in the discussion of the polyiodide network. Description made with reference to Fig. 17; symmetry equivalent interactions are not included.

| Phase | Interaction and Description | | Symmetry codes |
|---|---|---|---|
| | ***D-1*$_{\mathbf{intra}}$** | ***D-1*$_{\mathbf{inter}}$** | Phase 1A/B: |
| 1A/B | I1···I2 | I1···I2_#4 | _#1 = 4/3 − *x*, 2/3 − *x* + *y*, 2/3 − *z* |
| 2A/B | I1−I2 | I1···I3_$4 | _#2 = +*y* − *x*, 1 − *x*, +*z* |
| 3A | I1−I2; I1−I4 | I1···I3_&5; I1···I5_&4 | _#3 = 1 − *y*, 1 + *x* − *y*, +*z* |
| 3B | I1−I2; I1−I4 | I1···I3_£5; I1···I5_£4 | _#4 = −1/3 + *y*, 1/3 + *x*, 1/3 − *z* |
| | ***D-2*$_{\mathbf{inter}}$** | ***D-2*$_{\mathbf{inter}}$** | _#5 = 2/3 − *y* + *x*, 4/3 − *y*, 1/3 − *z* |
| 1A/B | I2···I2_#2 | I2_#4···I2_#5 | _#6 = 2/3 − *x*, 1/3 − *x* + *y*, 1/3 − *z* |
| 2A/B | I2···I2_$2 | I2_$4···I2_$5 | _#7 = −2/3 + *x*, −1/3 + *y*, −1/3 + *z* |
| 3A | I2···I4; I2···I2_&3 | I3_&5···I3_&6; I3_&5···I5_&4 | |
| 3B | I2···I4; I2···I2_£3 | I3_£5···I3_£6; I3_£5···I5_£4 | Phase 2A/B: |
| | ***D-3*** | | _$2 = +*y*, +*x* − *y*, +*z* |
| 1A/B | I2···I2_#4 | | _$3 = +*y* − *x*, −*x*, +*z* |
| 2A/B | I2···I3_#4 | | _$4 = 2/3 − *y*, 1/3 + *x* − *y*, 1/3 − *z* |
| 3A | I2···I3_&5; I2···I5_&4; I4···I3_&5; I4···I3_&6 | | _$5 = −1/3 + *y* − *x*, 1/3 − *x*, 1/3 + *z* |
| 3B | I2···I3_£5; I2···I5_£4; I4···I3_£5; I4···I3_£6 | | _$6 = −1/3 + *x*, −2/3 + *y*, 1/3 + *z* |
| | ***A-1*** | | |
| 1A/B | I2···I1···I2_#6 | | Phase 3A: |
| 2A/B | I2−I1···I3_$6 | | _&3 = +*x*, 1 − *y*, +*z* |
| 3A | I2-I1···I3_&6; I4−I1···I5_&4 | | _&4 = +*x*, 1 − *y*, 1 + *z* |
| 3B | I2-I1···I3_£6; I4−I1···I5_£4 | | _&5 = 1/2 + *x*, 1/2 − *y*, +*z* |
| | ***A-2*$_{\mathbf{intra}}$** | ***A-2*$_{\mathbf{inter}}$** | _&6 = 1/2 + *x*, 1/2 + *y*, +*z* |
| 1A/B | I2···I1···I2_#2 | I2_#4···I1···I2_#5 | |
| 2A/B | I2−I1−I2_$2 | I3_$4···I1···I3_$5 | Phase 3B: |
| 3A | I2−I1−I4; I2−I1−I2_&3 | I3_&5···I1···I3_&6; I3_&5···I1···I5_&4 | _£3 = +*x*, 1 − *y*, +*z* |
| 3B | I2−I1−I4; I2−I1−I2_£3 | I3_£5···I1···I3_£6; I3_£5···I1···I5_£4 | _£4 = 1 + *x*, 1 − *y*, +*z* |
| | ***A-3*** | | _£5 = −1/2 + *x*, 1/2 − *y*, −1/2 + *z* |
| 1A/B | I2···I1···I2_#4 | | _£6 = −1/2 + *x*, 1/2 + *y*, −1/2 + *z* |
| 2A/B | I2−I1···I3_$4 | | |
| 3A | I2−I1···I3_&5; I2−I1···I5_&4; I4−I1···I3_&5 | | |
| 3B | I2−I1···I3_£5; I2−I1···I5_£4; I4−I1···I3_£5 | | |
| | ***A-4*$_{\mathbf{intra}}$** | ***A-4*$_{\mathbf{inter}}$** | |
| 1A/B | I1···I2−I2_#1 | I1···I2_#6−I2_#7 | |
| 2A/B | I1···I2−I3 | I1···I3_#6−I2_#6 | |
| 3A | I1···I2−I3; I1···I4−I5 | I1···I3_&6−I2_&6; I1···I5_&4−I2_&4 | |
| 3B | I1···I2−I3; I1···I4−I5 | I1···I3_£6−I2_£6; I1···I5_£4−I2_£4 | |

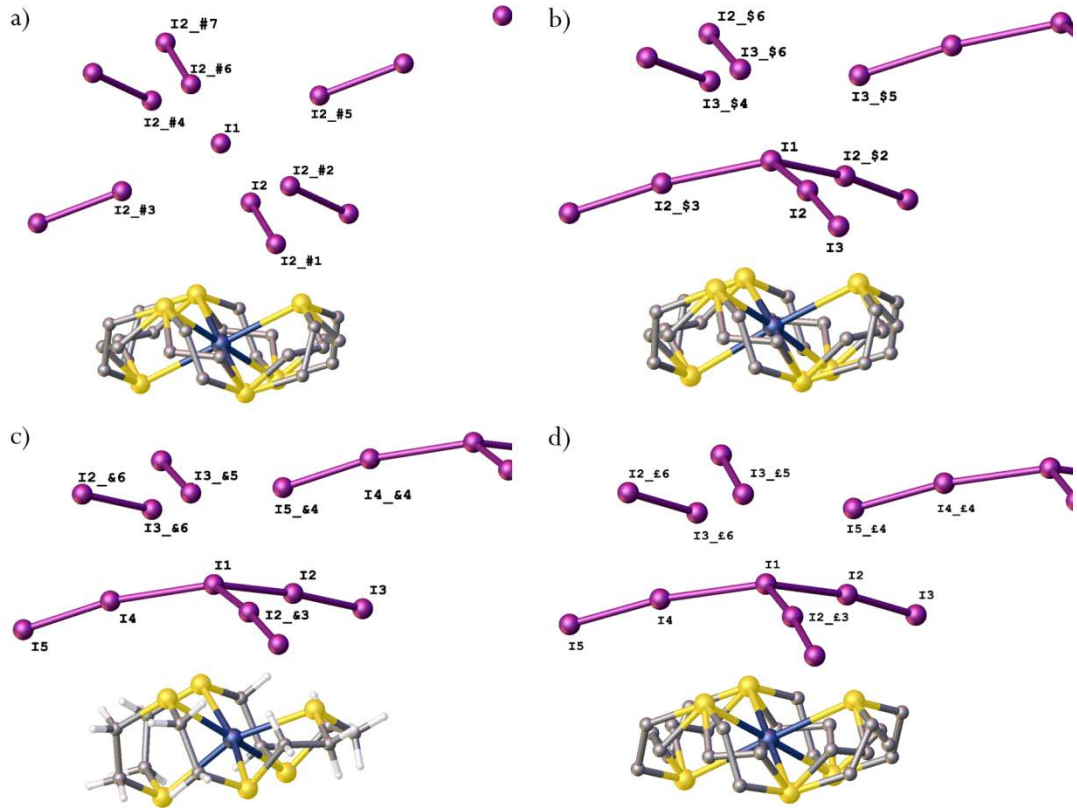



**Figure 17** Ball-and-stick representation of the arrangement at the iodide nodes in a) phase 1A/B, b) phase 2A/B, c) phase 3A and d) phase 3B residing over the cation and depicting the association of one node to another. Selected atoms are labelled as referred to in Table 2; hydrogen atoms omitted for clarity in disordered phases; symmetry codes in accordance with Table 2.

### 3.6.1. Interaction *D-1*: $I^{-}\cdots(I_2)$

The first interactions of note, designated *D-1*$_{intra}$ and *D-1*$_{inter}$, are those of the catenation between diiodine molecules and the central iodide nodes (*cf.* Table 2 & Fig. 17). For the duration of phase 1, all $I^{-}\cdots(I_2)$ interactions are equivalent and there is no distinction between those designated intermolecular and intramolecular contacts. These $I^{-}\cdots(I_2)$ linkages are highly compressible and, for phase 1A, a smooth, accelerating compression of 0.0694(13) Å is observed up to 10.4 kbar (Fig. 18). In phase 1B, *D-1* is recorded as compressing by 0.0304(6) Å by 7.0 kbar (Fig. 19) and the compression profile of the two crystals match well for phase 1.

Such accelerating compression is highly atypical for molecular contacts in the literature. Typically, the effects of pressure on an interaction decrease with increased compression, except in the event of a stepwise contraction.

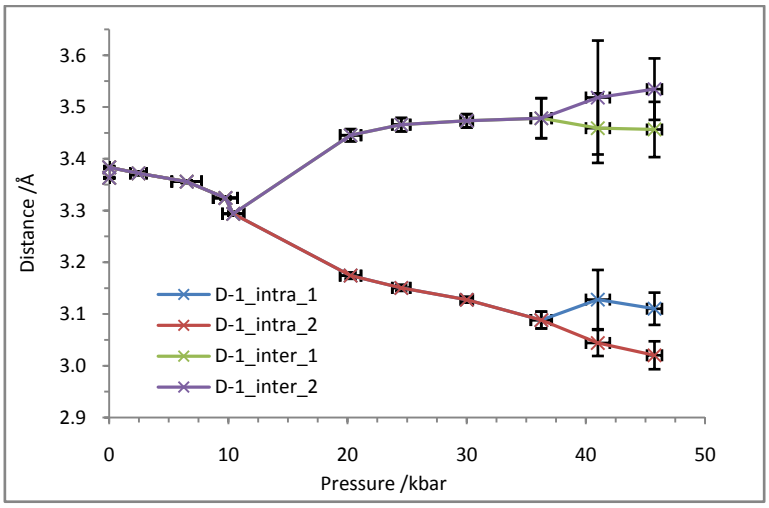



**Figure 18** The effects of pressure on *D-1*$_{\text{intra}}$ and *D-1*$_{\text{inter}}$ for crystal A. Lines track the progression of the experiment.

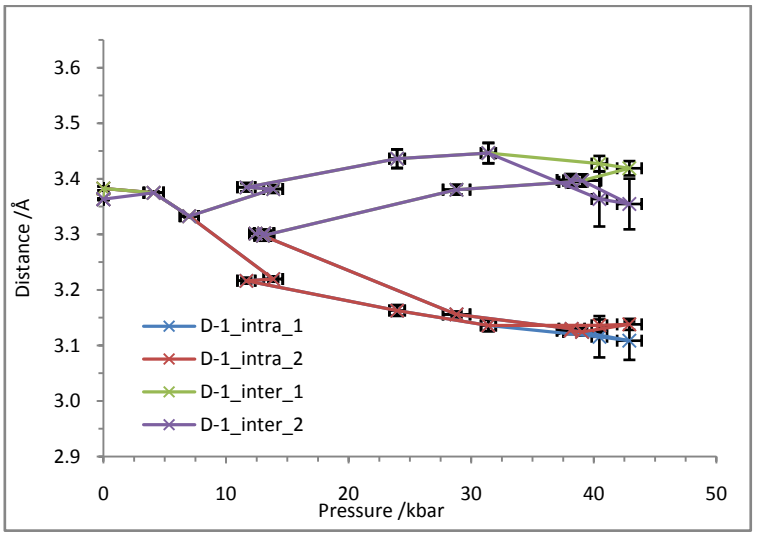



**Figure 19** The effects of pressure on *D-1*$_{\text{intra}}$ and *D-1*$_{\text{inter}}$ for crystal B. Lines track the progression of the experiment .

Across the phase transformation, the central iodide node is displaced from the centrosymmetric position that gives the equivalence of *D-1*$_{intra}$ and *D-1*$_{inter}$ and hence *D-1* diverges into two groups. These two groups are herein considered as three intramolecular $I^-$–($I_2$) interactions within $I_7^-$ anions (*D-1*$_{intra}$), and three intermolecular interactions that catenate terminal $I_2$ groups to the central $I^-$ of neighbouring anions (*D-1*$_{inter}$). In phase 2, each of a given interaction type are equivalent, but, for both sets of interactions in phase 3, two become inequivalent from the other.

Analysis of the data of both crystals as a whole indicates a *ca.* 0.08 Å stepwise compression and expansion in *D-1*$_{intra}$ and *D-1*$_{inter}$ which results in distances of 3.2167(17) and 3.338(3) Å, respectively, in phase 2B at 11.7 kbar. The continued application of pressure smoothly compresses *D-1*$_{intra}$ to 3.089(5) Å at 36.3 kbar for phase 2A, and 3.136(3) Å at 31.4 kbar for phase 2B.

In contrast to the intramolecular contact, *D-1*$_{inter}$ increases with the application of pressure to reach values of 3.478(13) Å at 36.3 kbar for phase 2A, and 3.446(6) Å at 31.4 kbar for phase 2B. This expansion occurs as the central iodide of the $I_7^-$ moiety is compressed further into the plane of three $I_2$ moieties while compression of *D-1*$_{inter}$ is potentially limited by compression of *D-2*$_{inter}$ and/or *D-3*. It may also be the case that polarisation of the diiodines through *D-1*$_{intra}$ by the central iodide node results in partial charges at the termini of the $I_7^-$ moiety that results in increasingly repulsive electrostatic charges in *D-1*$_{inter}$. It was not possible to run DFT calculations sufficiently large enough to overcome termination effects to establish the validity of this hypothesis.

The expansion in *D-1*$_{\text{inter}}$ is in no way sufficient enough to consider the contact as no longer catenating between moieties and remains well within the range reported by Kloo *et al.* (2002) as constituting a secondary bond. Consequently, the assignment of 'intra-' and 'intermolecular' to these interactions is not strictly accurate while both interactions occupy the same region of the histogram of I···I separation given in Figure 1. Nevertheless, the interactions are evidently quite distinct in their compression and also character (see Section 3.6.2). Furthermore, decompression appears to relax *D-1*$_{\text{intra}}$ at a rate that fits well with the compression profile whereas decompression of *D-1*$_{\text{inter}}$ differs quite notably and hysteresis is observed in its relaxation from the phase 3B. This would suggest that *D-1*$_{\text{inter}}$ is more affected by the conformation of the macrocycle and the separation between cations, while *D-1*$_{\text{intra}}$ is comparatively resistant to the changes brought by the 2B → 3B phase transition. Thus, *D-1*$_{\text{inter}}$ can be said to be remaining templated by the cation whereas *D-1*$_{\text{intra}}$ does not. This distinction indicates that *D-1*$_{\text{inter}}$ indeed constitutes an intermolecular, catenating interaction between distinct heptaiodides moieties. This highlights the progression from a $^{3}_{\infty}[I^{-}\cdot(I_2)_{6/2}]$ network to one describable as $^{3}_{\infty}[I_7^{-}]$.

There is no significant compression in the diiodine bond lengths throughout the study. Indeed, the maximum compression observed in the diiodine bond lengths within the first two phases [0.023(3) Å] is approximately equal to the compression of the coordination sphere of the cation across the range of only phase 1. This is most likely owed to the extreme compressibility of *D-1*$_{\text{intra}}$.

### 3.6.2. Bond order analysis for*D-1*

Before discussing the Mayer bond orders for *D-1* and indeed any of the parameters listed, attention should be drawn to the error associated with termination effects and the absence of the cation. Specifically, the so called intra- and intermolecular interactions discussed reside at differing distances from the termini of the fragment used in the majority of the calculations (Fig. 3) and thus under differing degrees of polarising partial charges; understanding the extent of these effects on the results is imperative to the validity of the discussion.

All calculations were run as single-point, gas-phase calculations and not periodic boundary calculations. In addition, to obtain an analysis of each, these were run without the presence of the cation owing to the computational cost of doing otherwise. Thus, they instead correspond to the precise fragment considered. Given the extended nature of the bonding in this system and the importance of charge distribution, it is possible that these factors will significantly affect the outcomes. Consequently, additional calculations were run which included cations for a select number of points so as to test the effect of the altered charge distribution. Further calculations to investigate the effects of centrosymmetry and termination of the framework on the results were run. These were again limited in number.

In the case of phase 1, *D-1*$_{\text{intra}}$ and *D-1*$_{\text{inter}}$ are equivalent in the crystal but not in the cation-free, non-centrosymmetric calculations that were run as standard. For these calculations, there is a difference of *ca.* 0.025 between calculated bond orders while the trends in the data match well (Fig. 20). With regards to the data calculated with the inclusion of eight cations, bond orders for *D-1*$_{\text{intra}}$ and *D-1*$_{\text{inter}}$ are indistinguishable in phase 1. The absolute values for phase 1 are slightly lower

than those for either parameter of the cation-free calculations but there is good agreement between calculated trends. Datafor*D-1*$_{inter}$ in the high pressure phases matches well between calculation types. The agreement of the absolute values is significantly lower for *D-1*$_{intra}$ in the high pressure phases but the trends still match well. There is little effect of the conformation of the macrocycle on the data. There was also no significant difference between calculations performed on centrosymmetric and non-centrosymmetric models. Consequently, although absolute values are of varied accuracy, discussion of the data can still be made owing to the prevalent consistency in the trends.

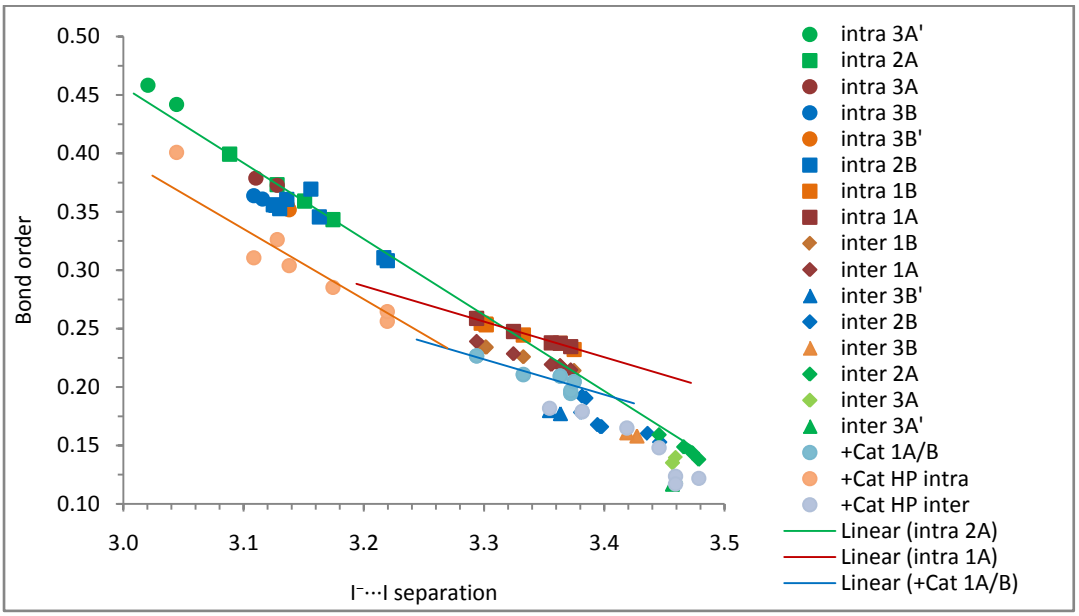



**Figure 20** The calculated Mayer bond orders as a function of atomic separation for *D-1* parameters for all phases studied. Linear polynomial fits extrapolated from specified data.

The Mayer bond orders calculated for *D-1* show linear dependence on distance for each interaction in phase 1, as can also be said for *D-1*$_{intra}$ in the high pressure phases. Significantly, the precise dependence differs between the centrosymmetric and non-centrosymmetric node. Where centrosymmetry is lost and increasingly distinct $I_7^-$ moieties are formed, there is a greater increase in bond order with

compression for *D-1*$_{intra}$ than *D-1*$_{inter}$. Thus, desymmetrisation of the iodide node gives rise to a new, stronger bonding interaction for *D-1*$_{intra}$ (Fig. 20).

The trend in bond order with compression for *D-1*$_{inter}$ shows a sigmoidal shape that appears to drop off as the separation increases towards 3.5 Å. The parameters which are displaced correspond to either those paired with *D-1*$_{intra}$ that is under additional compression (those of phase 3A) or to the sample under decompression (select data within phase 2B). In both cases, *D-1*$_{inter}$ is invariant while *D-1*$_{intra}$ is varied. This would imply that the compression of *D-1*$_{intra}$ weakens the bonding in*D-1*$_{inter}$, lending weight to the inference that compression of *D-1*$_{intra}$ in phase 2 results in the expansion of *D-1*$_{inter}$.

With the exception of the displaced values, the data for *D-1*$_{inter}$ in phases 2A/B and 3A/B show a displaced yet similar dependence on distance as for *D-1* in phase 1. This suggests that the nature of this interaction is relatively unchanged by the change in bonding for *D-1*$_{intra}$. Thus, the association of one iodide node with three diiodine moieties across the first phase transition constitutes a new mode of bonding and in turn weakens the remaining $I^{-}\cdots I$ interactions but the nature of *D-1*$_{inter}$ does not drastically change in the high-pressure phases.

Extrapolation of the linear polynomials fit to this data shows that the $I^{-}\cdots I$ separation at which a change in bonding becomes favoured is almost exactly that found at the phase transition. This gives a strong indication that the cause for the first phase transition is the favourability of a change in bonding at the iodide node and the formation of distinct $I_7^{-}$ anions. As the interaction is compressed towards this point, the depth of the energy minimum which corresponds to the centrosymmetric position of the iodide node decreases. Past this point, the position

becomes a local maximum and anisotropy or vibrations within the crystalline lattice would result in the iodide associating with three diiodines to from the heptaiodides anion. The weakening this serves to the surrounding *D-1*$_{\text{inter}}$ interactions results in a cascade response and the network collapses towards the $^{3}_{\infty}[I_7^-]$ network observed.

### 3.6.3. Interaction *D-2*: *1,3* $(I_2)\cdots(I_2)$ @ $I^-$

The two remaining separations of import to the discussion can be described as the separation of the diiodine molecules about the central iodide nodes. The first of these distances, *D-2* (*cf.* Table 2 & Fig. 17), can be considered as the closest separation of diiodines *1,3* separated about the node. In the same way as *D-1*, corresponds to both so-called intramolecular and intermolecular separations in the high-pressure phases; *D-2*$_{\text{intra}}$ and *D-2*$_{\text{inter}}$ are equivalent in phase 1.

Across all phases, excepting phase 3A, *D-2*$_{\text{intra}}$ remains relatively stable (Figs. 21 & 22). In phase 1, *D-2* is compressed by a total of 0.0959(17) Å to 10.4 kbar in a similar fashion as *D-1* (Fig. 21, *cf.* Fig. 18). This is a consequence of the mutual approach to the central iodide node of the iodine atoms in question, as shown by *A-2* being invariant in this phase (*vide infra*). Across the first phase transition, *D-2*-$_{\text{intra}}$ undergoes a small stepwise expansion [*ca.* 0.03 Å] as the iodide node collapses into the region between them and forces them apart, despite the stepwise compression in *D-1*$_{\text{intra}}$. This results in the separation adopting a value in the order of 5.30−5.35 Å, marginally greater than the separation at ambient temperature and pressure. The parameter remains at this distance for the duration of phase 2A/B and also for 3B.

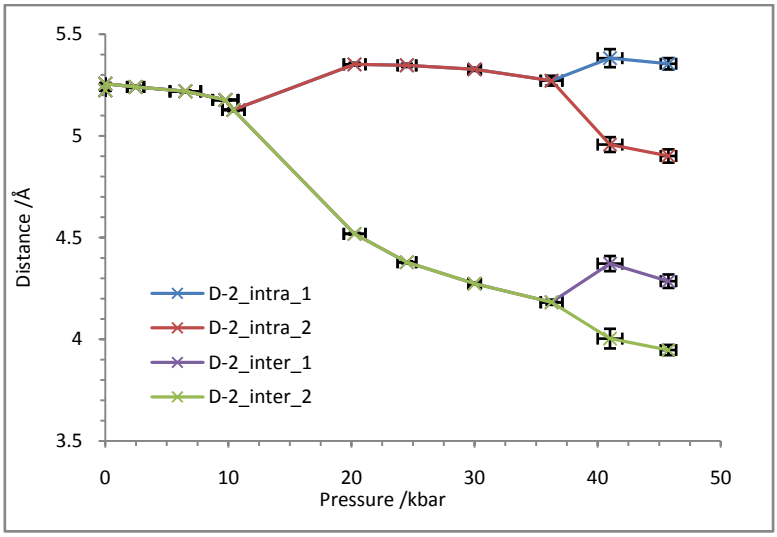



**Figure 21** The effects of pressure on *D*-$2_{intra}$ and *D*-$2_{inter}$ in crystal A. Lines track the progression of the experiment.

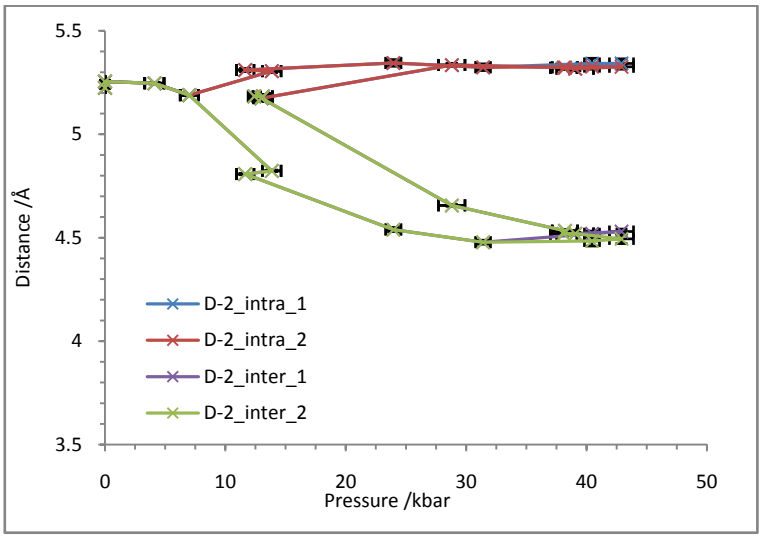



**Figure 22** The effects of pressure on *D*-$2_{intra}$ and *D*-$2_{inter}$ in crystal B. Lines track the progression of the experiment.

As the iodide node moves from a centrosymmetric position between the six diiodines to associate more closely with three of them, the remaining three now form the termini of three different heptaiodide moieties. The movement of the central node away from them necessitates that they come closer to one another else form a large region of highly compressible void space. The effect is such that

*D*-2$_{inter}$ undergoes a sharp compression of *ca.* 0.35 Å across the first phase transition, and at 11.7 kbar *D*-2$_{inter}$ = 4.8071(11) Å in phase 2B. In their study of bonding in $I_3^-$, Kloo *et al*. (2002) show that covalent bonding interactions are present up to a range of at least 5 Å and result in charge transfer interactions at this range. While this is not strictly applicable to *D*-2$_{inter}$ given as they comprise interaction between diiodine moieties rather than iodide and diiodine, it does imply that the formation of *D*-2$_{inter}$ from the preceding centrosymmetric phase corresponds to the formation of a new set of intermolecular interactions within the crystal.

With the continued application of pressure, *D*-2$_{inter}$ is found to be highly compressible in phase 2A and reaches a separation of 4.182(4) Å at 36.3 kbar. While it is still compressible in phase 2B, raising the pressure to 31.4 kbar only serves to compress *D*-2$_{inter}$to 4.478(3) Å. As the symmetry is further lowered from phase 2A/B to phases 3A and 3B, two inequivalent interactions are formed of both *D*-2$_{intra}$ and *D*-2$_{inter}$. In the case of phase 3B, neither of these differs within the certainty of the experiment and the two forms of *D-2* remain stable at the same distances found prior to the transition. This is not the case for phase 3A, in which the two inequivalent separations diverge significantly, with *D*-2$_{inter}$ adopting values of 4.372(12) and 4.004(16) Å at 41.0 kbar [*D*-2$_{intra}$ = 5.383(15) and 4.958(12) Å]. All *D-2* interactions in phase 3A continue to compress by *ca*. 0.06 Å to 45.8 kbar, with the shortest separation obtained for *D*-2$_{inter}$ being 3.947(8) Å. This divergence in the two parameters is believed to be directly related to the ordered desymmetrisation of the cation which templates the network.

Decompression of crystal B from phase 3B again reveals the intramolecular parameter following the profile of compression while reverse hysteresis is observed in *D-2*$_{inter}$. This again implies that the intermolecular parameter is most affected by the cations. The differing behaviour of *D-2*$_{inter}$ across phases 2A and 2B is, therefore, indicative of a different arrangement of macrocycle conformations between the crystals existing early on in the compression of these samples.

### 3.6.4. Interaction *D-3*: *1,2* $(I_2)\cdots(I_2)$ @ $I^-$

The third and final separation of note within the polyiodide network, *D-3* (*cf.* Table 2 & Fig. 17), can be regarded as the closest separation of *1,2* neighbouring diiodine moieties about the iodide nodes. Just as with *D-2*, the behaviour of *D-3* closely follows that of *D-1* across phase 1, and the behaviour of phase 1A and 1B both match (Figs. 23 & 24). Thus, *D-3* compresses from 4.2369(6) to 4.134(3) Å between ambient pressure and 10.4 kbar, at which point the pressure dependant behaviour abruptly changes. In phase 2A, *D-3* becomes almost entirely incompressible and remains at a distance about the edge of the sum of the van der Waals radii for the duration of the phase (Fig. 23). As pressure is further increased and phase 3A is formed there remains no significant deviation in this parameter despite the apparent divergence of the symmetry inequivalent interactions.

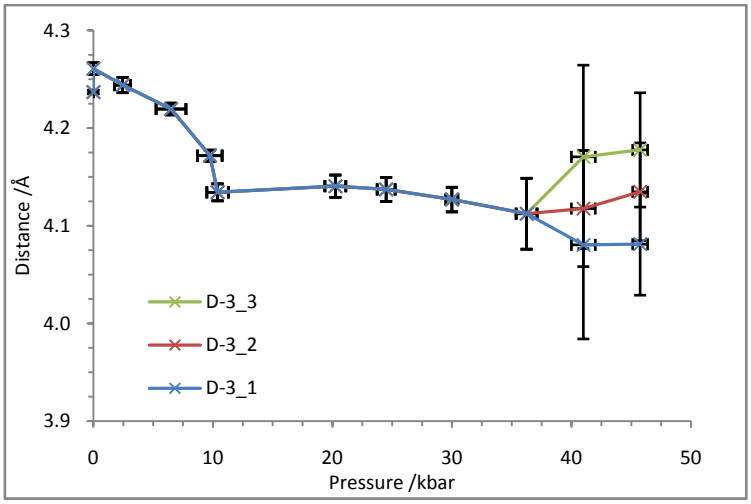



**Figure 23** The effects of pressure on *D-3* for crystal A. Lines track the progression of the experiment.

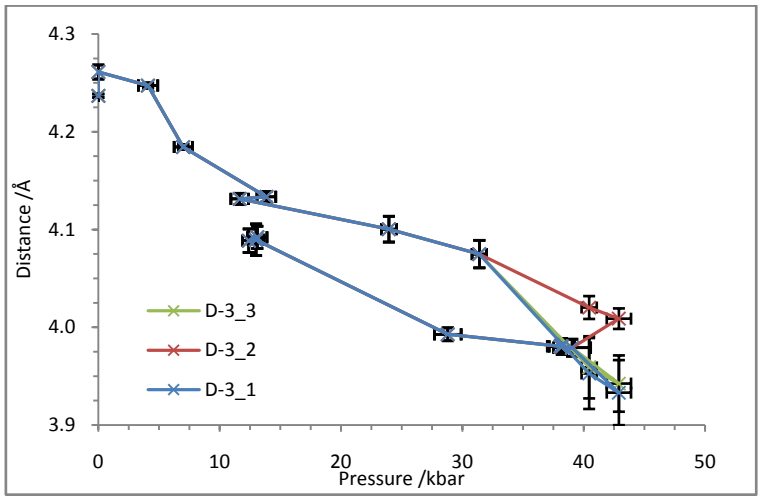



**Figure 24** The effects of pressure on *D-3* for crystal B. Lines track the progression of the experiment .

The behaviour in phase 2B is markedly different to that of 2A and *D-3* is seen to continue to compress across phase 2B, albeit at a reduced rate, with the appearance of a stepwise compression observed with formation of phase 3B (Fig. 23). The effect is that by 42.9 kbar the separation has come as close as 3.933(11) Å and might again be argued as constituting a new intermolecular interaction. It is interesting to note that decompression does not relax this stepwise compression.

Instead, while the parameter shows similar pressure dependence with decompression as compression, the absolute value remains displaced. This would suggest that the route of the discontinuity is not in change to the nature of the bonding but instead a response to other factors in the crystal, *i.e.*, the ordering of the cation in the third phase.

### 3.6.5. Bond order analysis for *D-2*$_{inter}$ and *D-3*

Calculations run with the inclusion of the cations show values for *D-2*$_{inter}$ to be grossly overestimated in the region dominated by electrostatic interaction (Fig. 25). In addition, calculations on non-centrosymmetric fragments were found to be a slight underestimate compared to those employing centrosymmetric fragments. Nevertheless, the trend otherwise showed a similar form as for the other main data calculated for *D-2*$_{inter}$. Results for *D-3* in the presence of the cations varied inconsistently, but grouped a region similar to that of those absent the cation.

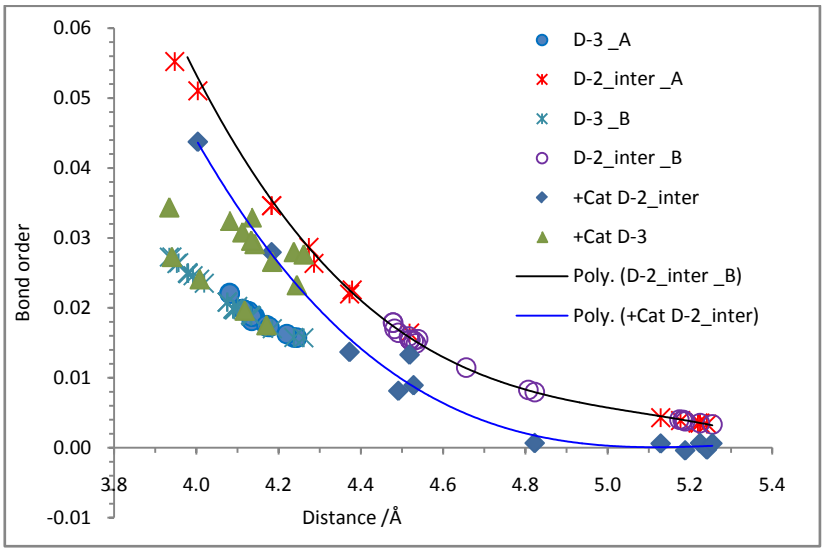



**Figure 25** The calculated Mayer bond orders as a function of distance for *D-2*$_{inter}$ and *D-3*. Black cubic polynomial fit to *D-2*$_{inter}$ for phase 2B and extrapolated.

The Mayer bond orders for *D-2*$_{inter}$ and *D-3* show that, despite their differing pressure dependence between crystals, the nature of the interactions is each the same in the two variants of phase 2 and phase 3. While there is some discussion surrounding the use of RS3000 as a PTM within the group, it is of note that the differences arise immediately following the first phase transformation which corresponds to a pressure well within the hydrostatic window established for the fluid by O'Connor (2014). Additionally, the 1 → 2 transformation is well rationalised by the DFT calculations and is not likely an effect of non-hydrostatic conditions. Thus it can be ruled out that the differing behaviour of *D-2*$_{inter}$ and *D-3* between crystals is a consequence of external effects. This corroborates the hypothesis that the differences between crystals are owed to differences in contacts between cations in the two crystals.

The sharp inflection and increase in bond order for *D-2*$_{inter}$ at *ca.* 4.7 Å is in corroboration with the work by Kloo *et al*. (2002) detailing the onset of covalent interactions dominating the bonding. These data show that compression of *D-2*$_{inter}$ across phases 2 and 3 corresponds to the formation of only a small bonding interaction, while prior to the collapse of the network over the 1 → 2 transition the interaction between these iodine atoms is negligible.

### 3.6.6. Angles about the iodide node

While much of their behaviour is intuitively linked to that of the distances already discussed, the pressure dependence of the angles outlined in Table 2 offer some important insight into the overall behaviour of the system. Angle *A-1* corresponds to the angle between diiodine moieties across the iodide node (*cf.* Table 2 &

Fig. 17) and is constrained to 180 ° by inversion symmetry in phase 1. As phase 2 is formed, the angle swiftly drops by *ca*. 15 ° with the displacement of the iodide from the centrosymmetric position (Figs. 26 & 27). The difference in behaviour of the two crystals at high pressure is again evident in this parameter, which continues to show that the polyiodide network in phase 3B is more symmetrical than that of phase 3A.

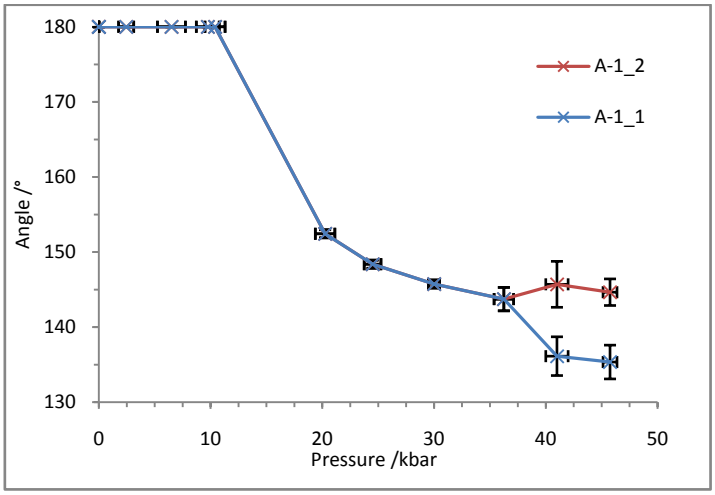



**Figure 26** The effects of pressure on angle *A-1* in crystal A. Lines track the progression of the experiment.

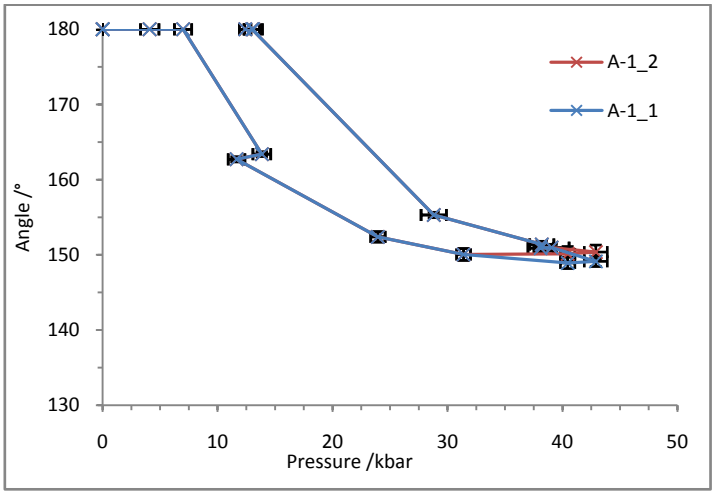



**Figure 27** The effects of pressure on angle *A-1* in crystal B. Lines track the progression of the experiment.

Angles *A*-$2_{intra}$ and *A*-$2_{inter}$ correspond to the $I_2\cdots I^-\cdots I_2$ angles *1*,*3* about the three-fold rotational axis (*cf.* Table 2 & Fig. 17), described with reference to phase 1 and 2, and graphically bare significant resemblance to the plots of *D-1* and *D-2* (Fig. 28 & 29, *cf.* Figs. 18 & 19, 21 & 22, respectively). These parameters again remain invariant across phase 1 and diverge at the first phase transition. The invariance across phase 1 shows that compression of *D-2* during this phase is associated to a compression of the diiodine moieties toward the iodide node without any other changes to the geometry at the node. The behaviour that follows the first phase transition reflects the movement of the iodide node into the plane of the three diiodine moieties it associates with, opening *A*-$2_{intra}$ and closing *A*-$2_{inter}$, with the extra compression of *D*-$2_{inter}$ in phase 2A serving additional contraction to *A*-$2_{inter}$.

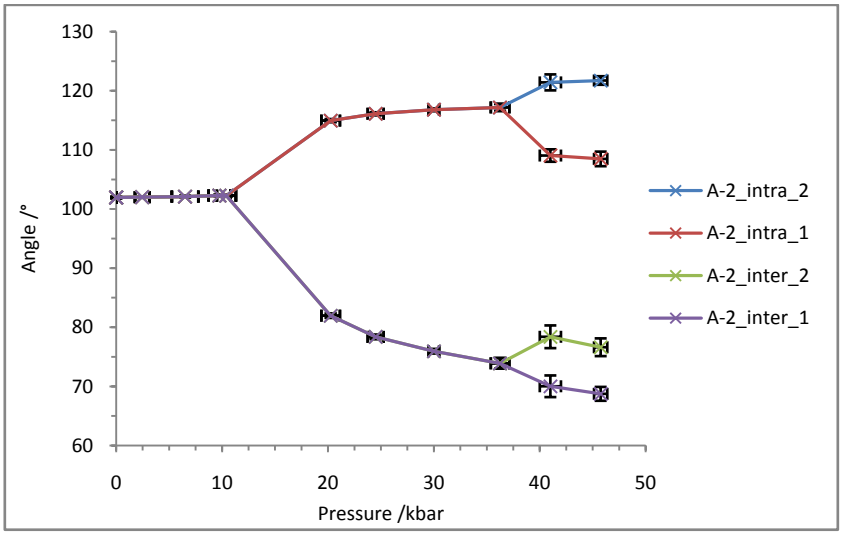



**Figure 28** The effects of pressure on angle *A*-$2_{intra}$ and *A*-$2_{inter}$ in crystal A. Lines track the progression of the experiment.

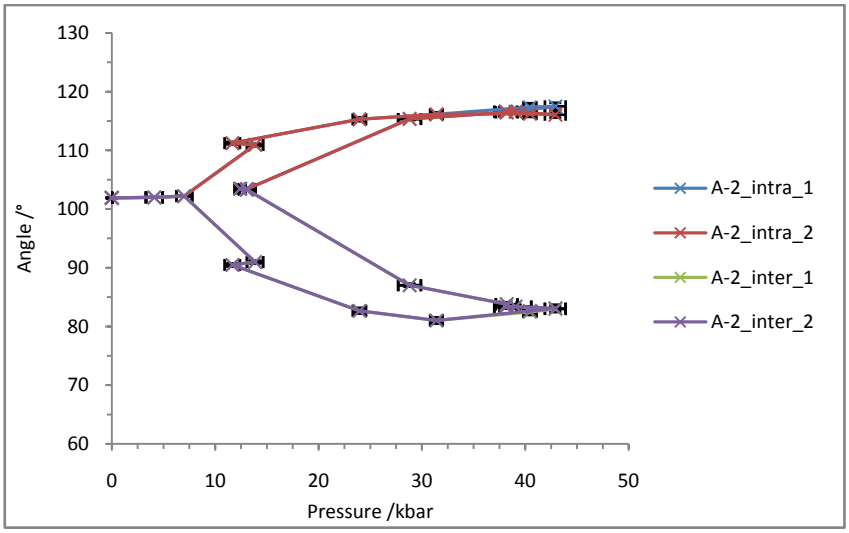



**Figure 29** The effects of pressure on angle *A-2*$_{intra}$ and *A-2*$_{inter}$ in crystal B. Lines track the progression of the experiment.

Angle *A-3* corresponds to the $I_2\cdots I^-\cdots I_2$ angle *1,2* about the three-fold rotational axis (*cf.* Table 2 & Fig. 17), described with reference to phase 1 and 2. It is the least variant of the angles described and relates most to *D-3* (Figs. 30 & 31, *cf.* Fig. 23 & 24). The parameter offers further corroboration of the rigidity of the geometry of the network across phase 1, but does not show a stepwise variation across the 1 → 2 phase transition. The smaller modal value in the bimodal distribution of angles found for I···I···I interactions in the CSD is *ca.* 85 ° (Fig. 2), reflective of iodide catenation occurring through the 5p orbitals. The behaviour of *A-3* might in turn reflect the fact that compression of the angle to below this is unfavourable and possibly resisted. Nevertheless, it is more likely limited by the sheer steric crowding about the iodide node.

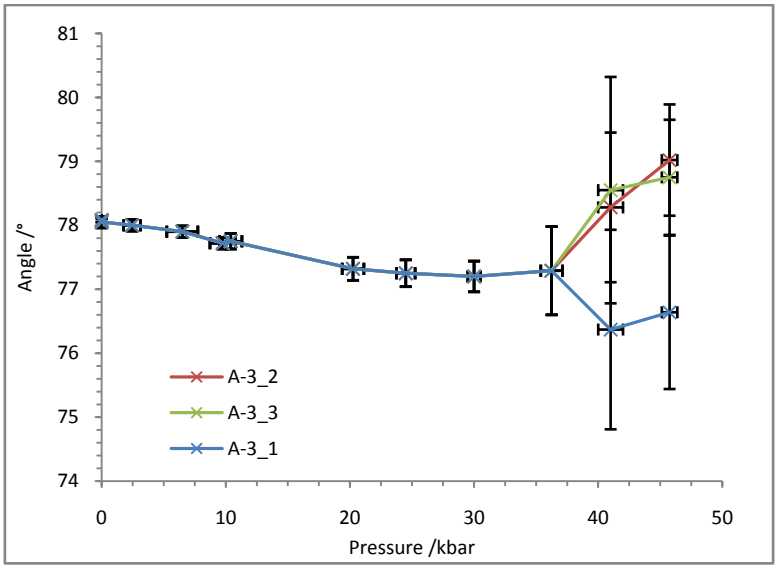



**Figure 30** The effects of pressure on angle *A-3* in crystal A. Lines track the progression of the experiment .

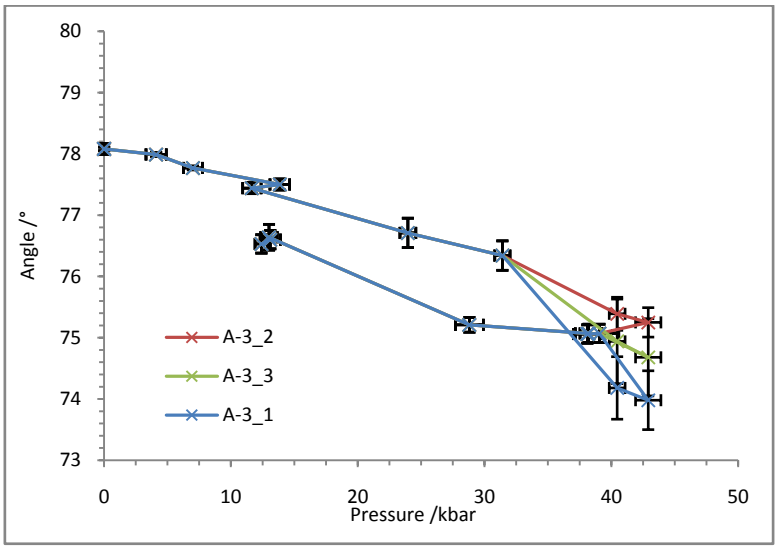



**Figure 31** The effects of pressure on angle *A-3* in crystal B. Lines track the progression of the experiment .

The final angles pertaining to the geometry of the polyiodide network, *A-4*, denote the angle of the diiodine moieties to the iodide node at the catenating iodine (*cf.* Table 2 & Fig. 17). In phase 1, $A\text{-}4_{\text{intra}}$ and $A\text{-}4_{\text{inter}}$ are again by necessity equivalent and are approximately invariant at 175.5 ° (Figs. 32 & 33). Transformation to

phase 2 sees little change in *A-4*$_{intra}$, the lowest value for which is 173.2(6) ° at 36.3 kbar in phase 2A with an approximately linear dependence on pressure. Additionally, the deviation between the two crystals appears negligible for this parameter during phases 1 and 2. The less symmetric geometry of phase 3A compared to phase 3B is again reflected here, with the inequivalent *A-4*$_{intra}$ interactions diverging by *ca*. 5 ° in the former and negligibly in the latter.

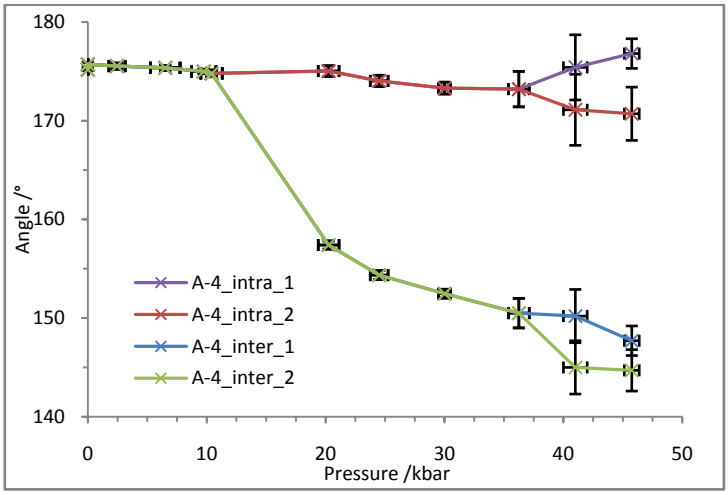



**Figure 32** The effects of pressure on angles *A-4*$_{intra}$ and *A-4*$_{inter}$ for crystal A. Lines track the progression of the experiment.

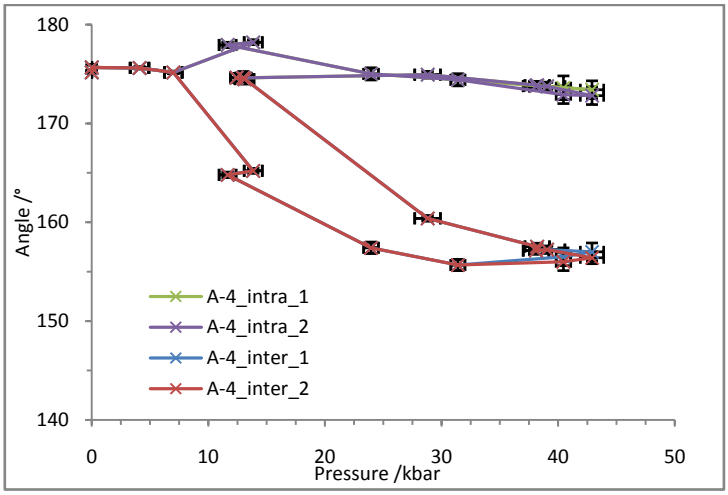



**Figure 33** The effects of pressure on angles *A-4*$_{intra}$ and *A-4*$_{inter}$ for crystal B. Lines track the progression of the experiment.

The deviation of *A-4*$_{inter}$ is much more significant after the first phase transformation, slightly more so in the case of crystal A, and in both cases is bent to below 160 ° by *ca*. 19 kbar. The matter of *A-4*$_{intra}$ remaining linear across the study is a reflection of the tendency of polyiodide bonding to adopt linear motifs. Thus, the behaviour of *A-4*$_{intra}$ further corroborates the description of the system as a $^{3}_{\infty}[I_7^-]$ network in the high pressure phases. Furthermore, the lack in deviation of *A-4*$_{intra}$, in association with the stepwise behaviour of *D-1* and *D-2* parameters, shows that as the iodide node is displaced and associates more closely with three diiodine moieties, the diiodines pivot about the closer iodine atom so as to remain in linear association with the node. This serves additional bending to *A-4*$_{inter}$.

### 3.7. Dominating interactions and differences between crystals

For crystal B, there is additional compression of *D-3* in phases 2 and 3 that is not seen in crystal A, while the opposite is the case for *D-2*$_{inter}$ and *D-1*$_{intra}$ in phase 3. The apparent difference in the conformation of the macrocycle between phase 3A and 3B offers a likely explanation for these differences in compression. The C−H···H−C contacts between cations are by far the most limiting contacts throughout the crystal. Unlike I···I or even H···I contacts, C−H···H−C contacts rapidly become repulsive as they are compressed to the edge of their van der Waals radii. In the absence of any cause indicated in the behaviour of the polyiodide network and while both forms of the 2 → 3 phase transition serve most change to the macrocycle, the generation of close contacts between cations is taken to be the driving force for this transition.

The differing appearance of the macrocycle between crystals in phase 3 implies that the major conformer and/or relative arrangement of the macrocycle and its neighbours differ between crystals at lower pressures. In such a case, so too would the specific manner in which the cations approach one another once these contacts dominate (Fig. 34). This phenomenon can be directly inferred by the relative compression of the unit cell axes (Figs. 5 & 6). In the event that their approaches differ, the effect of the cation in compressing the polyiodide network must too.

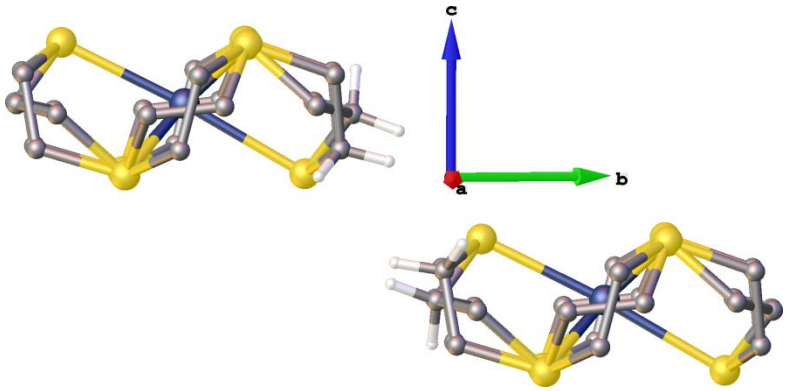



**Figure 34** Ball-and-stick image depicting the possible positions of the hydrogen atoms of neighbouring cations with cell vectors for phases 1 and 2 included. Clearly, the specific conformation of the macrocycle and its neighbours would have a large effect on the axial bias of compression.

Compression of the cations relative to one another along the *c* axis, a phenomenon observed to a far greater extent in crystal B than A (Fig. 35), serves compression to *D-3*. Accordingly, compression of *D-3* is observed in excess in crystal B (*cf.* Figs. 23 & 24). If compression in *c* is limited and instead *a* and *b* are preferentially compressed then $D\text{-}1_{\text{intra}}$ and $D\text{-}2_{\text{inter}}$ should receive additional compression while compression of *D-3* is stunted. This was seen to be the case across phases 2 and 3 for crystal A (Fig. 36). Thus, compression of the polyiodide framework is dependent on cation-cation contacts in phases 2 and 3.

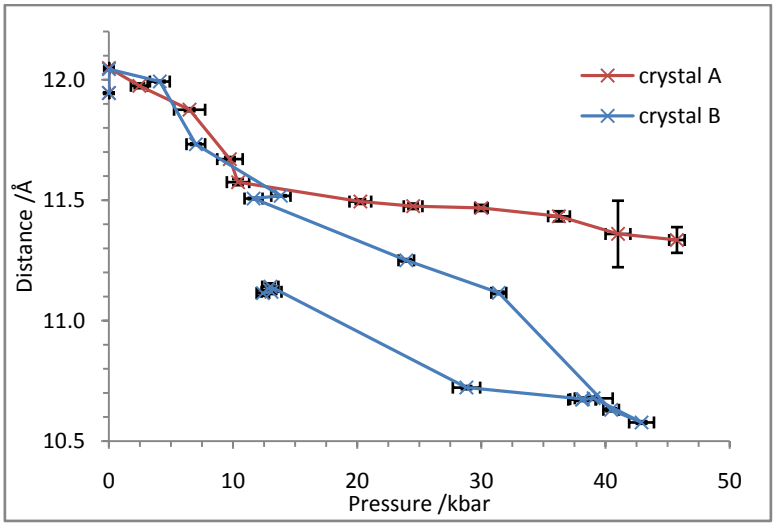



**Figure 35** The effects of pressure on the separation between silver centres separated directly along the vector corresponding to the *c* axis of phase 1.

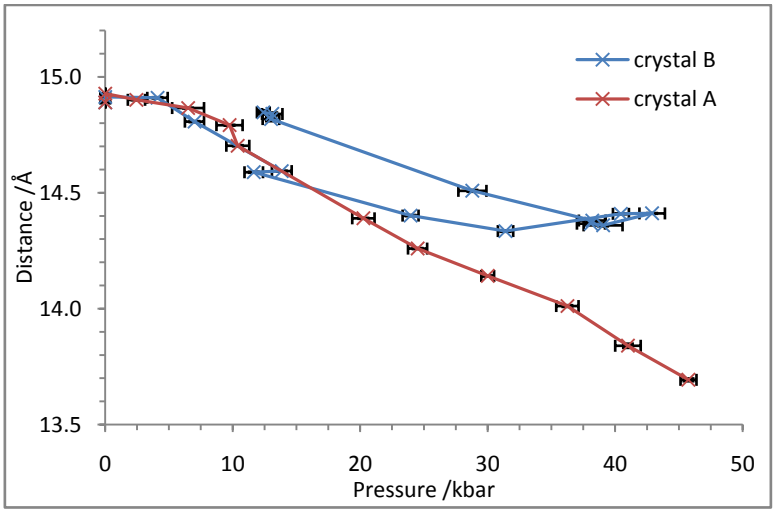



**Figure 36** The effects of pressure on the separation between silver centres separated directly along the vector corresponding to the *b* axis of phase 1.

This data corroborates the hypothesis that the change in pressure dependence of crystal B between compression and decompression is linked to the optimisation of contacts between cations across the second phase transition. The ordering of the cations in 3B appears to serve a stepwise compression to their separation in *c*. As mentioned previously, this additional compression would not be relieved unless the macrocycle conformation was to disorganise, a phenomenon for which there is no

significant driving force. This does not serve to further elucidate the specific differences in macrocycle conformation between crystals in the first two phases. However, it is interesting to note that two seemingly identical crystal structures at ambient pressure can have such unknown inherent differences that hold significant bearing on the compression of the system. This provides a prime example of why studying multiple crystals is so important in the field of high-pressure crystallography.

In the case that the differences in pressure dependence of the crystals in phases 2 and 3 are argued as being owed to the conformation of the macrocycle, the particulars of the disorder in phase 1 must also differ. Thus, the similar compression of both crystals in phase 1 indicates that compression of the phase is limited primarily by compression of the polyiodide network. This lends weight to the inference that the first phase transition is a response to factors intrinsic to the network.

## 4. Conclusions

Two crystals of [Ag([18]ane$S_6$)]$I_7$ were studied to *ca.* 45 kbar in RS3000, both yielding an $R\bar{3}m \rightarrow R3m$ phase transition at *ca*. 11 kbar and trigonal → monoclinic phase transitions at *ca*. 40 kbar. Compression across the first phase appears to be directly mediated through compression of the $I^{-}\cdots I$ separation which is compressed by 0.0695(13) Å up to 10.4 kbar, reaching 3.2937(12) Å in crystal A. This occurs with negligible distortion of the geometry of the polyiodide network. Interestingly, the rate of compression in this interaction accelerates across the range 6 to 11 kbar.

Across the first phase transition, the central iodide nodes are displaced from centrosymmetric positions to associate more closely with three diiodine moieties over the face of a cation. This affects a change in the polyiodide network from one described as $^{3}_{\infty}[I^{-}\cdot(I_2)_{6/2}]$ to $^{3}_{\infty}[I_7^{-}]$. The transition appears to be a ferroelectric transition given the sudden change in the polarisation that the change would bring to the $I_2$ linkers and indeed across the whole crystal.

Density functional theory calculations strongly suggest that this first phase transition is a response to the favourability of a change in bonding at the iodide node. The calculations indicate that below an $I^{-}\cdots I$ separation of *ca*. 3.27 Å it becomes favourable to form distinct heptaiodide moieties. This in turn weakens the remaining catenating interactions and so the formation of one unit results in a cascade effect.

Compression of phase 2 was found to differ between crystals, attributed to the likelihood of a difference in the major conformer and arrangement of neighbouring macrocycles. The differing compression is most notable in the parameters that define the compression of heptaiodide moieties towards one another. The application of pressure to this phase continues to compress the intramolecular $I^{-}\cdots I$ separation within heptaiodide moieties and the shortest such interaction observed in phase 2 is 3.089(5) Å at 36.3 kbar for crystal A. In contrast, the intermolecular $I^{-}\cdots I$ separation that catenates the termini of heptaiodides to central iodide nodes resists compression and even expands with continued application of pressure. This was attributed to the contraction of the intramolecular interactions serving to weaken these, potentially *via* a polarising effect of the central iodide node. Another notable phenomenon related to the compression of phase 2 is that the competitively

refined occupancies of the two disordered C sites for the macrocycle change from *ca*. 60:40 to 50:50 in both crystals.

Across the second phase transition, two related yet distinctly different phases are formed. In phase 3A, the macrocycle becomes fully ordered and an unprecedented, highly strained [84114] conformation is observed. This serves to significantly distort the cation but results in a reduction of close C−H···H−C contacts throughout the crystal. This decrease in symmetry of the cation in turn decreases the symmetry of the polyiodide network and there is a slight divergence in all of the parameters employed to describe it. The intramolecular $I^{-}\cdots I$ separations remain compressible and at 45.8 kbar the shortest of these reaches 3.020(9) Å.

Phase 3B differs from phase 3A most prominently in the conformation of the macrocycle, which adopts a [333333] conformation that also serves to reduce contacts between cations. This appears disordered from the perspective of the refinement but contacts are minimised only when the enantiomers of neighbouring sites differ. This case is entirely possible and thus has every reason to prevail. The greater symmetry of the cation and ordered alternation of enantiomers results in minimal desymmetrisation of the polyiodide network; the parameters describing it do not diverge in the manner seen for crystal A. In comparison to phase 3A, with the exception of an apparent stepwise compression upon formation, phase 3B is comparatively incompressible. Decompression of phase 3B back through phase 2B to phase 1 showed an altered response to pressure than that of compression. This was indicative of a retention of the ordered arrangement of cations in the [333333] conformation affecting a more dense phase.

The second phase transformation was concluded to be a response to close contacts between cations. The transition serves significant changes to the cations that in both cases minimise these contacts. The effects on the polyiodide network appear to be a consequence of said changes. The differing behaviour of the two crystals to compression highlights the need to study multiple crystals when undertaking high-pressure studies.

## References


Agilent (2014). *CrysAlis$^{PRO}$*. Agilent Technologies, Yarnton, England.

Allan, D. R.; Bailey, D.; Bird, N.; Blake, A. J.; Champness, N. R.; Huang, D., Keane, C. P.; McMaster, J.; Prior, T. J.; Tidey, J. P.; Schröder, M. (2014). *Acta Crystallogr., Sect. B*, **70**, 469-486.

Barnett, J. D.; Block, S.; Piermarini, G. J. (1973). *Rev. Sci. Instrum.* **44**, 1-9.

Becke, A. D. (1988). *Phys. Rev. A*, **38**, 3098-3100.

Bertolotti, F.; Curetti, N.; Benna, P.; Gervasio, G. (2013). *J. Mol. Struct.* **1041**, 106-112.

Blake, A. J.; Gould, R. O.; Lavery, A. J.; Schröder, M. (1986). *Angew. Chem.* **98**, 3, 282-283.

Blake, A. J.; Gould, R. O.; Parsons, P.; Radek, C.; Schröder, M. (1995). *Angew. Chem., Int. Ed. Engl.* **34**, 2374-2376.

Blake, A. J.; Devillanova, F. A.; Gould, R. O.; Li, W.-S.; Lippolis, V.; Parsons, P.; Radek, C.; Schröder, M. (1998). *Chem. Soc. Rev.* **27**, 195-205.

Clark, R. C.; Reid, J. S. (1995). *Acta Crystallogr., Sect A*, **51**, 887–897.

Cosier, J.; Glazer, A. M. (1986). *J. Appl. Crystallogr.* **19**, 105-107.

Dale, J. (1973). *Acta Chem. Scand.* **27**, 1115-1129.

Demartin, F.; Deplano, P.; Devillanova, F. A.; Isais, F.; Lippolis, V.; Verani, G. (1993). *Inorg. Chem.* **32**, 3694-3699.

Dolomanov, O.V.; Bourhis, L.J.; Gildea, R.J.; Howard, J.A.K.; Puschmann, H. (2009). *J. Appl. Cryst.* **42**, 339-341.

Fonseca-Guerra, C.; Snijders , J. G.; Te Velde, G.; Baerends, E. J. (1998). *Theor. Chem. Acc.* **99**, 391-403.

Grätzel, M. (2009). *Acc. Chem. Res.* **42**, 1788.

Groom, C. R.; Bruno, I. J.; Lightfoot, M. P.; Ward, S.C. (2016). *Acta Crystallogr., Sect. B*, **72**, 171–179.

Hach, R. J.; Rundle, R. E. (1951). *J. Am. Chem. Soc.* **73**, 4321-4324.

Holzapfel, W. B. (2003). *J. Appl. Phys.* **93**, 1813-1818.

Kahr, B.; Freuenthal, J.; Phillips, S.; Kaminsky, W. (2009). *Science*, **324**, 1407.

Kloo, L.; Rosdahl, J.; Svensson, P. H. (2002). *Eur. J. Inorg. Chem.* 1203-1209.

Li, B.; Nie, Z.; Vijayakumar, M.; Li, G.; Liu, J.; Sprenkle, V.; Wang, W. (2015). *Nature Commun.* **6**, 6303.

O'Connor, A. E. (2014). *Private communication*.

Perdew, J. (1986). *Phys. Rev. B*, **33**, 8822-8824.

Pickardt, J.; von Chrzanowski, L.; Steudel, R.; Borowski, M. (2004). *Z. Naturforsch., B: Chem. Sci.* **59**, 1077-1082.

Podsiadlo, M.; Katrusiak, A. (2006). *Acta Crystallogr., Sect. B*, **62**, 1090-1098.

Podsiadlo, M.; Katrusiak, A. (2008a). *CrystEngComm*. **10**, 1436-1442.

Podsiadlo, M.; Katrusiak, A. (2008b). *J. Phys. Chem. B*, **112**, 5355-5362.

Podsiadlo, M.; Katrusiak, A. (2009). *CrystEngComm*. **11**, 1951-1957.

Sheldrick, G. M. (2008). *Acta Crystallogr., Sect. A*, **64**, 112-122.

Sheldrick, G. M. (2015). *Acta Crystallogr., Sect. C*, **71**, 3-8.

Svensson, P. H.; Kloo, L. (2003). *Chem. Rev.* **103**, 5, 1649-1684.

Takemura, K.; Minomura, S.; Shimomura, O.; Fujii, Y. (1980). *Phys. Rev. Lett.* **45**, 1881-1884.

Te Velde, G.; Bickelhaupt, F. M.; Baerends, E. J.; Fonseca-Guerra, C.; van Gisbergen, S. J. A.; Snijders, J. G.; Ziegler, T. (2001). *J. Comput. Chem.* **22**, 931-967.

Tebbe, K.-F.; Buchem, R. (1997). *Angew. Chem. Int. Ed.* **36**, 12, 1345-1346.

Tebbe, K.-F.; Farida, T. (1995). *Z. Naturforsch*. **50b**, 1685-1691.

Tebbe, K.-F.; Gilles, T. (1996). *Z. Anorg. Allg. Chem*. **622**, 1587-1593.

Tebbe, K.-F.; Loukili, R. (1998). *Z. Anorg. Allg. Chem*. **624**, 1175-1186.

Tebbe, K.-F.; Nagel, K. (1996). *Z. Anorg. Allg. Chem*. **622**, 1323-1328.

Tidey, J. P.; Wong, H. L. S.; McMaster, J.; Schröder, M.; Blake, A. J. (2016). *Acta Crystallogr., Sect. B*, **72**, 3, 357-371.

Vosko, S. H.; Wilk, L.; Nusair, M. (1980). *Can. J. Phys.* **58**, 1200-1211.

Wang, Y.; Xue, Y.; Wang, X.; Cui, Z.; Wang, L. (2014). *J. Mol. Struct.* **1074**, 231-239.

Wiebenga, E. A.; Kracht, D. (1969). *Inorg. Chem.* **8**, 4, 738-746.

Zeng, Q.; He, Z.; San., X.; Ma., Y.; Tian., F.; Cui, T.; Liu, B.; Zou, G.; Mao, H.-K. (2008). *Proc. Nat. Acad. Sci.* **105**, 13, 4999-5001.

# Chapter 7

## Summary, Conclusions and Future Work

## 1. Introduction

This thesis constituted the continuation of our studies into the effects of pressure on macrocycle complexes of transition metals. It was largely the continuation and expansion of the work performed by Dr. Daniel Bailey, who reports the study of six complexes of the form [$MX_2$([9]ane$S_3$)], for which $M$ = Pd and Pt, and $X$ = Cl, Br and I (Bailey, 2013; Allan *et al.*, 2014). He showed that the interesting phenomena previously observed for $M$ = Pd, $X$ = Cl (Allan *et al.*, 2006) were in fact unique among the series. Despite being isomorphous and isostructural at ambient pressure, no other phase exhibited the stepwise contraction of the coordination sphere, piezochromic response or conformational rearrangement of the macrocycle. This was partly rationalised by the increased π-donation and crystal field stabilisation offered by the chloride donor serving to stabilise the unfavourable six-coordinate Pd(II) species. Why this was not observed for the Pt(II) species, however, was unclear. Clearly the behaviour of these metals differed in ways we do not yet understand.

## 2. Summary of scientific outcomes and proposals for future work

### 2.1. Chapters 2-4: studies of [$MX_2$([9]ane$S_2O$)] ($M$ = Pd, Pt; $X$ = Cl)

The first aim of this work was to expand our studies to include complexes of [9]ane$S_2O$, wherein the switching of one thioether donor for an oxygen ether donor serves most commonly to modulate the apical interaction. Previous work revealed the three phases of [$PdCl_2$([9]ane$S_2O$)] (**1**; Tidey, 2012), in which two conformers of the macrocycle existed. At that stage, it was becoming apparent that the β phase had been lost and might be described as a disappearing polymorph. It was thus a

logical step to investigate the comparable Pt(II) analogue, its crystallisation habits, and the high-pressure behaviour of all resulting phases of these compounds.

In Chapter 2, we see that [$PdCl_2$([9]ane$S_2O$)] (**2**) formed phases isostructural and isomorphous to the most stable α and 'lost' β phases of the Pd(II) complex, α-**1** and β-**1**, respectively. In contrast, no third phase corresponding to the favoured *exodentate* conformer of [$PdCl_2$([9]ane$S_2O$)], γ-**1**, was obtained. This was readily rationalised by DFT calculations which showed an equivalent "γ" phase for Pt(II) would be significantly less stable than the β phase. This was explained by the main directing interaction in the γ phase appearing to be an intermolecular chain-forming *M*···O interaction. In accordance with hard-soft acid-base principals, this interaction would be weaker for Pt(II) than Pd(II), corroborated by their differing cohesive energies.

Geometry optimised, periodic boundary DFT calculations also revealed that *exodentate* β-**1** and γ-**1** were similarly higher in energy compared to *endodentate* α-**1**. In addition, a β → α phase transition had been observed upon cutting a crystal of β-**1**. These factors indicate a favourability in β-**1** relaxing to α-**1**, a process that would be far more labile in the early stages of recrystallisation. With this competing mechanism and the discovery of γ-**1** potentially seeding future *exodentate* conformers to adopt its more favourable form, β-**1** was entirely lost. This disappearing phase was then recovered by employing the technique of epitaxy. It was found that **2** was significantly less soluble than **1** in the recrystallisation media, and β-**2** was isostructural and isomorphous to β-**1**. These factors enabled a crystal of β-**2** to be used to provide a surface upon which to seed the growth of β-**1**, and so the phase was recovered.

Chapters 3 and 4 provided the high-pressure and variable-temperature studies of the various phases of **1** and **2**, respectively, reported in Chapter 2. The experimental data was further complemented by single-point, gas-phase DFT calculations. For **1**, the γ phase was seen to be the most compressible with a bulk modulus of 7.6(6) GPa [$B'_0$ = 13.0(11)] for the third-order Birch-Murnaghan equation of state. The α and β phases of the two complexes were found to be similarly compressible as each other, with bulk moduli in the order 12-14 GPa [$B'_0$ = *ca.* 7-8] and differences between these being only in the order of 2σ significance. These points of general compressibility were rationalised by differences in the supramolecular motifs and distribution of compressible void space between phases.

For both complexes, study of the α phases provided smooth and continuous compression of the unit cell volume, with pressure serving to most compress the intradimer *M*···*M* and apical *M*···O interactions. These interactions proved only slightly harder in α-**2** than α-**1**, reflected to a greater extent in compression of the *M*···O rather than *M*···*M* interactions. The distinct similarity in the latter was taken as indicative of its compression being limited by contacts between equatorial donors in the base-to-base dimeric motif.

It was in the study of the two β phases that complexes **1** and **2** truly differed. In Chapter 3, a phase transition was observed at *ca.* 68.5 kbar for β-**1** accompanied by a tripling of the unit cell and extensive disorder owed to incomplete conformational rearrangement at two of the three resulting unique sites. This phase transition seemed immediately to be a response to a near-linear C−H···H−C approach between macrocycles. Behind the terminal carbons of this approach resided a pocket of highly-persistent void space. This space allowed the

macrocycle to undergo a conformational rearrangement that relieved the aforementioned close contact, seemingly at precisely the edge of the sum of the van der Waals radii. It was to be expected, therefore, that a similar transformation would be observed for β-**2** given the close similarity of these phases. A disordered conformational rearrangement was indeed observed at a similar pressure, rationalised by the same mechanism, but no extensive phase transition accompanied it. Further analysis of intradimer structural parameters, DFT calculated energies and Mayer bond orders revealed something quite interesting. The conformational rearrangement was found to be coincident in pressure as a seemingly repulsive change to the *M*···*M* bonding in β-**1** that was not seen for β-**2**. Given that the phase transition served a variety of changes to the specifics of this interaction in β-**1**, this was taken as indication that the full range of changes seen therein were a response to both the C−H···H−C approach and intradimer interactions.

Continuation of this project might include the extension to other halides. It was argued that the higher π-donation of the chlorides in [$PdCl_2$([9]ane$S_3$)] may have been a factor in bringing about its unique behaviour (Allan *et al.*, 2014). It would be interesting to see how changing the halide in **1** affects the plateau in the Pd···Pd bond order of the β phase. Indeed, the effect of switching the halide on the polymorphism of both **1** and **2** is itself uncertain and of interest to that area of the study. In any case, it may be possible to again use epitaxy to obtain phases of interest.

### 2.2. Chapter 5: piezochromism in $[Pd([9]aneS_3)_2](PF_6)_2 \cdot 2CH_3NO_2$

Chapter 5 primarily saw the study of piezochromism in the nitromethane solvate of $[Pd([9]aneS_3)_2](PF_6)_2$ (**3a**). Gradual piezochromism from a clear, sky-blue to a dull blue-green was observed up to 49.3 kbar, along with a 20% reduction in the unit cell volume and a 0.113(3) Å compression in the axial ligation. The equatorial bond lengths of this phase were found to be particularly compressible compared to compounds **1** and **2**, with this pressure bringing an average contraction of 0.025(3) Å to $Pd{-}S_{eq}$. These large compressions were attributed to the cations packing in sheets with C−H···S interactions between them to two of the three donors, while the third directed into regions of the anions and solvent molecules with which close S···O interactions were formed.

Between 49.3 and 51.0 kbar in the crystallographic experiment, a $P2_1/c \rightarrow P\bar{1}$ phase transition was observed with a doubling of the unit cell volume. The process was accompanied by two very striking changes in the crystal. The first was a discontinuity in the piezochromism from dull blue-green to dark orange. The second main change was in the orientation of the coordination axes. Across the phase transition there is an increase from one to four unique cations in the unit cell. In the former, elongated axial interactions align within the cationic sheets. In generating the high-pressure phase, **3a'**, an organised reorientation of the coordination axes occurs in two of the four resulting unique cations. This results in the axial interactions of the reoriented cations directing into the region of anion and solvent molecules. These interactions undergo no significant stepwise deviation across the transition, while the two that remain in the plane of the cationic sheets undergo stepwise compression of 0.052(7) and 0.116(8) Å.

The phase transition is also accompanied by a 2% stepwise compression of the unit cell volume. This corresponds to a decrease in the *PV* term of the Gibb's free energy of 32.2 kJ $mol^{-1}$. The phase transition was not found to exclusively reduce any close contacts without generating others of similar form. In the absence of any indication from DFT calculations that the axial Pd···S interactions were deviating to adopt / avoid a particular bond length, this large value for $\Delta PV$ was taken as the driving force for the phase transition.

Further application of pressure to **3a'** revealed continued smooth compression, and the total compression of *V/Z* from ambient pressure to 104.3 kbar was 28%. The axial interactions that remain in the plane of the cationic sheets were subject to continued compression of 0.64(14) Å. The reoriented interactions were subject to increased uncertainty in their lengths and appear not to undergo significant further compression. There was no further notable piezochromism.

Decompression of the sample revealed a *ca*. 10 kbar hysteresis loop and the return $P\bar{1} \rightarrow P2_1/c$ transition was found to occur between 37.9 and 40.7 kbar. The cause of the hysteresis was tentatively assigned to a lack of promoting forces for the reorientation of the coordination sphere against close and highly directional C−H···S interactions, and to the large expansion and increase in *PV* that it would bring likely favouring lower pressures.

Single-point, gas-phase DFT calculations were employed to further understand the piezochromism and found that calculated spectra of individual cations bore fair comparison with the experimentally obtained high-pressure solid-state UV/vis spectra. The piezochromism was thus attributed to compression of the axial

interaction, while differences between the calculated and experimental spectra were likely owed to outer-sphere effects

To further understand the effect of outer-sphere contacts on the piezochromism, a systematic study of the various phases of **3** is highly recommended and outlined in the closing paragraph of the chapter. Investigating the Pt analogue, which is isomorphous and isostructural to **3a** (Grant *et al.*, 2005), would also be of interest in expanding this study, seeing whether it differs in its propensity to reorganisation or exhibition of piezochromism. It might be that the phase transition occurs at a different pressure, with a different hysteresis loop, or perhaps with something else or even nothing at all of this kind occurring. In Chapters 3-4 and in the study of [$MX_2$([9]ane$S_3$)] we have already seen that isomorphous, isostructural complexes of Pd(II) and Pt(II) can differ significantly under pressure, and the phenomena surrounding **3a** provide a tantalising opportunity to further investigate this.

### 2.3. Chapter 6: compression of a templated polyiodide network

Following the observation that for the complexes [$M$$I_2$([9]ane$S_3$)] ($M$ = Pd, Pt) the iodides readily catenated with only moderate pressure (*ca.* 19 kbar), the aim arose to further investigate iodide catenation under pressure. The templated heptaiodide network in [Ag([18]ane$S_6$)]$I_7$ (**4**) provided an excellent opportunity to do this, with a highly symmetric $^3_\infty$[$I^-$·$(I_2)_{6/2}$] network. The six-fold arrangements of long $I^-\cdots I_2$ interactions were expected to offer interesting insight into polyiodide behaviour, and the phase did not disappoint. The interactions proved increasingly compressible up to *ca.* 11 kbar, at which point a reversible $R\bar{3}m \rightarrow R3m$ phase transition took place. The transition involved the collapse of the $^3_\infty$[$I^-$·$(I_2)_{6/2}$]

network towards one appearing to be of the form $^{3}_{\infty}[I_7^-]$. It was shown using single-point, gas-phase DFT calculations that this indeed constituted a change in the bonding about the central iodide node for the $I^-\cdots I_2$ interactions involved in forming the heptaiodide. This backed up the change in description for the polyiodide network. The transition also bore signs of constituting a ferroelectric transition, intuitively appearing to involve a distinct change in polarisation of the iodide framework and indeed the crystal as a whole.

Two crystals of **4** were studied that seemed indistinguishable under ambient conditions. During the first phase, phase 1, the crystals behaved near enough identically within expected error. After the first phase transition, in phase 2, their response to pressure differed significantly. In both cases, the $I^-\cdots I_2$ interactions within heptaiodide moieties remained highly compressible while those catenating these units instead expanded, reaching a limit slightly longer than their distance under ambient conditions. The particulars of these deviations, and also of the continued effect on the geometry of the framework, differed significantly. At *ca.* 40 kbar in both crystals, a second phase transition was observed that offered some insight into this difference. While cell parameters were similar and both phases formed in centred, monoclinic space groups, the resulting phase 3 differed between crystals. The phase transition occurred with only minor deformation to the polyiodide network that was in turn attributable to the more extensive changes in the cations. In one phase, ordered cations comprising the hitherto unseen [84114] conformation of the macrocycle were observed, while the other crystal appeared to contain a 50:50 proportion of the two possible enantiomers of the [333333] conformation. Both cases allow for a denser packing of cations that reduces the

more extreme H···H contacts that would be present in the earlier phases. This distinct difference between crystals in phase 3 of compound **4** was taken as indication that the conformers present and/or their arrangement in the lower pressure phases must differ. Taken in conjunction with the behaviour of various parameters describing the polyiodide network, this appeared to explain the differing response to pressure between crystals.

Future proposed targets lie firmly in the remit of our ongoing studies and are the reported polyiodides of Co(II) (Blake *et al.*, 1998) and Co(III) (Blake *et al.*, 2007) *bis*-[9]ane$S_3$ complexes. The former is the *bis*-triiodide, in which two triiodides reside end-to-end in an approximately linear fashion, separated by 4.874 Å. To the termini of these reside the cations which may affect in considerable compression of this central distance which resides at the long edge of the range of polyiodide interactions. The latter is a higher-order polyiodide that may be described as $3I_3^- \cdot I_2$ in which a wide range of catenating interactions appear. These interactions include some between $I_3^-$ and $I_2$ moieties that form the catenating interaction in asymmetric proto-pentaiodide moieties, and others at the edge of the van der Waals radii between said units. These two phases may allow the investigation of the range of polyiodide interactions and in a manner removed from the unusual case of a templated, highly-symmetric network.

**3. Wider conclusions**

While numerous phenomena have been observed and rationalised, these remain only individual insights into the high-pressure behaviour of a very particular class of compounds. Nevertheless, the studies presented in this body of work highlight a

few trends and key considerations applicable to high-pressure crystallographic studies. For example, the work of Chapters 3 and 4 show how supramolecular motifs and distribution of void space can dominate the high pressure behaviour of a phase. It may well have been foreseeable that γ-**1** would have been the most compressible phase of **1**, given the motif of complementary alternating chains surrounded by void space and largely quite compressible interactions. Furthermore, the conformational rearrangement in the β phases might well have been impossible or just destructive in the absence of such a well situated pocket of void space. Predicting that such a pocket would persist and facilitate such behaviour, however, would have required quite an extensive degree of modelling, the software for which may well not yet exist.

The work of this thesis also highlights the need for complementary techniques, specifically the value of DFT calculations. Without such work, rationalising the differing behaviour of β-**1** and β-**2** would have lacked supporting data and constituted a great deal more speculation. The use of DFT was further exemplified in both Chapters 5 and 6 where similar calculations provided the main basis for the rationalisation of piezochromism and a phase transition, respectively. Indeed, the absence of causative reasoning in said calculations for the two other phase transitions observed in those chapters further aided explaining the phenomena.

In Chapters 3 and 4, the added information brought by investigation of β-**2** served to further clarify the behaviour of β-**1** and indeed show that the phase transition was certainly a mixture of promoting factors. In contrast, the lack of any studies of the other phases of **3** in Chapter 5 is a notable absence with regards to our

understanding of its piezochromism. In this way, the benefits that are brought by more systematic studies are demonstrated.

The differing responses to decompression of the systems that gave phase transitions in Chapters 3, 5 and 6 together shows the importance of decompression studies being included in such experiments. To this end, it is notable just how few high-pressure crystallographic experiments actually report the decompression of samples. This may be owed to the difficulty of controlling decompression of a DAC. Also, the common and understandable practice of taking a sample to the maximum possible pressure will often result in the crystal failing before decompression can be considered. This is omitting the consideration that phase transitions will often greatly decrease the quality of a sample. In any case, it often seems more scientifically appealing to investigate a new sample under compression than spend expensive diffractometer hours or beam time decompressing a sample one believes to have investigated (the studies of α-**1**, α-**2** and γ-**1** reported herein all providing examples where this consideration won out).

A final point made by this work, and perhaps the most striking consideration raised, is the requirement of undertaking study of multiple crystals, particularly in the event of interesting phenomena. The difference in compression across the second phase of the two crystals of **4** were considerable and worked through to significantly differing third phases. While this was quite an extreme case, made possible by the very design of the phase as a templated framework, differences in the pressures obtained for the phase transition in studies of $[Pd([9]aneS_3)_2](PF_6)_2 \cdot 2CH_3NO_2$, and also differences between phase transitions

observed in the limited study of $[Pd([9]aneS_3)_2](PF_6)_2 \cdot 2CH_3CN$, yet highlight this point further.

## 4. Closing remarks

The conformational rearrangements of the β phases and also the phase 2 → 3 transitions in Chapter 6 were all shown to be responses to reducing C−H···H−C contacts with continued compression. In contrast, the β-**1** → β'-**1** transition in Chapter 2 and the phase 1 → 2 transition in Chapter 6 were both seemingly responses to changes in the bonding of more electronically complex Pd···Pd and I···I interactions. Even the **3a** → **3a'** transition in Chapter 5, which was seemingly a *PV* driven transition, was only made possible by the ability of the Pd(II) complex to undergo a reorganisation of its coordination axes. Clearly, the high-pressure chemistry of molecular crystals of coordination phases provides a complex and interesting area of scientific study with a great deal of potential for uncovering structural and related phenomena. Since such work is time consuming and expensive, it is likely that it will continue to be dominated by those studying structure-property relationships, particularly in this age of decreasing funding. Nevertheless, studies of this sort have a great deal to offer towards our understanding of chemical interactions, and many more are required if we are to begin understanding the processes which underpin phenomena such as those described herein.

## References


Allan, D. R.; Blake, A. J.; Huang, D.; Prior, T. J.; Schröder, M. (2006). *Chem. Commun.*, 4081-4083.

Allan, D. R.; Bailey, D.; Bird, N.; Blake, A. J.; Champness, N. R.; Huang, D.; Keane, C. P.; McMaster, J.; Prior, T. J.; Tidey, J. P.; Schröder, M. (2014). *Acta Crystallogr., Sect. B*, **70**, 469-486.

Bailey, D. (2013). *University of Nottingham*. PhD thesis: "High Pressure Studies of d-Block Thioether Co-ordination Complexes".

Blake, A. J.; Lie, W.-S.; Lippolis, V.; Parsons, S.; Schröder, M. (2007). *Acta Crystallogr., Sect. B*, **63**, 81-92.

Blake, A. J.; Lippolis, V.; Parsons, S.; Schröder, M. (1998). *Acta Crystallogr., Sect. C*, **54**, 293-295.

Grant, G. J.; Chen, W.; Goforth, A. M.; Baucom, C. L.; Patel, K.; Repovic, P.; VanDerveer, D. G.; Pennington, W. T. (2005). *Eur. J. Inorg. Chem.* 479-485.

Tidey, J. P. (2012). *University of Nottingham*. MSci dissertation: "High Pressure Crystallographic Study of Macrocyclic Platinum Group Complexes".

# Electronic Supplementary Information

# Index

| File name | Contents |
|---|---|
| | --------*Folder:*Chapter 2-------- |
| Chapter_2_combined.cif | Combined CIF for α-1 (aPd), β-1 (bPd), γ-1 (cPd), α-2 (aPt), β-2 (bPt) and β-epitaxy (bEpitaxy) as described in Chapter 2. |
| Chapter_2_tables.rtf | Combined crystallographic experimental tables for the above listed phases. |
| | --------*Folder:*Chapter 3-------- |
| alpha-Pd-Cl2-9S2O_high-pressure.rtf | Combined crystallographic experimental tables for the α-1 CIFs from high-pressure studies, listed by increasing pressure. |
| alpha-Pd-Cl2-9S2O_variable-temperature.rtf | Combined crystallographic experimental tables for the α-1 CIFs from variable-temperature studies, listed in order of collection. |
| beta-Pd-Cl2-9S2O_high-pressure.rtf | Combined crystallographic experimental tables for the β-1 and β'-1 CIFs from high-pressure studies, listed by increasing pressure. |
| beta-Pd-Cl2-9S2O_variable-temperature.rtf | Combined crystallographic experimental tables for the β-1 CIFs from variable-temperature studies, listed in order of collection. |
| gamma-Pd-Cl2-9S2O_high-pressure.rtf | Combined crystallographic experimental tables for the γ-1 CIFs from high-pressure studies, listed by increasing pressure. |
| gamma-Pd-Cl2-9S2O_variable-temperature.rtf | Combined crystallographic experimental tables for the γ-1 CIFs from variable-temperature studies, listed in order of collection. |
| HighPressure_aPd_combined.cif | Combined CIF for the high-pressure structures of α-1, listed by increasing pressure. |
| HighPressure_bPd_combined.cif | Combined CIF for the high-pressure structures of β-1 and β'-1, listed by increasing pressure. |
| HighPressure_cPd_combined.cif | Combined CIF for the high-pressure structures of γ-1, listed by increasing pressure. |
| SI_Chapter_3.docx | Supplementary information for Chapter 3 as referred to in the text. |
| VariableTemp_aPd_combined.cif | Combined CIF for the variable-temperature structures of α-1, listed in order of collection. |
| VariableTemp_bPd_combined.cif | Combined CIF for the variable-temperature structures of β-1, listed in order of collection. |
| VariableTemp_cPd_combined.cif | Combined CIF for the variable-temperature structures of γ-1, listed in order of collection. |

--------*Folder:*Chapter 4--------

| | |
|---|---|
| alpha-Pt-Cl2-9S2O_high-pressure.rtf | Combined crystallographic experimental tables for the α-1 CIFs from high-pressure studies, listed by increasing pressure. |
| alpha-Pt-Cl2-9S2O_variable-temperature.rtf | Combined crystallographic experimental tables for the α-1 CIFs from variable-temerature studies, listed in order of collection. |
| beta-Pt-Cl2-9S2O_high-pressure.rtf | Combined crystallographic experimental tables for the β-1 and β'-1 CIFs from high-pressure studies, listed by increasing pressure. |
| beta-Pt-Cl2-9S2O_variable-temperature-T0.rtf | Combined crystallographic experimental tables for the β-1 CIFs from variable-temperature studies on crystal T0, listed in order of collection. |
| beta-Pt-Cl2-9S2O_variable-temperature-T1.rtf | Combined crystallographic experimental tables for the β-1 CIFs from variable-temperature studies on crystal T1, listed in order of collection. |
| HighPressure_aPt_combined.cif | Combined CIF for the high-pressure structures of α-2, listed by increasing pressure followed by structure collected upon decompression. |
| HighPressure_bPt_combined.cif | Combined CIF for the high-pressure structures of β-2, listed by increasing pressure. |
| SI_Chapter_4.docx | Supplementary information for Chapter 4 as referred to in the text. |
| VariableTemp_aPt_combined.cif | Combined CIF for the variable-temperature structures of α-2, listed in order of collection. |
| VariableTemp_bPt-T0_combined.cif | Combined CIF for the variable-temperature structures of β-2 on crystal T0, listed in order of collection. |
| VariableTemp_bPt-T1_combined.cif | Combined CIF for the variable-temperature structures of β-2 on crystal T1, listed in order of collection. |

--------*Folder:*Chapter 5--------

| | |
|---|---|
| 3A_high-pressure_and_ambient.rtf | Combined crystallographic experimental tables for the 3A CIFs from high-pressure studies, listed by increasing pressure for those upon compression and followed by those upon decompression listed by decreasing pressure. |
| 3A-ambient_and_high-pressure-combined.cif | Combined CIF for the 3A structures from high-pressure studies, listed by increasing pressure for those upon compression and followed by those upon decompression listed by decreasing pressure. |
| 3A-high-pressure_decompression_cell-only_collections.cif | Combined CIF for the 3A cell determinations by decompression about the return phase transition, listed by decreasing pressure. |
| 3A-high-pressure_decompression_cell-only_collections-HKL_files.hkl | Combined HKL file for the 3A cell determinations by decompression about the return phase transition, listed by decreasing pressure. |
| 3B.cif | CIF for the routine structure determination of 3B. |
| 3B_ambient__3C-II_ambient_and_high-pressure.rtf | Combined crystallographic experimental tables for 3B, 3C-II and 3C-II_HP, in said order. |
| 3C-II.cif | CIF for the routine structure determination of 3C-II. |
| 3C-II_HP.cif | CIF for the 3C-II structure collected at 1.2 kbar in-house |

| | |
|---|---|
| SI_Chapter_5.docx | Supplementary information for Chapter 5 as referred to in the text. |
| --------*Folder:*Chapter 6-------- | |
| Crystal_A.rtf | Combined crystallographic experimental tables for the CIFs from high-pressure studies of crystal A of compound 4, listed by increasing pressure. |
| Crystal_A_combined.cif | Combined CIF for the high-pressure studies of crystal A of compound 4, listed by increasing pressure. |
| Crystal_B.rtf | Combined crystallographic experimental tables for the CIFs from high-pressure studies of crystal B of compound 4, listed by increasing pressure. |
| Crystal_B_combined.cif | Combined CIF for the high-pressure studies of crystal B of compound 4, listed by increasing pressure. |
| low-T.cif | CIF for the routine structure determination of compound 4. |
| low-T.rtf | Crystallographic experimental table for the routine structure determination of compound 4. |